Numerical Analysis of Wave-Seabed-Breakwater Interactions

Jianhong Ye
BEng MSc

A Thesis submitted for the degree of Doctor of Philosophy

Division of Civil Engineering

The University of Dundee

May 2012

To my wife Yan, son Dudu, my parents as well as parents-in-law

Publication list

[1]Ye J H & Jeng D-S (2012). Response of porous seabed to nature loadings-waves and currents. Journal of Engineering Mechanics, ASCE, In press, DOI: 10.1061/(ASCE)EM.1943-7889.0000356.

[2]Ye, J H & Jeng, D.-S. (2011). Effects of bottom shear stresses on the wave-induced dynamic response in a porous seabed: Poro-wssi (shear) model. Acta Mechanica Sinica, 27(6):898-910.

[3] D-S Jeng, Ye J H, PL-F Liu (2012). An integrated model for the wave-induced seabed response around marine structures: model, verifications and applications. Coastal Engineering, resubmitted.

[4] Ye J H & Jeng D-S (2012). Earthquake induced dynamic response of 3D poro-elastic unsaturated seabed under a rubble mound breakwater. Soil Dynamics and Earthquake Engineering. resubmitted.

[5] Ye J H & Jeng D-S (2012). The consolidation of 3D porous unsaturated seabed under rubble mound breakwater. Ocean Engineering, resubmitted.

[6] Ye J H & Jeng D-S (2010): Effects of bottom shear stresses on the wave-induced seabed dynamic response. The 11th BGA Young Geotechnical Engineers Symposium, Bristol, 6-8 July 2010.

Contents

List of Figures

List of Tables

List of Symbols

p_s	The pore pressure in seabed or porous medium
p_b	The wave induced pressure on the seabed surface
p	The water pressure in fluid domain
Δ	Laplace's operator
γ_ω	Unit weight of water
γ_s	Unit weight of soil
n	Porosity of porous medium
β	Compressibility of pore water
k, k_{ij}	Permeability of porous medium
k_x, k_y, k_z	Permeability of porous medium in the x, y, z direction
u_s, v_s, w_s	The displacement of soil in in the x, y, z direction
w_f	The relative displacement of pore water to soil particles
$u_{fi}, i = x, y, z$	The flow velocity of fluids in the x, y, z direction
G	Shear modulus
μ	Poisson's ratio
ϵ, ϵ_{ii}	volumetric strain of soil
α_B	Biot's coefficient
K_f	Volume modulus of water
K_s	Volume modulus of solid
p_{w0}	The absolute static pressure of pore water
S_r	Saturation
σ_{ij}	The total stresses
σ'_{ij}	The effective stresses
σ'_x, σ'_y, σ'_z	The effective stresses in the x, y, z direction
σ'_{x0}, σ'_{y0}, σ'_{z0}	The initial effective stresses in the x, y, z direction
τ_{xy}, τ_{yz}, τ_{xz}	The shear stress
τ	The magnitude of cyclic shear stress
g, g_i	Gravity
ρ_f	Density of pore fluid
ρ_s	Density of solid
ρ	Density of soil
L	Wave length
V_c	Velocity of compressive wave in soil
ω	Angular frequency of wave
λ	Wave number
h	Thickness of seabed
K_0	The lateral compression coefficient
d_{50}	The mean size of the soil particles
N_L	The cyclic number of loading making the soil reaching liquefaction
a, b	Fitting coefficients for N_L
D_r	The relative density of sand
C_a	The added mass coefficient for the porous flow

α	The empirical coefficients for linear porous flow
β	The empirical coefficients for nonlinear porous flow
$\langle u'_{fi} u'_{fj} \rangle$	Turbulence fluctuations on the mean flow in fluid domain
V	Volume of the elementary fluid
V_f	Portion occupied by fluid
$\langle\rangle$	Darcy's volume averaging operator
$\langle\rangle^f$	Intrinsic averaging operator
$\langle k \rangle$	Turbulent kinetic energy of fluid
$\langle \epsilon \rangle$	Dissipation rate of the turbulent kinetic energy
$\mathbf{u}$	Displacement vector of soil
$\mathbf{p}$	Pore pressure vector
$\mathbf{N^u}$	Shape function of displacement
$\mathbf{N^p}$	Shape function of pore pressure
$\bar{\mathbf{u}}$	vectors of node displacement
$\bar{\mathbf{p}}$	vectors of node pore pressure
M	Mass matrix
K	Stiffness matrix
Q	Coupling matrix
G'	Dynamic seepage force matrix
S	Compressibility matrix
H	Permeability matrixes matrix
$f^{(1)}$, $f^{(2)}$	Equivalent nodes forces
q	Water flux on the surface of computational domain
D, D^e_{ijkl}	Elastic matrix
D^{ep}, D^{ep}_{ijkl}	Elasto-plastic matrix
$H_{L/U}$	Plastic modulus at loading or unloading stage
m_{mn}	Plastic flow direction tensor
n_{st}	Loading or unloading direction tensor
f	Yield surface function
g	Plastic potential surface function
$\beta_1, \beta_2, \theta_1$	Coefficients used in Generalised Newmark time integration method
$d\epsilon_{ij}$	Strain increment
$d\epsilon^e_{ij}$	Elastic Strain increment
$d\epsilon^p_{ij}$	Plastic Strain increment
C^e_{ijkl}	Elastic compliance tensor
σ_{kl}	Stress increment
λ'	Lame's constant
ϵ^e_v	Elastic volumetric strain
ϵ^e_s	Deviatoric strain
K_{ev}	Bulk modulus of soil depending on the confined stress
G_{es}	Shear modulus of soil depending on the confined stress
p'	Mean effective stress
q'	Deviatoric stress
p'_0	Mean effective stress used to measure the elastic parameter of soil
K_{ev0}	Elastic bulk modulus of soil under p'_0
G_{es0}	Shear modulus of soil under p'_0

d_g	Dilatancy angle of soil
M_g	Slope of critical state line in $p' - q'$ plane
η	Ratio between the mean effective stress and deviatoric stress q'/p'
θ'	Lode's angle
ϕ	Residual internal frictional angle
$d\epsilon_v$	Increment of volumetric stain
$d\epsilon_v^p$	Plastic increment of volumetric stain
$d\epsilon_s^p$	Increment of deviatoric stain
p'_f	Constants characterizing the size of yield surface f
p'_g	Constants characterizing the size of plastic potential surface g
α_f, α_g	Coefficients related to the stress-dilatancy of soil
e	Ratio of soil
H	Wave height
d	Water depth
T	Wave period
U_0	Velocity of current
E	Young's modulus
j_x, j_y, j_z	Seepage force in the x, y, z direction
$L_{potential}$	Liquefaction potential of soil
d_{lique}	Maximum depth of transient liquefaction
θ	Angle between the incident wave and breakwater
$[\sigma']$	Effective stresses matrix
$[\epsilon']$	strain matrix

Acknowledgements

I would like to express my deepest thank to my supervisor Prof. Dongsheng Jeng, without whom, this thesis is impossible to be completed in the planned three years. In particular, I thank him for his valuable guidance and supervision in the three years of my PhD study, which makes me obtain a great number of knowledge on the ocean and coastal engineering. At the meantime, I would like to appreciate Prof. Dongsheng Jeng for his encouragement, patience towards me and my work, and selfless helps on my life in Dundee.

I would like to thank my co-supervisor Prof. Ping Dong for his kind help on my study and life in Dundee. His talk with me makes me more aware of what should be done in academic research. I also thank Prof. Ping Dong for introducing me to Prof. Dongsheng, which make me fortunately become a member in the present research group.

I would like to thank Prof. A H C Chan in University of Birmingham, and Prof. PL-F Liu in University of Cornell. Without their resource codes of soil model and wave model, it is impossible for me to develop the integrated numerical model in this thesis.

I would like to thank Dr Jisheng Zhang for his cooperative work on the 2D and 3D wave model. His work makes me develop the integrated model more conveniently.

I would like to thank my colleagues Huijie Zhang, Haixie Xu, Wenni Jeng, Jovan Stojsavljevic and Ismail Ahmed for their support and help on my study and life during this three years. Here, I specially express my appreciation to Ismail Ahmed. His talk and discussion with me greatly improve my ability of oral communication using English. Finally, I sincerely express my appreciation to Dr. A. Arora (Punjab Technical University), Jovan Stojsavljevic, Ismail Ahmed and S. Cosmin for their kind help to improve the writing in this thesis.

Declaration

I declare that this thesis is solely my work; that I have consulted all the references cited; that the work of which the thesis is a record has been done by myself, and that it has not been previously accepted for a higher degree.

The author Jianhong Ye © further solemnly declare that any content in this thesis, including texts, figures, tables are not allowed to be published in journal, conference proceedings, book or book chapter in the exactly same or similar form without the written permission from the author Jianhong Ye ©. Otherwise, the action of publishing any content in this thesis in the above mentioned medias is immoral plagiarism.

Signature:

Abstract

A 2D integrated numerical model PORO-WSSI II (Porous model for wave-seabed-structure interactions Version 2D) for the problem of wave-seabed-structures interaction is developed. Two sub-models are involved in this integrated numerical model: wave model and soil model. In the wave model, the Volume-Averaged Reynolds Averaged Navier-Stokes (VARANS) equation is used as the governing equation for wave motion and porous flow in porous medium. The linear, nonlinear drag force between pore water and solid matrix, and the inertial effect are all considered. In the soil wave, the dynamic Biot's equation known as "$u - p$" approximation is used to govern the soil behaviour, in which the acceleration of pore water and soil particles are included, however the relative displacement of pore water to soil particles is ignored. A coupling algorithm is developed in which the non-match mesh scheme and non-match time scheme are adopted, to integrate the two sub-models together. A series of validation works, mainly involving the progressive wave, standing wave, submerged breakwater and composite breakwater, are conducted for the developed numerical model. Under the same frame, the 2D integrated numerical model PORO-WSSI II is further extended to its 3D version PORO-WSSI III (Porous model for wave-seabed-structure interactions Version 3D) to investigate the three-dimensional wave-seabed-structures interaction.

First of all, the effect of a current on the wave-induced dynamic response of poro-elastic or poro-elastoplastic seabed is investigated adopting the developed 2D integrated model PORO-WSSI II. It is found that current has significant effect on the wave-induced response both in poro-elastic and poro-elastoplastic seabed.

Secondly, the developed 2D model PORO-WSSI II is further adopted to investigate the interactions between wave, a composite breakwater and its poro-elastic or poro-elastoplastic seabed foundation. A series of results, including the dynamics of the breakwater, variation of pore pressure and characteristics of wave-induced liquefaction in the seabed foundation are obtained.

Finally, due to the limitation of the 2D integrated model, the interaction between wave, breakwater and its seabed foundation in the region near to the breakwater head need to be investigated by adopting the developed 3D integrated model PORO-WSSI III. Under the same frame as that in 2D problem, the interactions between wave, a caisson breakwater and its poro-elastic or poro-elastoplastic seabed foundation are investigated using PORO-WSSI III. The results indicate that the caisson breakwater has significant effect on the wave-induced seabed response behind it. The caisson breakwater can effectively block the wave propagating to the zone behind it, and protect the seabed foundation behind it from liquefaction.

Chapter 1

Introduction

1.1 Background

The coastal zone is a unique geological, physical and biological area with vital economic, cultural and environmental value. More than two-thirds of the population in the world is concentrated in coastal zone, where the coastline is either the central or of great importance to trade, transport, tourism, leisure and the harvesting of marine food. In recent 20 years, marine structures, such as breakwaters, pipelines, turbines, and oil platforms, are widely constructed in offshore area to protect the coastline from erosion or damage, transport the fluid (petroleum, natural gas or fresh water), generate the green energy or extract crude oil from seabed. The research object involved in this thesis is mainly the breakwater built in offshore area. The functions of breakwaters in the offshore area include the following two points: (1) protecting a coast, ports, ship wharf fromm wave action (Figure 1.1 (a)); (2) manipulating the littoral transport condition, and thereby to trap same sand (Figure 1.1 (b)). However, these breakwaters built in offshore area are vulnerable to the liquefaction and shear failure of the seabed foundation due to the wave induced excess pore pressure and the excessive shear stress developed in their seabed foundation (Figure 1.2). Some failure examples of breakwaters have been reported in previous literatures (Table 1.1). In the practice of engineering, an inappropriate design and maintenance of a breakwater would result in the collapse of breakwater after construction, and bring great economic loss. Therefore, the response of seabed foundation, and the stability of breakwater built on the seabed foundation under ocean wave loading becomes the main concern for coastal engineers involved in design of marine structures.

(a) Breakwater to protect the port

(b) Breakwater to manipulate the transport condition of sand

Figure 1.1: Two typical functions of breakwater built in offshore area: protecting ports and/or manipulating the transport condition of sand

Table 1.1: Some failure examples of breakwaters in the world

Reporters	Year	Structure	Reason
Harlow (1980)	1980	breakwater	wave-induced liquefaction
Zen et al. (1985)	1985	breakwater	wave-induced liquefaction
Silvester and Hsu (1989)	1989	breakwater	wave-induced liquefaction
Lundgren et al. (1989)	1989	breakwater	wave-induced liquefaction
Sorenson (1992)	1992	breakwater	wave-induced liquefaction and impact
Oumeraci (1994)	1994	breakwater	wave-induced liquefaction and structures quality
Franco (1994)	1994	breakwater	wave-induced liquefaction and impact
Zhang and Ge (1996)	1996	breakwater	wave-induced liquefaction and impact
Chung et al. (2006)	2006	breakwater	soft foundation, sliding
Guillen (2008)	2008	breakwater	wave-induced impact
Puzrin et al. (2010)	2010	breakwater	wave-induced liquefaction
Campo and Vicente (2011)	2011	breakwater	sliding

(a) Breakwater failure in Prat Quay in Barcelona (Campo and Vicente, 2011)

(b) Breakwater failure in Barcelona Harbour, Spain (Puzrin et al., 2010)

Figure 1.2: Two typical breakwater failure examples in the offshore area occur in Spain recently

Through analyzing most of the failure examples of marine structures since 1930, Oumeraci (1994) pointed out that the reasons for the failure of marine structures could be classified into three categories: quality problems of structures, unexpected external wave loading on structures, and liquefaction and/or shear failure in seabed foundation. For the quality problems of structures, it could be solved through excellent project management methods and strategies. For the external wave loading on marine structures, a great number of investigations about the fluid-structure interaction have been conducted using experiments and numerical methods. A lot of mature commercial software and open source packages, such as FLOW-2D/3D, Fluids, OpenFoam etc., are released for the problem of fluid-structure interaction. However, as pointed out by Oumeraci (1994), wave induced loading on marine structures attracted most of the attention of scientists and coastal engineers in the engineering practice before 1990; the wave induced seabed response, and the wave-seabed-structure interaction was paid little attention. Unfortunately, the wave induced liquefaction and shear failure has been proven to be the main reason for collapse and instability of marine structures. Since the 1990's, a lot of investigations on the wave induced response, and the wave-seabed-structure interactions also are conducted (Jeng, 2003). At present, the literature in this field is abundant. However, the interaction mechanism between the ocean wave, marine structures, and their seabed foundation is still not fully understood.

Analytical approximations and decoupled numerical methods were widely adopted to study the wave-seabed-structures interaction (WSSI) in the early stage. However, the above two methods have inevitable limitations on understanding the WSSI mechanism. In the analytical approximations, only simple boundary conditions could be dealt with, for example, the breakwater was simplified as a line without width and weight. In the decoupled numerical model, some complex boundary conditions could easily be dealt with; however, the effect of outer shape of marine structures, and the porosity of seabed foundation on the wave field in the zone near to marine structures could not be taken into consideration. In recent ten years, some coupled numerical models were developed for the WSSI problem, in which the governing equation for fluid (Navier-Stokes, Laplace's equation), pore fluid (Modified Navier-Stokes), and the governing equation for porous seabed (Biot's equation) are integrated together. In the coupled models, both the effect of outer shape of marine structures, and the porosity of seabed foundation on wave field near to marine structures, and the effect of the gravity of marine structures on the seabed response can be considered. However, the wave-induced vibration of a breakwater, the wave-induced momentary liquefaction in poro-elastic seabed in front of a breakwater were not investigated so far by adopting a coupled numerical model.

Apart from elastic deformation, the wave-induced plastic deformation in seabed foundation is also sometimes very significant. It is well known that elastic deformation makes the excess pore pressure oscillate corresponding to the wave loading; the plastic deformation due to the compaction of soil particles makes the pore pressure in seabed foundation build up. If the residual pore pressure due to plastic deformation could overcome the overburdened weight at a position, the seabed foundation becomes liquefied at that position (residual liquefaction). The liquefied seabed behaves like a kind of liquid with heavy density without any shear resistance. As a result, the marine structures built on the liquefied seabed would collapse or tilt. Actually, the wave-induced pore pressure build up, and the residual liquefaction in seabed is much easier to occur than the oscillatory pore pressure and momentary liquefaction in engineering practice. At present, there is no literature available on investigation of the pore pressure build up, and evaluation of the residual liquefaction potential in a poro-elasto-plastic seabed foundation in front of a breakwater under wave loading by using a coupled model.

Additionally, to the author's best knowledge, all of previous coupled numerical model are limited to 2D. This limitation is serious under some situations. Figure 1.3 shows a sketch map for the wave-seabed-breakwater interaction in the offshore area. In Figure 1.3, it is illustrated that the 2D coupled numerical model is applicable at the middle part of the breakwater. However, it is not applicable in the zone near to the head of the breakwater. Generally, there are three types of wave field around the breakwater head. They are progressive wave far away from the breakwater, short-crested wave in front of the breakwater and diffracted wave behind the breakwater, respectively. The 2D coupled numerical model can not deal with the wave-seabed-breakwater interaction in the zone near to the head of breakwater. In this situation, 3D coupled numerical model are necessary.

1.2 Research tasks

To provide coastal engineers with a better understanding of the WSSI mechanism, an effective tool for the design and maintaining of marine structures, and avoiding the occurrence of failure due to

Figure 1.3: 3D integrated model is necessary for the wave-seabed-breakwater head interaction.

liquefaction or shear failure, a 2D coupled numerical model is first developed in this study. In this model, the dynamic Biot's equations (known as "$u - p$" approximation) and the Volume-Averaged Reynolds Averaged Navier-Stokes (VARANS) are taken as the governing equations respectively for porous medium and for wave motion and porous flow in the porous medium. A coupling algorithm is developed to integrate the two above governing equations together. Then, the developed 2D coupled model is validated by using a series of laboratory wave flume tests. Finally, this 2D coupled model is further extended to 3D coupled model for WSSI problem. The development of 3D coupled model is not to improve the computation accuracy, but to extend, enlarge and complete the application range of coupled numerical model for the problem of wave-seabed-breakwater interactions.

The development of the 2D and 3D integrated model PORO-WSSI II/III (Porous model for wave-seabed-structure interactions Version 2D/3D) are two original contributions in this research project. The solver of soil model in PORO-WSSI II/III is originally developed for the seismic soil dynamics, rather than for the wave-induced soil dynamics. A great number of source codes have been developed to make the solver of soil model can be applicable for the wave-induced soil dynamics problem. Additionally, a new loading system and a boundary conditions applying system in 2D and 3D space also have been developed, to make the developed 2D and 3D integrated model can deal with various types of loadings and boundary conditions. By applying the developed 2D and 3D model, specially, following problems are investigated. A series of innovative results and insights about the interaction between wave, breakwater and its poro-elastic or poro-elastoplastic seabed foundation are obtained.

- (1) The response of porous seabed to wave and current loading.
- (2) The wave induced vibration of breakwater, the wave induced momentary and residual liquefaction in poro-elastic and poro-elasto-plastic seabed in front of a composite breakwater (2D integrated model).
- (3) The wave induced vibration of breakwater, the wave induced momentary and residual liquefaction in poro-elastic and poro-elasto-plastic seabed around a caisson breakwater (3D integrated model).

1.3 Outline of this dissertation

This dissertation consists of seven chapters. Chapter 1 outlines the research background, and the research tasks of this dissertation. Chapter 2 is the ”Literature Review”, which summaries the previous works for the wave-seabed interaction, wave-seabed-breakwater interactions, and the wave induced liquefaction in a seabed. Chapter 3 detailedly describes the 2D/3D integrated numerical model, including the governing equations for seabed and seawater, numerical methods, and the coupling algorithm. Additionally, the verification of the developed numerical model by using a series of experimental data is performed. In Chapter 4, the response of porous seabed to wave and current loading is investigated. In chapter 5, the developed 2D numerical model is applied to investigate the wave-seabed-composite breakwater interaction; the wave induced momentary and residual liquefaction in the seabed foundation in front of the composite breakwater are paid special attention. In Chapter 6, the developed 3D numerical model is applied to investigate the the 3D wave-seabed-caisson breakwater interaction; the wave induced momentary and residual liquefaction in the seabed foundation around the caisson breakwater is specially studied. Finally, Chapter 7 presents the conclusions and the potential investigations that could be conducted in the future.

Chapter 2

Literature Review

2.1 Basic governing equations for seabed dynamics

It has been commonly known that soil is a multi-phase material consisting of soil particles, water and trapped air. Within the soil mixture, the soil particles form the skeleton; the water and the air fill the void of skeleton. Therefore, the soil is a three-phase porous material, but not a continuous medium. There are currently two kinds of theoretical models that are used to describe the mechanical properties of porous seabed soil :decoupled model and coupled model.

Prior to the development of coupled model, the decoupled model was widely adopted to investigate the problem of interaction between waves and the porous flow in sandy bed due to its simplicity. The decoupled model has two forms: Laplace's equation and Diffusion's equation.

2.1.1 Laplace's Equation

If the pore fluid and the soil particles are both considered as incompressible mediums, and the acceleration of fluid and soil are ignored, the Laplace's equation will govern the flow of pore fluid in porous soil, i.e.,

$$\nabla^2 p_s = 0 \tag{2.1}$$

where p_s is the wave-induced pore pressure in the seabed. ∇^2 is the Laplace operator.

A number of investigations on the interaction between sandy seabed and waves have been conducted based on the assumption of incompressible pore fluid, or incompressible soil particles. By treating the sandy seabed as a rigid and permeable medium, and the pore fluid as incompressible medium (Laplace's equation was adopted to govern the wave-induced dynamic pore pressure), Putnam (1949) proposed a simple solution for the wave induced percolation in an isotropic and finite porous seabed under linear wave loading. Putnam (1949) recognized that energy of the wave propagating on a porous seabed would attenuate significantly due to the friction and drag force between the pore fluid and the soil when percolating; and this seepage flow of pore fluid is driven by the dynamic pressure acting on the seabed surface. Sleath (1970) investigated the wave-induced pore pressure in a finite porous seabed with anisotropic permeability based on the Laplace's equation. The experiments conducted by Sleath (1970) with the aim of verifying his predicted results unexpectedly resulted in the discovery of the phase lag of wave-induced pore pressure in the sandy bed. Based on the current knowledge, this phase lag of wave induced pore pressure in sandy bed is the main reason for the transient liquefaction under wave trough. Liu (1973) simulated the porous flow in a permeable sand bed, and the damping rate of the wave propagating on sand bed based on the Laplace's equation. In this model, the viscous effect of the boundary layer was considered. After that, an analytical solution was further proposed for the damping of wave-induced pore pressure in a two-layered porous bed by Liu (1977).

2.1.2 Diffusion Equation

Another kind of uncoupled model was proposed by Nakamura et al. (1973), and Moshagen and Torum (1975) based on the diffusion equation, which treated the pore fluid as a compressible medium, while the seabed as a rigid medium. The governing equation for the mass conservation is expressed as:

$$\nabla^2 p_s - \frac{\gamma_w n\beta}{k_z}\frac{\partial p_s}{\partial t} = 0. \tag{2.2}$$

where γ_w is the unit weight of water, n is the porosity, β is the compressibility of pore water, and k_z is the permeability in z direction. Moshagen and Torum (1975) concluded that the compressibility of pore fluid greatly influenced the wave-induced pore pressure and the seepage force in porous medium. However, the experimental data obtained by Moshagen and Torum (1975) indicated that the coarse sand couldn't be represented by the Diffusion's equation due to its high permeability in coarse sand.

All aforementioned theories are decouped models, which consider the soil as incompressible medium, and the pore fluid as either incompressible medium (governed by Laplace's equation) or compressible medium (governed by Diffusion's equation). In fact, the pore fluid and the soil in the seabed is an integrated system. There are some complicated interactions between them. For example, an increase of pore pressure will compress the soil particles, and therefore make the volume of soil decrease correspondingly. This results in decrease of pore pressure in the soil, leading to the rebound of soil particles. Finally, a balance would be reached between the pore fluid and the soil particles in seabed. The conclusion drawn by Putnam (1949), that the pore pressure distribution in the sand bed has nothing to do with soil characteristics obviously is unacceptable. The theoretical results predicted by Sleath (1970) and Nakamura et al. (1973) could't agree with their own experimental data. These works therefore indicated that it is not reasonable to assume the soil and/or the pore fluid to be incompressible medium. Therefore, the Laplace's equation and Diffusion's equation are only applicable to some special cases, i.e. the Laplace's equation for very permeable medium, such as coarse sand and gravel; the Diffusion's equation for poorly permeable bed, such as clay. A reasonable method for investigating the interaction between pore fluid and soil is to adopt a coupled model.

2.1.3 Biot's equation

Coupled models generally treat both the soil and the pore fluid as compressible medium. They can more precisely describe the mechanical properties of porous medium and the soil-pore fluid interaction. Recently, the investigations of the consolidation or the dynamic response of seabed soil are conducted using this coupled models. The Biot's theory is the coupled model most widely used for the soil-pore fluid interaction. Depending on the inclusion of acceleration of soil particles and pore fluid, and the relative displacement of pore fluid to soil particles, there are three types of expression of Biot's equation: Quasi-static model, Full Dynamic model and "$u - p$" approximation.

2.1.3.1 Quasi-static model

Biot (1941) first formulated a three-dimensional consolidation equation treating the soil as an isotropic poro-elastic porous medium with compressible pore water and deformable soil particles. This was an extention from the one-dimensional consolidation theory of Terzaghi (1925). The formulas of stress equilibrium in the x, y, z direction are as following:

$$G\nabla^2 u_s + \frac{G}{1-2\nu}\frac{\partial \epsilon}{\partial x} = \alpha_B \frac{\partial p_s}{\partial x}, \tag{2.3}$$

$$G\nabla^2 v_s + \frac{G}{1-2\nu}\frac{\partial \epsilon}{\partial y} = \alpha_B \frac{\partial p_s}{\partial y}, \tag{2.4}$$

$$G\nabla^2 w_s + \frac{G}{1-2\nu}\frac{\partial \epsilon}{\partial z} = \alpha_B \frac{\partial p_s}{\partial z}. \tag{2.5}$$

where ∇^2 is the Laplace operator, u_s, v_s, w_s are the displacement of soil in the x-, y- and z- direction, respectively; p_s is the pore pressure. ϵ is the volume strain with $\epsilon = \epsilon_x + \epsilon_y + \epsilon_z$. Here, the effective stress principle is used: $\sigma'_{ij} = \sigma_{ij} - \alpha p \delta_{ij}$ (the compressibility is taken as positive). α_B is the Biot's coefficient. For saturated medium, α_B generally equals 1. G is the shear modulus of soil, and ν is the Poisson's ratio. The effect of gravity is not considered in the above equations.

The mass conservation equation of pore fluid, can be expressed as:

$$k\nabla^2 p_s = \alpha_B \frac{\partial \epsilon}{\partial t} + \frac{1}{Q}\frac{\partial p_s}{\partial t}, \tag{2.6}$$

where $1/Q = 1/K_f + (\alpha - n)/K_s$. K_f and K_s are the volume modulus of fluid and solid. Generally, K_s is much more greater than the K_f (2.25×10^9Pa). n is the porosity of soil, k is the Darcy's permeability coefficient. The coefficient $1/Q$ is to consider the compressibility of the pore fluid.

In Biot's model (Biot, 1941), the following assumptions are made:

1. The soil is homogeneous and isotropic.

2. The stress-strain relation is reversible under final equilibrium (linear elastic).

3. The soil is fully saturated.

4. Small deformation of solid and pore fluid are considered.

5. The pore fluid in porous, and soil particles are compressible.

6. The water flows steadily within porous medium, e.g. the Darcy's flow ($R_e \leq 1$ (Gu and Wang, 1991)).

In the Biot's theory, the flow of fluid in porous medium is generally treated as steady flow. Therefore, Darcy's law is used in formulating the equations. Also only the small deformation problem could be applicable. For large deformation nonlinear problem, the variation of G, μ, n and k in the deformation process have to be considered. It is worth noting that the Biot's consolidation equations (Biot, 1941) ignored the inertia terms of the solid and fluid. This kind of simplification is acceptable for consolidation process with small permeability or low frequency loading problems as the acceleration of the solid or fluid is apparently small under this situation.

Later, Equation (2.5) and (2.6) were further modified to include the effect of gravity, and to consider the behaviour of unsaturated soil:

$$G\nabla^2 w_s + \frac{G}{1-2\mu}\frac{\partial \epsilon}{\partial z} + \rho g = \alpha_B \frac{\partial p_s}{\partial z}, \tag{2.7}$$

$$k\nabla^2 p_s - \gamma_w n\beta \frac{\partial p_s}{\partial t} + k\rho_f \frac{\partial^2 \epsilon}{\partial t^2} = \gamma_w \frac{\partial \epsilon}{\partial t}. \tag{2.8}$$

where $\rho = \rho_f n + \rho_s(1-n)$ is the average density of porous seabed; ρ_f = the fluid density ; ρ_s = solid density; g= the gravitational acceleration, γ_ω is unit weight. In equation (2.8), the compressibility of pore fluid (β) is defined as

$$\beta = \left(\frac{1}{K_f} + \frac{1-S_r}{p_{w0}}\right), \tag{2.9}$$

where S_r = the degree of saturation of seabed, p_{w0} = the absolute static pressure

Equation (2.3), (2.4), (2.7) and (2.8) could be used to investigate the consolidation process of unsaturated soil foundation under compression of structures. This development is a substantial improvement for the application of Biot's consolidation equation in engineering practice.

2.1.3.2 Full-Dynamic models

Biot (1955, 1956a) further extended the above quasi-static model from isotropic to anisotropic cases, and from poro-elastic to viscoelastic medium. Later, based on the stress balance, momentum conservation and mass conservation, Biot (1956c,b) extended the above consolidation theory to dynamic theory by introducing the inertia terms of solid and fluid, to investigate the propagation of elastic waves in saturated porous medium. Then, Biot (1962) proposed a set of general fully coupled governing equations for saturated porous medium with compressible fluid and incompressible soil particles for consolidation and dynamic problems, in which the effect of inertia terms of solid and fluid, and the interaction (drag force) between soil and pore fluid are taken into consideration. The stress equilibrium equation, momentum equilibrium equation and continuity equation respectively are (in the form of tensor):

$$\sigma_{ij,j} + \rho g_i = \rho \ddot{u}_{si} + \rho_f \ddot{w}_{fi}, \tag{2.10}$$

$$(p_s)_{,i} + \rho_f g_i = \rho_f \ddot{u}_{si} + \frac{\rho_f}{n} \ddot{w}_{fi} + \frac{\rho_f g}{k_{ij}} \dot{w}_{fj}, \tag{2.11}$$

$$\dot{\epsilon}_{ii} + \dot{w}_{fi,i} + \frac{n}{K_f} \dot{p}_s = 0. \tag{2.12}$$

where σ_{ij} is the total stresses, ϵ_{ii} is the volumetric strain . $\rho = (1-n)\rho_s + \rho_f$ is the average density of the porous medium, ρ_f and ρ_s are the density of the solid and fluid. $(u_s)_i$ and $(w_f)_i$ are the displacement of the solid and the relative displacement of fluid to solid, respectively. g_i is the gravity. p_s, n and k are the pore pressure, porosity and permeability coefficient respectively. From the equilibrium equations (2.10) , it can be seen that the inertia effects of solid and fluid have been considered and are crucial influence factor for some dynamic problems. In the momentum equilibrium equation (2.11), the interaction force between the solid and fluid is included. The drag force is expressed as:

$$F = \frac{\rho_f g}{k_{ij}} \dot{w}_{fj} = \frac{\gamma_\omega}{k_{ij}} \dot{w}_{fj}. \tag{2.13}$$

The above expression is a linear approximation for the interaction force between soil and pore fluid, which is only applicable for fluid whose Reynolds number is limited to a certain value, and for the dynamic loading with low-frequency (Biot, 1956b). For the cases in which porous flow with large Reynolds number or high-frequency loading are involved, this kind of linear approximation is not reasonable. In the continuity equation (2.12), it is found that only the pore fluid is compressible, the solid is considered as an incompressible particles. These equations can be easily generalized to non-linear and anisotropic material behaviour if the constitutive relation between strain and stress is written in incremental form.

Zienkiewicz et al. (1980) further extended and improved the above governing equations to consider the compressibility of solid, and the acceleration convective term of fluid which is brought by the transformation from Lagrange coordinate system to Euler coordinate system. The governing equations are expressed as:

$$\sigma_{ij,j} + \rho g_i = \rho \ddot{u}_{si} + \rho_f (\ddot{w}_{fi} + \dot{w}_{fj} \dot{w}_{fi,j}), \tag{2.14}$$

$$-(p_s)_{,i} + \rho_f g_i = \rho_f \ddot{u}_{si} + \frac{\rho_f}{n} (\ddot{w}_{fi} + \dot{w}_{fj} \dot{w}_{fi,j}) + \frac{\rho_f g}{k_{ij}} \dot{w}_{fj}, \tag{2.15}$$

$$\dot{\epsilon}_{ii} + \dot{w}_{fi,i} + \frac{1}{Q} \dot{p}_s = 0. \tag{2.16}$$

where

$$\frac{1}{Q} = \frac{n}{K_f} + \frac{1-n}{K_s}. \tag{2.17}$$

For unsaturated soil (saturation S_r), the volume modulus of fluid with air bubbles K_f is determined by (Verruijt, 1969)

$$K_f = \frac{1}{\frac{1}{2.25 \times 10^9} + \frac{1-Sr}{Pw0}}. \tag{2.18}$$

In the equilibrium equations (2.14) and (2.15), the term $\ddot{w}_{f\,i} + \dot{w}_{f\,j} \dot{w}_{f\,i,j}$ is the relative acceleration of fluid to solid; the $\dot{w}_{f\,j} \dot{w}_{f\,i,j}$ is the convective term generated due to the coordinate transformation from Lagrange to Euler. The inclusion of the compressibility of solid and the convective term of acceleration in governing equations results in a better description for the mechanical behaviour of porous medium. However, Zienkiewicz et al. (1999) also pointed out that the convective term of fluid acceleration is apparently small for Darcy flow in porous medium. Usually, it could be eliminated from the above equations for the sake of simplicity. Therefore, the governing equations can be written as:

$$\sigma_{ij,j} + \rho g_i = \rho \ddot{u}_{si} + \rho_f \ddot{w}_{fi}, \tag{2.19}$$

$$-(p_s)_{,i} + \rho_f g_i = \rho_f \ddot{u}_{si} + \frac{\rho_f}{n}\ddot{w}_{fi} + \frac{\rho_f g}{k_{ij}}\dot{w}_{fj}, \tag{2.20}$$

$$\dot{\epsilon}_{ii} + \dot{w}_{fi,i} + \frac{1}{Q}\dot{p}_s = 0. \tag{2.21}$$

where the $\frac{1}{Q}$ is the same with equation (2.17). The above equations are a complete form with relative high accuracy widely used in numerical calculation. It is usually referred as to the "$u - w$" form. The unknowns are $(u_s)_i$ (displacement of solid), $(w_f)_i$ (the relative displacement of fluid), and p_s (the pore pressure). In numerical calculation, such as FEM, the degree of freedom is 5 for 2D condition, and 7 for 3D condition.

2.1.3.3 "$u - p$" approximation

Zienkiewicz et al. (1980) proposed another simplified form of the Biot's equation. In this model, the relative acceleration of fluid to solid is eliminated from the stress equilibrium equations (2.19) and (2.20), because the relative acceleration of fluid is apparently small for porous medium with a low permeability, and acted by low-frequency dynamic loading. After substituting the (2.21) into (2.20), the governing equation becomes:

$$\sigma_{ij,j} + \rho g_i = \rho \ddot{u}_i, \tag{2.22}$$

$$\dot{\epsilon}_{ii} + (\frac{k_{ij}}{\gamma_\omega}(-p_{s,j} - \rho_f \ddot{u}_j + \rho_f g_j))_{,i} + \frac{1}{Q}\dot{p}_s = 0. \tag{2.23}$$

The above governing equations are usually referred to as to "$u-p$" approximation. It is also a popular form used for porous medium with small permeability. In this thesis, the "$u - p$" approximation is adopted as the governing equation for the porous seabed foundation. The unknowns are u_i and u_j (the displacement of solid), and p_s (the pore pressure). In numerical calculations, the degree of freedom is 3 for 2D condition, and 4 for 3D condition. Therefore, the degree of freedom and calculation work can be decreased greatly, if the "$u-p$" form is used for cases with low permeability and low frequency loading, without sacrificing too much accuracy. For the quasi-static consolidation problems, the above equations can be further reduced to the Biot's consolidation equations by ignoring the inertia term:

$$\sigma_{ij,j} + \rho g_i = 0, \tag{2.24}$$

$$\dot{\epsilon}_{ii} + (\frac{k_{ij}}{\gamma_\omega}(-p_{s,j} + \rho_f g_j))_{,i} + \frac{1}{Q}\dot{p}_s = 0. \tag{2.25}$$

It is noted that equations (2.24) and (2.25) are the tensor form of equation (2.3) to (2.8).

2.1.4 Applicable range of Biot's equation

To date, the "$u - w$" form, "$u - p$" approximation, and the Biot's consolidation equations have been widely used for investigating the quasi-static and dynamic problems. Basically, the "$u - w$" form is applicable for all quasi-static and dynamic problems due to its relatively complete form to describe the mechanical behivor of porous medium, in which the acceleration of soil particles and pore fluid, and the relative displacement of pore fluid to soil particles are all included. However, some preconditions have been assumed when deriving the "$u - p$" approximation, and the Biot's consolidation equations. Therefore, there are some limitations for applying the "$u - p$" approximation and the Biot's consolidation equations to engineering problems.

Zienkiewicz et al. (1980) first made their attempt to investigate the applicable range of the "$u-p$" approximation and Biot's consolidation equations. Based on a simple linear one-dimensional model, in which only one soil layer is contained, and subjected to periodic loading, the "$u - w$" form, "$u - p$" approximation, and the Biot's consolidation equations are all analytically solved with the same boundary conditioins. After comparing the solutions obtained from the three kinds of governing equations, Zienkiewicz et al. (1980) produced a graph (Figure 2.1) to illustrate the applicable range of frequency and permeability for the "$u - p$" approximation, and the Biot's consolidation equations. As shown in Figure 2.1, there are totally three zones (I, II and III), where the abscissa $\Pi_1 = \frac{k\rho V_c^2}{\omega L^2}$ is related to the permeability of soil; the longitudinal coordinate $\Pi_2 = \frac{\omega^2 L^2}{V_c^2}$ is related to the frequency of dynamic loading. From Figure 2.1, Zienkiewicz et al. (1980) concluded that "$u - w$" form can be used in all zones, including I, II, and III. The "$u - p$" approximation can be used in zone I and II with the largest applicable frequency approximately 1000Hz. The Biot's consolidation equations only can be used within zone I. It is only applicable for low frequency and low permeability problems.

It is noted that Figure 2.1 is obtained from the simplest one-dimensional soil layer; and the values of some property parameters of soil are assumed, such as $V_c = 1000m/s$. As pointed out by Cha et al. (2002) and Jeng and Cha (2003), the velocity of wave in soil is significantly dependent on the saturation of soil and the water depth. The value of wave velocity used in Zienkiewicz et al. (1980) is

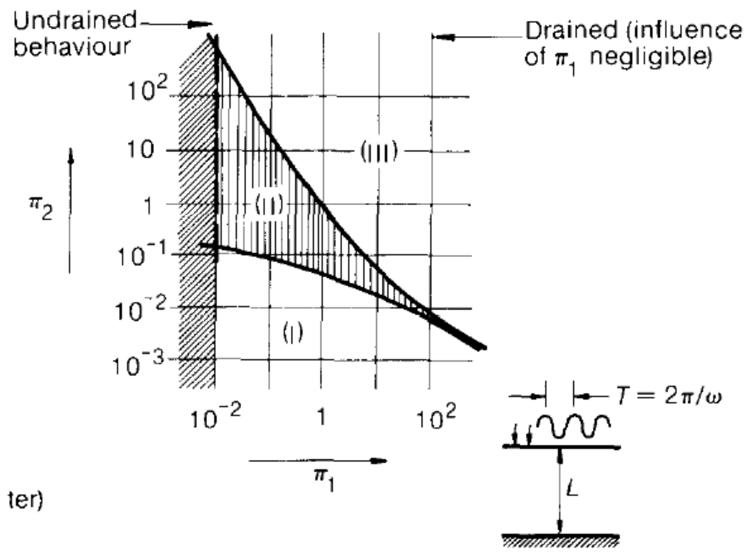

Figure 2.1: The applicable zone of "$u - w$" form, "$u - p$" approximation and Biot's consolidation equations in frequency-permeability coordinate (Zienkiewicz et al., 1980).

only a special case. Therefore, the information coming from Figure 2.1 is just a rough approximation, its applicability is limited.

Later, Cha et al. (2002) further analytically investigated the applicable range of the "$u - p$" approximation and Biot's consolidation equations for the 2D model of soil-wave interaction based on the "$u - w$" form. Through solving the partial differential equations in the "$u - w$" form, Cha et al. (2002) obtain the analytical solution of the pressure of the pore fluid, and the displacement of soil in a finite or an infinite seabed under wave loading. Then the analytical solutions based on the "$u - p$" form and Biot's consolidation equations are accordingly determined by ignoring the effects of inertial term in the solution derived from the "$u - w$" form. In the above three analytical solutions, a linear ocean wave is used as the dynamic loading acting on the seabed.

Due to the fact that the frequency of ocean wave is the magnitude of O(10^{-1})Hz. It can definitely be clarified into the range of low-frequency. Therefore, it is not surprising that the results from the "$u - p$" approximation and "$u - w$" form are always basically the same. A comparison has also been performed between the results obtained from the "$u - w$" form and from Biot's consolidation equations. Figure 2.2 shows the boundary line of applicable ranges for different permeabilities between the conditions under which "$u - w$" form or "$u - p$" approximation must be adopted and the conditions under which the Biot's consolidation equations could be used. In Figure 2.2, The abscissa Π_1 and the longitudinal coordinates Π_2 are defined as:

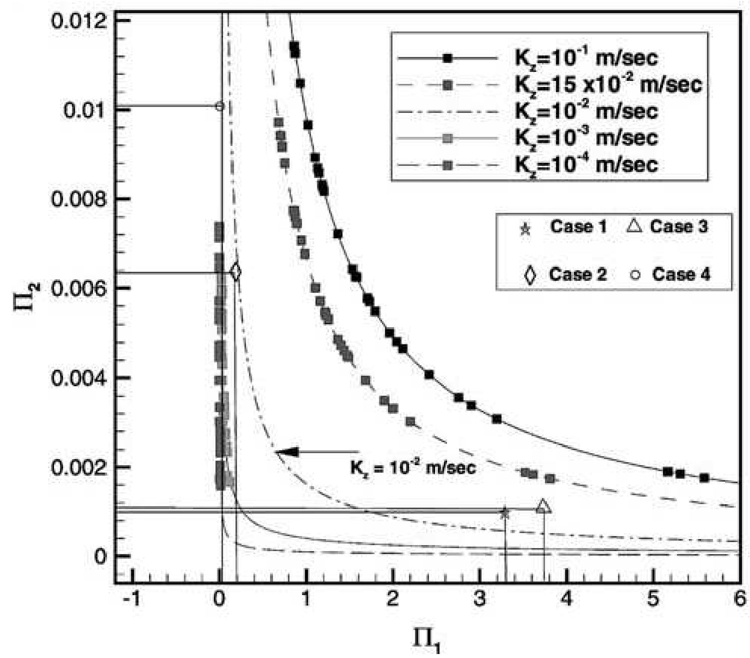

Figure 2.2: The boundary line of applicable range for different permeabilities for "$u - w$" form and Biot's consolidation equations (Cha et al., 2002)

$$\Pi_1 = \frac{k_z V_c^2 \lambda^2}{\rho_f g \omega} \quad \text{and} \quad \Pi_2 = \frac{\rho_f \omega^2}{(\frac{G}{1-2\nu} + \frac{K_f}{n})\lambda^2}, \tag{2.26}$$

where k_z is the permeability coefficient, and λ is the wave number. V_c^2 is the velocity of the compressibility wave in porous soil, and could be expressed as:

$$V_c^2 = \frac{\frac{G}{1-2\nu} + \frac{K_f}{n}}{\rho_f}. \tag{2.27}$$

The abscissa Π_1 is related to the permeability of soil, and Π_2 is related to the frequency of the ocean wave acting on the seabed. Cha et al. (2002) and Jeng and Cha (2003) proposed an equation to describe the boundary line in the $\Pi_1 - \Pi_2$ non-dimensional space:

$$\Pi_2 = C\Pi_1^m. \tag{2.28}$$

Using the regression analysis, the parameter m is determined as a constant (m=0.5356), and the coefficient C is:

$$C = 0.0298(k_z)^{0.5356}. \tag{2.29}$$

For certain soil conditions, the "$u - w$" form or "$u - p$" approximation should be adopted if the point (Π_1, Π_2) is located above the boundary line, else a large computational error would result. The result obtained by Cha et al. (2002) is more liable than that of Zienkiewicz et al. (1980) due to the fact that the soil model used by Zienkiewicz et al. (1980) is one dimensional, and the velocity of compressibility wave in the soil is assumed as 1000m/s which is invalid for most soil layers.

Recently, Ulker et al. (2009); Ulker and Rahman (2009) further investigated the applicable range of the "$u - w$" form (Full dynamic), "$u - p$" approximation (Partial dynamic) and Biot's consolidation equation (Quasi static). Firstly, a generalized analytical solution is developed for the wave-induced seabed response by adopting the similar method used by Cha et al. (2002). In the analytical solution, the "$u - w$" form is taken as the governing equation with the additon of the gravitational term, which was not considered by Cha et al. (2002). The solution for the "$u - p$" approximation and Biot's consolidation equations are obtained by reducing the analytical solution from the "$u - w$" form. The linear wave and poro-elastic model are adopted as the external loading and the constitutive model of seabed soil. Through comparing the results of pore pressure, shear stress and effective vertical stress obtained from the three types of governing equations, Ulker et al. (2009) proposed a graph to illustrate the applicable range of the three types of governing equations (Figure 2.3). In Figure 2.3, two non-dimensional parameters Π_1 and Π_2 are defined, $\Pi_2 = \frac{\omega^2 h^2}{V_c^2}$). As previously, the Π_1 and Π_2 are related to the permeability and the frequency of loading. Ulker et al. (2009); Ulker and Rahman (2009) conclude that the Biot's consolidation equations are accurate for clay soils; the"$u - p$" approximation is necessary for silty soils. For the sand soil, the formulation required is dependant on the permeability and the loading frequency; the "$u - w$" form (full dynamic) has to be used for gravels whose permeability is generally relatively a large magnitude.

In summary, the "$u - p$" approximation and Biot's consolidation equations are sufficient for the cases with low frequency loading and small permeability soils; the "$u - w$" form has to be used for the cases with high frequency loading and/or high permeability soil. In this dissertation, the permeability

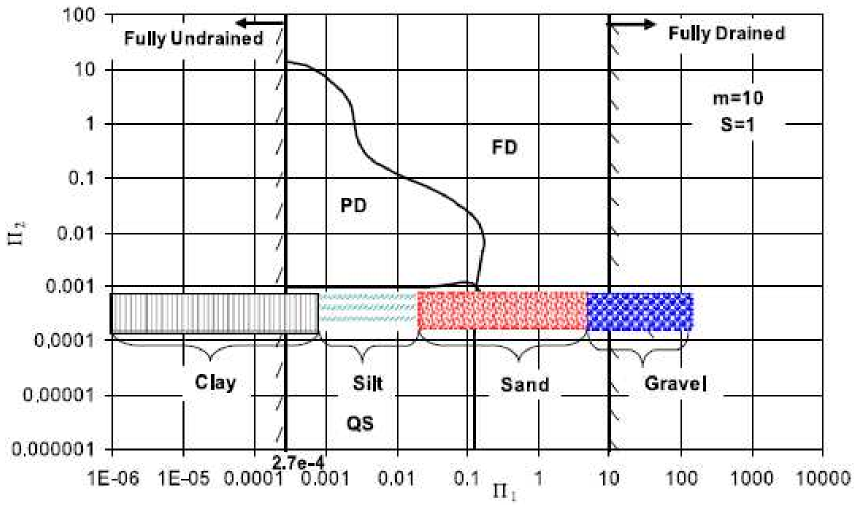

Figure 2.3: Regions of applicability of the three types of governing equations for the wave-induced seabed response (Ulker et al., 2009).

of seabed is generally 1.0×10^{-5}m/s to 1.0×10^{-4}m/s (Maximum 1.0×10^{-2}m/s for parametric study); and the magnitude of dominant frequency is $O(10^{-1})$Hz for ocean wave and $O(10^{1})$Hz for earthquake loading. The "$u - p$" approximation is sufficient to describe the dynamic behaviour of seabed foundation under marine structures.

2.2 Decoupled Analysis of Wave-Seabed Interactions

In the real ocean environments, the ocean wave and seabed form an interaction system. This interaction has attracted a great deal of attention from researchers and coastal engineers. The problem of interaction between wave and seabed has been extensively investigated in the past three decades by using both analytical and numerical methods. The uncoupled method is widely used, in which the wave pressure acting on seabed is taken as the active force. The response of seabed has no effect on the wave characteristics. There is no damping for the wave propagating on porous seabed. This assumption could be acceptable for clay, silty sand and fine sand seabed. For coarse sand seabed, the wave damping is important factor in the interaction process.

2.2.1 Analytical approximations

At the early stage, due to the undeveloped computational technology and limited computer facilities, the analytical method was the main tool used to investigate the interaction between waves and the seabed. Most previous investigations are based on the Biot's consolidation equaitons (Biot, 1941) and the storage equation (Verruijt, 1969) to obtain the wave-induced dynamic pore pressure, soil displacement, and effective stresses. Yamamoto et al. (1978) and Madsen (1978) may be the first to investigate the wave-induced dynamic response of seabed under ocean wave by using the Biot's theory.

Yamamoto et al. (1978) derived an analytical solution for an isotropic, poro-elastic, infinite seabed by treating the pore water and seabed as compressible and deformable medium. Yamamoto et al. (1978) concluded that the soil response is independent on permeability and has no phase lag if the compressibility of the porous soil is much smaller than that of the pore water. However, the pore pressure would decrease quickly, and the phase lag increases with depth if permeability k and compressibility of pore water β are small.

Madsen (1978) investigated the wave-induced response for a partially saturated and hydraulically anisotropic seabed with infinite thickness. Madsen (1978) found that the hydraulically anisotropy could have great influence on the effective stresses for coarse sand, and the degree of saturation has significant effect on the wave-induced response.

Yamamoto (1977) and Yamamoto (1981) further extended his analytical solution from a infinite seabed to partial saturated and layered seabed of finite depth. However, both the solutions are semi-analytical, not a closed form. The solution in Yamamoto (1981) has been comprehensively verified by the data obtained from Mississippi Delta (Bennett, 1978; Bennett and Faris, 1979).

Okusa (1985) developed a simple analytical solutions for wave-induced response in unsaturated seabed by using the compatibility equation based on the plane stress assumption, and reducing the governing equation to a fourth-order differential linear equation.

Zienkiewicz et al. (1980) derived a set of one-dimensional analytical solutions for soil column under a sinusoidal loading based on the "$u-w$" , "$u-p$" form and Biot's consolidation equations. The applicable range of "$u-w$" form , "$u-p$" approximation and Biot's consolidation equations was first investigated by adopting these solutions.

Zhang and Gu (1993) developed a general analytical solution for the linear progressive wave induced response in a finite seabed with anisotropic permeability based on the work of Yamamoto et al. (1978) and Madsen (1978). As a general solution, the coefficients in the solution could be determined based on the given boundary conditions. Some experiments also have been conducted to verify the general solutions.

The linear progressive wave is adopted in most of the aforementioned investigations. Tsai and Lee (1995) developed an analytical solution for the response of an isotropic seabed of finite thickness under standing wave loading. A good agreement between the analytical solution and the wave flume experimental data indicated the reliability of this solution. Hsu et al. (1993) proposed an analytical solution of the dynamic response in a poro-elastic, isotropic seabed of infinite thickness under short-crested waves, based on the Biot's consolidation equations. Later, the solution was extended to more complicated conditions. For example, Hsu and Jeng (1994) and Jeng and Hsu (1996) developed analytical solutions for an unsaturated seabed of finite thickness. Hsu et al. (1995) developed a semi-analytical solution for an unsaturated layered seabed . Seymour et al. (1996) proposed a solution for the seabed with variable permeability along the seabed depth. However, in this model, the first-order derivation with respect to vertical depth was excluded. Later, Lin and Jeng (1997) and Jeng and Seymour (1997) further extended the analytical solution to general seabed soil conditions. It is reported that the difference of wave-induced pore pressure would be over 20% between the variable permeability and the uniform permeability. Recently, Kitano et al. (1999) and Kitano and Mase (2001) also proposed another simple solution for the variable permeability seabed. Jeng (1996b), Jeng (1998a) and Jeng (1997a) derived the solutions for saturated or unsaturated, anisotropic seabed with finite thickness. Similar work also has been done by Yuhi and Ishida (2002) for a cross-anisotropic seabed. In these analytical solutions, the ocean waves used are generally the linear waves, including progressive wave, short-crested wave and standing wave. These analytical solutions are normally used to investigate the liquefaction potential of the seabed under wave loaing (Lin and Jeng, 2000; Jeng, 1996b; Hsu et al., 1995) or to predict the possibility of shear failure.

The common characteristics of the aforementioned analytical solutions is the usage of Biot's consolidation equation as the governing equations, in which the terms of gravity and acceleration of both soil and fluid are ignored. As stated above, the preconditions of acceptable error when adopting the Biot's consolidation equations are that the frequency of loading is low, and/or the permeability of the soil is small. For other problems such as the cases with high frequency loading and/or high permeability, a relatively accurate solution only can be obtained using the full dynamic ("$u - w$") or partial dynamic ("$u-p$") equations, which include the effect of inertia term of solid and/or fluid. Jeng and Rahman (2000) and Cha et al. (2002) proposed the analytical solutions of dynamic response for a poro-elastic, isotropic seabed under wave loading based on the "$u-w$" form or "$u-p$" approximation, in which the inertia effect of the solid and/or pore fluid are included. However, the gravitational term is ignored in all three solutions. Recently, Ulker et al. (2009); Ulker and Rahman (2009) develop an analytical solution for the wave-induced response of a poro-elastic, isotropic and finite seabed under linear wave loading by taking the "$u-w$" form as the governing equations, and has included the gravitational term. By adopting this analytical solution, Ulker et al. (2009); Ulker and Rahman (2009) further investigated the applicable range of the "$u-w$" form, "$u-p$" approximation and consolidation equation. Most recently, Zhou et al. (2011) proposesd a complex analytical solution for the multi-layers poro-elastic seabed under second-order progressive wave based on the full dynamic Biot's equation. In the derivation process, the Fourier transformation and its inverse transformation are used.

All aforementioned analytical solutions are based on the poro-elastic constitutive model. Under certain conditions, such as large deformations, the poro-elastic model can not accurately predict the dynamic response of seabed under wave loading. The poro-elastoplastic model has to be used in these cases. However, due to the complexity of poro-elastoplastic model, only few works on this aspect are available. Sekiguchi et al. (1995) proposed a closed-form analytical solution of the wave-induced pore pressure in a cohesionless seabed under a standing wave by adopting the poro-elastoplastic model. The solution is capable of taking into account the cumulative contraction of soils under cyclic loading, and could be used to assess the liquefaction potential due to the oscillatory excess pore pressure as well as the residual pore pressure. Their results which agreed well with centrifugal experiment indicated that the difference between the poro-elastic and poro-elastoplastic model is significant.

The analytical solutions of the wave-induced response of the seabed mentioned above are all obtained based on the linear or second-order wave theory, including progressive, short-crested and standing wave; and the seabed is treated as a rigid, and impermeable medium in wave field. The ocean wave exerts loading on the surface of seabed when propagating on it. However, the response of seabed under the wave loading has no effect on the propagation of wave. There is no wave damping. In fact, as observed in the laboratory, the wave will be significantly influenced by the porous seabed with high permeability, and there is intensive fluid exchange between both fluid and porous domain. To consider the wave damping, the coupled analysis between wave and seabed is needed.

2.2.2 Numerical models

In engineering application, analytical solutions are only applicable for some simple cases, in which the simple boundary conditions, such as linear progressive or standing wave, and poro-elastic constitutive model, are involved. For problems with complex boundary conditions (higher order wave and wave breaking) or poro-elastoplastic constitutive models, the analytical solutions basically are not able to deal with. The numerical method is another useful tool to investigate the seabed response under wave loading. Due to the development of numerical techniques in the past 20 years, the numerical method owns much wider application range than the analytical solutions. In numerical models, the complex wave loading boundary conditions and complicated constitutive models for seabed soil can be dealt with efficiently. Generally, the numerical methods include Finite Defference Method (FDM), Boundary Element Method (BEM), Finite Element Method (FEM) and Meshless Method. At present, the FEM is the most popular numerical method to investigate the wave-induced response of seabed with complex boundary conditions and the Wave-Seabed-Structures Interactions (WSSI).

FDM is a relatively simple numerical method. Its implementation efficiency is high relative to other methods. However, its convergence conditions are relatively strict. Sometimes, the mesh size and the time interval for dynamic problem have to be set as a small value for convergence requirement. Some models based on FDM have been established. Madga (1990) developed a one dimensional FDM model for the wave-induced pore pressure in a nearly saturated sandy bed. His results indicated that the wave-induced pore pressure is significantly influenced by the permeability, saturation and compressibility of the soil skeleton. Cheng et al. (2001) also developed a one dimensional FDM numerical model to investigate the pore pressure build up in a seabed under progressive wave loading. Sawicki and Staroszczyk (2008) investigated the plastic yield zone in seabed under wave loading adopting a FDM model, which is developed taking the Biot's consolidation equation as the governing equation; and the elasto-plastic Mohr-Coulomb model is used for seabed.

Raman and Sabin (1991) developed a BEM model to investigate the wave-induced failure of a poro-elastic seabed slopes. Karim et al. (2002) and Wang et al. (2004b) developed a meshless numerical model based on the radial point interpolation to investigate the wave-induced response of seabed without any structures. Recently, Wang et al. (2007) further applied this numerical model to investigate the liquefaction potential and shear failure probability of the seabed subjected to the progressive wave. Recently, Hua and Yu (2009b) also develops a meshfree numerical model for the problem of seabed response under wave loading. This meshfree model is adopted to investigate the dynamic response of stratified seabed (Hua and Yu, 2009a).

Gatmiri (1990) developed a FEM numerical model to investigate the wave-induced response (pore pressure and effective stresses) in an isotropic and saturated seabed. However, the distribution of wave-induced pore pressure along the depth was found to be inconsistent with the analytical solution proposed by Hsu and Jeng (1994) and Jeng and Hsu (1996). Later, Gatmiri (1992) further extended his numerical model to investigate the dynamic response of a cross-anisotropic seabed. The results indicated that the difference between the isotropic seabed and the anisotropic seabed was significant; and the phase lag of the wave-induced pore pressure was obtained from his model. However, the boundary conditions applied to the both sides of the computational domain contradicted with the real situation in ocean environment. In his model, the left and right side are fixed.

Luan and Wang (2001) and Zhou et al. (2005) investigated the dynamic response of a saturated seabed under linear and nonlinear wave loading adopting a FEM model developed based on the partial dynamic equation ("$u - p$"approximation). Jeng and Lin (1996) and Lin and Jeng (1996) developed a finite element model for the wave-induced soil response in a porous seabed with variable permeability and shear modulus along burial depth. The seabed soil is unsaturated and hydraulically anisotropic, and subjected to a three-dimensional wave system. Later, Jeng and Lin (1997) further investigated the wave-induced soil response under the nonlinear wave system.

2.3 Coupled Analysis of the Wave-Seabed Interactions

In offshore environments, the ocean wave and seabed consist of an integrated interaction system. In the interaction process, the wave propagating on the seabed exerts dynamic water pressure on the seabed, makes the porous seabed deform; and there is fluid exchange between the sea water and the pore water in seabed at the surface of seabed. Consequently, the properties of the porous seabed, such as saturation, permeability, seabed thickness and stiffness, would have a significant influence on the wave characteristics propagating on the porous seabed. Under the influence of porous seabed, the height of wave propagating on it would significantly attenuates. This damped wave continues to apply dynamic pressure on seabed; and the seabed also continue to modify the wave field. Finally, an equilibrium status will be reached between the wave field and porous seabed.

In the decoupled model for the wave-seabed interactions, the seabed is treated as rigid and impermeable medium when determining the wave field. There is no wave damping when the wave propagates on the seabed. Obviously, the interaction mechanism between wave and porous seabed could not be described adequately by the decoupled model. Only the approximate results could be obtained by the decoupled model. In recent 10 years, some works have been conducted to investigate the wave-seabed interaction using coupled method. In these coupled model, the wave motion on porous seabed is governed by Laplace's equation, the seabed dynamics under the wave loading is described by Biot's equation. The continuity of pressure, seepage velocity of water and the mass flux at the interface of sea water and porous seabed are implemented for the fluid domain and porous medium domain. By adopting the coupled model, the exchange between sea water and pore water, and the wave damping can be captured in the interaction process.

2.3.1 Analytical solutions

In investigation of wave-seabed interaction using coupled model, the analytical solutions are the most popular method in available literature. Among them, Lee et al. (2002a) proposed a coupled analytical solution for the wave-seabed interaction. In this analytical coupled model, the wave motion on porous seabed is determined based on potential theory (Laplace's equation); the dynamic behaviour of seabed soil is governed by the poro-elastic Biot's equation ("$u - p$" approximation). The dynamic and kinematic free surface boundary conditions are applied to the Laplace's equation to determine the surface wave, in which a complex wave number is introduced to consider the wave damping when propagating on the porous seabed. The boundary conditions between the Laplace's equation and the Biot's equation are that the pressure, velocity and flux are all continuous at the interface of the domains. Unlike the decoupled model, the complex wave number is an unknown which needs to be determined according to the flux continuity conditions at the interface. From their results, it is found that the soil properties, such as permeability, stiffness have significant effect on the coupled wave field, for example, the wave damping is much stronger for wave propagating on coarse sand bed than the wave propagating on fine sand bed; and the wave damping is very significant if the wave propagating on soft seabed. Similar work is also done by Jeng (2000), Jeng (2001), Zhang and Li (2010) and Tsai et al. (2009) recently. However, the Biot's consolidation equation is used for the porous seabed.

Later, under a different frame, Lee and Lan (2002) proposed another similar analytical solution for the wave-seabed interaction. However, in their model, the viscous force of pore water and the drag force between pore water and soil particles are all included in the Biot's equations; and the wave number is a real number, rather than a complex number. As that in Lee et al. (2002a), the dynamic and kinematic free surface boundary conditions, and the continuous pressure, velocity and flux at the interface between seabed and fluid domain are also adopted in coupled process. From their analysis, it is found that the wave damping on porous seabed is positively related to the permeabiliy of seabed, and is negatively related to the stiffness of seabed. Unfortunately, this analytical solution is only applicable for an infinite seabed.

Based on the foundation work conducted by Lee et al. (2002a) and Lee and Lan (2002) for the wave-seabed interaction, Lee et al. (2002b) further developed a coupled analytical solution for the interaction between the ocean wave and the Coulomb-damped poro-elastic finite seabed. In this model, the wave motion is still determined by potential theory; however, the energy dissipation due to the friction between the soil particles in seabed is considered in the governing equation for the seabed soil. The solving process and boundary conditions used are basically same with the that in Lee et al. (2002a) and Lee and Lan (2002). Their solution reveals that the wave damping is apparently significant for the wave propagating on clay and fine sand bed if considering the energy dissipation due to particles friction. This 2D coupled analytical solution was further extended to its 3D situation by Lin and Jeng (2004). Based on the previous work (Lee et al., 2002a,b; Lee and Lan, 2002), Lin and Jeng (2003) compared the existing several models (full dynamic, consolidation, coulomb-damping) governing the dynamic behaviour of porous seabed used in the investigation of wave-seabed interaction; and proposed the applicable range of these models.

All coupled models mentioned above only contain one layer fluid. The interaction between porous seabed and wave which propagates in a two layers fluid systems also has been investigated. Due to the fact that the two layers fluid have different viscosity and density, there is a internal wave propagating on porous seabed. The interaction between the surface wave, internal wave and porous seabed is also significant. Chen and Hsu (2005) first investigated the interaction between the internal wave and an infinite porous seabed. In their model, the Boit's consolidation equation is used for the porous seabed; the wave motion in the two layer fluid is also governed by the Laplace's equation. The velocity, pressure and flux at the interface of the two layers fluid, and at the interface between the fluid domain and porous seabed domain is applied in the solution procedure. From their analysis, the damping of the internal wave propagating on porous seabed basically has the same trend with the surface wave when there is only one layer fluid. Similar work also was done by Williams and Jeng (2007). However, the anisotropic permeability of porous seabed could be considered in their model.

The porous seabed in all above mentioned models is treated as poro-elastic medium. Under the similar frame with Lee et al. (2002a), Hsieh (2006) proposed another coupled analytical solution for the interaction between wave and visco-elastic seabed. Hsieh (2006) concluded that the discrepancies of the dynamic response of seabed between the simulations of viscoelastic model and elastic model are found to be strongly dependent on the wave frequency; the viscosity of seabed soil can be significantly stimulated by the dynamic loading with high frequency.

2.3.2 Numerical solutions

The numerical simulation is another method to investigate the coupled interaction between wave and seabed. Comparing with the analytical methods, the numerical methods are more difficult to implement the coupling analysis for the wave-seabed interaction. The reason is that the governing equation for fluid (Navier-Stokes equation or Laplace's equation) and the governing equation for porous seabed (Biot's equation) can not be solved simultaneously. In the Navier-Stokes equation or Laplace's equation, the unknowns are the velocities of fluid; while in the Biot's equation, the unknowns are displacements of soil. In the analytical method, two governing equations for fluids and porous seabed could be solved simultaneously through the continuity condition of pressure, velocity of fluid at the interface of two material domains. However, the iterative algorithm is the only applicable method for the numerical model to investigate the coupled interaction between wave and seabed. In the iterative process, the continuity of pressure and velocity of fluid at the interface between fluid domain and porous seabed are taken as the criterion of convergence. In most of previous literatures, this iterative algorithm was still not widely used in solving the N-S equation/Laplace's equation and the Biot's equation when investigating the wave-seabed interactions. Only the one-way coupling algorithm was used in them. For the cases in which the exchange between sea water and pore water is not strong, this one-way coupling algorithm is applicable; and the predicted results could agree very well with the experimental data, i.e. Tsai (1995). At present, few literatures are available in which the two-way iterative algorithm are adopted.

From the analytical solutions, it is well known that the wave propagating on porous seabed could damp in wave energy and wave height due to energy dissipation of porous flow. The characteristics of wave damping on porous seabed can be easily captured by the numerical method. For example, Kim et al. (2006) proposed a BEM numerical model to study the wave damping propagating on porous seabed. In their model, the wave motion is governed by Laplace's equation; the porous flow is governed by Darcy's flow principle. The continuity of pressure and velocity are implemented at the interface of the two domains. However, this model has some limitations, for example, the complicated wave motion can not be modeled; the effect of inertia and drag force between pore water and soil particles are not considered; the stress status in porous seabed under wave loading can not be determined. Meanwhile, Karunarathna and Lin (2006) investigated the wave damping on porous seabed adopting a more advanced model, in which the N-S equation for wave motion, and Reynolds Average N-S equation for porous flow in porous seabed are used. The inertia term, and the drag force between pore water and soil particles are both included in the equilibrium equations. The N-S and RANS equations are solved simultaneously using FDM. The continuity of pressure and velocity are automatically satisfied at the interface of two domains. The biggest drawback of this model is that the Biot's equation is not involved; the stress status in seabed can not be determined.

Later, some works were conducted to determine the stress status and deformation of porous seabed when interacting with wave. Liu and Garcia (2007) developed a 3D numerical model to study the wave-seabed interaction based on the platform of OpenFoam, in which the N-S equation for fluid, and Biot's consolidation equation for porous seabed are adopted. The one-way coupling algorithm is used when solving the governing equations of fluid domain and porous seabed domain. It means that the velocity of fluid at the interface of the two domains could not be guaranteed to be continuous, and the porous flow in seabed in not considered. Similar one-way coupling algorithm is also adopted in Cheng et al. (2008), and Xiao et al. (2010a). The differences between these coupled models are that the different kinds of governing equations for fluid and porous seabed, and different numerical methods are used. For example, the nonlinear shallow water equation is used for fluid in Xiao et al. (2010a); the "$u - p$" approximation is used for seabed in Cheng et al. (2008). The finite volume method is used in Liu and Garcia (2007).

The one-way coupling algorithm is used in most of previous literatures. This algorithm is insufficient to investigate the wave-seabed interaction for some cases, for example, the coarse sand bed. To the author's best knowledge, the only available work investigating the wave-seabed interaction problem adopting the two-way iterative algorithm is conducted by Wang et al. (2004a). In their model, the Navier-Stokes equations for incompressible fluid in the fluid domain; the Biot's consolidation equations for porous seabed are used. The continuity conditions when coupling the two equations are again the pressure and velocity continuity at their interface. The iterative process is implemented at one time step as following loop: (1) the N-S equation is solved first. (2) taking the pressure acting on seabed as boundary condition, the Biot's equation is solved. (3) The velocity of fluid at the interface is determined using Darcy's flow. (4) The N-S equation is solved again taking the velocity of fluid on seabed as boundary condition. (5) Repeating the whole loop until the iterative process converge. This coupled model is much more advanced than the one-way coupling. However, for the cases with complicated boundary, the application of two-way algorithm is constrained. Anther drawback is that the effect of deformation of seabed on the wave field is not considered, even through this effect is significant only when the seabed is too soft, such as a silt bed.

2.4 Wave-Seabed-Breakwaters Interactions

Breakwaters are widely constructed in offshore area to protect the coastal line or ports from erosion or damage. The main function of breakwater is to decrease the energy of wave propagating from the seaward side. The wave-seabed-breakwater interaction (WSSI) is always the main concern of coastal engineers when designing the foundations of marine structures. In the last two decades, a great number of investigations about the wave-seabed-breakwater interaction have been conducted.

2.4.1 Analytical approximations

Due to the existence of complicated boundary conditions, the application of analytical method to investigate the problem of wave-seabed-breakwater interaction is constrained. The main reason includes: (1) the effect of weight of breakwater on the stress field in seabed foundation is difficult to be considered, (2) the effect of outer shape of breakwater on the wave field is difficult to be considered. The breakwater frequently is simplified as an impermeable line without any weight. The continuity of pressure and velocity of fluid at the interfaces between seabed, breakwater and sea water is very difficult to be implemented in the analytical process; hence there is no a coupled analytical solution available so far for the wave-seabed-breakwater interaction. The decoupled analytical process is widely adopted in the present available literatures. It means that there is no wave damping for the wave propagating on seabed.

Adopting the poro-elastic Biot's consolidation equations, Tsai (1995) extended the solution of Hsu et al. (1993) to investigate the seabed response in front of a breakwater under partially reflected short-crested wave system loading. Jeng (1996a) proposed an analytical solution to investigate the wave-induced liquefaction potential at the tip of a breakwater located on a finite, unsaturated, isotropic seabed. He found that the diffracted wave component has significant effect on the distribution of wave-induced pore pressure in the seabed behind of breakwater; and there may be a liquefaction hole existing at the vicinity of the breakwater head. Later, another analytical solution was developed by Jeng (1997b) and Jeng (1998b) for the dynamic response in front of a breakwater located on an unsaturated, isotropic or anisotropic seabed of finite thickness. Tsai et al. (2000) and Oh et al. (2002) further investigate the influence of nonlinearity of the wave on the response in front of a breakwater. In their models, the breakwaters both are simplified as a impermeable line without weight. This simplification results in a simple boundary condition for the analytical model. Kumagai and Foda (2002) developed an analytical solution for the response of seabed beneath a composite breakwater to standing wave adopting the complex Fourier series technique. In their solution, the effect of outer shape of the composite breakwater on the seabed response is considered. However, the effect of shape of rubble mound under caisson on the wave field is ignored because the standing wave is used to apply loading on seabed foundation.

2.4.2 Numerical solutions

The analytical solutions can only be applicable to solve WSSI problems with simple boundary conditions. For those problems involving complex boundary conditions, the only feasible method would be the numerical methods. In numerical models, the complex boundary condition for wave motion, complex outer shape and material properties of a breakwater, and the complex constitutive models for seabed soil all could be effectively dealt with. As that in the investigations of wave-seabed interaction, there are also decoupled numerical models in which the stokes wave is used to apply wave load, and coupled numerical models in which the wave motion is determined by solving Laplace's equation or Navier-Stokes equation. At present, to the author's best knowledge, there is no numerical model implements the continuity condition of velocity of fluid at the interface between seabed, breakwater and sea water. Therefore, the numerical model in which Laplace's equation or Navier-Stokes equation is used for sea water, and the continuity condition of water pressure at the interface between seabed, breakwater and sea water is implemented are referred as integrated or coupled model here.

2.4.2.1 Decoupled model

Mase et al. (1994) developed a FEM numerical model to investigate the wave-induced pore water pressures and effective stresses in a sand seabed, and in the rubble mound of a composite caisson-type breakwater or in a rubble mound breakwater under linear standing waves. In his model, the Biot's consolidation equation is employed for seabed and breakwater; and the lateral boundary conditions are provided by the analytical solution proposed by Yamamoto (1977). The numerical model is only applicable for the isotropic and homogeneous seabed; and the effect of outer shape of rubble mound and its porosity on the wave field is completely not taken into considered.

Jeng et al. (2001) developed a 2D general FEM numerical model (GFEM-WSSI) to investigate the wave-induced pore pressure around a composite breakwater located at a finite, isotropic and homogeneous seabed under linear standing wave. In their model, the right side of seabed is fixed, and the boundary value on the left side of seabed is provided by the numerical results obtained from the case without the composite breakwater. In the case without a breakwater, the principle of repeatability (Zienkiewicz and Scott, 1972) is adopted for the boundary conditions on the left and right side. This method applying the lateral boundary condition obviously is inappropriate. Their analysis indicated that the pore pressure in coarse sand was more sensitive to the existence of a breakwater than that of fine sand; and the degree of saturation and Poisson's ratio also significantly affected the pore pressure. Jeng et al. (2000) further applied this 2D FEM numerical model to investigate the influence of anisotropic soil on the wave-induced pore pressure under linear standing loading. As that in Mase et al. (1994), the effect of rubble mound on the wave field is also not considered. The standing wave in front of a composite breakwater is only an approximate wave field.

Ulker et al. (2010) also investigated the dynamic response and instability of the seabed around a caisson breakwater under standing wave using a FEM numerical model, which is developed by taking the fully dynamic "$u - w$" form as the governing equation. In their model, the wave-induced pore pressure and effective stresses were used to predict the liquefaction potential, and to investigate the development process of liquefaction in the seabed around a breakwater. Their results indicated that there was always a liquefaction zone at the toe of the rubble-mound breakwater, which would directly result in the instability of the breakwater. The linear standing wave was used is also based on the assumption that the rubble mound has no effect on the wave field. Recently, Ulker et al. (2012) further applied this FEM model to investigate the breaking wave induced response and instability of seabed around a composite breakwater, in which the breaking wave induced pressure on lateral side of composite breakwater is determined based on the probability theory proposed by PROVERBS (Oumeraci et al., 2001); the breaking wave induced pressure on seabed in applied according to the standing wave. From the author's opinion, the method of applying the breaking wave induced wave force on seabed and composite breakwater is unacceptable.

Li and Jeng (2008) proposed an 3D analytical solution for the linear wave around a breakwater taking the Laplace's equation as the governing equation for the wave motion (oblique/normal incident wave). There are three wave components around the breakwater head: short-crested wave in front of breakwater, progressive wave near to the breakwater head and the diffracted wave behind of the breakwater. In this analytical solution, the breakwater is simplified as a line without width and weight. Adopting this proposed analytical solution, Li and Jeng (2008) further investigated the dynamic response of poro-elastic seabed foundation around the breakwater. Later, adopting the analytical solution proposed by Li and Jeng (2008), the dynamic response and residual liquefaction potential of poro-elasto-plastic seabed foundation around a breakwater head was studied by Ou (2009) and Jeng and Ou (2010).

2.4.2.2 Coupled model

The coupled or integrated numerical model is much more suitable to investigate the wave-seabed-breakwater interaction than the decoupled model, because the effect of outer shape of breakwater, and the porous flow in seabed foundation and rubble mound on the wave field can be sufficiently taken into consideration. The wave damping due to the wave energy dissipation in porous medium also could be captured. Generally, there are two types of coupled numerical method for the wave-seabed-breakwater interaction depending on whether the Biot's equation is used for the porous seabed or not.

The first type method is that only the flow field in seawater domain and porous medium domain is investigated based on the modified Navier-Stokes equation. The Biot's equation is not involved. Therefore, the effective stress in seabed and composite breakwater can not be determined. The representative works have been done by Hur and Mizutani (2003), Hur et al. (2008) and Hur et al. (2010). Hur and Mizutani (2003) developed a coupled numerical model (FDM) to investigate the nonlinear wave force acting on a submerge breakwater, in which the modified continuity equation and modified Navier-Stokes equation were adopted to govern the wave motion and the porous flow in porous medium. In the modified Navier-Stokes equation, the inertia forces and the nonlinear drag force due to turbulence flow were considered. Later, Hur et al. (2008) further developed the coupled model to include the laminar flow induced drag force, to investigate the nonlinear dynamic interactions between waves, a submerged breakwater and the seabed. In the submerged breakwater, the turbulence flow induced drag force is the dominant part; while, the laminar flow induced drag force is the dominant part in seabed. Hur et al. (2010) also developed another coupled model for nonlinear interaction between the wave, seabed and composite breakwater. In their model, the modified continuity equation and modified Navier-Stokes equation are still taken as the governing equation for the wave motion and porous flow. However, the linear and nonlinear drag force, inertial force for the porous flow are estimated according to the Darcy-Brinkman-Forchheimer equation. The viscous force for the porous flow is also included in Darcy-Brinkman-Forchheimer equation. The coupled model proposed by Hur et al. (2008) and Hur et al. (2010) could appropriately describe the nonlinear interaction between the wave, seabed and breakwater. However, the stress status in breakwater and its seabed foundation can not be determined.

Based on the first type method for the wave-seabed-breakwater interaction, the Biot's equation is adopted to determine the effective stress status in seabed and breakwater in the second type method. Liu and Garcia (2006) and Liu and Garcia (2007) developed a 3D numerical model (FVM) for the wave-seabed-breakwater interaction based on the free platform of OpenFoam. In their model, the Navier-Stokes equation for seabed water, and the Biot's consolidation equation for seabed are adopted as governing equations. Due to the fact that porous flow in seabed foundation is not considered in the Navier-Stokes equation, the effect of porous seabed foundation on the wave field could not be simulated. The stress status of seabed foundation can be determined by solving the Biot's consolidation equation taking the wave induced pressure on seabed as the boundary condition. However, the breakwater was not taken as a computational sub-domain when solving the Biot's consolidation equation. Therefore, the wave induced dynamic response of breakwater could not be captured in their model. Cheng et al. (2007) developed a similar numerical model for the wave-seabed-breakwater interaction. But it is limited to two dimensional cases. In their model, the Navier-Stokes equation is solved using FDM, the Biot's equation is solved adopting FEM.

Mizutani et al. (1998) and Mostafa et al. (1999) developed a BEM-FEM combination numerical model to investigate the interaction of wave-seabed-breakwater. In their models, the Laplace's equation for fluid domain, the modified Navier-Stokes equation for the porous flow in seabed and rubble mound are used as the governing equations; and the Biot's consolidation equation is adopted to determine the stress status in poro-elastic seabed foundation. The Laplace's equation and modified Navier-Stokes equation are solved using BEM. The continuity of pressure, velocity, flux at the common interface are applied when solving the Laplace's equation and modified Navier-Stokes equation. The Biot's consolidation equation is solved adopting FEM taking the wave induced pressure acting on seabed and breakwater as the external loading boundary condition. This model has been adopted to investigate the interaction between wave, seabed and composite breakwater (Mostafa et al., 1999; Mizutani et al., 1999), submerged breakwater (Mizutani et al., 1998), sea wall (Mizutani and Mostafa, 1998). This coupled model processed the advantages: (1) the wave motion in fluid domain and the porous flow in porous medium could be coupled together; the effect of porous seabed and rubble mound on the wave characteristics can be considered. (2) the corresponding effective stress status and dynamic response of seabed foundation can be determined simultaneously. However, the weak point of this model includes: (1) the complex wave motion, for example, wave breaking, can not be simulated by the Laplace's equation. (2) The seabed foundation must be poro-elastic medium; for poro-elasto-plastic seabed, it is not applicable.

2.5 Wave induced liquefaction in sandy bed

Liquefaction is the act or process of transforming any substance into a kind of liquid resulting from increasing of pore pressure and/or decreasing of inter-granular effective stresses. It often plays an important role around and beneath marine structures (pipeline or breakwater), because it may appear in saturated or nearly saturated seabed, under ocean loading. The resulting loss of soil shear strength may cause catastrophic consequences, such as large horizontal displacements of pipelines on the seabed, floating up of buried pipelines, collapse or tilting of breakwaters. The possibility of wave-induced liquefaction occurring in saturated seabed sediments was first recognized and analyzed by Bjerrum (1973). Based on the observations in laboratory experiments (Nago et al., 1993; Zen and Yamazaki, 1990a) and field measurements Zen and Yamazaki (1991), two types of distinct mechanisms for wave-induced liquefaction in sandy bed are identified: transient or momentary liquefaction and residual liquefaction. The transient liquefaction of seabed foundation is mainly related to the phase lag between the dynamic pore pressure in seabed and the dynamic pressure induced by the wave propagating on seabed. The transient liquefaction zones in seabed would appear and disappear periodically in the zone under wave trough (Zen and Yamazaki, 1990a). The residual liquefaction is mainly due to the build-up of pore pressure in soil under wave loading. Accompanying with the build-up of pore pressure in soil, the inter-granular contact effective stresses decrease between soil particles. When the contact effective stresses become zero, the soil becomes liquefied. The transient liquefaction occurs mainly in elastic seabed, in which the plastic deformation under wave loading is insignificant. While, the residual liquefaction only could occurs in elasto-plastic seabed. The irreversible plastic deformation due to the compaction of soil particles makes the void between soil particles decrease, resulting in the pore pressure build up. The detailed review on liquefaction mechanism can be found in Groot et al. (2006a) and Groot et al. (2006b). Following, the liquefaction criterion widely used, the investigation on transient and residual liquefaction are summarized.

2.5.1 Liquefaction criterion

Generally, the definition for liquefaction is based on following three categories: excess pore pressure based criterion, strength based criterion, and shear deformation based criterion. The excess pore pressure based criteria thinks the soil is liquefied if the excess pore water pressure becomes equal to the initial vertical effective overburden stress. The strength based criterion requires the liquefied soils completely lose their shear strength and cannot regain strength. Because soils gain strength as a result of an effective contact stresses, they will lose strength completely if and only if the effective contact stress becomes zero. It is therefore obvious that this type of liquefaction definition is essentially equivalent to excess pore pressure criteria based criterion. The shear deformation based criterion suggests that a threshold of shear strain exists above which the soil could have been liquefied. Due to the fact that the threshold of shear deformation for different soil in liquefied status is significantly different, the application of the shear deformation based criterion is limited. Here, only the excess pore pressure based criterion is summarized.

Okusa (1985) firstly proposed a 1D liquefaction criterion based on the vertical effective stress:

$$-(\gamma_s - \gamma_w)z = \sigma'_{z0} \leq \sigma'_{zd}, \tag{2.30}$$

in which the γ_s and γ_w are the unit weight of soil and water. z is the depth of soil. σ'_{z0} is the initial vertical effective stress in seabed. σ'_{zd} is the dynamic vertical effective stress induced by the dynamic loading. This liquefaction criterion means that if the upward dynamic vertical effective stress is greater than the initial downward effective stress, the soil will liquefied. This criterion has clear physical meaning. But the effect of horizontal effective stresses σ'_x and σ'_y are not taken into consideration. Under the same frame, Tsai (1995) extended the above 1D liquefaction criterion to 3D condition by adopting the average of the effective stresses:

$$-(\gamma_s - \gamma_w)(\frac{1+2K_0}{3})z \leq \frac{1}{3}(\sigma'_{xd} + \sigma'_{yd} + \sigma'_{zd}), \tag{2.31}$$

K_0 is the lateral compression coefficient of soil. This liquefaction criterion only adopts the average idea. There is no clear physical meaning of how the horizontal effective stresses σ'_x and σ'_y affect the liquefaction potential of soil.

Zen and Yamazaki (1990b) developed another liquefaction criterion based on the dynamic pore pressure:

$$-(\gamma_s - \gamma_w)z = \sigma'_{z0} \leq p_s - p_b, \tag{2.32}$$

in which p_s and p_b is the dynamic pore pressure in seabed, and the pressure acting on seabed. This liquefaction criterion means that the seabed will liquefy if the upward seepage force can overcome the weight of overburdened soil and/or structures. Similar with the liquefaction criterion proposed by Okusa (1985), the physical meaning of this criterion is clear. However, the horizontal effective stresses σ'_x and σ'_y are also not taken into consideration. Zen and Yamazaki (1991) validated the feasibility of this liquefaction criterion to judge the wave induced liquefaction in seabed using a field data. Actually, this liquefaction criterion is essentially the same with the one proposed by Okusa (1985), because the vertical effective contact stress is certainly zero if the upward seepage force could overcome the overburdened soil weight. Jeng (1997c) further extended the above liquefaction criterion into 3D situation:

$$-(\gamma_s - \gamma_w)(\frac{1 + 2K_0}{3})z \leq p - p_b. \tag{2.33}$$

Similarly, the average idea is used. How the initial horizontal effective stresses σ'_{x0} and σ'_{y0} affect the liquefaction potential of soil is not clear.

2.5.2 Transient liquefaction

The transient liquefaction occurs in elastic deformation dominated seabed under wave loading. The insignificant plastic deformation in seabed soil makes the void between soil particles basically unchanged. Hence, the pore pressure in seabed could not be built-up continuously. The transient liquefaction mainly depends on the wave induced upward seepage force. It could only liquefy momentarily in the seabed under wave trough. Although it is observed that the pore pressure in sandy soil could continuously built up under wave loading in most previous conducted tests, the transient liquefaction still has also been observed in few laboratory tests and field tests.

Zen and Yamazaki (1990b) conducted a one-dimensional experimental test to investigate the wave-induced liquefaction in sandy bed. In this test, the fine sand (d_{50}=0.181mm) was installed in a sealed hollow cylinder steel tank, and filled with fresh water. The wave loading on sandy bed was modeled by hydraulic pressure applied by a hydraulic machine. It was observed that the pore pressure in the fine sand didn't built up, but oscillated periodically corresponding to the wave loading; and the caisson type block placed on the surface of fine sand seriously tilted. It was indicated that the fine sand has liquefied under the wave loading, and without the built-up of pore pressure. Based on the phenomenon observed, Zen and Yamazaki (1990b) identified the existence of transient/momentary liquefaction in sandy bed under wave loading; and proposed the liquefaction criterion mentioned above. Later, Zen and Yamazaki (1991) further applied the the liquefaction criterion proposed by themselves to investigate the liquefaction of seabed using field data measured in Haziki, Japan. They found that the pore pressure in real seabed at Haziki also didn't built up under wave loading; the transient liquefaction is the main liquefaction phenomenon observed.

Choudhury et al. (2006) also conducted a similar one-dimensional experimental test as that in Zen and Yamazaki (1990b). The height and diameter of the cylinder tank were 2.5m and 0.8m respectively. Therefore, this test is a large scale laboratory test. An object was placed on the sandy bed to identify the liquefaction. Their test results also shown that the object sank downward into the sandy bed due to the liquefaction under wave loading. Choudhury et al. (2006) claimed that the liquefaction observed in this large scale test is momentary liquefaction.

Mory et al. (2007) performed a long term field test to study the wave induced liquefaction around a coastal structure at Capbreton, 30km north of Biarritz on the Atlantic coast of Aquitaine, in southwest France. Analyzing of the field test data, they found that the wave induced momentary liquefaction in the seabed near to a coastal structure really existed. The observed maximum liquefaction depth reach up to 0.54m-0.62m. Another important finding was that the existence of a significant amount of gas inside soil which was captured by an advanced image technology.

Due to the fact that the transient liquefaction mainly attributes to the elastic deformation of seabed under wave loading, the characteristics of wave induced transient liquefaction in seabed could be easily captured by using the poro-elastic constitutive model for seabed. So far, a great number of investigations on wave induced transient liquefaction in poro-elastic seabed, including analytical solutions and numerical solutions, have been conducted adopting the decoupled or coupled model. For example, Tsai (1995) analytically studied the short-crested wave induced liquefaction in poro-elastic seabed in front of a breakwater adopting the 3D stress based liquefaction criterion; Zen et al. (1998) analytically investigated the difference between the progressive wave induced liquefaction and the shear failure in poro-elastic seabed adopting the 3D pore pressure based liquefaction criterion; Recently, Ulker et al. (2010) and Ulker et al. (2012) develops a decoupled numerical model to investigate the standing wave induced transient liquefaction in front of a composite breakwater. Actually, the review of the wave induced transient liquefaction in poro-elastic seabed with or without a breakwater basically could overlap with the review about the wave-seabed interaction (Section 2.2 and 2.3) and the wave-seabed-breakwater interaction (Section 2.4), because the wave induced liquefaction in seabed or seabed foundation is always the main concern in the problem of wave-seabed interaction or wave-seabed-breakwater interaction.

Recently, Young et al. (2009) and Xiao et al. (2010b) perform the numerical analysis of the liquefaction potential in a coastal slope under normal solitary wave or breaking solitary wave loading. From their analysis, it is found that the coastal slope could liquefy in a large range under solitary wave loading (Young et al., 2009); and the maximum liquefaction depth could reach up 2.5m when the permeability is 1.0×10^{-4}m/s to 1.0×10^{-7}m/s (Xiao et al., 2010b). However, it is noted that their results are doubtable. There are two reasons: (1) There is no obvious wave trough for solitary wave when interacting with coastal slopes expect in the process of wave run-up and run-down; however, the transient liquefaction only could occur under wave trough. (2) the liquefaction criterion adopted in their analysis is not correct. They treat the coastal slopes is liquefied when the wave induced vertical effective stress is greater 0. Obviously, the liquefaction resistance due to the initial inter-granular effective stresses is not taken into consideration.

In recent ten year, the neural network method is applied to predict the maximum liquefaction depth in a poro-elastic seabed under wave loading. Jeng et al. (2004) first proposed a neural network model to predict the maximum depth of transient liquefaction in a poro-elastic seabed under linear progressive wave loading, based on these sample data obtained by adopting the analytical solution developed by Jeng and Cha (2003), Most recently, Cha et al. (2011) further extend the above simple neural network to a more complicated multi-artificial neural network model to predict the maximum liquefaction depth.

2.5.3 Residual liquefaction

The residual liquefaction mechanism is completely different with that of transient liquefaction in sandy bed. The occurrence of residual liquefaction is due to the plastic deformation in sandy bed. As a kind of granular material filled with pore water, the plastic deformation of sandy bed is mainly the volumetric compaction of soil element due to the re-arrangement of soil particles under wave induced cycle shear loading. The deformation of soil particles and pore water under wave loading is apparently small in poro-elasto-plastic sandy bed. The decrease of void ratio in sandy soil makes the pore pressure build up. Once the excess pore pressure could overcome the overburdened soil weight, the residual liquefaction occurs in sandy bed. Generally, the shear stress ratio τ/σ_0' (τ is the magnitude of wave induced shear stress, σ_0' is the initial vertical effective stress) plays an important role in the process of residual liquefaction. It directly determines the possibility of residual liquefaction, and the period to reach the residual liquefaction.

Some wave flume tests have been performed to prove the existence of residual liquefaction in sandy bed under wave loading (Sumer et al., 1999, 2006a, 2010; Teh et al., 2003; Tzang and Ou, 2006; Tzang et al., 2009, 2011). The pore pressure built-up in sandy bed under wave loading also has been widely monitored in these testing process. Sassa et al. (2006) conducted a field measurements to monitor the pore water pressures in the seabed sands at Kouchi port, Japan during the period of six days involving the passage of Typhoon No.9, 2002. It was found that the pore water pressures also built-up at various depths shallower than 2.0m when the significant wave heights were greater than 2.0m. The centrifuge test for the wave induced liquefaction also has been performed by Sassa and Sekiguchi (1999). They found that there is a critical cyclic shear stress ratio below which the residual pore pressure could not occur; and the wave induced residual liquefaction in sandy bed had the progressive nature. The residual liquefaction front advanced downward from the surface of sandy bed. Their centrifuge test further indicated that the sand bed which has experienced a residual liquefaction process owned greater liquefaction resistance under wave loading.

Adopting to the laboratory tests and field measurements, the mechanism of residual liquefaction, and the key factors affecting the liquefaction process have been deeply recognized in recent ten years. So far, some theoretic works, including analytical approximation and numerical simulation, have been conducted to make their attempts to appropriately describe the soil behaviour in the process of liquefaction.

2.5.3.1 Analytical approximation

Based on a series of laboratory tests for cohesionless soil under cyclic loading, it is recognized that the pore pressure build up in sandy soil is mainly related to the shear stress ratio τ/σ'_0, the period of cyclic loading and the the cyclic number of loading reaching the liquefaction status. Seed et al. (1976) and Seed and Rahman (1978) proposed a governing equation to investigate the pore pressure build up in sand soil under wave loading, read as

$$\frac{\partial p_s}{\partial t} = c_v \frac{\partial^2 p_s}{\partial z^2} + f, \tag{2.34}$$

where p_s is the wave induced excess pore pressure, c_v is the consolidation coefficient, f is a source term to describe the mechanism of pore pressure built up. It was expressed by Seed et al. (1976) and Seed and Rahman (1978) as

$$f = \frac{\sigma'_{z0}}{N_L} \frac{1}{T}, \tag{2.35}$$

where σ'_{z0} is the initial vertical effective stress. T is the period of cyclic loading. N_L is the cyclic number of loading making the soil reaching liquefaction. Generally, It is directly related to the shear stress ratio τ/σ'_{z0}, could be determined fitting and regressing the laboratory test data:

$$N_L = (\frac{1}{a} \frac{\tau}{\sigma'_{z0}})^{\frac{1}{b}}. \tag{2.36}$$

in which a and b are the fitting coefficients. Generally, they are dependent on the relative density of soil D_r.

By adopting the above governing equation for the pore pressure build-up, Rahman and Jaber (1986) developed a simplified analytical solution for wave induced excess pore pressure generation in seabed. In Rahman and Jaber (1986)'s solution, the wave induced shear stress ratio τ/σ'_{z0} was estimated according to the analytical solution for the wave induced seabed response in a infinite seabed (Madsen, 1978; Yamamoto et al., 1978). In recent 10 years, some analytical approximations are also proposed for the wave induced pore pressure build up in sand soil based on the governing equation

(2.34). Among them, Cheng et al. (2001) proposed an analytic approximation for the excess pore pressure generation under wave loading, in which the shear stress ratio τ/σ'_{z0} is determined by solving the Biot's consolidation equation using finite difference method. They found that the small error of shear stress in the soil can lead to a large error in the accumulated pore pressure. Therefore, it is indicated that the determination of the shear stress ratio τ/σ'_{z0} was significantly important for the pore pressure build-up in soil if equation (2.34) was adopted. Most recently, the analytic approximation proposed by Cheng et al. (2001) is validated using some experimental data obtained in a wave flume test (Sumer et al., 2011). However, Jeng et al. (2007) claimed that there are some errors in the formulations in Cheng et al. (2001); and proposed analytical solution for the wave induced pore pressure build up in Shallow soil, finite soil, and deep soil using Fourier series expansion or Laplace transformation. These solutions is further simplified by Jeng and Seymour (2007). Under the same frame, Jeng (2007) further extended these analytical approximations to the cases in which the random waves were involved. In Jeng et al. (2007), Jeng and Seymour (2007) and Jeng (2007), it is predicted that the soil only could liquefy after $t/T = 10000$. This prediction is obviously contradictory with that observed in laboratory tests. In most wave flume or centrifuge tests, the sand soil is observed to be liquefaction status before $t/T = 100$. The difference of time reaching the liquefaction status between the laboratory tests and the analytical approximation is significantly huge.

It is worth to note here that the wave induced shear stress ratio τ/σ'_{z0} in all above mentioned analytical approximations are estimated adopting the poro-elastic Biot's equation. This method is inappropriate due to the fact that mechanism of residual pore pressure build up in sand is contradictory with the assumption of poro-elastic sandy bed. In poro-elastic sandy bed, it is well known that the pore pressure could not build up under wave loading. Additionally, the pore pressure build-up in poro-elasto-plastic sand bed makes the effective contact stresses between soil particles decrease according to the effective stresses principle. It directly leads to the decrease of the wave induced shear stress. The wave induced shear stress between soil particle become zero if the sand reaching the liquefaction status. Therefore, the estimation of wave induced shear stress based on the poro-elastic Biot's equation is not reasonable.

2.5.3.2 Numerical simulation

The numerical methods to simulate the wave induced pore pressure build-up in sand soil are classified into three types. The first types numerical method takes the equation (2.34), (2.35) and (2.36) as the governing equation for the excess pore pressure generation under wave loading. The representative work can be found in Li and Jeng (2008), in which the finite difference method was adopted to solve the equation (2.34), (2.35) and (2.36). Similar with that in these analytical approximation mentioned above, the wave induced shear stress ratio τ/σ'_{z0} in source term f is still determined by the poro-elastic Biot's consolidation equation. The rationality of this assumption is doubtful. Again, the predicted time t/T reaching the liquefaction status for the sand soil under wave load is the order of magnitude of $O(10^4)$. This predicted time is much longer than that observed in most of laboratory tests (Sumer et al., 1999, 2006a, 2010; Teh et al., 2003; Tzang and Ou, 2006; Tzang et al., 2009, 2011; Sassa and Sekiguchi, 1999). Similar work also has been conducted by Yang et al. (1995). However, it is predicted that the liquefaction depth in silty seabed reached 1m when t/T=75.

The second type numerical method takes the Biot's equation as the governing equation, and adopts the poro-elasto-plastic models to describe the behaviour of sand soil. This type of method is better than the first method due to the fact that the wave induced shear stress ratio τ/σ'_{z0} in sandy bed does not need to be estimated using the poro-elastic theory; and the poro-elasto-plastic models is more reasonable than the equation (2.34), (2.35) and (2.36) to describe the wave induced excess pore pressure generation. Oka et al. (1994) developed a FEM model to study the pore pressure build-up in sand bed under linear wave loading, in which the "$u - p$" was taken as the governing equation, and a poro-elasto-plastic model was used. Their results indicated that this model could be capable of modeling the wave induced pore pressure build-up. However, there was no oscillation component in the total pore pressure after the soil was liquefied. That was a drawback. Later, Di and Sato (2003) further extended Oka et al. (1994)'s model to consider the variation of porosity and permeability of sand soil in the process of liquefaction. Their results indicated that the consideration of variation of porosity and permeability made the soil reach the liquefaction status more quickly. Some laboratory tests shown that the porosity and permeability of soil only a little decreased in the process of liquefaction; however they significantly decreased in the process of densification. Generally, the variation of porosity and permeability of soil is not necessary to be considered in the liquefaction process for dense sand. Similar work was also performed by Lu and Cui (2004), a one-dimensional FDM model is developed taking the fully dynamic Biot's equation as the governing equation, in which the variation of porosity and permeability also were considered. A simple elasto-plastic model proposed by Lu (1999) are adopted to model the behaviour of sand soil under cyclic loading. From their analysis, the soil could be liquefied after only several cycles of wave loading (t/T=2-4). This is impossible from the practical point of view. This could attribute to the application of an immature elasto-plastic model for soil.

As a kind of complicated non-associated elasto-plastic model, the Pastor-Zienkiewicz Model Mark-III (PZIII) proposed by Zienkiewicz and Mroz (1984) and Pastor et al. (1990) has been widely validated by a series of laboratory test data (Zienkiewicz et al., 1999). It can effectively model the drained or undrained behaviour of soil under cyclic or monotonic loading. Adopting the elasto-plastic model PZIII, Dunn et al. (2006) investigated the wave induced liquefaction around a buried pipelines under linear progressive wave loading. The pore pressure build up in sandy bed, and the sinking/flotation of the pipeline all could be captured by using PZIII; however, this model is limited to 2D. Later, Jeng and Ou (2010) extended the above 2D model to 3D model. By using this 3D model, the wave induced residual liquefaction potential in seabed foundation around a caisson breakwater head was investigated adopting the analytical solution of 3D linear wave around the breakwater head (Li and Jeng, 2008) to apply the wave loading. However, the breakwater was simplified as a line without weight. The effect of gravity of breakwater is not taken into consideration. Sassa and Sekiguchi (2001) proposed a modified version of PZIII model to consider the effect of rotation of principle stress axis on the soil behaviour. However, this modified PZIII model was not validated using laboratory test data. By adopting this modified PZIII mode, Sassa and Sekiguchi (2001) studied the mechanism of wave induced residual liquefaction in a sandy bed.

Although the Pastor-Zienkiewicz Model Mark-III (PZIII) could be relatively accurate to describe the soil behaviour in the process of reaching liquefaction status, it is incapable of describe the behaviour of liquefied soil. Once soil is liquefied, it losses all its shear strength, and behaves like a kind of liquid. The sea water and the below liquefied soil are consist of two layers fluid system with significant difference on density and viscosity. The boundary between the liquefied soil and sub-liquefied soil moved downward. This phenomenon was observed by a CCD camera in the centrifuge test performed by Sassa and Sekiguchi (1999). The second type method is incapable of modelling of this progressive liquefaction characteristics. The third type numerical method is to consider the moving boundary between the liquefied soil and sub-liquefied soil in the process of wave-seabed interaction. Sassa et al. (2001) proposed numerical model to investigate the progressive property of wave induced residual liquefaction, in which the moving boundary between the liquefied soil and sub-liquefied soil was taken into consideration. In Sassa et al. (2001)'s model, a similar equation with equation (2.34) was used as the governing equation, rather than the Biot's equation. The source term f was related to the rate of plastic volumetric deformation $\partial\epsilon^p/\partial t$. A simple elasto-plastic model (without verification) was used to determine the rate of plastic volumetric deformation $\partial\epsilon^p/\partial t$. Like that in these analytical approximation (Rahman and Jaber, 1986; Cheng et al., 2001; Jeng et al., 2007), the shear stress ratio τ/σ'_{z0} was still estimated by the poro-elastic solutions. This was a drawback. It is noted that the viscosity of liquefied soil is not taken into consideration in Sassa et al. (2001)'s model. Later, Liu et al. (2009) further extended Sassa et al. (2001)'s model to consider the effect of viscosity of liquefied soil. Their results indicated that the viscosity of liquefied soil should not always be ignored.

Recently, Sassa et al. (2001)'s model is further extended by Xu and Dong (2011) to investigate the random wave induced progressive residual liquefaction in sandy bed. It is noted that the viscosity of liquefied soil is not considered in Xu and Dong (2011). The laboratory wave flume test investigating the sediment behaviour during wave-induced liquefaction (Sumer et al., 2006b) found that the wave induced liquefaction and the densification appeared at different stage in the long-term wave loading process. At the early stage, the contraction in sandy soil made the pore pressure increase continuously to overcome the overburdened soil weight finally, and the front of liquefied soil progressively advanced downward. At the medium stage, the residual liquefaction reached its maximum depth, and the pore pressure basically kept its value to sustain the liquefaction status of soil for a while. At the later stage, due to the dissipation of pore pressure, the densification process occurred. Finally, all the liquefied soil contacted together again in a more compact form. The porosity and permeability of soil decreased in the process of densification. Based on Sassa et al. (2001)'s model, Miyamoto et al. (2004) developed a numerical model to investigate this densification process of liquefied soil under long term wave loading, in which the variation of porosity and permeability, and the moving boundary between the liquefied soil and densified soil were all considered. It is noted that all the above mentioned models belong to the third type numerical method are limited to one dimension. At present, it is a challenge to simulate the progressive residual liquefaction considering the moving boundary between the liquefied soil and sub-liquefied soil using 2D or 3D model.

2.6 Summary

Over the past 30 years, a great number of works have been done on the problem of Wave-Seabed Interaction and Wave-Seabed-Breakwater Interactions. A series of the analytical solutions and numerical models have been developed to investigate the interaction mechanism. However, there are still some limitations in previous literature, some of which are discussed as following:

- In previous models, the current is not considered. The effect of ocean current on the seabed response is far from being understood.

- Basically, the proposed analytical solutions are only applicable to the cases in which simple boundary conditions and elastic deformation are involved, for example, the breakwater is simplified as a line without width and weight; and the theoretic Stokes waves, such as progressive wave, standing wave, short crested wave etc., are used to apply the wave induced pressure on seabed.

- For the cases in which complex boundary conditions, or plastic deformation is involved, the numerical model should be used. However, the decoupled numerical models can not consider the effect of outer shape of breakwater, and the porosity of seabed and rubble mound on the wave field near to the breakwater.

- In coupled numerical models, either the effect of outer shape of breakwater, the porosity of seabed and rubble mound on the wave field can be taken into consideration, however, the effective stress status in seabed foundation could not be determined (Hur and Mizutani, 2003; Hur et al., 2008, 2010); or the effect of breakwater, and porosity of seabed and rubble mound can be considered, however, the momentary liquefaction in the seabed foundation in front of a breakwater is not investigated by using a coupled model.

- The wave induced residual liquefaction potential in the seabed foundation near to a breakwater is never investigated considering the effect of outer shape and gravity of breakwater adopting a coupled numerical model, in which mature elasto-plastic constitutive models are used to describe the soil behaviour under cyclic loading.

- Unfortunately, the vast majority of present coupled numerical models are limited to two-dimension. The investigation of the wave-seabed-breakwater interaction around a breakwater head need the 3D coupled numerical model.

Chapter 3

An integrated model for the Wave-Seabed-Structure Interactions: PORO-WSSI II/III [1*]

3.1 Wave model

The flow field inside and outside of porous media is governed by the VARANS (Volume-Averaged Reynolds Averaged Navier-Stokes) equations (Hsu et al., 2002), which are derived by integrating the RANS equations over the control volume. The mass and momentum conservation equations can be expressed as:

$$\frac{\partial \langle \overline{u}_{fi} \rangle}{\partial x_i} = 0, \tag{3.1}$$

$$\begin{aligned} \frac{\partial \langle \overline{u}_{fi} \rangle}{\partial t} + \frac{\langle \overline{u}_{fj} \rangle}{n(1+c_A)} \frac{\partial \langle \overline{u}_{fi} \rangle}{\partial x_j} = & \frac{1}{1+c_A}\left[-\frac{n}{\rho_f}\frac{\partial \langle \overline{p} \rangle^f}{\partial x_i} - \frac{\partial \langle \overline{u'_{fi} u'_{fj}} \rangle}{\partial x_j} + \frac{1}{\rho_f}\frac{\partial \langle \overline{\tau}_{ij} \rangle}{\partial x_j} + n g_i \right] \\ & - \frac{\langle \overline{u}_i \rangle}{1+c_A}\left[\frac{\alpha'(1-n)^2}{n^2 d_{50}^2} + \frac{\beta(1-n)}{n^2 d_{50}} \sqrt{\langle \overline{u}_{f1}, \rangle^2 + \langle \overline{u}_{f2} \rangle^2} \right], \end{aligned} \tag{3.2}$$

where u_{fi} is the flow velocity, x_i is the Cartesian coordinate, t is the time, ρ_f is the water density, p is the pressure, τ_{ij} is the viscous stress tensor of mean flow, g_i is the acceleration due to gravity, and n and d_{50} are the porosity and the equivalent mean diameter of the porous material. c_A denotes

[1*] Contents in this chapter are included in Jeng et al. (2012): D-S Jeng, Ye J H, PL-F Liu (2012). An integrated model for the wave-induced seabed response around marine structures: model, verifications and applications. Coastal Engineering, Resubmitted.

the added mass coefficient, calculated by $c_A = 0.34(1-n)/n$. $\alpha' = 200$ and $\beta = 1.1$ are empirical coefficients associated with the linear and nonlinear drag force, respectively (Liu et al., 1999).

The influence of turbulence fluctuations on the mean flow, denoted as $\langle u'_{fi} u'_{fj} \rangle$, is obtained by solving the volume-averaged $k-\epsilon$ turbulence model. The symbol of over bar stands for the Reynolds average. The symbols "$\langle\rangle$" and "$\langle\rangle^f$" stand for Darcy's volume averaging operator and the intrinsic averaging operator, respectively, which are defined as:

$$\langle a \rangle = \frac{1}{V}\int_{V_f} a\,\mathrm{d}v, \text{ and } \langle a \rangle^f = \frac{1}{V_f}\int_{V_f} a\,\mathrm{d}v \tag{3.3}$$

where V is the total averaging volume, and V_f is the portion of V that is occupied by the fluid. The relationship between the Darcy's volume averaging operator and intrinsic volume averaging is $\langle a \rangle = n\langle a \rangle^f$.

In the VARANS equations, the interfacial forces between the fluid and solids have been modeled according to the extended Forchheimer relationship, in which both linear and nonlinear drag forces between the pore water and the skeleton of porous structures are included in the last term of equation (3.2). More detailed informations of the RANS and VARANS models are available in Lin and Liu (1998) and Hsu et al. (2002). It is noted that the above VARANS equations become RANS equations for the wave motions in fluid domain when n=1.0.

The volume-averaged $k-\epsilon$ equations for the volume-averaged turbulent kinetic energy k and its dissipation rate ϵ of the porous flow in porous structures which are derived by taking the volume-average of the standard $k-\epsilon$ equations are expressed as:

$$\frac{\partial\langle k\rangle}{\partial t} + \frac{\langle\overline{u_{fj}}\rangle}{n}\frac{\partial\langle k\rangle}{\partial x_j} = \frac{\partial}{\partial x_j}[(\frac{\langle\nu_t\rangle}{\sigma_k}+\nu)\frac{\partial\langle k\rangle}{\partial x_j}] - \frac{\langle\overline{u'_{fi}u'_{fj}}\rangle}{n}\frac{\partial\langle\overline{u_{fi}}\rangle}{\partial x_j} - \langle\epsilon\rangle + n\epsilon_\infty, \tag{3.4}$$

$$\frac{\partial\langle\epsilon\rangle}{\partial t} + \frac{\langle\overline{u_{fj}}\rangle}{n}\frac{\partial\epsilon}{\partial x_j} = \frac{\partial}{\partial x_j}[(\frac{\langle\nu_t\rangle}{\sigma_\epsilon}+\nu)\frac{\partial\epsilon}{\partial x_j}] - C_{1\epsilon}\frac{\langle\epsilon\rangle}{n\langle k\rangle}\langle\overline{u'_{fi}u'_{fj}}\rangle\frac{\partial\langle\overline{u_{fi}}\rangle}{\partial x_j} - C_{2\epsilon}\frac{\langle\epsilon\rangle^2}{\langle k\rangle} + nC_{2\epsilon}\frac{\epsilon_\infty^2}{k_\infty}. \tag{3.5}$$

The definition and determination of other parameters in equation (3.4) and (3.5) could be referred to Hsu et al. (2002)

In the two-dimensional integrated model PORO-WSSI II, the above VARANS equation for flow field outside and inside of porous seabed are solved by using the finite difference two-step projection method on a staggered grid system for the space discretization, and the forward time difference method for the time derivative. The VOF method is applied to track water free-surface. The combined central difference method and upwind method are used to solve the $k-\epsilon$ equations. The detailed numerical solving process can be found in Lin and Liu (1998); Liu et al. (1999); Hsu et al. (2002).

In the three-dimensional integrated model PORO-WSSI III, the above VARANS equations for the wave motion and the porous flow in porous marine structures is solved by using the free platform provided by the open source code TRUCHAS (Truchas, 2009) developed by the US Los Alamos National Laboratory (LANL). In TRUCHAS, the finite volume method is adopted to solve the governing equations, and the VOF method is also adopted to trace the free surface of wave motion. The detailed physical algorithms can be found in the manual (Truchas, 2009).

In the 2D and 3D wave model, the internal wave maker proposed by Lin and Liu (1999) is applied to generate the target wave train, in which a mass function is added to the continuity equation (3.1) at the position where the wave maker is located. By applying different mass function, various waves could be generated, for example, the linear wave, solitary wave, 2nd-order and 5th-order stokes wave, cnoidal wave etc..

3.2 Soil model

3.2.1 Governing equations

It has been commonly known that soil is a multi-phase material consisting of soil particles, water and trapped air. In the soil mixture, the soil particles form the skeleton; the water and the air fill the void of skeleton. Therefore, soil is a three-phase porous material, rather than a continuous medium. In this thesis, the dynamic Biot's equation known as "$u - p$" approximation proposed by Zienkiewicz et al. (1980) are used to govern the dynamic response of the porous response under wave loading, in which the relative displacements of pore fluid to soil particles are ignored, but the acceleration of the pore water and soil particles are included:

For two-dimension condition:

$$\frac{\partial \sigma'_x}{\partial x} + \frac{\partial \tau_{xz}}{\partial z} = -\frac{\partial p_s}{\partial x} + \rho \frac{\partial^2 u_s}{\partial t^2}, \tag{3.6}$$

$$\frac{\partial \tau_{xz}}{\partial x} + \frac{\partial \sigma'_z}{\partial z} + \rho g = -\frac{\partial p_s}{\partial z} + \rho \frac{\partial^2 w_s}{\partial t^2}, \tag{3.7}$$

$$k\nabla^2 p_s - \gamma_w n\beta \frac{\partial p_s}{\partial t} + k\rho_f \frac{\partial^2 \epsilon}{\partial t^2} = \gamma_w \frac{\partial \epsilon}{\partial t}. \tag{3.8}$$

For three-dimension condition:

$$\frac{\partial \sigma'_x}{\partial x} + \frac{\partial \tau_{xy}}{\partial y} + \frac{\partial \tau_{xz}}{\partial z} = -\frac{\partial p_s}{\partial x} + \rho \frac{\partial^2 u_s}{\partial t^2}, \tag{3.9}$$

$$\frac{\partial \tau_{xy}}{\partial x} + \frac{\partial \sigma'_y}{\partial y} + \frac{\partial \tau_{yz}}{\partial z} = -\frac{\partial p_s}{\partial y} + \rho \frac{\partial^2 v_s}{\partial t^2}, \tag{3.10}$$

$$\frac{\partial \tau_{xz}}{\partial x} + \frac{\partial \tau_{yz}}{\partial y} + \frac{\partial \sigma'_z}{\partial z} + \rho g = -\frac{\partial p_s}{\partial z} + \rho \frac{\partial^2 w_s}{\partial t^2}, \tag{3.11}$$

$$k\nabla^2 p_s - \gamma_w n\beta \frac{\partial p_s}{\partial t} + k\rho_f \frac{\partial^2 \epsilon}{\partial t^2} = \gamma_w \frac{\partial \epsilon}{\partial t}, \tag{3.12}$$

where (u_s, v_s, w_s) are soil displacements in the x-, y- and z- directions, respectively; n is soil porosity; σ'_x and σ'_z are effective normal stresses in the horizontal and vertical directions, respectively; τ_{xz} is shear stress; p_s is pore water pressure; $\rho = \rho_f n + \rho_s(1-n)$ is the average density of porous seabed; ρ_f is fluid density ; ρ_s is solid density; k is Darcy's permeability; g is the gravitational acceleration, γ_ω is unit weight of water, and ϵ is the volumetric strain of soil. In equation (3.8) and (3.12), the compressibility of pore fluid (β) and the volume strain (ϵ) are defined as

$$\beta = \left(\frac{1}{K_f} + \frac{1-S_r}{p_{w0}}\right), \tag{3.13}$$

$$\epsilon = \frac{\partial u_s}{\partial x} + \frac{\partial w_s}{\partial z}, \qquad \text{for 2D condition} \tag{3.14}$$

$$\epsilon = \frac{\partial u_s}{\partial x} + \frac{\partial v_s}{\partial y} + \frac{\partial w_s}{\partial z}, \qquad \text{for 3D condition} \tag{3.15}$$

where S_r is degree of saturation of seabed, p_{w0} is the absolute static pressure and K_f is bulk modulus of pore water.

3.2.2 Constitutive model

In the above governing equations, the effective stresses can be determined through multiplying the corresponding strains by a so call 'elastic matrix' D

$$[\sigma'] = \mathrm{D}[\epsilon'] \tag{3.16}$$

where $[\sigma']$ is the effective stresses matrix, $[\epsilon']$ is the strain matrix. Under plane strain conditions, the elastic matrix D can be expressed as:

$$\mathrm{D} = \frac{E}{(1+\nu)(1-2\nu)} \begin{bmatrix} 1-\nu & \nu & 0 \\ \nu & 1-\nu & 0 \\ 0 & 0 & \frac{1-2\nu}{2} \end{bmatrix}, \tag{3.17}$$

where E and ν are the elastic modulus and Poisson's ratio respectively. In this soil model, both elastic model and elasto-plastic model, such as PZIII (Pastor et al., 1990), Camb clay, Mohr Coulomb etc. could be applied in computation. If elasto-plastic constitutive model is used in computation, the elastic matrix D should be replaced by elasto-plastic matrix D^{ep}:

$$\mathrm{D}^{ep}_{ijkl} = \mathrm{D}^{e}_{ijkl} - \frac{\mathrm{D}^{e}_{ijmn} m_{mn} n_{st} \mathrm{D}^{e}_{stkl}}{H_{L/U} + n_{st}\mathrm{D}^{e}_{stkl} m_{kl}}, \tag{3.18}$$

in which D^{e}_{ijkl} is the tensor form of elastic matrix D. $H_{L/U}$ is the plastic modulus at loading or unloading stage. m_{mn} plastic flow direction tensor, n_{st} is the loading or unloading direction tensor. The above two direction tensors are formulated as:

$$m_{mn} = \frac{\left(\frac{\partial g}{\partial \sigma'_{mn}}\right)}{\left\|\frac{\partial g}{\partial \sigma'_{mn}}\right\|} \text{ and } n_{st} = \frac{\left(\frac{\partial f}{\partial \sigma'_{st}}\right)}{\left\|\frac{\partial f}{\partial \sigma'_{st}}\right\|}, \tag{3.19}$$

where $\left\|\frac{\partial g}{\partial \sigma'_{mn}}\right\|$ and $\left\|\frac{\partial f}{\partial \sigma'_{st}}\right\|$ represent the norm of the tensor $\frac{\partial g}{\partial \sigma'_{ij}}$ and $\frac{\partial f}{\partial \sigma'_{ij}}$, respectively. f and g are the yield surface function and plastic potential surface function in stress space. If the same function is adopted for both yield surface f and plastic potential surface g, then associated flow rule will be applied, otherwise, non-associated flow rule will be applied. In this numerical model, the generalized non-associated elasto-plastic constitutive model Pastor-Zienkiewicz Model Mark-III (PZIII), proposed by Zienkiewicz and Mroz (1984) and Pastor et al. (1990) is used to describe the wave induced elasto-plastic behavior of seabed foundation. The detail information about the Pastor-Zienkiewicz Model Mark-III (PZIII) soil model is presented in the following. It has been validated by a series of laboratory tests that the Pastor-Zienkiewicz Model Mark-III soil model is very suitable to describe the behavior of soil under monotonic and cyclic loading (Zienkiewicz et al., 1999).

In the generalised plasticity theory, the strain increment is generally decomposed into two components: elastic part and plastic part:

$$d\epsilon_{ij} = d\epsilon_{ij}^{e} + d\epsilon_{ij}^{p}. \tag{3.20}$$

The elastic strain increment can be expressed by linear elastic model:

$$d\epsilon_{ij}^{e} = C_{ijkl}^{e} d\sigma_{kl}, \tag{3.21}$$

where C_{ijkl}^{e} is the elastic compliance tensor, equals to the inverse of the elastic tensor D_{ijkl}^{e}. Under the linear elastic frame, the elastic tensor D_{ijkl}^{e} is expressed as:

$$D_{ijkl}^{e} = \lambda' \delta_{ij}\delta_{kl} + 2G\delta_{ik}\delta_{jl}, \tag{3.22}$$

where λ' is a Lame's constant and G is the shear modulus. In computation, the elastic volumetric strain-rate and deviatoric strain-rate are generally considered separately as:

$$\dot{\epsilon}_{v}^{e} = \frac{\dot{p}'}{K_{ev}}, \text{ and } \dot{\epsilon}_{s}^{e} = \frac{\dot{q}'}{G_{es}}, \tag{3.23}$$

where the ϵ_{v}^{e} and ϵ_{s}^{e} is the elastic volumetric strain and deviatoric strain, respectively. The symbol (.) means time derivative. K_{ev} is the bulk modulus of soil, and G_{es} is the shear modulus. p' and q' is the mean effective stress and deviatoric stress respectively, defined as:

$$p' = \frac{1}{3}\left(\sigma'_{11} + \sigma'_{22} + \sigma'_{33}\right), \tag{3.24}$$

$$q' = \sqrt{\frac{\left(\sigma'_{11} - \sigma'_{22}\right)^2 + \left(\sigma'_{11} - \sigma'_{33}\right)^2 + \left(\sigma'_{22} - \sigma'_{33}\right)^2 + 6\left(\sigma_{12}^2 + \sigma_{23}^2 + \sigma_{31}^2\right)}{3}}. \tag{3.25}$$

In Pastor-Zienkiewicz Model Mark-III model, the elastic constants K_{ev} and G_{es} are positively dependent on the mean effective stress p', expressed as:

$$K_{ev} = K_{evo}\frac{p'}{p'_0} \text{ and } G_{es} = G_{eso}\frac{p'}{p'_0}, \tag{3.26}$$

in which K_{ev0} and G_{es0} is the elastic bulk modulus and shear modulus of soil measured when the mean effective stress is p'_0.

In generalised plastic theory, the plastic strain $d\epsilon^p_{ij}$ can be expressed by the yield surface function f, plastic potential surface function g and the plastic modulus $H_{L/U}$ at loading or unloading stage:

$$d\epsilon^p_{ij} = \frac{1}{H_{L/U}} m_{ij} n_{ij} d\sigma_{ij}, \tag{3.27}$$

where $d\sigma_{ij}$ is the stress increment. m_{ij} plastic flow direction tensor, n_{ij} is the loading or unloading direction tensor. The above two direction tensors are formulated as:

$$m_{ij} = \frac{\left(\frac{\partial g}{\partial \sigma'_{ij}}\right)}{\left\|\frac{\partial g}{\partial \sigma'_{ij}}\right\|} \text{ and } n_{ij} = \frac{\left(\frac{\partial f}{\partial \sigma'_{ij}}\right)}{\left\|\frac{\partial f}{\partial \sigma'_{ij}}\right\|}, \tag{3.28}$$

where $\left\|\frac{\partial g}{\partial \sigma'_{ij}}\right\|$ and $\left\|\frac{\partial f}{\partial \sigma'_{ij}}\right\|$ represent the norm of the tensor $\frac{\partial g}{\partial \sigma'_{ij}}$ and $\frac{\partial f}{\partial \sigma'_{ij}}$, respectively. If the same function is adopted for both yield surface f and plastic potential surface g, then associated flow rule will be applied, otherwise, non-associated flow rule will be applied.

In plastic theory, the loading status and unloading status are generally defined by following criterion:

$$\begin{array}{ll} n_{ij} d\sigma_{ij} > 0; & \text{for loading,} \\ n_{ij} d\sigma_{ij} = 0; & \text{for neutral-loading,} \\ n_{ij} d\sigma_{ij} < 0; & \text{for unloading.} \end{array} \tag{3.29}$$

For the situation of softening, the plastic strain could be developed under loading condition even when the stresses decrease, In this case, following criterion should be used instead.

$$\begin{array}{ll} n_{ij} d\sigma^e_{ij} > 0; & \text{for loading,} \\ n_{ij} d\sigma^e_{ij} = 0; & \text{for neutral-loading,} \\ n_{ij} d\sigma^e_{ij} < 0; & \text{for unloading.} \end{array} \tag{3.30}$$

The $H_{L/U}$ stands for the plastic modulus of soil at loading or unloading stage. Positive $H_{L/U}$ means the soil is hardening; while, negative $H_{L/U}$ means the soil is softening. In computational analysis, if the total strain increment $d\epsilon_{kl}$, including elastic and plastic parts, is determined, then the stress increment $d\sigma_{ij}$ can be formulated as:

$$d\sigma_{ij} = D^{ep}_{ijkl} d\epsilon_{kl}, \tag{3.31}$$

in which D^{ep}_{ijkl} is the elasto-plastic tensor, expressed as:

$$D^{ep}_{ijkl} = D^{e}_{ijkl} - \frac{D^{e}_{ijmn} m_{mn} n_{st} D^{e}_{stkl}}{H_{L/U} + n_{st} D^{e}_{stkl} m_{kl}}. \tag{3.32}$$

In Pastor-Zienkiewicz Model Mark-III model, three are three basic assumptions:

First, the dilatancy of soil is approximately described by a straight line in the $p' - q'$ plane, expressed as:

$$d_g = \frac{d\epsilon^p_v}{d\epsilon^p_s} = (1 + \alpha')(M_g - \eta), \tag{3.33}$$

where $d\epsilon_v$ and $d\epsilon_s$ are the total increment of volumetric and deviatoric strain. M_g is the slope of critical state line in $p' - q'$ plane. η is the ratio between the mean effective stress and deviatoric stress q'/p'. α' is a constant.

Second, a smoothed Mohr-Coulomb criterion is assumed to generalize the critical state line to three dimensional stress status. Therefore

$$M_g = \frac{6 \sin\phi}{3 - \sin\phi \sin 3\theta'}, \tag{3.34}$$

in which θ' is the Lode's angle, ϕ is the residual internal frictional angle of sand obtained when θ'=30° in triaxial compression test.

Third, the ratio between the plastic increment of volumetric strain $d\epsilon^p_v$ and deviatoric stain $d\epsilon^p_s$ is approximately the same with the ratio between the total increment of volumetric strain $d\epsilon_v$ and deviatoric stain $d\epsilon_s$:

$$\frac{d\epsilon^p_v}{d\epsilon^p_s} = \frac{d\epsilon_v}{d\epsilon_s} = (1 + \alpha')(M_g - \eta). \tag{3.35}$$

Under the frame of generalised plastic theory, Pastor et al. (1990) proposed the form of yield surface function f and plastic potential surface g as:

$$f = q' - M_f p' \left(1 + \frac{1}{\alpha_f}\right)\left[1 - \left(\frac{p'}{p'_f}\right)^{\alpha_f}\right] = 0, \tag{3.36}$$

$$g = q' - M_g p' \left(1 + \frac{1}{\alpha_g}\right)\left[1 - \left(\frac{p'}{p'_g}\right)^{\alpha_g}\right] = 0, \tag{3.37}$$

in which p'_f and p'_g are constants characterizing the size of yield surface f and plastic potential surface g , α_f and α_g are coefficients related to the stress-dilatancy of soil, M_g is the slope of critical state line in $p' - q'$ plane, and M_f is a material parameters, which can be given by:

$$\frac{M_f}{M_g} = D_r, \tag{3.38}$$

where $D_r = \frac{e - e_{min}}{e_{max} - e_{min}}$ represents the relative density of soil, e is the viod ratio of soil.

The plastic modulus at loading and unloading stage $H_{L/U}$ in PZIII model is defined as:

$$H_L = H_0 p' \left(1 - \frac{q'/p'}{\eta_f}\right)^4 \left[1 - \frac{q'/p'}{M_g} + \beta_0 \beta_1 exp\left(-\beta_0 \xi\right)\right] \left(\frac{q/p'}{\eta_{max}}\right)^{-\gamma_{DM}}, \tag{3.39}$$

$$H_U = \begin{cases} H_{u0} \left(\frac{M_g}{\eta_u}\right)^{\gamma_U} & \text{for} \left|\frac{M_g}{\eta_u}\right| > 1 \\ H_{u0} & \text{for} \left|\frac{M_g}{\eta_u}\right| \leq 1 \end{cases}, \tag{3.40}$$

where η_u is the stress ratio from which the unloading takes place, while γ_U is the material constant controlling the influence of that. In (3.39) and (3.40), H_0 and H_{U0} are model parameters which scale the plastic modulus; the dependency on p' in equation (3.39) is consistent with the fact that the plastic strain reduces if the effective mean stress increases. The term $\left(1 - \frac{q'/p'}{\eta_f}\right)^4$ illustrates the fact that the plastic strain increment increases when the stress ratio increases, and the stress ratio cannot exceed η_f, where $\eta_f = M_f (1 + 1/\sigma_0)$.

In (3.39), the term $\left[1 - \frac{q'/p'}{M_{g0}}\right]$ accounts for influence of volumetric hardening, which approaches to zero when the stress ratio reaches the critical line. This implies that sand fails when the stress ratio reaches the critical line. The term $[\beta_0 \beta_1 \exp(-\beta_0 \xi)]$ accounts for the influence of deviatoric strain hardening, where β_0 and β_1 are material constants, with suggested value from 1.5 to 5.0 and 0.1 to 0.2, respectively.

Again, in (3.39), the term $\left(\frac{q/p'}{\eta_{max}}\right)^{-\gamma_{DM}}$ accounts for the plastic modulus in reloading stage, which illustrates the fact that higher the stress ratio reaches, the less plastic deformation occurs in reloading stage. In (3.39), η_{max} is the largest value of stress ratio the soil reached, and γ_{DM} is a degradation constant.

3.2.3 Numerical method

The finite element method is used to solve the governing equation (3.6) to (3.12). For dynamic problems, the spatial discretization and temporal discretization have to be performed for the above three governing equations.

3.2.3.1 Spatial discretization

The spatial discretization involves the replacement of variables **u** and **p** by suitable shape functions in the governing equations

$$\mathbf{u} = \sum N_i^u u_i = \mathbf{N^u}\bar{\mathbf{u}} \tag{3.41}$$

$$\mathbf{p} = \sum N_i^p p_i = \mathbf{N^p}\bar{\mathbf{p}} \tag{3.42}$$

where **u** and **p** are the displacement vector of soil and the pore pressure. The $\bar{\mathbf{u}}$ and $\bar{\mathbf{p}}$ are the vectors of node displacement and pore pressure. The $\mathbf{N^u}$ and $\mathbf{N^p}$ are the shape function of displacement and pore pressure. Their expressions are listed as following:

For two-dimension condition:

$$\bar{\mathbf{u}}_s = \begin{bmatrix} u_{s1} & v_{s1} & u_{s2} & v_{s2} & \cdots & u_{sn} & v_{sn} \end{bmatrix}^{\mathrm{T}}, \tag{3.43}$$

$$\bar{\mathbf{p}}_s = \begin{bmatrix} p_{s1} & p_{s2} & \cdots & p_{sn} \end{bmatrix}^{\mathrm{T}}, \tag{3.44}$$

$$\mathbf{N^u} = \begin{bmatrix} N_1^u & 0 & N_2^u & 0 & \cdots & N_n^u & 0 \\ \\ 0 & N_1^u & 0 & N_2^u & \cdots & 0 & N_n^u \end{bmatrix}, \tag{3.45}$$

$$\mathbf{N^p} = \begin{bmatrix} N_1^p & N_2^p & \cdots & N_n^p \end{bmatrix}. \tag{3.46}$$

For three-dimension condition:

$$\bar{\mathbf{u}}_s = \begin{bmatrix} u_{s1} & v_{s1} & w_{s1} & u_{s2} & v_{s2} & w_{s2} & \cdots & u_{sn} & v_{sn} & w_{sn} \end{bmatrix}^{\mathrm{T}}, \tag{3.47}$$

$$\bar{\mathbf{p}}_s = \begin{bmatrix} p_{s1} & p_{s2} & \cdots & p_{sn} \end{bmatrix}^{\mathrm{T}}, \tag{3.48}$$

$$\mathbf{N^u} = \begin{bmatrix} N_1^u & 0 & 0 & N_2^u & 0 & 0 & \cdots & N_n^u & 0 & 0 \\ 0 & N_1^u & 0 & 0 & N_2^u & 0 & \cdots & 0 & N_n^u & 0 \\ 0 & 0 & N_1^u & 0 & 0 & N_2^u & \cdots & 0 & 0 & N_n^u \end{bmatrix}, \tag{3.49}$$

$$\mathbf{N^p} = \begin{bmatrix} N_1^p & N_2^p & \cdots & N_n^p \end{bmatrix}. \tag{3.50}$$

Substituting equations (3.41) and (3.42) into the governing equations (3.6) to (3.8) or Equation (3.9) to (3.12), and applying the variation principle, the "$u - p$" governing equations are discretized in space as:

$$\mathrm{M}\ddot{\bar{\mathbf{u}}} + \mathrm{K}\bar{\mathbf{u}} - \mathrm{Q}\bar{\mathbf{p}} = f^{(1)}, \tag{3.51}$$

$$\mathrm{G}'\ddot{\bar{\mathbf{u}}} + \mathrm{Q}^{\mathrm{T}}\dot{\bar{\mathbf{u}}} + \mathrm{S}\dot{\bar{\mathbf{p}}} + \mathrm{H}\bar{\mathbf{p}} = f^{(2)}, \tag{3.52}$$

where $\bar{\mathbf{u}}$ and $\bar{\mathbf{p}}$ are the nodal displacements and the pore pressure vectors respectively. M, K, Q, G, S,and H are the mass, stiffness, coupling, dynamic seepage force, compressibility, and permeability matrixes, respectively. The terms of $f^{(1)}$ and $f^{(2)}$ are the node force vectors. Their expressions are listed following

$$\mathrm{M} = \int (\mathbf{N^u})^{\mathrm{T}} \rho \mathbf{N^u} d\Omega, \tag{3.53}$$

$$\mathrm{K} = \int \mathbf{B}^{\mathrm{T}} \mathbf{D} \mathbf{B} d\Omega, \tag{3.54}$$

$$\mathrm{Q} = \int \mathbf{B}^{\mathrm{T}} m \mathbf{N^p} d\Omega, \tag{3.55}$$

$$\mathrm{S} = \int (\mathbf{N^p}) n\beta \mathbf{N^p} d\Omega, \tag{3.56}$$

$$\mathrm{H} = \int (\triangledown \mathbf{N^p})^{\mathrm{T}} k \triangledown \mathbf{N^p} d\Omega, \tag{3.57}$$

$$\mathrm{G}' = \int (\triangledown \mathbf{N^p})^{\mathrm{T}} k \rho_f \mathbf{N^u} d\Omega, \tag{3.58}$$

For two-dimension condition:

$$\triangledown = \begin{bmatrix} \frac{\partial}{\partial x} \\ \frac{\partial}{\partial z} \end{bmatrix}, \tag{3.59}$$

$$\mathrm{B} = \begin{bmatrix} \frac{\partial}{\partial x} & 0 \\ 0 & \frac{\partial}{\partial z} \\ \frac{\partial}{\partial z} & \frac{\partial}{\partial x} \end{bmatrix} \mathbf{N^u}. \tag{3.60}$$

For three-dimension condition:

$$\triangledown = \begin{bmatrix} \frac{\partial}{\partial x} \\ \frac{\partial}{\partial y} \\ \frac{\partial}{\partial z} \end{bmatrix}, \tag{3.61}$$

$$\mathrm{B} = \begin{bmatrix} \frac{\partial}{\partial x} & 0 & 0 \\ 0 & \frac{\partial}{\partial y} & 0 \\ 0 & 0 & \frac{\partial}{\partial z} \\ \frac{\partial}{\partial y} & \frac{\partial}{\partial x} & 0 \\ 0 & \frac{\partial}{\partial z} & \frac{\partial}{\partial y} \\ \frac{\partial}{\partial z} & 0 & \frac{\partial}{\partial x} \end{bmatrix} \mathbf{N^u}, \tag{3.62}$$

$$f^{(1)} = \int (\mathbf{N^u})^{\mathrm{T}} \rho \mathbf{g} d\Omega + \int (\mathbf{N^u})^{\mathrm{T}} \bar{\mathbf{t}} d\Gamma, \tag{3.63}$$

$$f^{(2)} = -\int (\mathbf{N^p})^{\mathrm{T}} \nabla^{\mathrm{T}} (k\rho_f \mathbf{g}) d\Omega + \int (\mathbf{N^p})^{\mathrm{T}} \bar{\mathbf{q}} d\Gamma, \tag{3.64}$$

where $m = [1, 1, 1, 0, 0, 0]^{\mathrm{T}}$, $\bar{t}$ is the stress acting on the surface of computational domain, $\bar{q}$ is the water flux on the surface of computational domain. The matrix G' could be neglected in low frequency analysis proposed by Chan (1988), such as under ocean wave loading.

3.2.3.2 Temporal discretization

The general procedure adopted in this study to solve the governing equation (3.51) and (3.52) at each time step, is the GNpj (Generalized Newmark p^{th} order scheme for j^{th} order equation) time integration scheme. This method is originally proposed by Newmark (1959), and later extended by Katona and Zienkiewicz (1985).

If the governing equation (3.51) and (3.52) are satisfied at the n^{th} time step, then they will also be satisfied at the $(n+1)^{th}$ time step (G is neglected):

$$\mathrm{M_{n+1}} \ddot{\bar{\mathbf{u}}}_{n+1} + \mathrm{K_{n+1}} \bar{\mathbf{u}}_{n+1} - \mathrm{Q_{n+1}} \bar{\mathbf{p}}_{n+1} = f^{(1)}_{n+1}, \tag{3.65}$$

$$\mathrm{Q^{T}_{n+1}} \dot{\bar{\mathbf{u}}}_{n+1} + \mathrm{S_{n+1}} \dot{\bar{\mathbf{p}}}_{n+1} + \mathrm{H_{n+1}} \bar{\mathbf{p}}_{n+1} = f^{(2)}_{n+1}. \tag{3.66}$$

By applying the GN22 method for the soil displacements, the acceleration, velocity and displacement at time $t_n + \Delta t$ are expressed as:

$$\ddot{\bar{\mathbf{u}}}_{n+1} = \ddot{\bar{\mathbf{u}}}_n + \Delta \ddot{\bar{\mathbf{u}}}_n, \tag{3.67}$$

$$\dot{\bar{\mathbf{u}}}_{n+1} = \dot{\bar{\mathbf{u}}}_n + \ddot{\bar{\mathbf{u}}}_n \Delta t + \beta_1 \Delta \ddot{\bar{\mathbf{u}}}_n \Delta t, \tag{3.68}$$

$$\bar{\mathbf{u}}_{n+1} = \bar{\mathbf{u}}_n + \dot{\bar{\mathbf{u}}}_n \Delta t + \frac{1}{2} \ddot{\bar{\mathbf{u}}}_n \Delta t^2 + \frac{1}{2} \beta_2 \Delta \ddot{\bar{\mathbf{u}}}_n \Delta t^2. \tag{3.69}$$

And applying the GN11 method for pore pressure, the the rate of pore pressure and the pore pressure are expressed as:

$$\dot{\bar{\mathbf{p}}}_{n+1} = \dot{\bar{\mathbf{p}}}_n + \Delta \dot{\bar{\mathbf{p}}}_n, \tag{3.70}$$

$$\bar{\mathbf{p}}_{n+1} = \bar{\mathbf{p}}_n + \dot{\bar{\mathbf{p}}}_n \Delta t + \theta_1 \Delta \dot{\bar{\mathbf{p}}}_n \Delta t. \tag{3.71}$$

In the above schemes, if the parameters β_1, β_2 and θ_1 satisfy following conditions:

$$\beta_2 \geq \beta_1 \geq \frac{1}{2} \quad \text{and} \quad \theta_1 \geq \frac{1}{2}, \tag{3.72}$$

then the GNpj time integration scheme is unconditionally stable (Chan, 1988). In this study, the three parameters are chosen as: $\beta_2 = 0.605$, $\beta_1 = 0.6$ and $\theta_1 = 0.6$. It has been shown by Chan (1988) that the above three values work well to evaluate the dynamic response of soil under earthquakes and ocean waves.

Substituting equations (3.67), (3.68), (3.69), (3.70) and (3.71) into equations (3.65) and (3.66), we obtain following matrix governing equation:

$$\begin{bmatrix} \mathrm{M}_{n+1} + \frac{1}{2}\mathrm{K}_{n+1}\beta_2\Delta t^2 & -\mathrm{Q}_{n+1}\theta_1\Delta t \\ \mathrm{Q}^{\mathrm{T}}_{n+1}\beta_1\Delta t & \mathrm{S}_{n+1} + \mathrm{H}_{n+1}\beta_1\Delta t \end{bmatrix} \begin{bmatrix} \Delta\ddot{\bar{\mathbf{u}}}_n \\ \Delta\dot{\bar{\mathbf{p}}}_n \end{bmatrix} = \begin{bmatrix} F^{(1)}_{n+1} \\ F^{(2)}_{n+1} \end{bmatrix}, \tag{3.73}$$

where $F^{(1)}_{n+1}$ and $F^{(2)}_{n+1}$ are formulated as:

$$F^{(1)}_{n+1} = f^{(1)}_{n+1} + \mathrm{Q}_{n+1}\bar{p}_n + \mathrm{Q}_{n+1}\dot{\bar{p}}_n\Delta t - \mathrm{M}_{n+1}\ddot{\bar{\mathbf{u}}}_n - \mathrm{K}_{n+1}(\bar{\mathbf{u}}_n + \dot{\bar{\mathbf{u}}}_n\Delta t + \frac{1}{2}\ddot{\bar{\mathbf{u}}}_n\Delta t^2), \tag{3.74}$$

$$F^{(2)}_{n+1} = f^{(2)}_{n+1} - \mathrm{S}_{n+1}\dot{\bar{p}}_n - \mathrm{H}_{n+1}(\bar{p}_n + \dot{\bar{p}}_n\Delta t) - \mathrm{Q}_{n+1}(\dot{\bar{\mathbf{u}}}_n + \ddot{\bar{\mathbf{u}}}_n\Delta t). \tag{3.75}$$

In equation (3.73), the unknowns are $\Delta\ddot{\bar{\mathbf{u}}}_n$ and $\Delta\dot{\bar{\mathbf{p}}}_n$. At $(n+1)^{th}$ time step, they can be determined by solving equation (3.73) by taking the values determined at the n time step as the initial conditions. In this investigation, the Newton-Raphson method is adopted to solve equation (3.73). Once the incremental acceleration $\Delta\ddot{\bar{\mathbf{u}}}_n$ and incremental rate of pore pressure $\Delta\dot{\bar{\mathbf{p}}}_n$ are determined, the displacement of the soil and pore pressure can be accordingly obtained by applying equations (3.69) and (3.71).

3.3 Integration method

In the process of coupling the VARANS equations and the dynamic Biot's equations, two problems have to be considered: time scheme and mesh system respectively.

Time scheme: In numerical coupling computation, there are generally two kinds of time schemes: matching time scheme and non-matching time scheme. The matching time scheme requires that the time interval for the fluid domain and solid domain is the same. The time interval for the fluid domain is generally set as a very small value, for example, 0.005s. The time interval for the solid domain could be a value which is much greater than that of the fluid domain, for example 0.2s. The difference of the time interval in the fluid domain and solid domain can be significantly different.

Mesh system: There are also two kinds of mesh system: matching mesh and non-matching mesh, in numerical coupling computation. The matching mesh system requires that the elements in the fluid domain and the elements in the solid domain have to share the same nodes on the surface of seabed and marine structures. However, the size of elements in the fluid domain is generally also very small relative to the size of elements in solid domain. The ratio of the size of elements in solid domain and fluid domain can be up to 5 to 20.

If both matching time scheme and matching mesh system are adopted in computational domain, it requires huge amount of CPU computation time and the memory due to the small time interval and small size of element in fluid and solid domain. However, it is useless to improve the computation accuracy. In this study, both non-matching time scheme and non-matching mesh system are used to avoid the aforementioned problems.The non-matching time scheme and non-matching mesh system can make the time interval for fluid domain and solid domain be set as different values, and make the mesh systems in fluid/solid domain are independent completely.

In order to couple the seawater and the seabed together at the interface with the non-matching time scheme and non-matching mesh system, a data exchange interface between the VARANS equations and the dynamic Biot's equations is developed. The Point Radius Interpolation Method (Wang et al., 2004b) is adopted in this study to implement the data exchange between the wave model and soil model. Here, the validation of the Radius Point Interpolation Method is performed by using four functions: (a) sin(x), (b) cos(x), (c) parabolic function, and (d) power function. The curves of the interpolation functions and the scatter interpolation points for the four functions are shown in Figure 3.1. As illustrated in Figure 3.1, it can be concluded that the Radius Point Interpolation method is sufficiently accurate to exchange the data between the fluid domain and porous medium domain. After being proven, the maximum relative error can be constrained under 0.6%.

Coupling process: In the integrated/coupled model, the wave motion and the porous flow is governed by the Volume-Averaged Reynolds Averaged Navier-Stokes equations; and the soil model is governed by the dynamic Biot's equations. In the wave model, the continuity of pressure, velocity/flux of fluid at the interface between seawater and porous seabed/marine structures have been considered. The flow field in fluid domain and in porous seabed/marine structures is fully coupled.

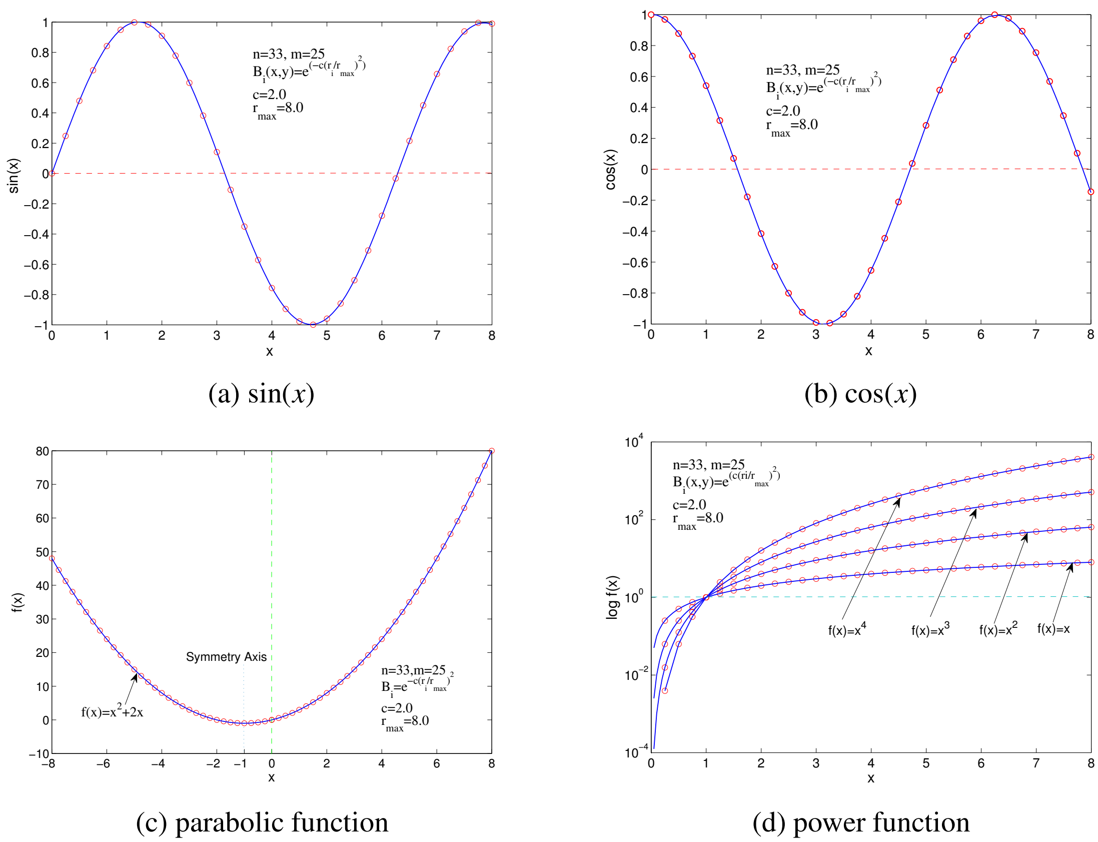

(a) $\sin(x)$ (b) $\cos(x)$

(c) parabolic function (d) power function

Figure 3.1: The interpolation curves determined by Point Radial Interpolation Method for sin(x), cos(x), parabolic function and power function. ∘: the scatter interpolation points; −: the interpolation curves

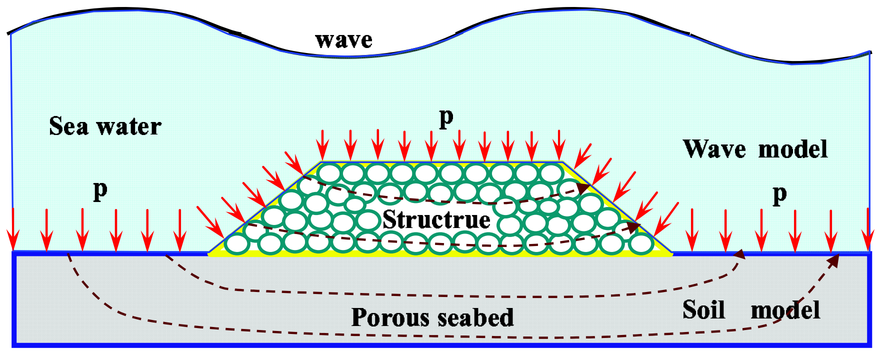

Figure 3.2: The structural map of the coupling between the wave model and soil model

When coupling the VARANS equations to dynamic Biot's equations, only the pressure continuity is applied in computation. (Figure 3.2). Actually, other quantities, such as velocity/flux of fluid has little effect on the dynamic response of marine structures and their seabed foundation if the permeability of seabed is limited (Bierawski and Maeno, 2004).

In the coupling computation, the wave model is responsible for the generation, propagation of wave, and the porous flow in porous structures, such as a seabed, rubble mound breakwater etc.; and determines the pressure acting on the seabed and marine structures. Due to the fact that the VARANS equations is coupled at the interface between the fluid domain and the porous structures through the pressure and velocity/flux continuity, the pressure and the flow field are continuous in the whole computational domain. At the meantime, the pressure/force acting on seabed and marine structures determined by the wave model is provided to the soil model through the data exchange interface developed to calculate the dynamic response of seabed and marine structures, including the displacements, pore pressure and the effective stresses. The coupling process is illustrated in Figure 3.3.

3.4 Verification of models

It is necessary to show that the developed integrated numerical model could accurately predict the dynamic response of marine structures and seabed foundation under wave loading. In this section, the analytical solution of linear wave-induced seabed response proposed by Hsu and Jeng (1994), and

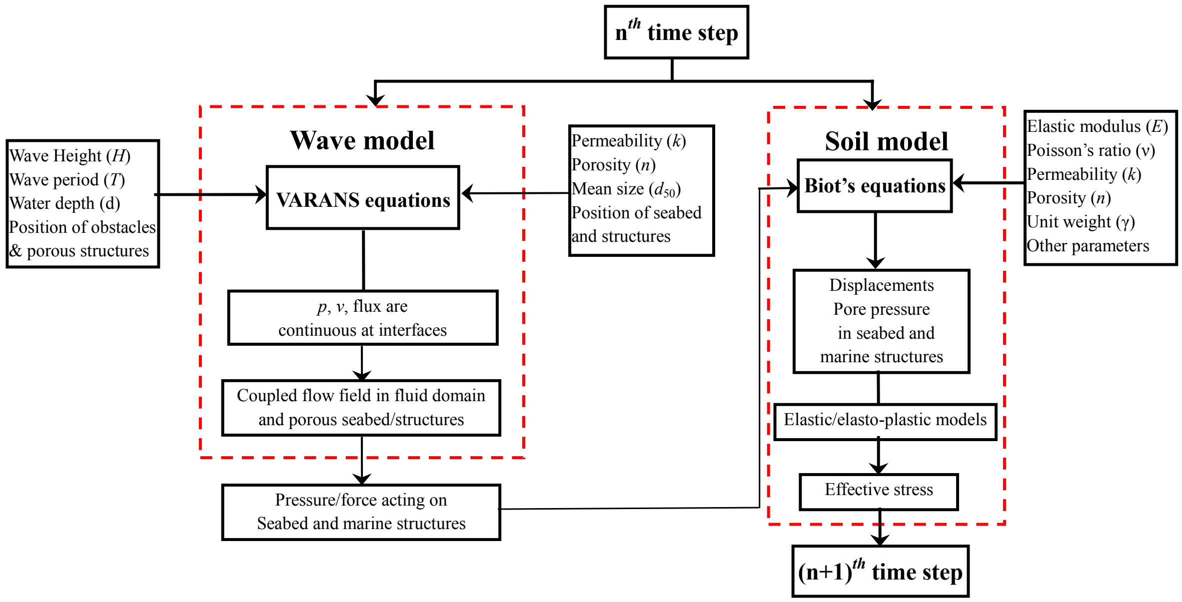

Figure 3.3: The coupling precess between the wave model and soil model adopted in PORO-WSSI II/III

some experiments which are available in previous investigations in which structure is included or not included are used to verify the integrated model developed.

3.4.1 Analytical solution (Hsu and Jeng, 1994)

Numerical results of the maximum values of wave-induced pore pressure and effective stresses in partially saturated coarse/fine sand (the degree of saturation=98%) determined by PORO-WSSI II are shown in Figure 3.4. The results of the analytical solution (Hsu and Jeng, 1994) are also plotted in the figure. From Figure 3.4(a) and (b), it is found that the results of the numerical model overall agree well with analytical solution. The minor differences between two models come from that the analytical solution was based on quasi-static soil behaviour and the present numerical model is based on "$u - p$" approximation.

3.4.2 Lu (2005) 's experiment-Regular wave and Cnoidal wave

Lu (2005) conducted a series of lab experiments about the dynamic response of sand bed to the waves propagating on it in a wave flume which is 60m long, 1.5m wide and 1.8m high. The waves generated in the wave flume include regular waves and cnoidal waves. The periods of wave are from 1.0s to

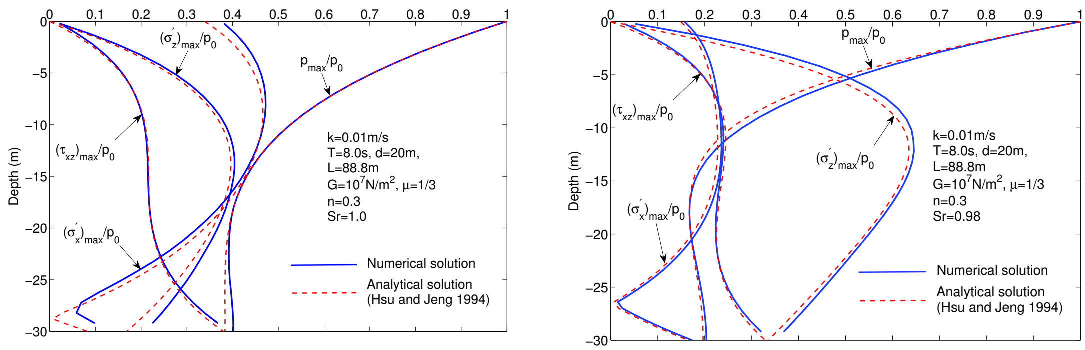

(a) Coarse sand

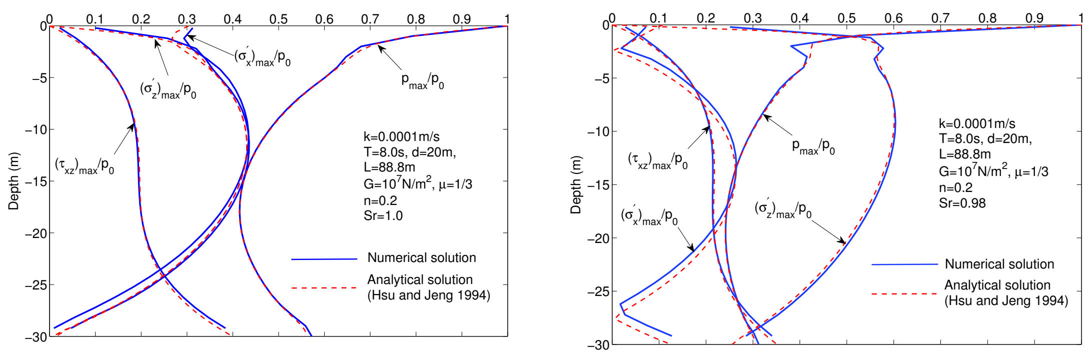

(b) Fine sand

Figure 3.4: Vertical distributions of the wave-induced soil response in (a) coarse sand and (b) fine sand (PORO-WSSI II).

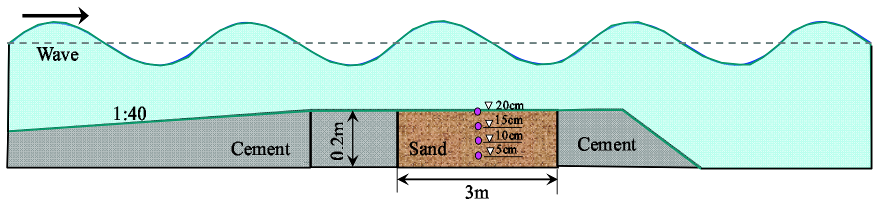

(a) Lu (2005) 's experiment-Fifth-order wave and Cnoidal wave

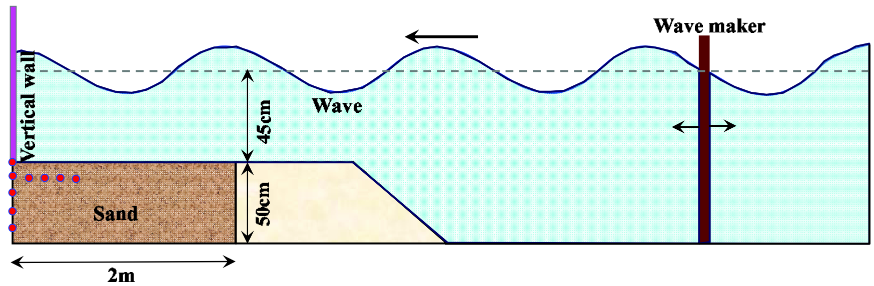

(b) Tsai and Lee (1995)'s experiment-Standing wave

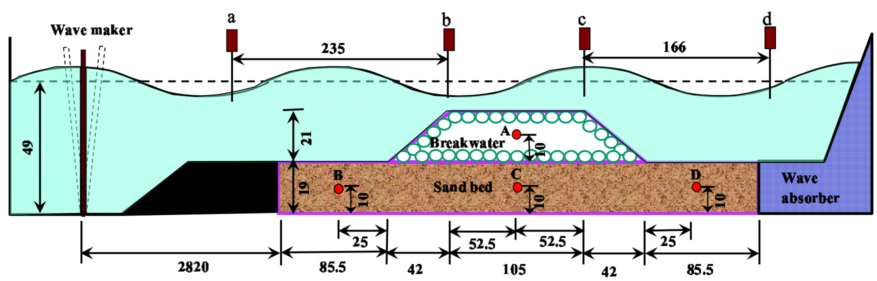

(c) Mizutani et al. (1998)'s experiment-Submerged breakwater (unit: mm)

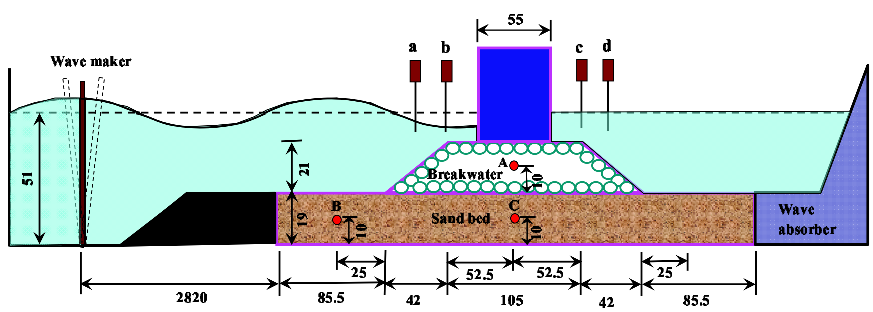

(d) Mostafa et al. (1999)'s experiment-Composite breakwater (unit: mm)

Figure 3.5: Experiment setup of the wave flume laboratory tests used for the verification of developed integrated model

1.8s. The wave height is from 8cm to 16cm. The sand bed is consisted of coarse sand or fine sand. The experiment setup is shown in Figure 3.5 (a). The pore pressure at the four points on the midline of sand bed are monitored in experiments.

In this part, the dynamic response of coarse sand under regular wave and cnoidal wave loading are respectively predicted by the integrated model developed. The comparison between the predicted results determined by the numerical integrated model and the experiment data about the dynamic pore pressure at the four points are conducted to show the accuracy and reliability of the integrated model. The properties of coarse sand and the wave characteristics in the two tests (regular wave and cnoidal wave) provided by Lu (2005) are listed in Table 3.1

The wave model is used to simulate the generation of wave and its propagation in wave flume according to the wave parameters, and exert the pressure on sand bed. At the meantime, the soil model obtains the pressure acting on the sand bed through the coupling algorithm, and determines the dynamic response of the sand bed, including displacements, pore pressure and stress state in sand bed. It is commonly known that linear wave is only an approximation for the real waves, high order wave can more accurately simulate the real waves. Here, in order to obtain a more reasonable results, the 5^{th}-order stokes wave is adopted to generate the regular wave (H=12cm, d=0.4m, T=1.4s).

The comparisons of the regular and cnoidal wave induced dynamic pore pressure at the four points on the midline of sand bed between the numerical results determined by the integrated model and the experimental data are shown in Figure 3.6 (a) and (b).

As illustrated in Figure 3.6 (a) and (b), it can be seen that the numerical results predicted by the integrated model developed could agree well with experimental data provided by Lu (2005). It is also can be seen that the agreement of the wave induced pore pressure between the numerical results and the experiments is better for the regular wave (5^{th}-order wave) than that of cnoidal wave. It is indicated that the high order wave in numerical model indeed could simulate the real wave more accurately. Figure 3.6 (b) shows that the predicted maximum and minimum pressure in sand bed both are a little greater than that of experimental data. It would attribute to the relative large ratio between the wave height and water depth ($0.12/0.3 = 0.4$) is relatively large, which will bring some difficulties for the wave model to simulate such a wave. As a whole, the good agreement between the numerical results and the experimental data indicates that the integrated model developed is reliable.

Table 3.1: Soil properties and wave characteristics in verification cases

Experiments	Wave type	Medium	H (cm)	d (m)	T (s)	G (N/m^2)	ν	k m/s	n	d_{50} (mm)	Sr
Lu (2005)'s experiment	5^{th}-order	Wave	12.0	0.4	1.4						
		sand bed				1.0×10^7	0.3	1.0×10^{-3}	0.3893	0.44	0.98
	Cnoidal	Wave	12.0	0.3	2.0						
		sand bed				1.0×10^7	0.3	1.0×10^{-3}	0.3893	0.44	0.98
Tsai and Lee (1995)'s experiment	2^{nd}-order	Wave	5.1	0.45	1.5						
		sand bed				2.64×10^7	0.3	1.2×10^{-4}	0.38	0.187	0.98
Mizutani et al. (1998)'s experiment	2^{nd}-order	Wave	3.0	0.3	1.4						
		sand bed				1.0×10^8	0.33	2.2×10^{-3}	0.3	1.0	0.99
		Breakwater				1.0×10^9	0.24	1.8×10^{-1}	0.33	30	0.99
Mostafa et al. (1999)'s experiment	2^{th}-order	Wave	5.0	0.32	2.2						
		sand bed				5.0×10^8	0.33	2.3×10^{-3}	0.3	0.8	0.98
		Rubble mound				1.0×10^9	0.24	1.6×10^{-1}	0.33	27	0.99

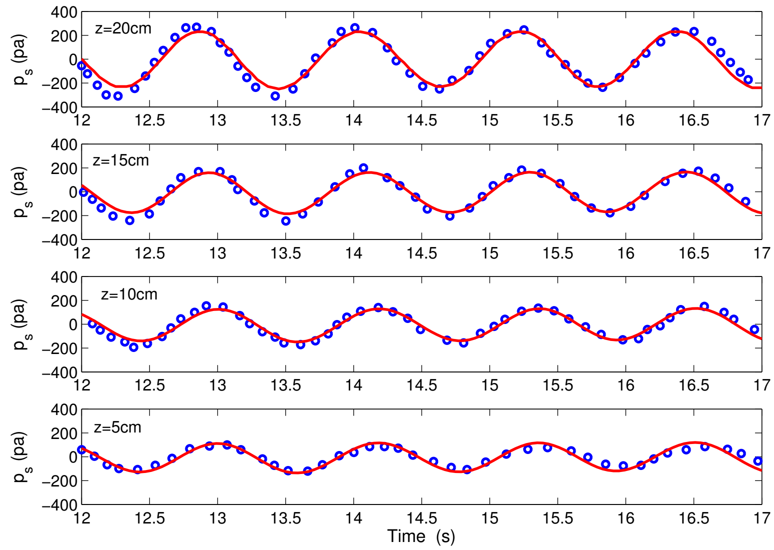

(a) Fifth-order wave

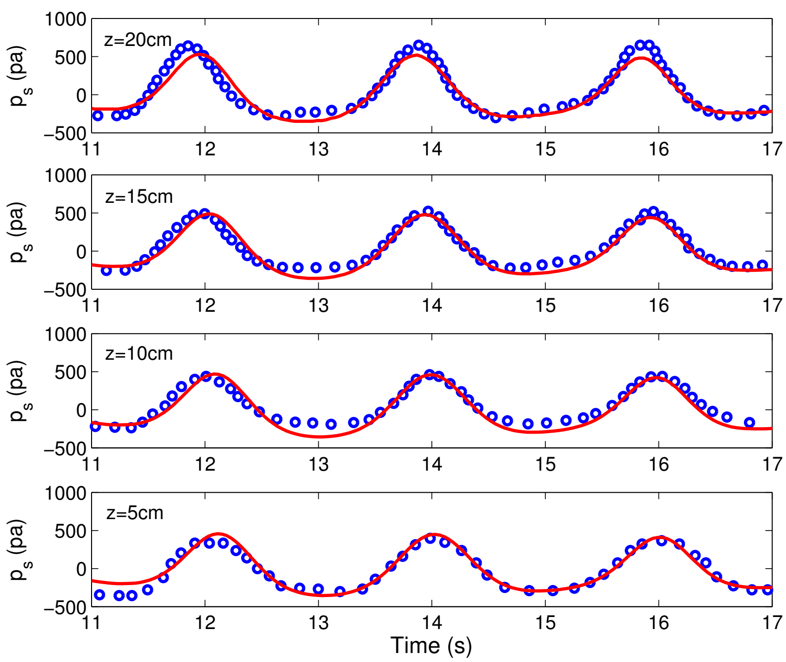

(b) Cnoidal wave

Figure 3.6: Comparisons of wave induced dynamic pore pressure on the midline of sand bed between the numerical results and the experimental data in Lu's experiments. —: numerical results (PORO-WSSI II), ∘ : experimental data.

3.4.3 Tsai and Lee (1995)'s experiment-Standing wave

Tsai and Lee (1995) conducted a experiment in a wave flume to verify the analytical solution of standing wave induced pore pressures in a sand bed. The experiment setup is shown in Figure 3.5 (b). In the experiment, the wave generated by the wave maker propagates to the sand bed, and to the vertical wall. Then the perfect reflection of wave is expected to occur at the vertical wall. The standing wave forms after the reflected wave and the incident wave superimposing on the sand bed. Finally, the standing wave induced dynamic response in the sand bed can be monitored. In the sand bed, there are 9 points (shown in Figure 3.5 (b)) at which the pore pressure are recorded in the test. Five of them are on the left end side of the sand bed, four of them are on the line parallel with the seabed surface, and the distance to the seabed surface is 10cm. The intervals between the nine points are also all 10cm. The properties of sand bed and the wave characteristics provided by Tsai and Lee (1995) in this test are listed in Table 3.1.

The integrated model is adopted to simulate the dynamic response of sand bed under standing wave loading. The 2^{th}-order stokes wave is used to simulate the generation and propagation of the wave (H=5.1cm, d=0.45m, T=1.5s) in wave flume.

The comparisons of the standing wave induced pore pressure at the nine points between the numerical results predicted by the integrated model and the experimental data are shown in Figure 3.7.

As shown in Figure 3.7, it is found that the numerical results predicted by the integrated model can basically agree with the experimental data. However, some differences for the minimum standing wave induced pore pressure can be observed at the upper four points on the left end side of sand bed, and the left four points on the line parallel with sand bed surface. This differences for the minimum dynamic pore pressure may attribute to the measurement errors. The standing wave is a kind of periodic wave. therefore, the dynamic response to the standing wave in the sand bed should be also periodic. The absolute value of standing wave induced maximum and minimum pore pressure should be very closed when H/d is relatively small. However, it can be seen from the distribution of measured pore pressures that the dynamic pore pressures are periodic, but the absolute value of the maximum and minimum pore pressure are significantly different at some times. Therefore, the measurement errors may be responsible for the little differences of the minimum pore pressure between the numerical results and the measured results.

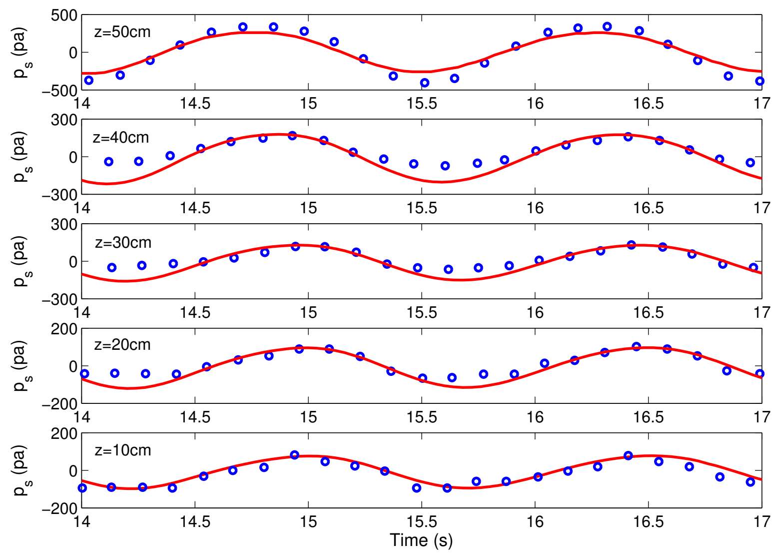

(a) Pressure on the left end side of sand bed

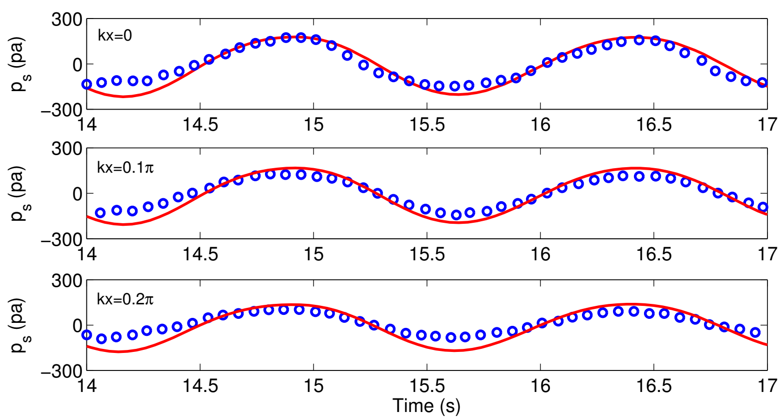

(b) Pressure on the line parallel with seabed surface (0.0π-0.2π)

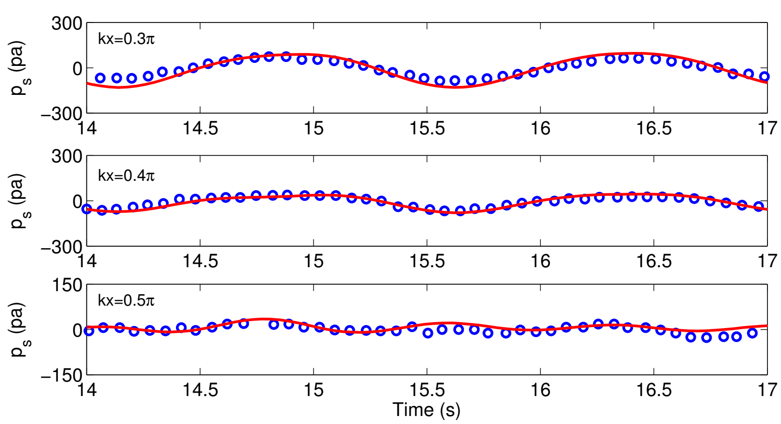

(c) Pressure on the line parallel with seabed surface (0.3π-0.5π)

Figure 3.7: Comparisons of the standing wave induced dynamic pore pressure at the nine points in sand bed between the numerical results and the experimental data in Tsai's experiment. —: numerical results (PORO-WSSI II), ∘: experimental data.

In the Figure 3.7(c), it is interesting to note that the dynamic pore pressure at the point $kx = 0.5\pi$ which is under a stationary vibrates with very small amplitude around 0. It is indicated that the wave model in the integrated model is successful to simulate the generation, propagation, reflection and interference of wave in the wave flume using the 2^{th}-order stokes wave theory; and the soil model can accurately determine the dynamic response of sand bed under the standing wave.

3.4.4 Mizutani et al. (1998)'s experiment-Submerged breakwater (PORO-WSSI II)

Mizutani et al. (1998) conducted a series of experiments in a wave flume to investigate the interactions between the regular wave, submerged breakwater and sand bed. The experiment setup is shown in Figure 3.5 (c). In the experiments, a submerged breakwater is constructed on the sand bed. Four wave height meters are installed at point a, b, c and d to monitor the wave profile. Four poressure sensors are installed at point A, B, C and D to record the pore pressure. The properties of the sand bed and breakwater, and the wave characteristics provided by Mizutani et al. (1998) are listed in Table 3.1. Due to the fact that the wave steepness is $0.03/2.1 = 0.014286$, the second-order wave model is sufficient to accurately simulate the generation, propagation of the wave in the wave flume.

In the tests, the test tank is firstly filled with sandy soil, and the breakwater is built on the sandy bed later. Then, the wave flume is filled with water to the specified depth. The sandy bed consolidates under the breakwater and hydrostatic water pressure for several days. This consolidation process of sandy bed under breakwater and hydrostatic pressure can be simulated by PORO-WSSI II seting the wave height as zero. Figure 3.8 shows the distribution of pore pressure and effective stresses in sandy bed and breakwater when the consolidation process is finished. From Figure 3.8, it can be seen that there is no excess pore pressure in sandy bed and breakwater, and the pore pressure is layered. The construction of breakwater on sandy bed makes the effective stress σ'_x and σ'_z in the zone under the breakwater increase significantly. There is tensile σ'_x in the bottom zone of breakwater. This could attribute to the reason that the sandy bed is much softer than the breakwater, and the deformation of breakwater and sandy bed is inconsistent. There are two shear stress concentration zone near to the two lateral sides in breakwater. Meanwhile, the shear stress in the zone under the two feet of breakwater is also significant.

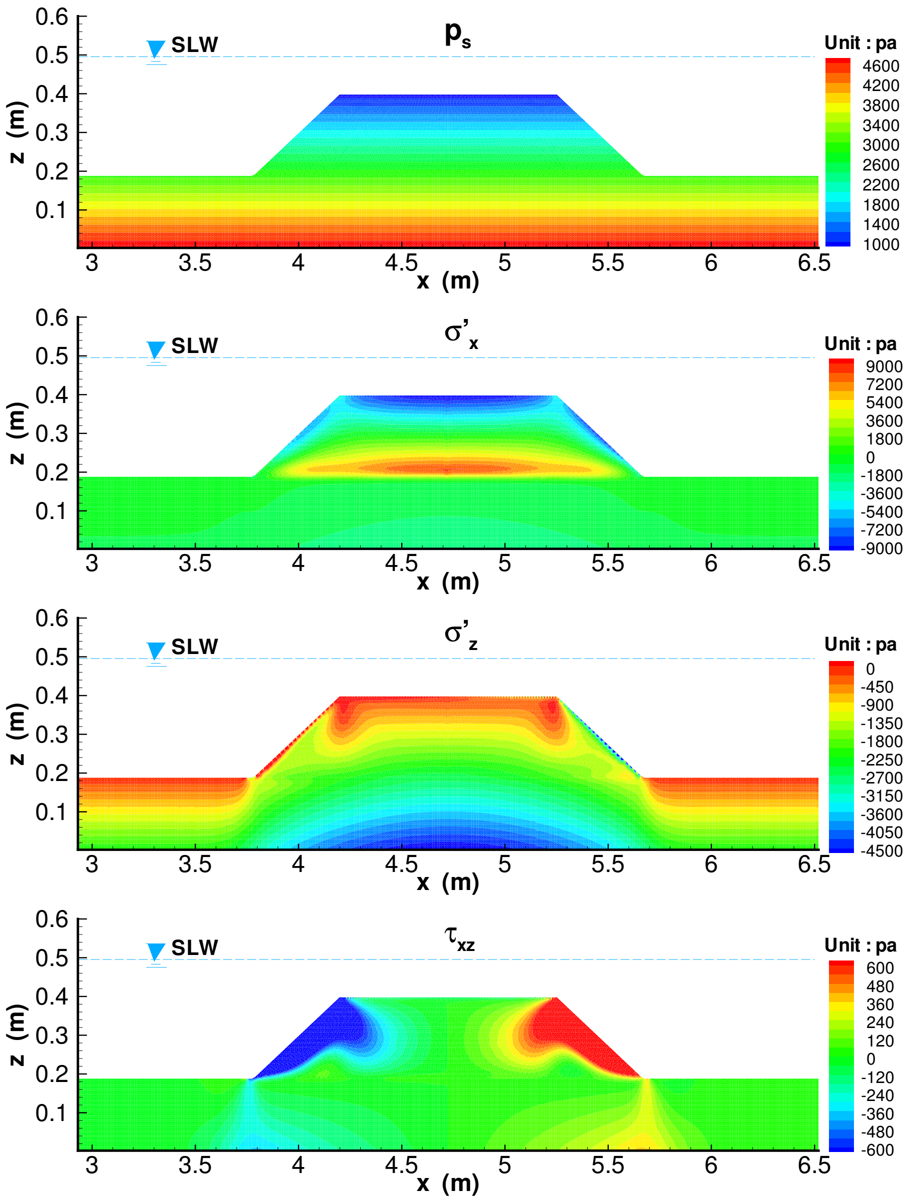

Figure 3.8: Distribution of pore pressure and effective stresses in sandy bed and breakwater in the consolidation status. Note: p_s: pore pressure; σ'_x, σ'_z: effective normal stresses, τ_{xz}: shear stress.

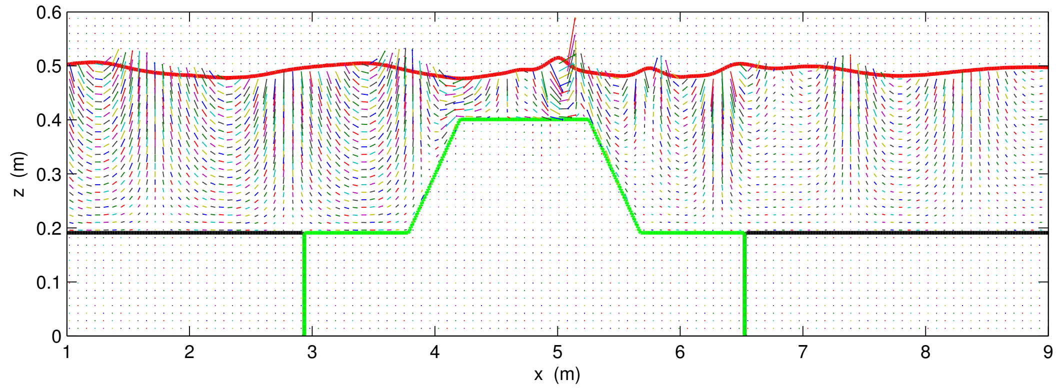

Figure 3.9: Velocity field in the fluid domain, the sandy bed and in the breakwater at time t=8.0s. The red line is the free surface of wave

By taking the above consolidated status of sandy bed under breakwater and hydrostatic pressure as the initial condition, the integrated numerical model PORO-WSSI II is continuously adopted to simulate the interaction between the wave, submerged breakwater and sandy bed. In coupling computation, the sand bed and breakwater are treated as different porous structures in fluid domain in the wave model. The data exchange is implemented by the coupling algorithm at the interface between the solid domain (sand bed, breakwater) and the fluid domain. In the soil model, the sand bed and breakwater are also treated as different porous mediums with different properties listed in Table 3.1.

Figure 3.9 illustrates the velocity field in the fluid domain, the sandy bed and in the breakwater at time t=8.0s. It is observed that the breakwater indeed has significant effect on the wave propagating on sandy bed. It is further indicated that the analytical solution of pressure based on Laplace's equation and Stokes wave theory can not be used to apply the force acting on seabed and marine structures due to that the effect of marine structures on the wave field is not considered. The flow velocity of pore water in breakwater and sandy bed is relatively small; therefore, the velocity vectors in breakwater and sandy bed look like points.

The comparisons for the wave profile and the wave-induced dynamic pore pressure in sand bed and breakwater between the numerical results predicted by the integrated numerical model PORO-WSSI II and the experiment data are shown in Figures 3.10 and 3.11. As illustrated in Figures 3.10 and 3.11, the agreements for the wave profile at a and b are excellent, while, some differences are observed at c and d which locate at the behind of the breakwater. The agreements for the wave induced dynamic response at A, B, C and D in sand bed are all excellent. It is clearly indicated

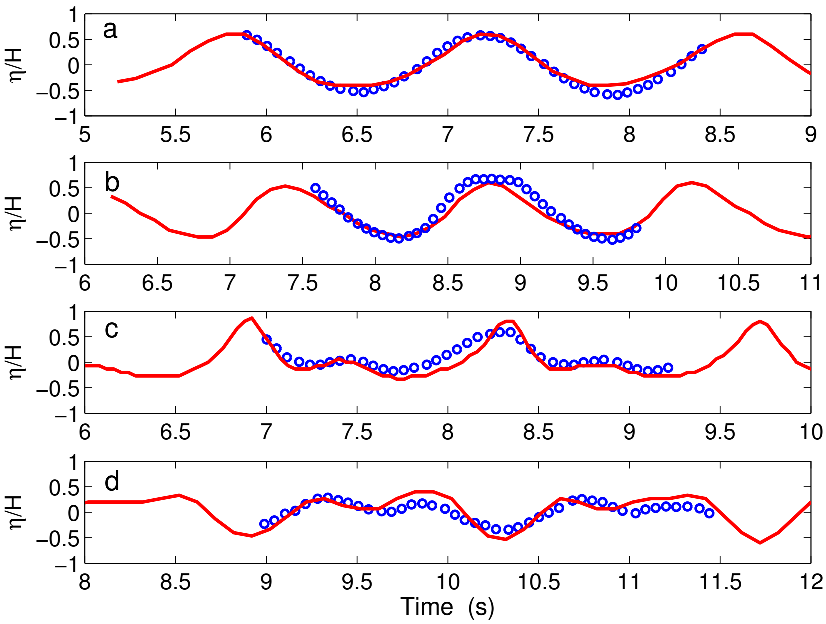

Figure 3.10: Comparison between the numerical results determined by the integrated model and the experimental data in Mizutani et al. (1998) for the wave profile. —: numerical results, ∘: experimental data.

that the numerical model PORO-WSSI II is applicable for the problems of Wave-Seabed-Breakwater Interaction.

Under the wave loading, the breakwater built on seabed will vibrate accordingly. This vibration of breakwater under wave loading can be captured by the integrated model developed in this part. Figure 3.12 are the historic curves of horizontal and vertical displacement at the left top corner of breakwater under the wave loading. Due to that the elastic modulus of breakwater and sandy soil used in Mizutani et al. (1998)'s experiment is relatively huge (see Table 3.1), The magnitude of displacement of breakwater under the wave loading is apparently small. Even so, the tiny vibration of breakwater under wave loading still can be captured in numerical analysis.

Here, it is worth discussing a problem about application of Biot's equation for the turbulent porous flow in porous medium with very high permeability. Biot's equation is established based on the assumption of laminar flow (Darcy's flow) in porous medium. It is generally believed that Biot's equation can not be applied to the turbulent flow with high Reynolds number. In this verification case, the permeability of the submerged breakwater is high (1.8×1.0^{-1}m/s); and the mean particles

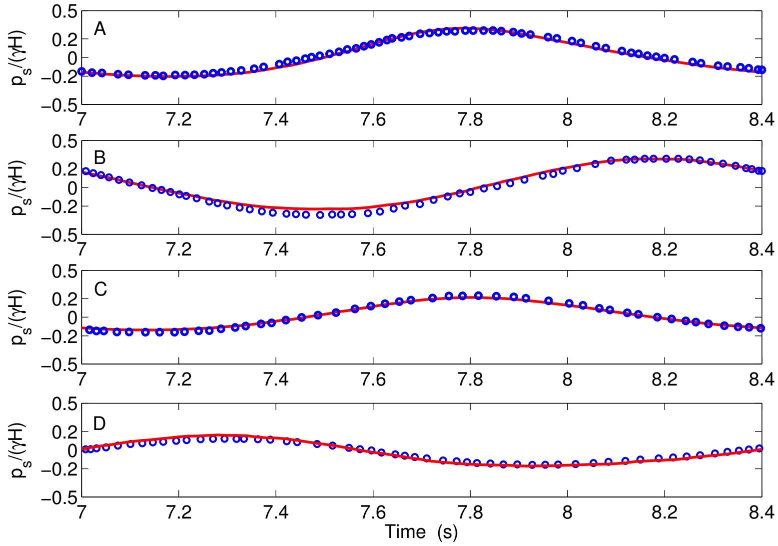

Figure 3.11: The comparison between the numerical results determined by PORO-WSSI II and the experiment data Mizutani et al. (1998) for the wave induced dynamic pore pressure. —: numerical results, ○: experimental data.

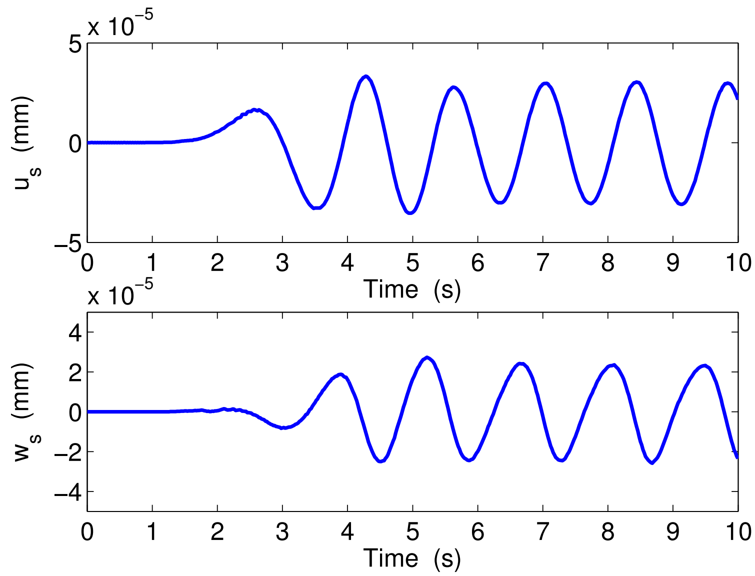

Figure 3.12: The horizontal displacement u_s (top) and vertical displacement w_s (bottom) of left top corner of breakwater under wave loading

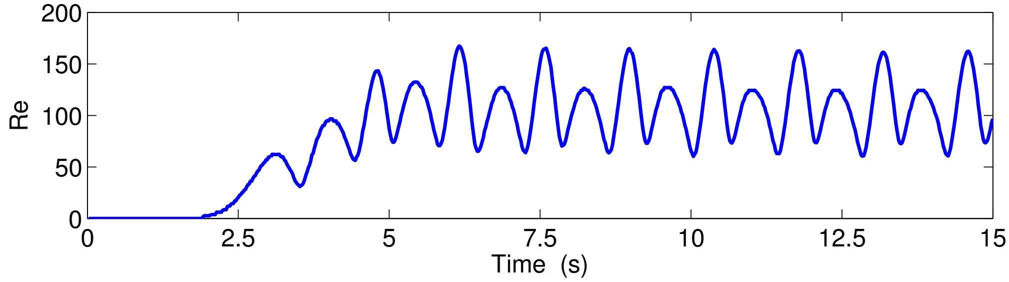

Figure 3.13: Variation of Reynolds number ($Re = \frac{\sqrt{u_{fx}^2+u_{fz}^2}d_{50}}{\nu}$) of the porous flow at x=4.715m, z=0.2905m in the rubble mound

size is relatively large (30mm). It is believed that wave-induced porous flow in the rubble mound breakwater is turbulent. It is interesting to illustrate whether Biot's equation can predict the wave induced porous flow in the rubble mound as the VARANS equation. Through the computation using the VARANS equation, it is found that the velocity of pore water in the submerged rubble mound breakwater is the magnitude of $O(10^{-1})$ m/s. The Reynolds number ($Re = \frac{Ud_{50}}{\nu}$) can reach up to 180 at the center of the rubble mound (Figure 3.13). Figure 3.13 indicates that the porous flow in the rubble mound breakwater in this verification case is turbulent flow, rather than a laminar flow.

Figure 3.14 shows the comparison of the wave induced pore pressure determined by Biots equation and VARANS equation at the position A, B, C and D in the rubble mound and sand bed. Among the four positions, A is located at the center in the rubble mound. In Figure 3.14 , it is found that the pore pressure at position A determined by VARANS equation and Biots equation are exactly the same. It is indicated that Biots equation can be used if the Reynolds number is less than 200 for small-scale cases. It is not surprised that the wave-induced pore pressure at position B, C and D determined by the two models are the same, because the porous flow in the sand bed with small permeability is laminar flow.

3.4.5 Mostafa et al. (1999)'s experiment-Composite breakwater

Based on the experiment conducted by Mizutani et al. (1998), Mostafa et al. (1999) further conducted an experiment in the same wave flume to investigate the interaction between the wave, composite breakwater and sand bed. The experiment setup is shown in Figure 3.5 (d). In the experiment, a wooden box (the width is 55cm) is placed on the breakwater to form a composite breakwater in the

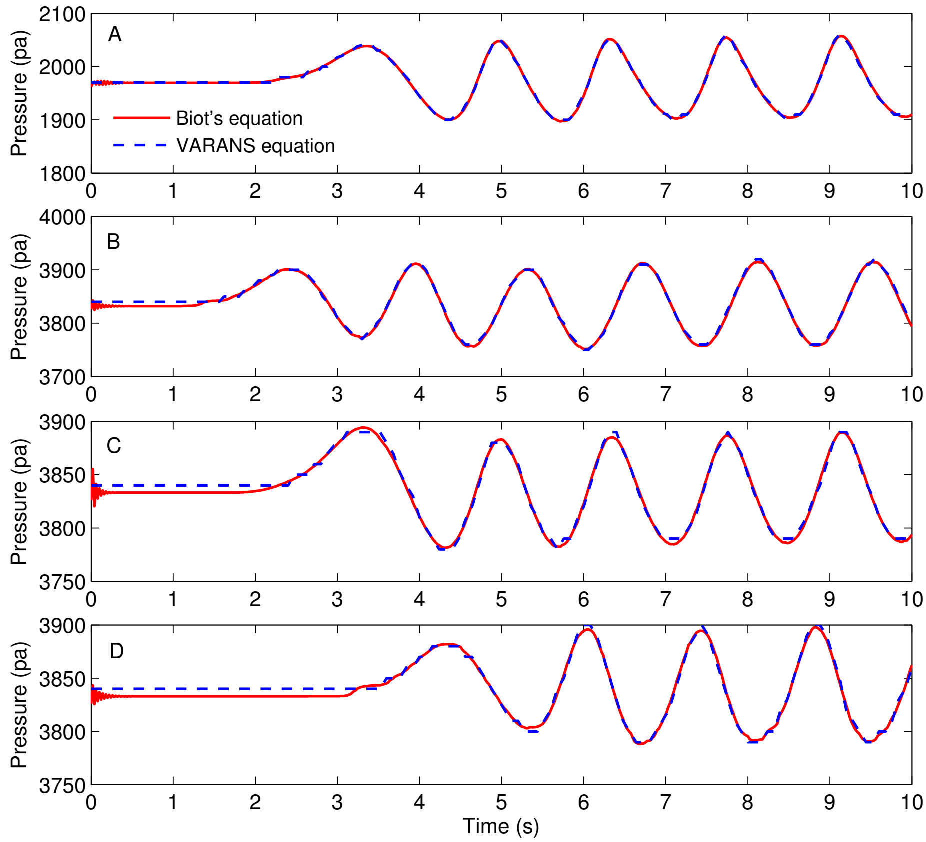

Figure 3.14: Comparison of the pore pressure determined by the Biot's equation and the VARANS equation in the rubble mound and sandy bed

wave flume. Four wave height gages are installed at point *a*, *b*, *c* and *d* to measure the wave profile; two of them are in front of the composite breakwater, the other two are behind of the composite breakwater. Three pore pressure transducers are installed at point A, B and C to record the pore pressure. The properties of the sand bed and breakwater, and the wave characteristics provided by Mostafa et al. (1999) are listed in Table 3.1. Here, the 2^{th}-order wave model are adopted to simulate the generation, propagation, reflection and interference of wave.

By taking the same analysis procedures as that in Mizutani et al. (1998)'s experiment, PORO-WSSI II is adopted to simulate the interaction between the wave, composite breakwater and sand bed. In coupling computation, the sand bed and the rubble mound of the composite breakwater are treated as different porous structures in fluid domain; the wooden box is treated as impermeable structure in fluid domain in the wave model. The data exchange is implemented at the interface by the coupling algorithm at the interface between the solid domain (sand bed, rubble mound and wooden box) and the fluid domain. In the soil model, the sand bed and the rubble mound are treated as different porous mediums with different properties, see Table 3.1; and the wooden box is treated as a rigid and impermeable object located at the rubble mound. It is noted that the buoyancy acting on the bottom of the wooden box applied by the pore water in the rubble mound has been considered in this case.

The comparisons for the wave profile and the wave-induced dynamic pore pressure in sand bed and the rubble mound between the numerical results predicted by PORO-WSSI II and the experiment data are shown in Figure 3.15 and 3.16. Due to the blocking effect of the impermeable wooden box, only little water can flow into and out the right side of the composite breakwater through the rubble mound. Therefore, the amplitude of wave behind the composite breakwater is very small. In Figure 3.15, only the wave profile of point *a* and *b* are used to make the comparison between numerical results and experiment data. From the two figures, it can be seen that the numerical results obtained by the integrated model agree well with the experiment data both for wave profile and wave induced dynamic pore pressure.

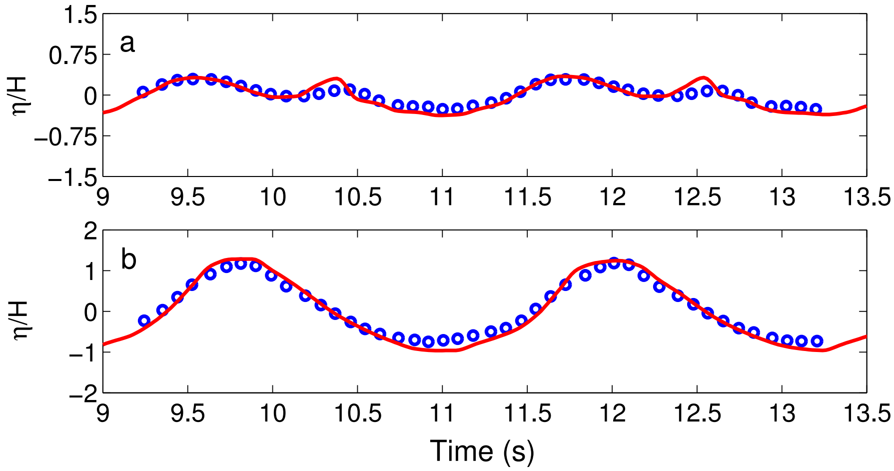

Figure 3.15: The comparison between the numerical results determined by the integrated model and the experimental data in Mostafa et al. (1999) for the wave profile. —: numerical results, ○: experimental data.

3.4.6 Analytical solution (Hsu and Jeng, 1994)-3D FEM soil model

The analytical solution of dynamic response of seabed (without marine structure) under linear wave loading proposed by Hsu and Jeng (1994) is used to verify 3D model PORO-WSSI III. Four cases, including coarse sand (k=10^{-2}m/s) and fine sand (k=10^{-4}m/s), saturated (S_r=100%) and unsaturated (S_r=98%) sandy bed loaded by a linear wave are used to compare the results (the maximum response to linear wave) determined by the analytical solution and present soil model. The length of computational domain is one wave length, and the periodical boundary condition is applied to the two lateral boundaries along the wave propagating direction. The thickness and width of model are both 30m. The comparisons between the numerical and analytical results are illustrated in Figure 3.17. As shown in Figure 3.17, the numerical results determined by the present soil model agree well with the analytical solution. It is indicated that the dynamic modulus in the developed 3D FEM soil model is applicable for prediction of the dynamic behaviour of soil under dynamic loading, including wave and earthquake.

3.4.7 Mizutani et al. (1998)'s experiment-Submerged breakwater (PORO-WSSI III)

The 2D integrated model PORO-WSSI II for wave-seabed-structures interaction is extended to its 3D version PORO-WSSI III. PORO-WSSI 2D has been verified by a series of experimental data available

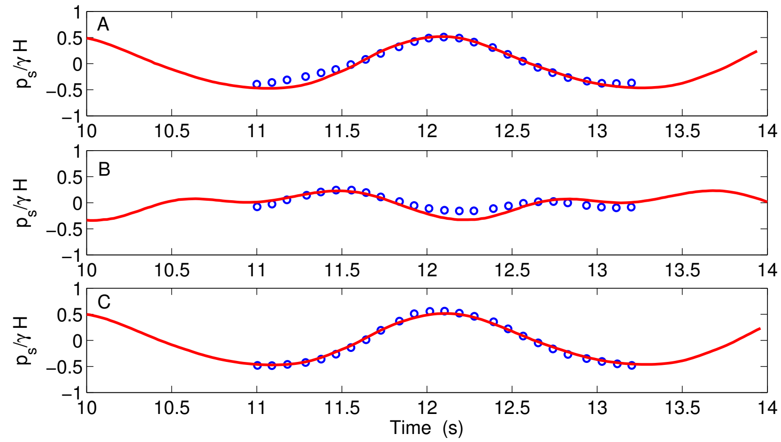

Figure 3.16: The comparison between the numerical results determined by PORO-WSSI II and the experiment data in Mostafa et al. (1999) for the wave induced dynamic pore pressure. —: numerical results, ∘: experimental data.

in previous literature in above parts. In this part, the wave flume experiment conducted by Mizutani et al. (1998) is again adopted to validate the 3D integrated model PORO-WSSI III.

The experiment setup and the wave characteristics, properties of sandy bed and rubble mound breakwater all are the same with that used in the verification of PORO-WSSI 2D (Table 3.1 and Figure 3.5 (c)). In the experiment (Mizutani et al., 1998), the width of the sandy bed and rubble mound breakwater is 1.0m. The 27 nodes isoparametric hexahedral element are used to discretize the computational domain (Figure 3.18).

Based on the integrating process illustrated in Figure 3.3, the 3D FVM wave model is used to generate the 3D wave propagating on the sandy bed and rubble mound breakwater (Figure 3.19); the 3D FEM soil model is used to determine the corresponding dynamic response of sandy bed and rubble mound breakwater to the wave propagating on them.

Figure 3.20 shows the comparison of the wave profile between the numerical results and experimental data (Mizutani et al., 1998). It can be seen that the agreement between the numerical results and experimental data at position *a*, *b* and *c* are very well. However, the agreement at position *d* is not ideal. Two characteristics could be observed from the comparison at position *d*: (1) there is phase lag for the numerical results relative to the experimental data. (2) The maximum wave height determined by PORO-WSSI III is greater than that measured. Comparing the results of wave profile shown in Figure 3.10 for 2D integrated model and in Figure 3.20 for 3D integrated model, it is found that the

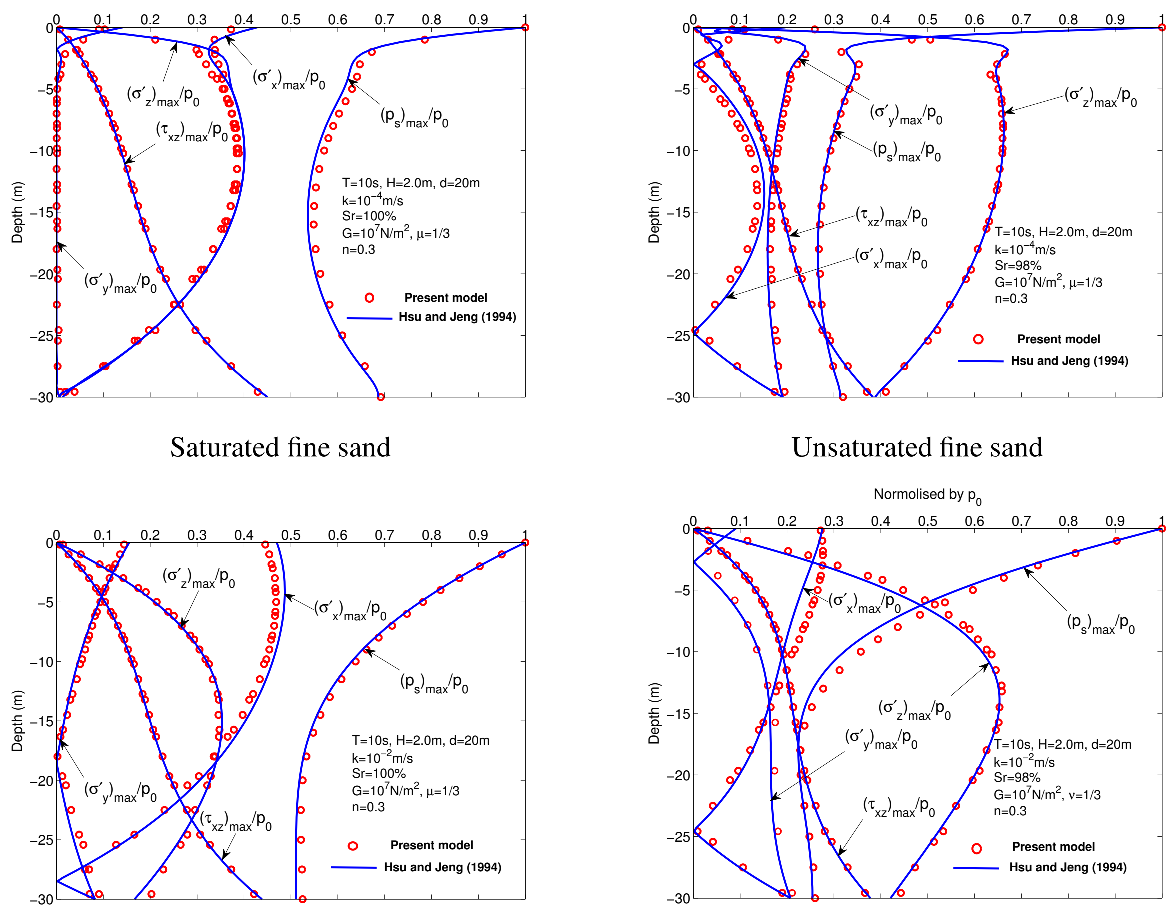

Saturated fine sand

Unsaturated fine sand

Saturated coarse sand

Unsaturated coarse sand

Figure 3.17: The comparison of the linear wave-induced maximum dynamic response in seabed determined by present model (PORO-WSSI III) and the analytical solution Hsu and Jeng (1994).

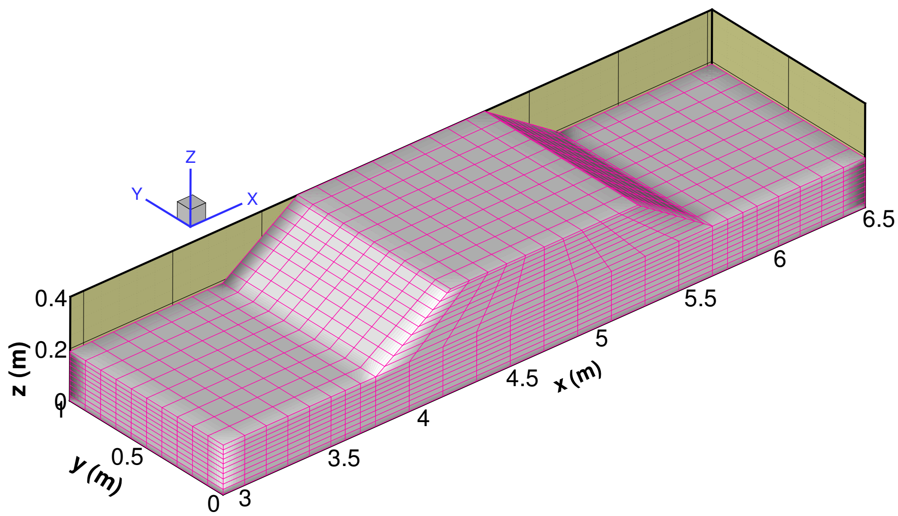

Figure 3.18: The 3D mesh system for the sandy seabed and the rubble mound breakwater in the verification case of Mizutani et al. (1998).

2D integrated model could determine more reliable results for the WSSI problem. It attributes to that the porous flow in porous medium and porous structures can be included through the volume average method (Hsu et al., 2002) in 2D wave model. However, the porous flow can not be considered in 3D FVM wave model at present. All marine structures have to be treated as rigid and impermeable medium in the 3D wave model. In the experiment conducted by Mizutani et al. (1998), the submerged rubble mound breakwater is a kind of porous structures with porosity n=0.24, and large permeability k=1.8×10^{-1}cm/s. The resistance for the wave propagating on it is much weaker than that if it is impermeable structure. In the 3D wave model, the rubble mound breakwater is treated as impermeable structure built on the sandy bed, the stronger resistance for wave propagating on it makes the phase of wave lag, and the height of wave higher relative to the real wave height. Therefore, the application of 3D integrated model PORO-WSSI III to the porous structures with large porosity and permeability should be constrained. The work to make the 3D wave model could include porous flow in porous structures would be done in future.

Figure 3.21 shows the comparison of the wave induced pore pressure in the sandy bed and the rubble mound breakwater between the numerical results and experimental data (Mizutani et al., 1998). As illustrated in Figure 3.21, the comparison of the dynamic pore pressure at position A, B and C between the numerical results determined by PORO-WSSI III and the experiment data is acceptable.

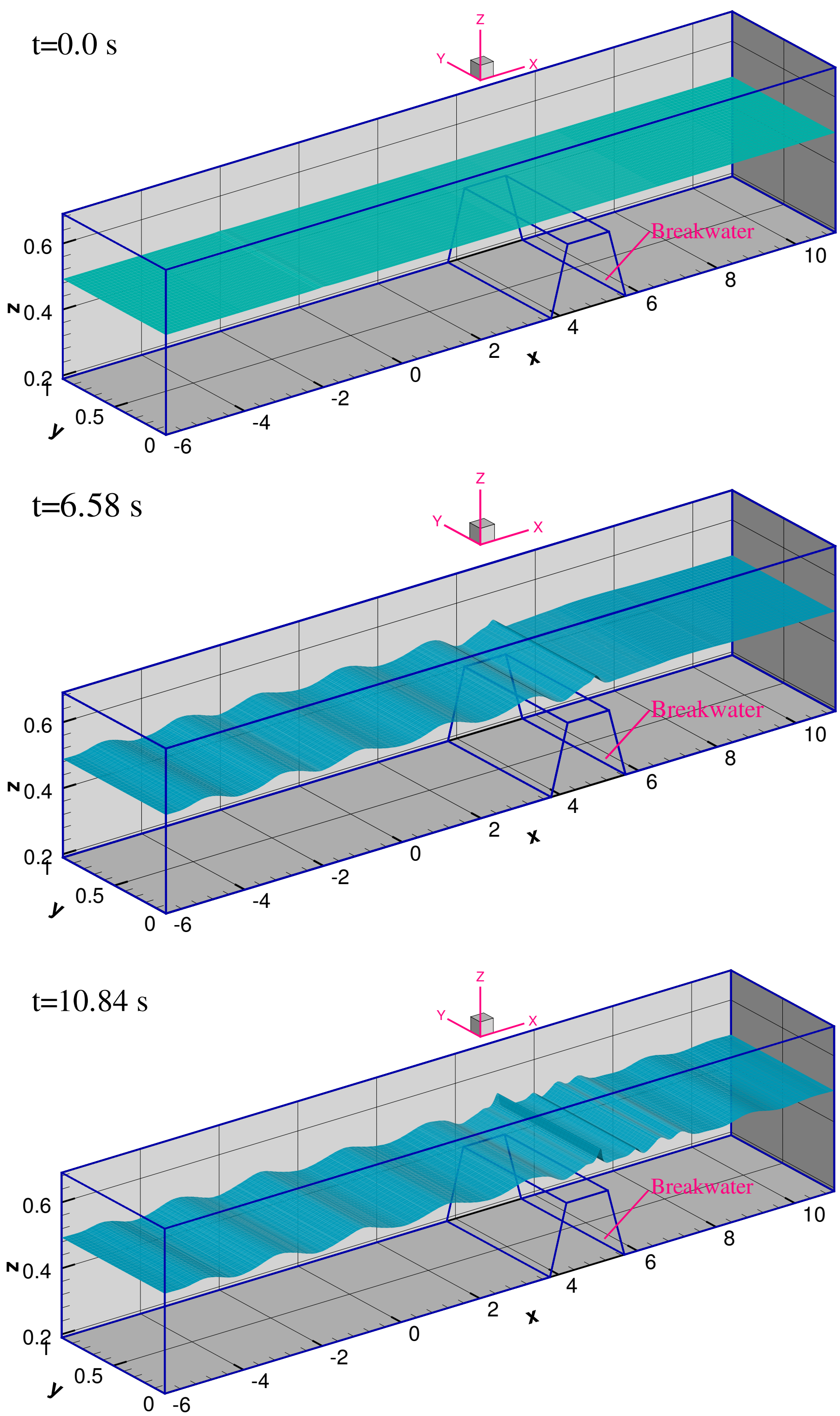

Figure 3.19: The wave profile at three typical times determined by the 3D FVM wave model.

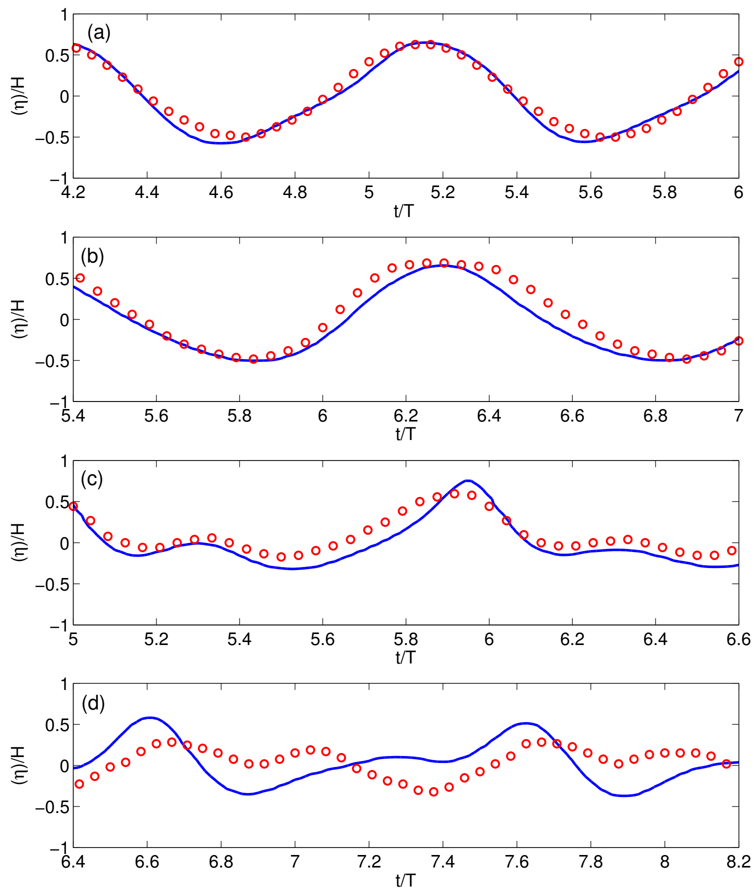

Figure 3.20: The comparison of the wave profile propagating on sandy bed and rubble mound breakwater between the numerical results and experimental data (Mizutani et al., 1998). —: numerical results (PORO-WSSI III), ○: experimental data.

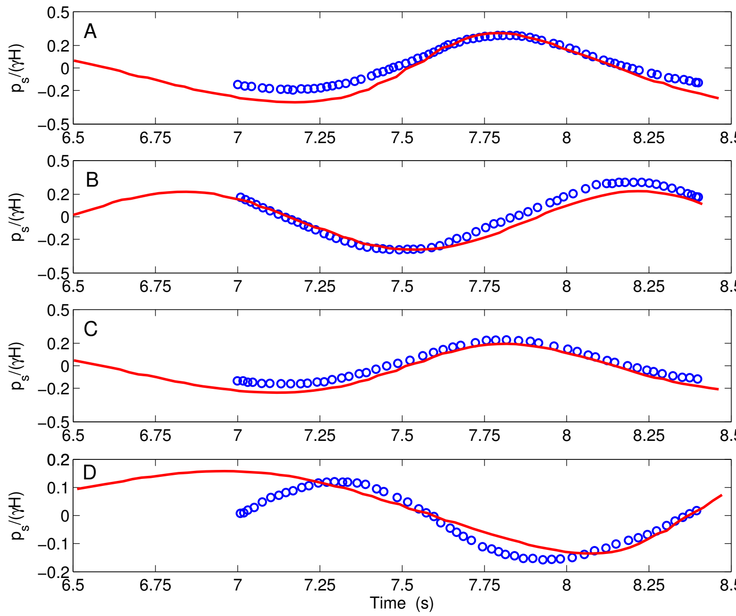

Figure 3.21: The comparison of the wave induced pore pressure in sandy bed and rubble mound breakwater between the numerical results and experimental data (Mizutani et al., 1998). —: numerical results (PORO-WSSI III), ○: experimental data.

However, the agreement for the wave induced dynamic pore pressure at position D is not good. The reason for this phenomenon also could attribute to that the porous rubble mound breakwater is treated as impermeable structures in 3D wave model; it results in that the 3D numerical wave field behind the rubble mound breakwater is not as that in experiment. As a whole, the 3D integrated model PORO-WSSI III for WSSI problem is reliable.

3.5 Summary

In this Chapter, the integrated numerical models PORO-WSSI II (2D Version) and III (3D Version), are developed. The detailed information about the governing equations and the numerical methods adopted for wave motion and porous flow in porous medium, and for the seabed soil are presented. A coupling algorithm in which the non-match mesh scheme and non-match time scheme for dynamic problem is developed to integrate the two governing equation together to investigate the wave-seabed-breakwater interaction. The generalized non-associate elasto-plastic constitutive model Pastor-Zienkiewicz Model Mark-III, which will be used in this thesis to evaluate the wave induced residual liquefaction in seabed foundation, is also presented detailedly in Appendix. Finally, the developed numerical model PORO-WSSI II/III are validated by a series of laboratory wave flume tests reported in previous literatures. The good agreement between the predicted results by the PORO-WSSI II/III and the experimental data indicates the the developed numerical model PORO-WSSI II/III is applicable to the WSSI problem.

Chapter 4

Response of Porous Seabed to Nature Loadings-Waves and Currents[2*]

4.1 Introduction

It has been well documented that the ocean waves/currents exert dynamic pressure on a porous seabed. These dynamic variations will further cause the pore pressure, effective normal stresses and shear stresses in a porous seabed. When the pore pressure in the seabed becomes excessive, the effective stresses between soil particles become zero, liquefaction will then occur and result in the collapse of marine structures built on seabed.

Numerous investigations of the wave-induced transient dynamic response of seabed under wave loading have been carried out based on Biot's poro-elastic theory since the 1970's. In real ocean environments, the ocean waves and currents generally exist simultaneously. However, the aforementioned investigations have only considered wave loading without currents. Thus, how the ocean currents affect the wave-induced seabed response haven't been examined before. Actually, the pressure acting on seabed is significantly different when there is a current in flow field, according to the potential flow theory. Therefore, it is of interest to examine the influences of currents on the seabed response.

In this chapter, the effect of currents on seabed response is numerically examined. The third-order approximation of non-linear wave–current interaction (Hsu et al., 2009) is outlined first. The boundary value problem of wave/current-seabed interactions is presented with a brief numerical scheme and the treatment of lateral boundary conditions. Then, based on the numerical model, the effects of

[2*]Contents in this chapter are included in Ye and Jeng (2012): Ye J H & Jeng D-S (2012). Response of porous seabed to nature loadings-waves and currents. Journal of Engineering Mechanics, ASCE, In press, DOI: 10.1061/(ASCE)EM.1943-7889.0000356.

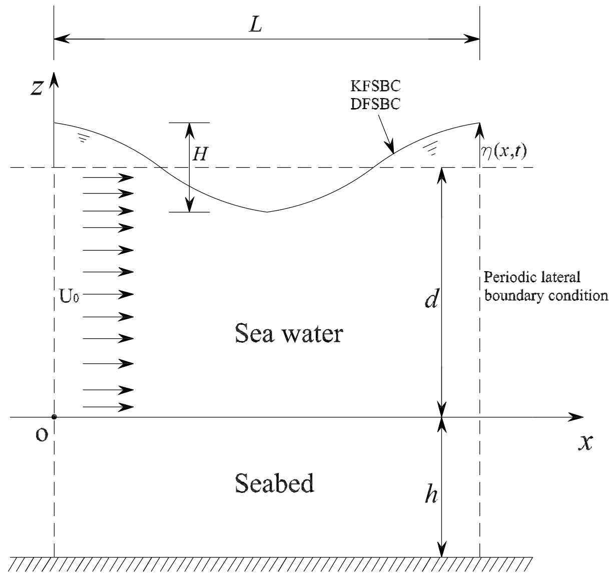

Figure 4.1: Sketch of wave/current-seabed interaction.

current on seabed response is investigated; a parametric study is carried out to investigate the effects of wave and soil characteristics on the seabed response. The momentary and residual liquefaction under the combined loading of non-linear waves and currents is also examined as well.

4.2 Third-order approximation of non-linear wave-current interactions

The co-existence of waves and currents in offshore area is a common physical phenomenon and their interaction is an important topic in the practice of coastal and ocean engineering. The presence of a current in propagating wave will change the original characteristics of wave. For example, the following current will elongate the wave length; and the opposing current will shorten the wave length. In this section, to obtain more accurate results of seabed response under combined wave and current loadings, the third-order solution of wave-current interactions (Hsu et al., 2009) is used to determine the dynamic wave pressures acting on the seabed.

The sea water is considered as an incompressible and in-viscid fluid and the flow is irrotational. The flow field of sea water can be described by Laplace's equation:

$$\nabla^2\phi = \frac{\partial^2\phi}{\partial x^2} + \frac{\partial^2\phi}{\partial z^2} = 0, \tag{4.1}$$

where ϕ is the velocity potential. The horizontal and vertical velocity of the flow can be formulated as:

$$u_f = -\frac{\partial\phi}{\partial x} \text{ and } w_f = -\frac{\partial\phi}{\partial z}, \tag{4.2}$$

where u_f and w_f are the horizontal velocity and vertical velocity of sea water in flow field.

The dynamic and kinematic boundary conditions at the free surface are:

$$-\frac{\partial\phi}{\partial t} + \frac{1}{2}(\phi_x^2 + \phi_z^2) + g\eta = C(t) \text{ at } z = d, \tag{4.3}$$

$$\frac{\partial\eta}{\partial t} - \frac{\partial\phi}{\partial x}\frac{\partial\eta}{\partial x} + \frac{\partial\phi}{\partial z} = 0 \text{ at } z = d, \tag{4.4}$$

where η is the elevation of free surface relative to the static water level. $C(t)$ is the Bernoulli's constant. The bottom of fluid domain is considered as impermeable:

$$\frac{\partial\phi}{\partial z} = 0 \text{ at } z=0. \tag{4.5}$$

Using the perturbation technique, Hsu et al. (2009) derived a third-order approximation for the wave-current interactions, which is summarised here:

$$\begin{aligned}
\phi(x,z,t) = &- U_0 x + \frac{Hg\cosh\lambda z}{2(U_0\lambda - \omega_0)\cosh\lambda d}\sin(\lambda x - \omega t) \\
&+ \frac{3H^2\cosh 2\lambda z}{32\sinh^4\lambda d}(U_0\lambda - \omega_0)\sin 2(\lambda x - \omega t) \\
&+ \frac{3\lambda^3 H^3}{512}\frac{(9 - 4\sinh^2\lambda d)\cosh 3\lambda z}{\sinh^7\lambda d}(U_0\lambda - \omega_0)\sin 3(\lambda x - \omega t),
\end{aligned} \tag{4.6}$$

$$\begin{aligned}
\eta(x,t) = &\frac{H}{2}\cos(\lambda x - \omega t) + \frac{\lambda H^2}{16}\frac{(3 + 2\sinh^2\lambda d)\cosh(\lambda d)}{\sinh^3\lambda d}\cos 2(\lambda x - \omega t) \\
&+ \frac{\lambda^2 H^3}{512}\frac{(3 + 14\sinh^2\lambda d + 2\sinh^4\lambda d)}{\sinh^4\lambda d}\cos(\lambda x - \omega t) \\
&+ \frac{\lambda^2 H^3}{512}\frac{3(9 + 24\sinh^2\lambda d + 24\sinh^4\lambda d + 8\sinh^6\lambda d)}{\sinh^6\lambda d}\cos 3(\lambda x - \omega t),
\end{aligned} \tag{4.7}$$

$$C(t) = \frac{U_0^2}{2} - \frac{H^2}{16}\frac{(\omega_0 - U_0\lambda)^2}{\sinh^2\lambda d}, \tag{4.8}$$

where the H is the wave height of first-order wave, λ is the wave number ($\lambda = \frac{L}{2\pi}$), d is the water depth, U_0 is the current velocity, g is the gravity.and the dispersion relation is given by,

$$\omega = \omega_0 + (\lambda H)^2 \omega_2, \tag{4.9}$$

where ω is the angular frequency ($\omega = \frac{2\pi}{T}$), $\omega_0 = U_0\lambda + \sqrt{g\lambda \tanh \lambda d}$ and

$$\omega_2 = \frac{(9 + 8\sinh^2 \lambda d + 8\sinh^4 \lambda d)}{64 \sinh^4 \lambda d}(\omega_0 - U_0\lambda). \tag{4.10}$$

The dynamic pressure acting on the seabed can be expressed:

$$\begin{aligned} P_b(x,t) =& \frac{\rho_f g H}{2\cosh \lambda d}\left[1 - \frac{\omega_2 \lambda^2 H^2}{2\,(U_0\lambda - \omega_0)}\right]\cos(\lambda x - \omega t) \\ &+ \frac{3\rho_f H^2}{8}\left\{\frac{\omega_0(\omega_0 - U_0\lambda)}{2\sinh^4(\lambda d)} - \frac{g\lambda}{3\sinh 2\lambda d}\right\}\cos 2(\lambda x - \omega t) \\ &+ \frac{3\rho_f \lambda H^3 \omega_0(\omega_0 - U_0\lambda)}{512}\frac{(9 - 4\sinh^2(\lambda d)}{\sinh^7 \lambda d}\cos 3(\lambda x - \omega t), \end{aligned} \tag{4.11}$$

where ρ_f is the density of sea water. When there is no current in wave($U_0 = 0$ m/s), the above third-order solution can be reduced to the classic form of the solution of third-order non-linear wave.

The presence of a current in wave propagating on seabed will change the original wave characteristics due to the interactions between the currents and waves. The effect of uniform current on the wave characteristics (wave number, wave length, maximum pressure and wave celerity) are illustrated in Figure 4.2. It can be seen that the following current (i.e., the current in the same direction of wave propagation) could significantly elongate the wave length, and make the maximum pressure acting on seabed increase greatly. On the other hand, the opposing current significantly shorten the wave length, and make the maximum pressure acting on seabed decrease. The effect of an uniform current on the wave characteristics determined by the linear theory of wave-current interaction are also plotted in Figure 4.2. It is found that the linear theory overestimates the wave number, but underestimates the wave length. In particularly, the linear theory of wave-current interaction significantly underestimate the maximum pressure acting on seabed relative to that determined by the third-order theory.

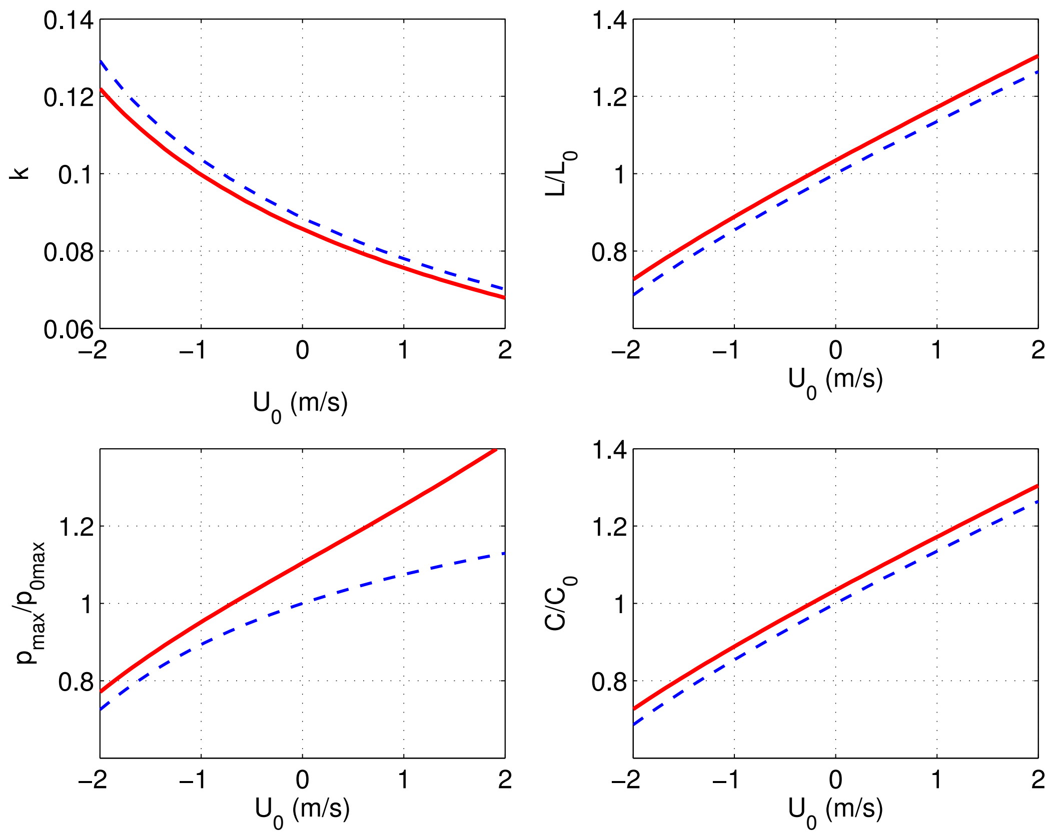

Figure 4.2: The effect of the current on the wave number k, wave length L, induced maximum pressure acting on seabed p_{max}, and the wave celerity C (H=3.0m, d=10m, t=8.0s). L_0, $(p_0)_{max}$ and C_0 is the wave length, maximum pressure and wave celerity determined by the linear wave theory without a current (i.e., U_0=0 m/s). Notation: solid lines=third-order theory; dashed lines=linear theory.

To solve the governing equations, several boundary conditions will be applied. First, the bottom of seabed is considered to be rigid and impermeable. Therefore, there is no displacement and vertical flow at this bottom (Notes: the x axis coincides with seabed surface when studying the seabed response).

$$u = w = 0 \text{ and } \frac{\partial p}{\partial z} = 0 \text{ at } z = -h. \tag{4.12}$$

Second, The boundary conditions along the surface of the seabed can be expressed as,

$$p(x, z = 0, t) = P_b(x, t) \text{ and } \tau_{xz} = 0 \text{ at } z = 0. \tag{4.13}$$

It is noted that the boundary condition (4.13) implies our approach doesn't consider the damping due to porous seabed. It is a one-way coupling (or so-called weakly coupling), rather than two-way coupling (i.e., fully coupling) process. As concluded in Liu et al. (2007), the damping of wave magnitude is less than 5% in 100 second for a solitary wave propagating in shallow water, and on coarse sand seabed (k=10^{-2}m/s). In our study, the length of computational domain is 250 m which is 2 or 3 times of the wave length. It means that the inputting wave into the computational domain will leave after 30 second. Comparing with the case given by Liu et al. (2007), the damping of wave magnitude could be less than 2% when the wave going through the computational domain even it is coarse sand. Therefore, the damping of wave magnitude is small in the cases we considered here. Another simple analytical approach to examine the effects of seabed characteristics on the wave characteristics was proposed byJeng (2001). In the paper, he demonstrates the influence of seabed on the wave parameters such as wave height, wave length etc. However, the influence was less than 2% only, and after 100 wave cycles. Therefore, in this study, we use one-way coupling (or called-weakly coupling), which has been widely used and provide reasonable prediction of seabed response i.e. (Lu, 2005) and Tsai (1995).

4.3 Treatment of lateral boundary conditions

Generally speaking, at two lateral boundaries, the horizontal and vertical displacements, and the flow out/in of pore water don't vanish. The principle of repeatability (Zienkiewicz and Scott, 1972) has been employed to handle the periodic problems such as the wave-seabed interaction (Jeng et al., 2000). However, the periodic boundary condition requires that the length of computational domain must be integer of the wave length. It is not an effective way to generate mesh systems repeatedly for different computational domains corresponding to different wave lengths. Furthermore, the principle of periodic condition is applied to the problems of neither non-periodic loading nor with a structure.

An alternative method is to use a large computational domain and fix both the lateral conditions in the horizontal direction, rather than applying the periodic boundary condition. This method is based on the assumption that the effects of the fixed lateral boundaries are only limited to the region near the lateral boundaries. In the region far away the lateral boundaries, the effect of the fixed lateral boundaries will disappear. The computational results are the same with that when the periodic boundary condition is applied to the lateral sides of computational domain whose length equals to the wave length.

In principle, a larger computational domain will reduce the effect of the fixed lateral boundaries on the results in the concerned region. However, a large computation domain will require huge computational time and larger memory. Therefore, in this study, the length of computation domain is chosen as 1.5 to 3.0 times of the maximum wave length adopted in all cases. Herein, we will investigate the effects of lateral boundaries on the soil response in the region we are interested in. A numerical example, with the input data given in Table 4.1, is illustrated in Figure 4.4. In the numerical example, We consider a computational domain of 250m long that is about 2.8 times of the wavelength (88.8m). In the figure, both results from the present model (fixed boundaries) and the previous model with the principle of repeatability (Jeng et al., 2000) are included for the comparison.

The results presented in Figure 4.4 at three sections x=50m, 125m and 200m are considered. As shown in Figure 4.4(a) and (c), the pore pressure and vertical effective stress are basically identical for both treatments; however, significant differences between two treatments are observed for the horizontal effective stress and shear stress. This indicates that the method of a fixed lateral boundary may

Table 4.1: Input data for numerical examples.

Wave characteristics	
Wave period (T)	8.0 s
Wave height (H_s)	2.0 m
Water depth (d)	20 m
Current (U_0)	1 m/s (following current)
	-1 m/s (opposing current)
Soil characteristics	
Permeability (k)	10^{-2} m/s(Coarse sand)
	10^{-4} m/s (Fine sand)
Porosity (n)	0.3 (Coarse sand)
	0.2 (Fine sand)
Shear modulus (G)	10^7N/m^2
Poisson's ratio (μ)	1/3
Saturation (S_r)	0.98
Thickness (h)	30 m

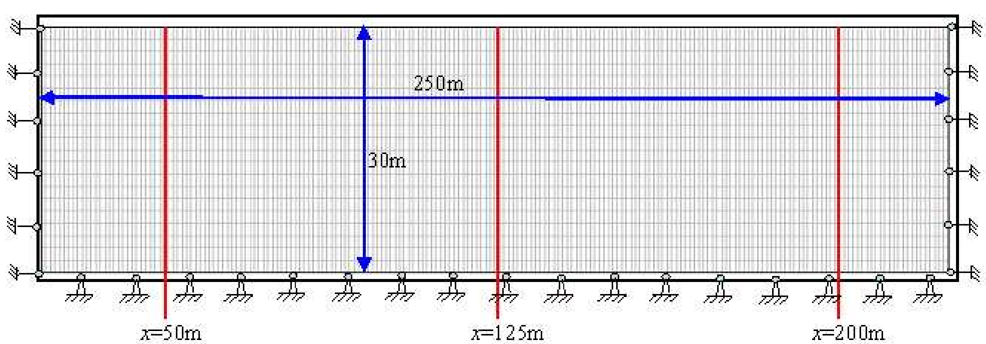

Figure 4.3: The mesh system and the boundary conditions at bottom, lateral sides of computational domain adopted in computation (length of element is 1m at horizontal, and 0.5m at vertical direction).

not be applicable at position x=50m and x=200m. In contract, Figure 4.4 (b) shows the comparison of the seabed response at the mid-line x=125m for both treatments of lateral boundary conditions, and indicates that the effect of the fixed lateral boundaries disappears completely at the region far away the fixed lateral boundaries. Based on this numerical exercise, it can be concluded that the proposed treatment method for lateral boundaries is acceptable under the condition of sufficient large computational domain. Therefore, the same mesh system is used for all cases in which different feasible wave lengths are involved., and the accurate results could be obtained at the region far away the fixed lateral boundaries, which is our main investigation zone. A series of numerical tests for the usage of the proposed treatment and the concept of repeating loading are performed. It is found that the proposed method for treatment of lateral boundary conditions will not waste computation time.

4.4 Results and Discussions

The main objective of this study is to examine the influence of currents on the seabed response, including the pore pressures, effective stresses, shear stresses and liquefaction potential. In this section, we first examine the effect of ocean currents on the seabed dynamic response through comparing with the case without currents (i.e., wave only). Four cases (two for following currents, and another two for opposing currents) in coarse and fine sand are considered. The soil characteristics used in numerical examples are given in Table 4.1. The wave characteristics used here are in the range of non-linear wave (H=3.0 m, T=8.0 s, d=10.0 m). In these examples, the length of computation domain is set as 250m for all the four cases, that is 2.7 times of the maximum wave length involved. The current velocity is chosen as 1 m/s for the following current, and -1 m/s for opposing current.

4.4.1 Effects of Currents

In this section, we compare the seabed response for the cases under waves loading with and without currents. Figure 4.5 illustrates the vertical distributions of the seabed response under wave and following current (U_0=1 m/s) loading at x=125m in both coarse and fine sand. Due to the fact that the absolute value of maximum and minimum dynamic response in seabed is greatly different under highly non-linear wave loading, the maximum and minimum dynamic responses in seabed are

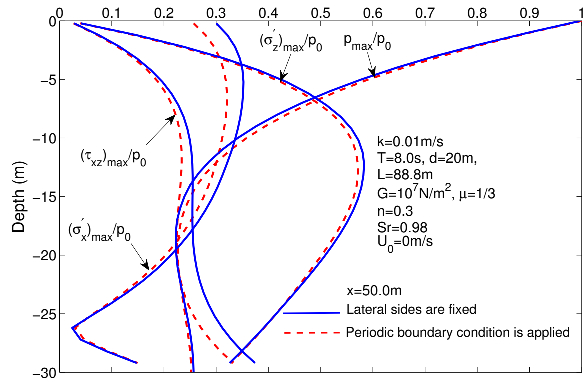

(a) $x = 50$ m

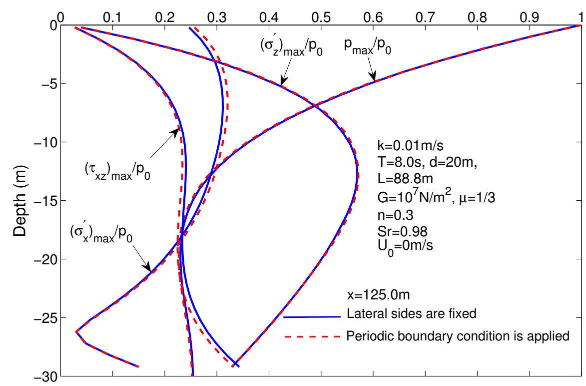

(b) $x = 125$ m

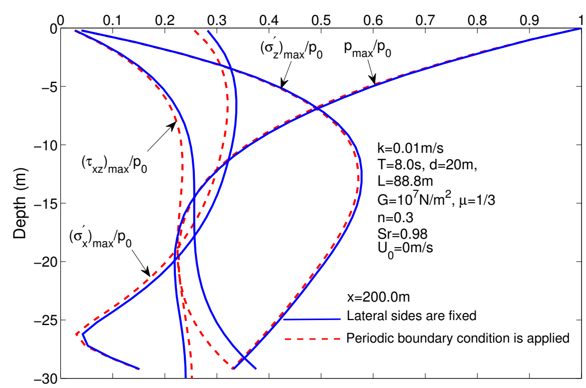

(c) $x = 200$m

Figure 4.4: Comparison of the seabed response under the same wave loading at the x=50m, 125m and 200m between the case in which the lateral boundaries are fixed and the case in which the periodic boundary condition is applied. $p_0 = \gamma_w H/2\cosh(\lambda d)$

compared respectively with their corresponding values when U_0=0 m/s. In the figures for maximum/minimum response, all seabed response variables are normalised by the maximum dynamic wave pressure along the seabed surface without current, i.e., $(p_0)_{max}$ and $\mid (p_0)_{min} \mid$, given in (4.11) when $U_0 = 0$ m/s.

It is clearly observed from the Figure 4.5, the effect of ocean currents on the seabed response is significant in both coarse and fine sand. If a following current exists in the wave field, the magnitudes of the maximum/minimum seabed response, including pore pressure and effective stresses, are basically greater than that without currents. For the maximum/minimum shear stress in seabed, both cases are almost identical in the upper part of seabed. In the lower part of seabed, the magnitude of shear stress is greater when there is a following current. In coarse sand, the maximum relative difference between the two cases with/without currents can up to 15% for maximum/minimum pore pressure, and 10% for $(\sigma'_z)_{max/min}$, 5% for $(\sigma'_x)_{max/min}$ and 10% for the shear stress $(\tau_{xz})_{max/min}$. It is noted that although the magnitude of the relative difference of seabed response between the two cases is not large, the absolute difference is huge because all quantities have been normalised by a great value ($(p_0)_{max}$ or $\mid (p_0)_{min} \mid$). All these results indicate that the seabed instability (such as liquefaction) is more likely to occur (will show in the latter section) if the ocean wave and following current co-exist simultaneously regardless of soil type.

Figure 4.6 further presents the vertical distributions of the maximum/minimum seabed response under non-linear wave and opposing current loading at x=125m in coarse sand and fine sand when the current velocity U_0=-1m/s. It is also clearly observed that the effect of opposing current on the seabed response is also significant, as shown in Figure 4.6. However, the seabed response will be smaller than the case without current, which may reduce the potential of seabed instability.

4.4.2 Effect of the magnitude of current velocity

In the ocean environments, the velocity of ocean current generally is less than 2 m/s except for some special situations, such as storm, tsunami. Therefore, the current velocities used in numerical examples are 0.5m/s, 1 m/s, 1.5 m/s and 2.0 m/s. Additionally, the following current and opposing current with the four magnitudes of velocity are respectively investigated to show the effects of flow direction of currents.

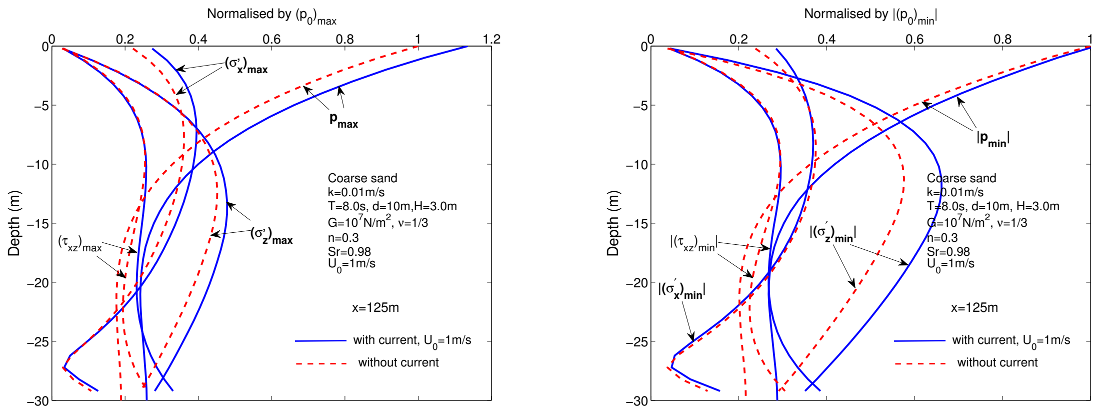

(a) coarse sand

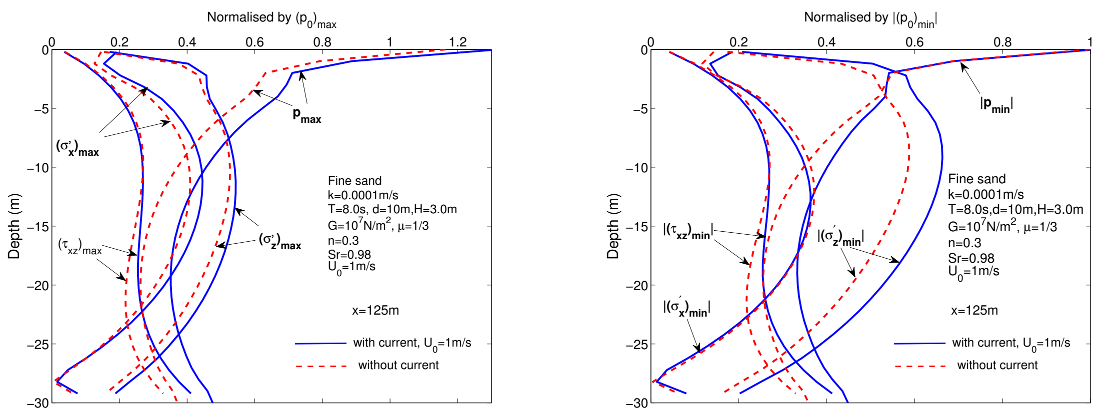

(b) fine sand

Figure 4.5: Vertical distributions of seabed response under wave and following current (U_0=1m/s) loading in (a) coarse sand and (b) fine sand

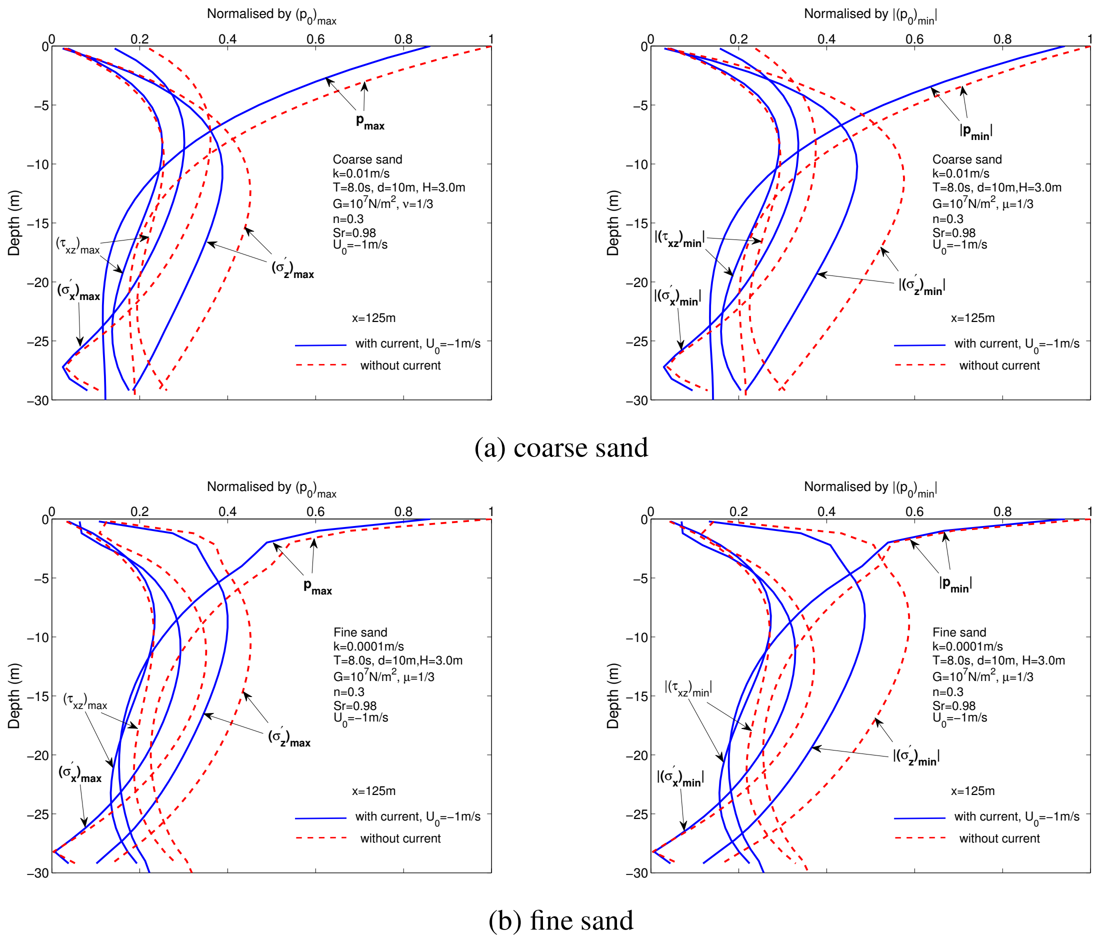

(a) coarse sand

(b) fine sand

Figure 4.6: Vertical distributions of seabed response under wave and opposing current (U_0=-1m/s) loading in (a) coarse sand and (b) fine sand

Figure 4.7 and 4.8 show the vertical distributions of the relative difference of seabed response under nonlinear wave-current loading in coarse and fine sand for different current velocity U_0. Here, all relative differences are normalised by the $p_0 = (p_0)_{max} + |(p_0)_{min}|$ which is the sum of maximum wave pressure (induced by wave crest) and the absolute value of minimum wave pressure (induced by wave tough) when $U_0 = 0$m/s. As shown in the figures, it is observed that the response of seabed, including pore pressure, effective stresses and shear stress, under wave and following current loading, is greater than those under wave loading only; and the seabed response under wave and opposing current loading is smaller than those under wave loading only. The greater the magnitude of the current velocity, the greater the relative difference relative to that condition when U_0=0m/s. The maximum relative differences of pore pressure between the two conditions U_0=-2 m/s and $U_0 = 0$ m/s can reach 25%, as seen in Figure 4.7(a). It is also observed that the relative differences of seabed response under nonlinear wave and opposing current are overall greater than that of seabed response under nonlinear wave and following current even the magnitude of current velocity is the same, for example, U_0=-2 m/s and U_0=2m/s.

If there is a current in the wave field, the maximum relative difference of vertical effective stress (σ_z') occurs at the middle part of seabed in coarse sand while it occurs at the region near the seabed surface in fine sand (see Figures 4.7 and 4.8). The maximum relative difference of (τ_{xz}) occurs at impermeable bottom of seabed both in coarse sand and fine sand.

Based on the numerical examples presented, it is noted that the combined wave and following current loading will enhance the potential of seabed instability such as liquefaction, while the opposing current is beneficial to prevent the seabed from liquefaction or shear failure. Once the liquefaction occurring, the maximum depth of liquefaction would be deeper than the situation in which there is no current. Therefore, the following current will aggravate the instability of seabed. It is a potential risk for marine structures located on seabed.

4.4.3 Effect of wave characteristics

In this section, we further investigate the effects of wave parameters on the relative differences of pore pressure $((p_{\text{current}} - p_{\text{no-current}})/p_0)$. Two wave characteristics, wave period and water depth, are examined here.

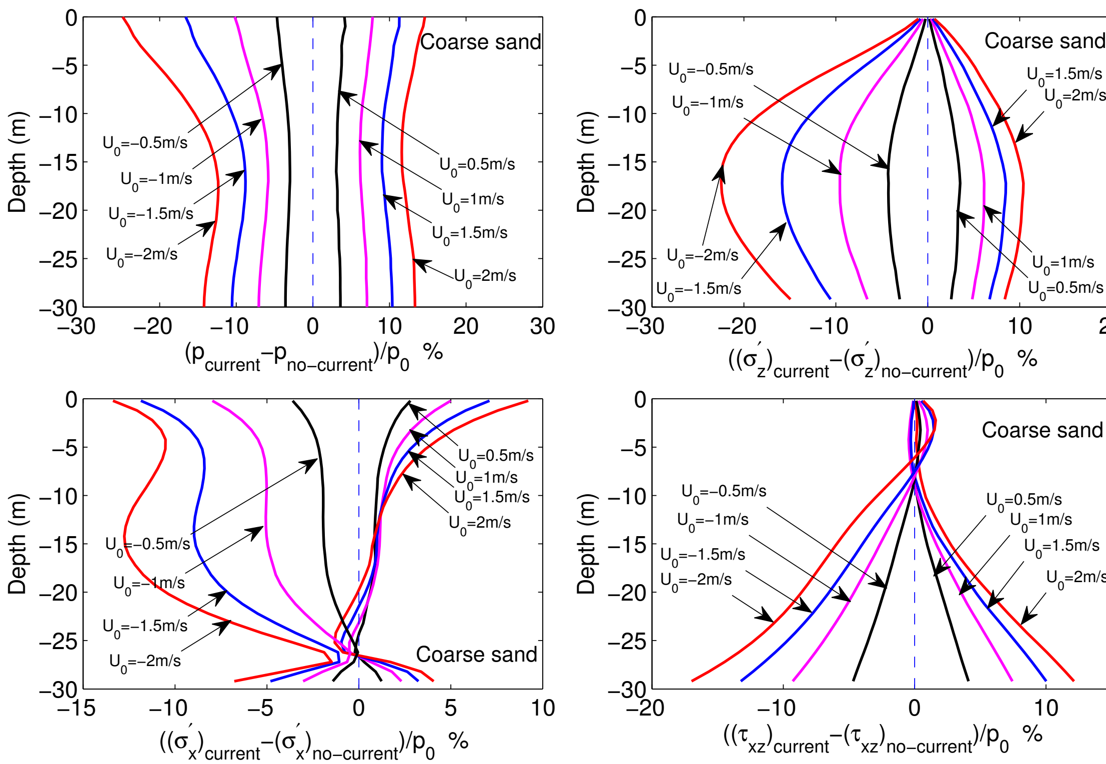

Figure 4.7: Vertical distributions of the relative differences of wave-current induced seabed response in coarse sand for different U_0.

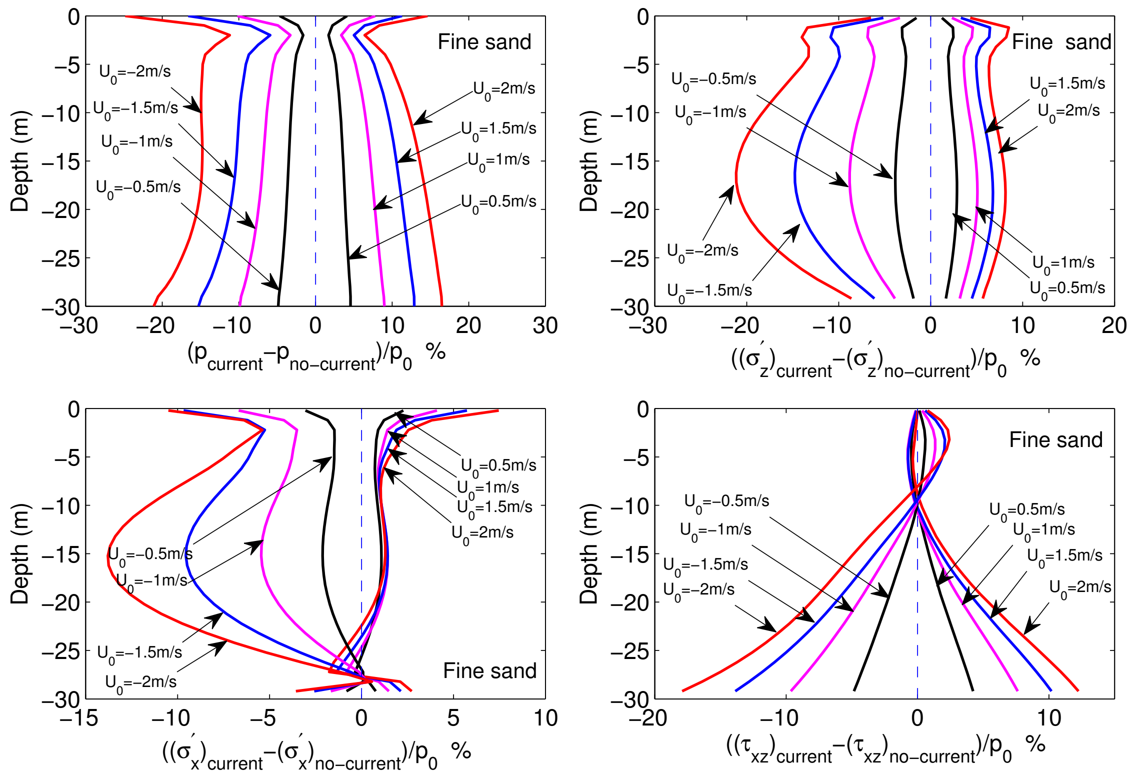

Figure 4.8: Vertical distributions of the relative differences of wave-current induced seabed response in fine sand for different U_0.

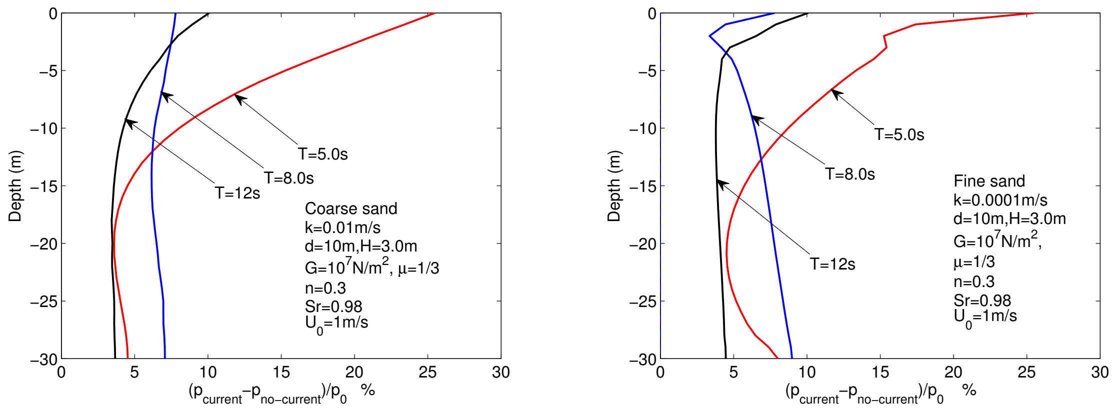

(a) coarse sand (b) fine sand

Figure 4.9: Vertical distributions of the relative difference of pore pressure, $((p_{\text{current}} - p_{\text{no-current}})/p_0)$, for various wave periods

As shown in Figure 4.9, the effect of following current on the seabed response is significant for short period wave in the upper part of seabed. For example, the maximum relative difference is up to 25% at the surface of seabed when (T=5.0s); While, the effect of following current on seabed response for large period wave (T=12.0s) is not so significant like that for short period wave. However, it is interesting to point out that the effect of following current on seabed response for medium period wave (T=8.0s) is not in the range of relative differences of short period wave and large period wave. If the relative difference is smallest in the region near to seabed surface for medium period wave, then the relative difference increases gradually along the seabed depth. At the bottom of seabed, the relative difference becomes to be the greatest one for medium period wave.

Figure 4.10 illustrates the vertical distributions of the relative difference of pore pressure versus soil depth in coarse and fine sand for various water depth. It is observed in the figure that the water depth has significant effect on wave-current induced pore pressure in seabed. Deeper the water depth, more significant the effect of following current on the seabed response both in coarse sand and fine sand. This can be explained as that: when a wave propagates in deep water, the current-induced pressure accounts for a major proportion in the whole wave-current induced pressure acting on seabed surface. Therefore, the effect of current is relatively significant.

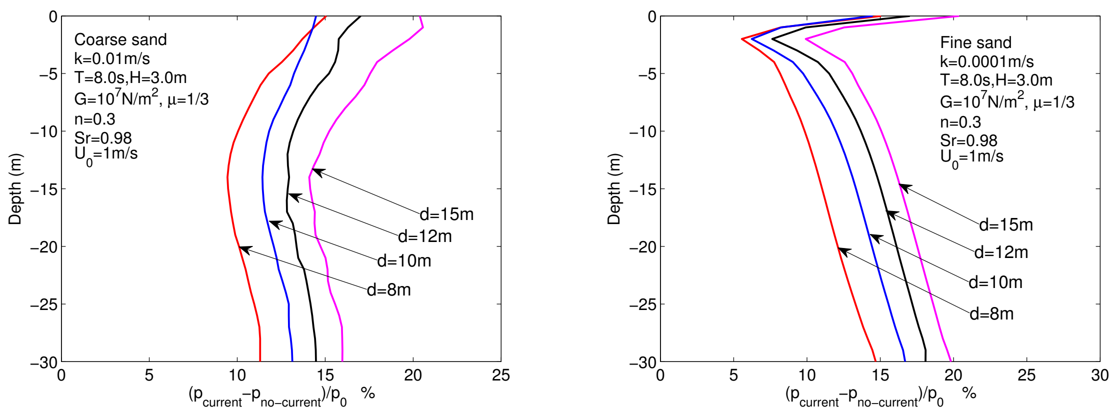

(a) coarse sand (b) fine sand

Figure 4.10: Vertical distributions of the relative difference of pore pressure, $((p_{\text{current}} - p_{\text{no-current}})/p_0)$, for various water depth

4.4.4 Effect of soil characteristics

Soil characteristics are also important parameters that must be considered in the analysis of seabed instability. Among these, three parameters are examined here, they are: the degree of saturation, seabed thickness and soil type (in term of soil permeability).

The degree of saturation has been recognized as one of dominant factors in the evaluation of the wave-induced seabed response. The compressibility of pore water in seabed is mainly dependent of the degree of saturation. It is reported that in-site degree of saturation of marine sediments normally lies in the range of 85% to 100% (Esrig and Kirby, 1977; Pietruszczak and Pande, 1996). In this study, three representative degree of saturation are chosen to investigate the effect of current on the seabed response in seabed with different saturation. They are 95%, 98% and 100%, respectively.

Figure 4.11 presents the vertical distributions of the relative difference of dynamic pore pressure, $((p_{\text{current}} - p_{\text{no-current}})/p_0)$, in coarse and fine sand for various degrees of saturation. As shown in Figure 4.11, it is found that the degree of saturation indeed has significant effect on the wave-current induced pore pressure both in coarse sand and fine sand. The relative difference between the wave-current induced pore pressure and the wave induced pore pressure (without current) increase as the degree of saturation increasing. It means that the effect of current is most significant in fully saturated seabed. The maximum relative difference occurs at impermeable bottom of seabed both in coarse sand and fine sand if the seabed is fully saturated.

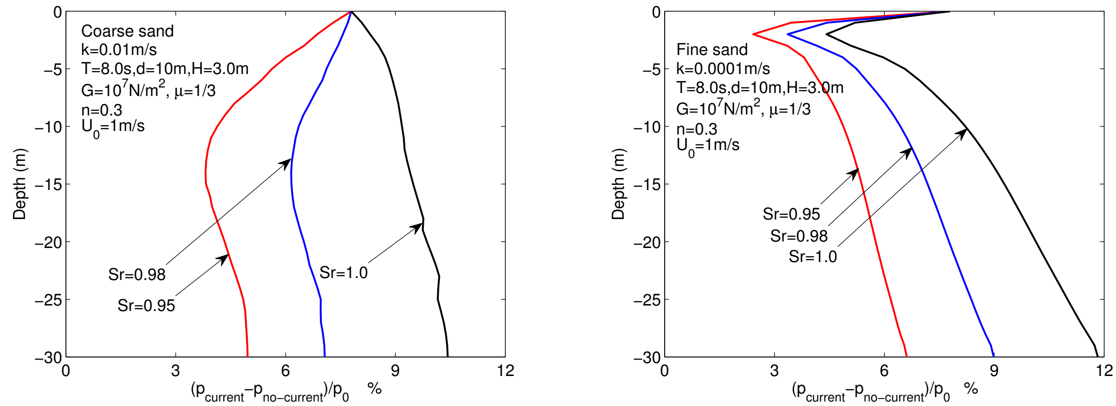

(a) coarse sand (b) fine sand

Figure 4.11: Vertical distributions of the relative difference of pore pressure, $((p_{\text{current}} - p_{\text{no-current}})/p_0)$, for various degree of saturation

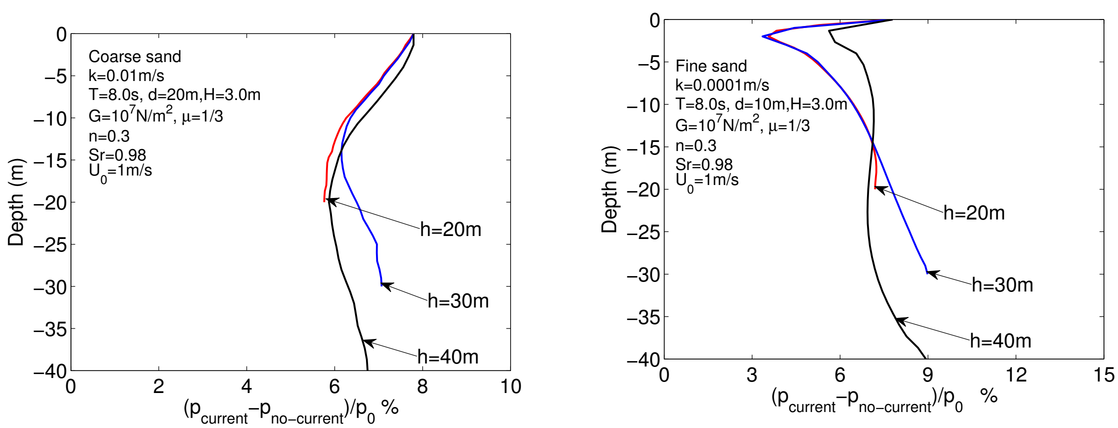

(a) coarse sand (b) fine sand

Figure 4.12: Vertical distributions of the relative difference of pore pressure, $((p_{\text{current}} - p_{\text{no-current}})/p_0)$, for various seabed thickness

The thickness of seabed is another factor which would affect the effect of current on seabed response. Figure 4.12 illustrates the vertical distributions of the relative difference of pore pressure, $((p_{\text{current}} - p_{\text{no-current}})/p_0)$, in coarse sand and fine sand for various seabed thicknesses. From the figures, it is found that the effect of following current (U_0=1 m/s) on the seabed response is almost the same at the top of seabed (0 to -15 m) in coarse sand. In the lower part of seabed (less than -20 m), the relative difference of pore pressure is greater in thin seabed. In find sand, the situation is different in the upper part of seabed. The relative difference of pore pressure is greatest in thick seabed.

In addition to the degree of saturation and seabed thickness, soil permeability is another important factor in the analysis of wave/current induced soil response. Based on the results presented in Figures 4.9–4.12, the influence of currents on the seabed response is more significant in fine sand, compare with that in coarse sand.

4.4.5 Momentary liquefaction of seabed under combined non-linear wave and current loading

It is well known that the porous seabed would liquefy under wave loading due to the variation of excess pore pressure in seabed. In this study, to investigate the momentary liquefaction properties in seabed under combined non-linear wave and current loading, the liquefaction criterion proposed by Okusa (1985) are adopted. It is expressed as:

$$-(\gamma_s - \gamma_w)z \le \sigma'_{zd}, \tag{4.14}$$

where the γ_s is the saturation unit weight of seabed soil, γ_w is the unit weight of water, σ'_{zd} is the wave induced vertical dynamic effective stress. Actually, the liquefaction criterion (equation (4.14)) means that the seabed will liquefy if the wave induced vertical dynamic effective stress σ'_z (Noted: compressive stress is negative) is equal to or greater than original vertical effective stress $(\gamma_w - \gamma_s)z$. In this study, the dynamic effective stresses are determined through following three steps: (1) calculating the consolidation state of seabed under the static water pressure, (2) calculating the full effective stresses state of seabed under full water pressure including static pressure and the wave-induced dynamic pressure, (3) the dynamic effective stresses is determined by subtracting the effective stresses of consolidation state from the full effective stresses.

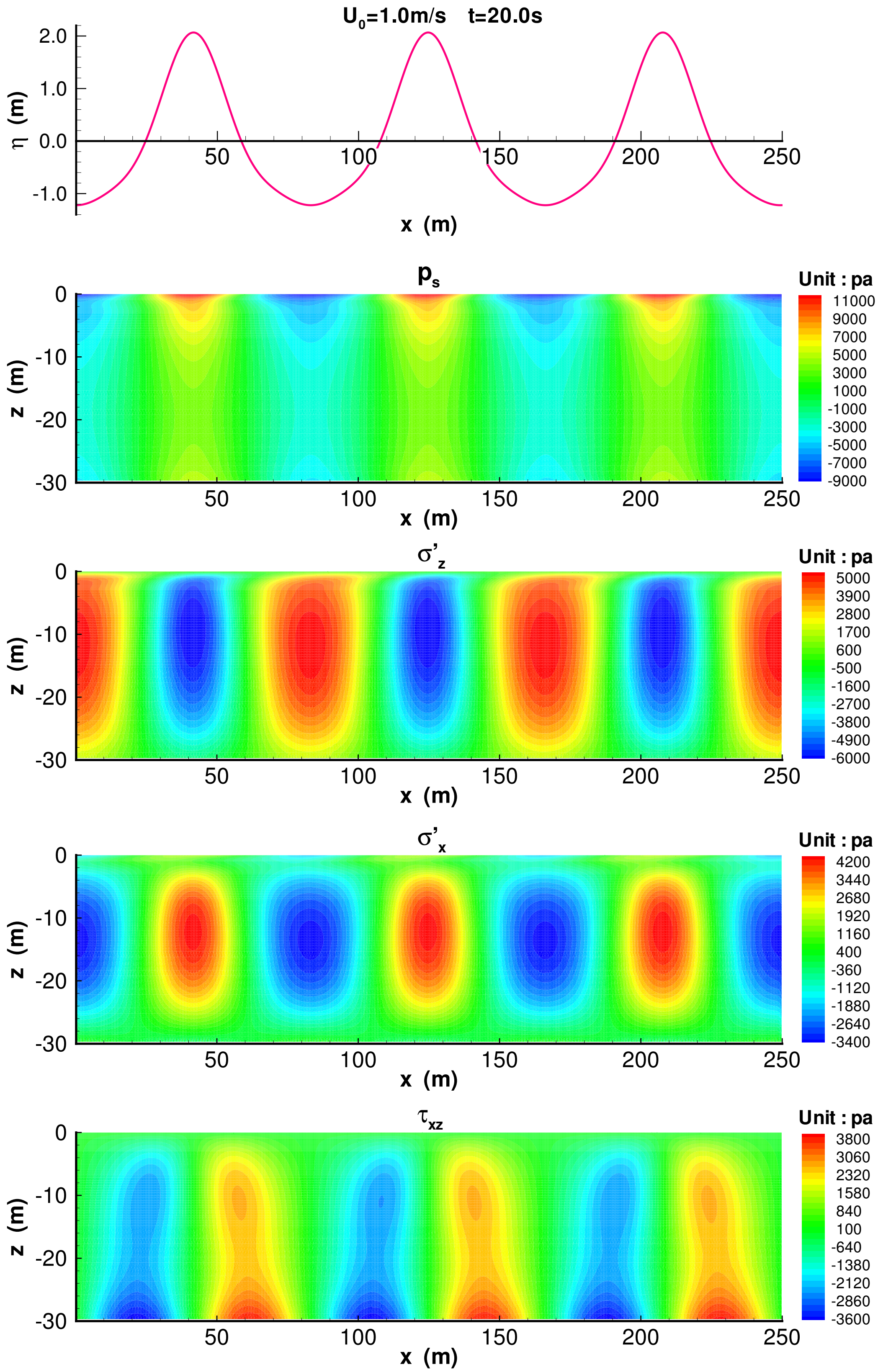

Figure 4.13: The free surface of third-order wave, and the distribution of wave-induced dynamic pore pressure p_s, effective stresses σ'_x, σ'_z, and shear stress τ_{xz} in fine sand at time t=20.0s (U_0=1 m/s)

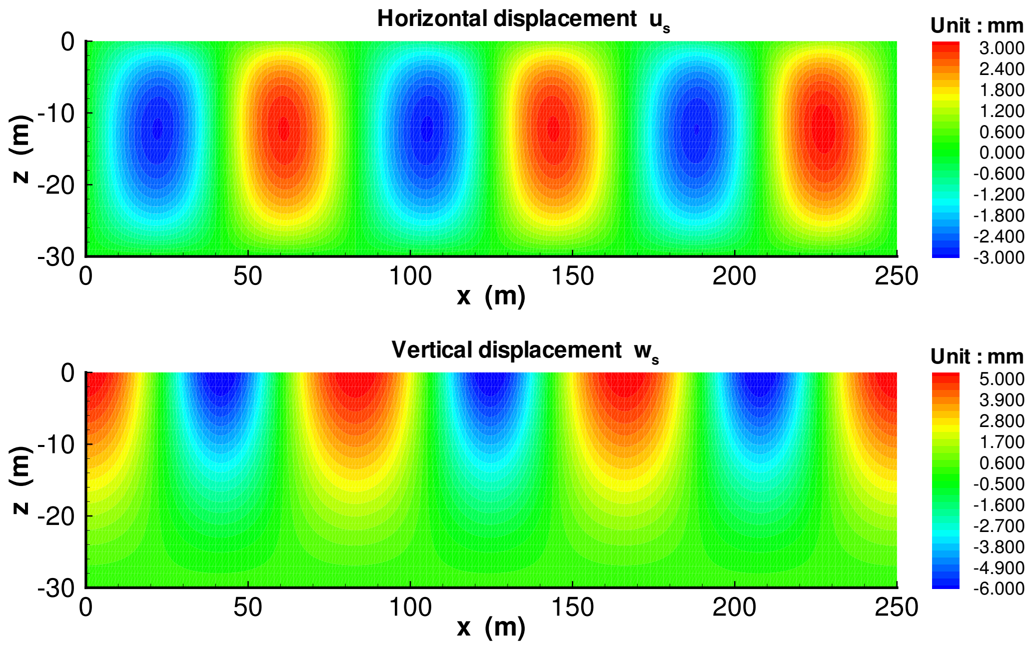

Figure 4.14: Distribution of wave-induced displacements in seabed (fine sand) under nonlinear wave loading at time t=20.0s (H=3.0m, d=10.0m, T=8.0s, U_0=1 m/s)

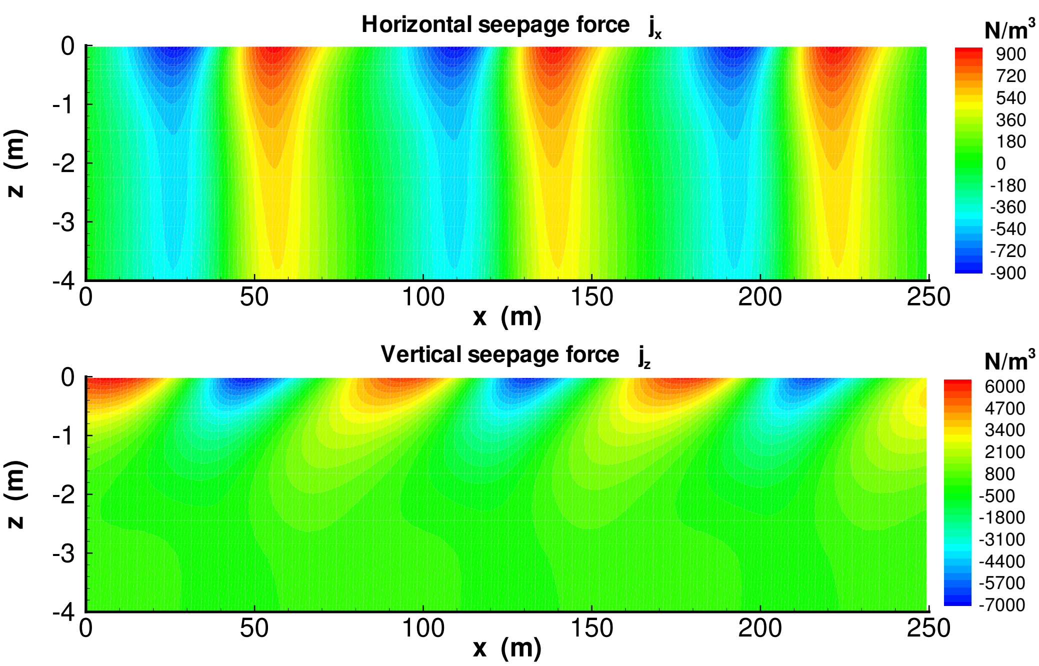

Figure 4.15: Distribution of wave-induced seepage force in seabed (fine sand) under nonlinear wave loading at time t=20.0s (H=3.0m, d=10.0m, T=8.0s, U_0=1 m/s)

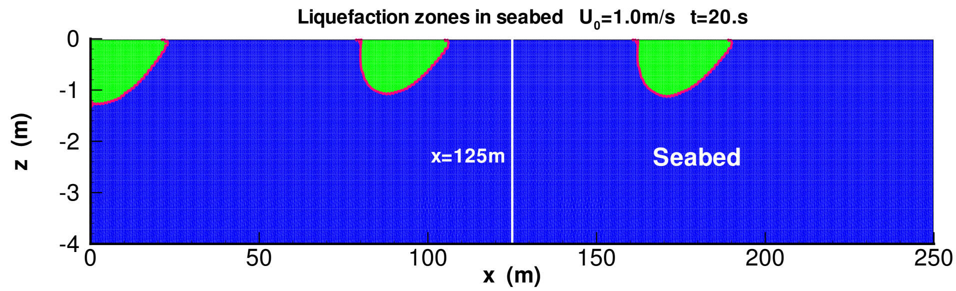

Figure 4.16: Liquefaction zones in seabed (fine sand) under nonlinear wave loading at time t=20.0s (H=3.0m, d=10.0m, T=8.0s, U_0=1 m/s)

Figure 4.13 shows the elevation of free surface of third-order stokes wave with a following current at time t=20.0 s (U_0=1 m/s), and the distribution of the corresponding dynamic pore pressure p_s and effective stress σ'_z, σ'_x and τ_{xz} in fine sand. As illustrated in Figure 4.13, in the region in seabed under wave crest, the dynamic pore pressure is positive; and the dynamic vertical effective stress is compressive, the dynamic horizontal effective stress is tensile. While, in the region in seabed under wave trough, the dynamic pore pressure is negative; and the dynamic vertical effective stress is tensile, the dynamic horizontal effective stress is compressive. Therefore, the seabed under wave trough is most likely to be liquefied. The distribution of shear stress is symmetric, and mainly concentrates at the lower part of seabed foundation. Figure 4.14 is the distribution of non-linear wave induced displacements in seabed. It is shown that the wave-induced displacements are also symmetric. The maximum horizontal displacement appears at the middle part of seabed; while the maximum vertical displacement occurs at the surface of seabed. Figure 4.15 illustrates the distribution of wave-induced seepage force (defined as the gradient of wave-induced pore pressure) in seabed. It is found that the vertical seepage force is much more greater than the horizontal seepage force. It is indicated that the vertical porous flow in seabed driven by the wave is the dominant part, and mainly appears in the zones near to the seabed surface. When the upward seepage force under wave trough is great enough to overcome the weight of overburden soil, the seabed will liquefy in that zone.

Figure 4.16 shows the liquefied zones in seabed under nonlinear wave loading at time t=20.0s. It can seen from Figure 4.16 that all liquefied zones in seabed are located in the regions near the wave troughs due to that the tensile vertical effective stress is generated; and only the upper part of seabed could be liquefied. Comparing the Figure 4.16 and Figure 4.15, it is found that the liquefied zones in seabed is highly consistent with the regions in which the seepage force is upward. It is indicated that the upward seepage is the mainly reason for the transient liquefaction of seabed.

The transient liquefied zones move in the seabed accompanying the movement of the third-order progressive wave. Therefore, there is no a place which is always in the liquefied state or non-liquefied state if the elastic model is used for porous seabed. Figure 4.17 (a) illustrates the variation process of liquefied depth in fine sand seabed in time domain at x=125m under nonlinear wave and current (U_0=-1m/s, 0m/s and 1m/s) loading. As shown in Figure 4.17(a), the maximum liquefied depth in seabed is 1.16m, 0.98m and 0.58m when the velocity of current U_0 is 1m/s, 0m/s and -1m/s. Relative to the condition without current, the following current U_0=1m/s make the maximum liquefied depth increase 18%; while the opposing current make the maximum liquefied depth decrease 57%. From this result, It is found that the following current make the liquefied zone in seabed becomes larger than that when there is no current; and the opposing current is beneficial to prevent the seabed from liquefying. Figure 4.17 (b) shows the relationship between the maximum liquefied depth and the current velocity under condition H=3.0m, d=10.0m, T=8.0s. As illustrated in Figure 4.17 (b), the following current makes the fine sand seabed more easy to occur liquefaction, the opposing current makes the fine sand seabed more difficult to be liquefied.

4.4.6 Residual liquefaction of seabed under combined non-linear wave and current loading

It is recognized that there are two liquefaction mechanism in seabed: momentary liquefaction and residual liquefaction. The wave-current induced momentary liquefaction in poro-elastic seabed has been intensively investigated in above section. In this section, the wave-current induced residual liquefaction in poro-elasto-plastic seabed is investigated. The Pastor-Zienkiewicz Model Mark-III model is adopted to describe the wave-current induced elasto-plastic behavior of seabed soil. The Nevada dense sand is taken as the seabed sand soil in this computation. The parameters of Nevada dense sand are listed in Table 4.2. The same computational domain, mesh system, boundary conditions are applied as that in poro-elastic seabed; and the same wave-current is used to apply the wave-current induced pressure on seabed floor: H=3.0m, d=10.0m, T=8.0s, U_0=1.0m/s.

Figure 4.18 shows the wave-current induced pore pressure build up in the seabed floor at three typical depth z=27m, z=15m, and z=3m, respectively. As illustrated in Figure 4.18, the pore pressure

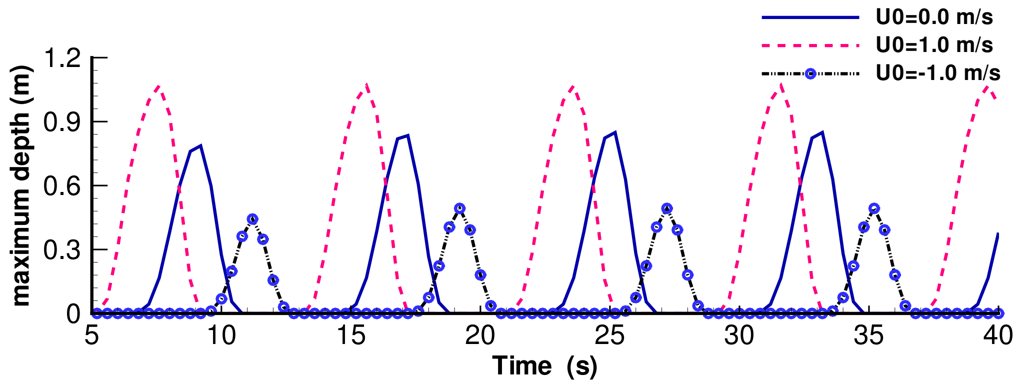

(a)

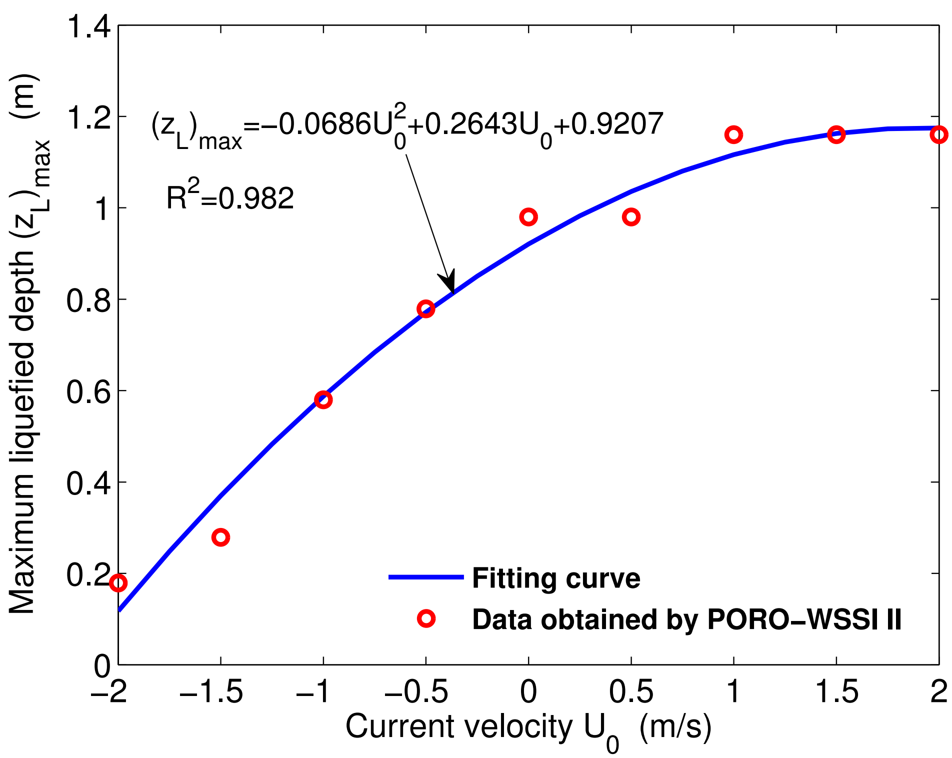

(b)

Figure 4.17: (a) The variation process of the momentary liquefied depth in seabed (fine sand) at x=125m under non-linear wave and different current loading, (b) the wave-current induced maximum liquefied depth in seabed (fine sand) at x=125m versus different current velocity U_0, and the fitting curve (H=3.0m, d=10.0m, T=8.0s)

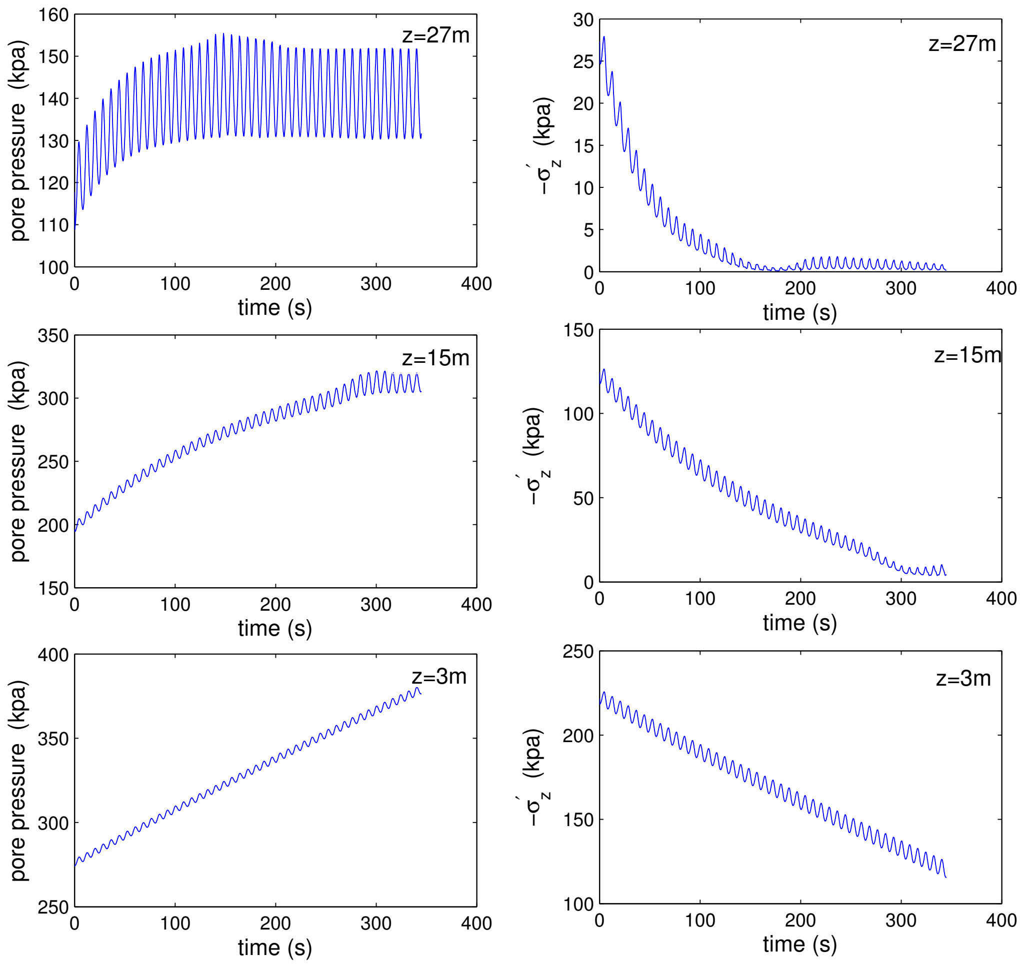

Figure 4.18: Wave-current induced pore pressure build up, and reduction of vertical effective stresses σ_z' in poro-elasto-plastic seabed at three typical depths z=27m, z=15m, and z=3m.

Table 4.2: Parameters of Nevada dense sand for PZIII model used (Zienkiewicz et al., 1999)

Iterm	Value	Unit
K_{evo}	2,000	[kpa]
G_{eso}	2,600	[kpa]
p'_0	4	[kPa]
M_g	1.32	-
M_f	1.3	-
α_f	0.45	-
α_g	0.45	-
β_0	4.2	-
β_1	0.2	-
H_0	750	-
H_{U0}	40,000	[kPa]
γ_u	2.0	-
γ_{DM}	4.0	-

in seabed builds up under the wave and current loading; and the inter-granular effective stresses between soil particles significantly decrease when the pore pressure builds up. The variation of pore pressure in a elasto-plastic seabed floor under wave-current loading is completely different with that in a poro-elastic seabed floor. There is not only the residual part, but also the oscillatory part in the wave-current induced excess pore pressure in the poro-elasto-plastic seabed. The residual excess pore pressure is positively related to the depth in seabed. The deeper the position of point in seabed, the greater the final residual excess pore pressure. However, there is only oscillatory pore pressure in a poro-elastic seabed under wave-current loading; and the magnitude of wave-current induced oscillatory pore pressure damps with the depth in seabed. The different development models of the pore pressure in elastic and elasto-plastic seabed floor under wave-current loading result in the different liquefaction mechanism.

In elasto-plastic seabed floor, when the wave-current induced excess residual pore pressure at a position is sufficient to overcome the overburdened weight of soil, the seabed soil at that position liquefied. Then, the liquefied seabed soil behaves like a heavy liquid. There is no inter-granular effective stress, and the shear resistance is completely lost. As shown in Figure 4.18, the vertical effective stress σ'_z at position z=27m(near to seabed surface) decreases finally to the value which is nearly 0, but never decreases to 0. This result indicates that the seabed soil never really reaches to

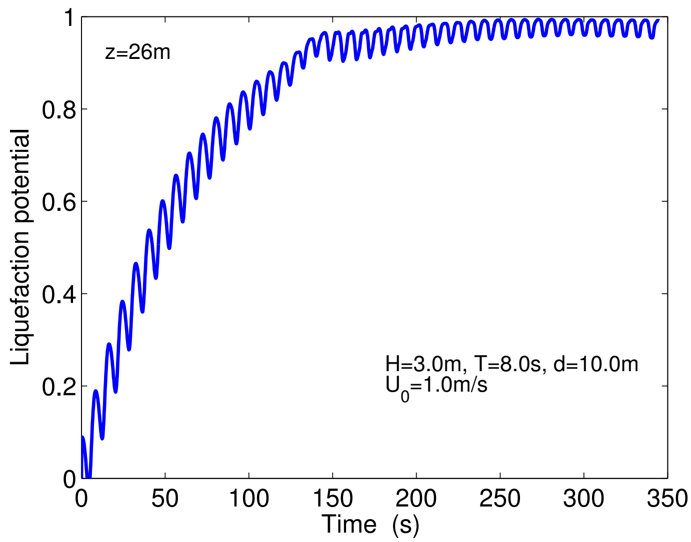

Figure 4.19: Historical curve of residual liquefaction potential of seabed floor at position z=26m under wave-current loading

the complete liquefied status. This attributes to that the soil constitutive model (PZIII) used in this computation only could describe the soil behavior under compression/shear environment. There is no yield surface and plastic potential surface in the space of tension stress in the stress space. The soil is assumed as cohesionless soil, which can not bear any tensive stress. Additionally, the PZIII model also can not describe the behavior of liquefied soil. In this thesis, the liquefaction potential $L_{potential}$ is defined to evaluate the possibility of residual liquefaction:

$$L_{potential} = \frac{\sigma'_{zd}}{|\sigma'_{z0}|}, \tag{4.15}$$

where σ'_{zd} is the wave-current induced effective vertical stress; σ'_{z0} is the initial effective vertical stress in consolidation status. When the $L_{potential}$ is greater than or equal to 1.0 at a position, the soil is completely liquefied at that position.

Figure 4.19 illustrates the historical curve of residual liquefaction potential of seabed floor at z=26m under wave-current loading (U_0=1.0m/s). In Figure 4.19, it is found that the wave-current induced liquefaction potential in seabed increases gradually at the initial stage of loading. At time t=150s, the liquefaction potential $L_{potential}$ increases to a value which is greater than 0.9. After t=150s,

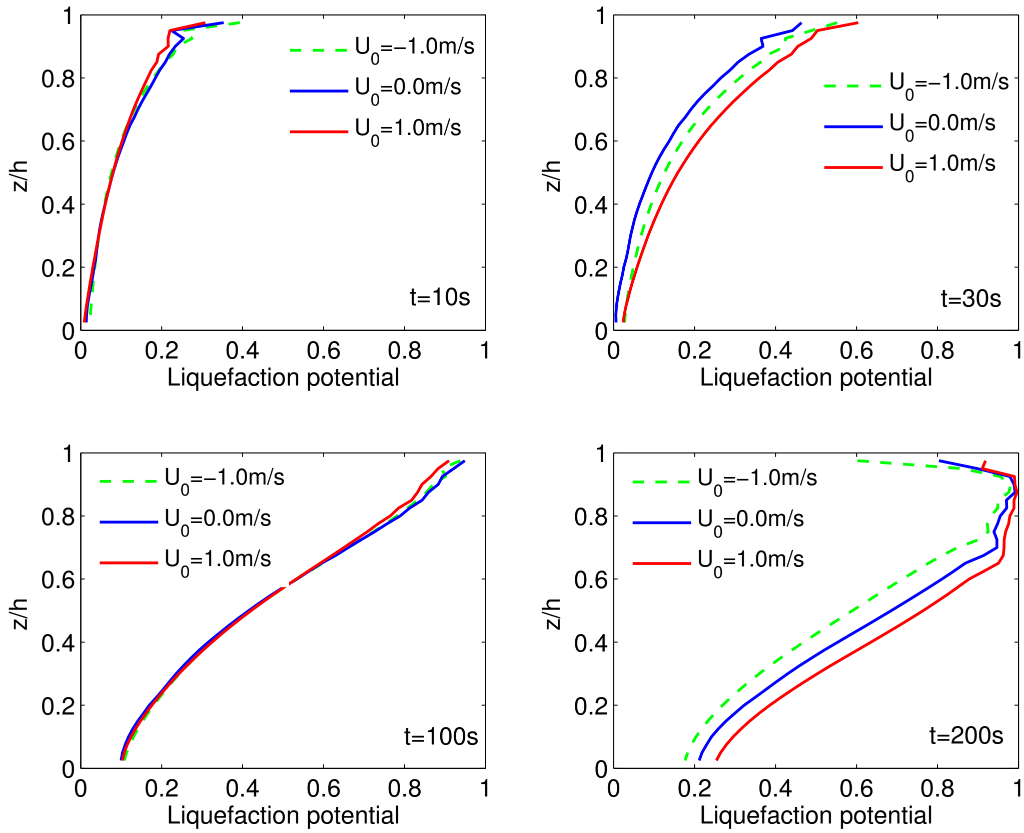

Figure 4.20: Comparison of the wave-current induced residual liquefaction potential in seabed at different times under different current conditions

the liquefaction potential $L_{potential}$ basically only oscillates around its equilibrium position or increases slightly. This variation process basically is consistent with that of excess pore pressure in the seabed under wave-current loading.

Figure 4.20 illustrates the effect of current on the wave-current induced residual liquefaction potential in the elasto-plastic seabed at different times. From Figure 4.20, it can be seen that the wave-current induced residual liquefaction potential in upper seabed is significantly greater than that in lower part of seabed. As the duration of wave-current applying the force on the seabed increases, the residual liquefaction potential increases gradually in the whole seabed. It seems that the effect of current on the wave-current induced residual liquefaction potential in the elasto-plastic seabed is significant at some stages, for example t=30s and t=200s, while it is insignificant at other stages, for example t=10s and t=100s. Overall, after long term loading, the effect of current on the liquefaction potential is significant. The distributions of liquefaction potential along seabed depth at time t=200s indicate that the following current (U_0=1.0m/s) makes the liquefaction potential in whole seabed is higher than that when there is no a current (U_0=0.0m/s); and the opposing current (U_0=-1.0m/s) makes the liquefaction potential in whole seabed is lower than that when there is no a current (U_0=0.0m/s). Therefore, the effect of current on the excess pore pressure build up and residual liquefaction potential in seabed floor is significant after long term wave-current loading.

In Figure 4.20, it is also found that the residual liquefaction potential is greater than 0.95 in the upper seabed (z/h=0.65-0.95), near to the seabed surface when t=200s. But it never reaches to 1.0. The reason is attributed to that the constitutive model used in computation can not describe the mechanical behavior of cohesionless soil under tensile stress. The inter-granular effective stresses between soil particles can not completely decrease to 0.

4.5 Summary

In this Chapter, the effect of ocean current, which generally exists simultaneously with the ocean wave, on the seabed response under third-order nonlinear wave and current loading are investigated. Based on the numerical analysis presented, the following conclusions can be drawn.

1. The following current in non-linear wave field make the seabed response, including pore pressure, effective stresses, shear stress, basically become greater than that without currents in both coarse and fine sand. On the other hand, the opposing current make the seabed response basically become smaller than that when there is no current both in coarse sand and fine sand.

2. It is also found that the following current make the seabed more likely to be liquefied momentarily; the opposing current is beneficial to prevent the seabed from liquefaction or shear failure.

3. The magnitude of current velocity directly determine the effect extent of the current on the seabed response. Greater the current velocity, more significant the effect of current on the seabed response.

4. Exclusion of the following current will result in the underestimation of the wave-induced seabed response, such as the maximum momentary liquefaction depth in seabed.

5. The parametric study indicates that the wave and seabed characteristics significantly affect the effects of current on seabed response under non-linear wave and current loading.

6. Under the wave-current loading, the pore pressure in a elasto-plastic seabed floor (PZIII model is used) continuously builds up, until the seabed soil nearly is a liquefied state. In the process of pore pressure build up, the inter-granular effective stresses between soil particles decrease correspondingly, until they nearly reach to 0.

7. Under wave-current loading, the residual liquefaction potential in upper seabed is obviously greater than that in lower seabed at the same time. As the duration for wave-current loading on seabed floor increases, the residual liquefaction potential gradually increases in the whole seabed. After long time loading, the residual liquefaction potential in the upper seabed near to the seabed surface is nearly to 1.0, but never reaches to 1.0; and the following current makes the liquefaction potential in seabed greater, and opposing current makes the liquefaction potential smaller comparing with that when there is no current (U_0=0.0m/s).

Chapter 5

2D Wave-Seabed-Composite breakwater Interactions: PORO-WSSI II

5.1 Introduction

In the offshore area, breakwaters are widely used to protect the ports or coastline from wave induced damage and erosion. Inappropriate design and maintenance due to incomplete understanding of the mechanism of wave-seabed-structures interaction would result in the failure of marine structures foundation (Lundgren et al., 1989; Zen et al., 1985; Silvester and Hsu, 1989; Oumeraci, 1994; Franco, 1994; Zhang and Ge, 1996; Takahashi et al., 2000; Chung et al., 2006). Therefore, it is important to provide coastal engineers with an effective tool to fully understand the mechanism of wave-seabed-breakwater interaction. Some investigations have been conducted on the problem of wave-seabed-breakwater interaction. Detailed review on the wave-seabed-breakwater interaction, and the residual liquefaction in front of a breakwater can be found in part 2.4, and 2.5 in Chapter *Literature Review*. However, there are always some limitations in previous literature (see part 2.6 in Chapter *Literature Review*).

In this chapter, the developed integrated model PORO-WSSI II is applied to investigate the response of poro-elastic and poro-elasto-plastic seabed and a composite breakwater under wave loading, and the mechanism of wave-seabed-breakwater interaction in the offshore environments. Special attention is paid to the wave induced momentary and residual liquefaction in the seabed foundation near the composite breakwater.

5.2 Poro-elastic seabed foundation[3*]

5.2.1 Computational domain and Boundary condition

In the computation domain, there is a composite breakwater constructed on the seabed. The composite breakwater consists of a permeable rubble mound and an impermeable caisson. The thickness of seabed is 30m, and the horizontal computational length of seabed beneath the composite breakwater truncated from the infinite seabed is chosen as 600m, which is much greater than the horizontal dimension of the composite breakwater. The dimensions and position of composite breakwater are shown in Figure 5.1. In this analysis, only the results in the zone near to the composite breakwater are illustrated.

In order to study the wave-seabed-breakwater intraction, following bounary conditions are applied in computation:

(1) The bottom of seabed foundation is treated as rigid and impermeable.

$$u_s = w_s = 0 \quad \text{and} \quad \frac{\partial p_s}{\partial z} = 0 \quad \text{at z=0m.} \tag{5.1}$$

(2) The two lateral sides of computational domain are fixed in horizontal direction.

$$u_s = 0 \quad \text{at} \;\; \text{x=0m} \;\; \text{and} \;\; \text{x=600m.} \tag{5.2}$$

(3) The pressure including the hydrostatic pressure and the wave induced dynamic pressure, is applied to the surface of seabed and the outer surface of composite breakwater.

5.2.2 Consolidation of seabed under composite breakwater and static water pressure

In the real offshore environment, the seabed generally has experienced the consolidation process under the seawater loading and self-gravity in the geological history. Additionally, after the composite breakwater is constructed on the seabed, the seabed beneath and near to the composite breakwater will be compressed and deform under the gravity of composite breakwater. Finally, the seabed will reach a new balanced state based on the previous consolidation state under sea water and composite breakwater loading. Therefore, in order to simulate the real interaction between the ocean wave,

[3*]Contents in this section are included in Jeng et al. (2012): D-S Jeng, Ye J H, PL-F Liu (2012). An integrated model for the wave-induced seabed response around marine structures: model, verifications and applications. Coastal Engineering, Resubmitted.

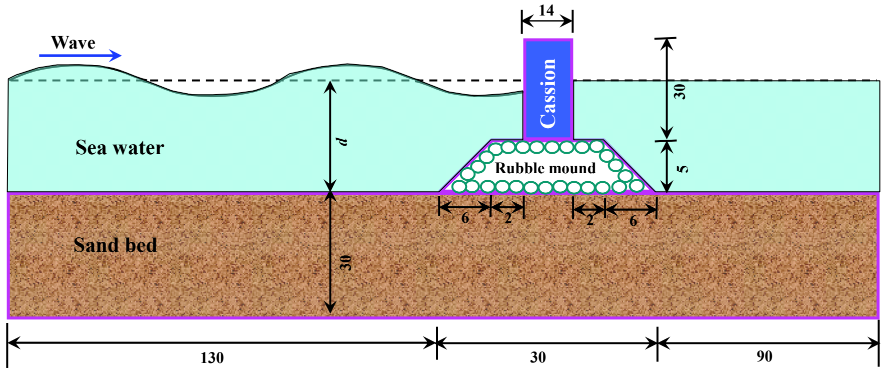

Figure 5.1: Dimensions and position of composite breakwater in computational domain of large-scale model. unit: m

Table 5.1: Properties of seabed soil, rubble mound and caisson adopted in large-scale model

Medium	G (kN/m^2)	ν	k m/s	n	d_{50} (mm)	Sr
Seabed soil	1.0×10^5	0.33	0.0001	0.25	0.5	98%
Rubble mound	5.0×10^5	0.33	0.2	0.35	400	98%
caisson	1.0×10^7	0.25	0.0	0.0	-	0%

seabed and marine structures, the initial consolidation state of seabed under static sea water pressure and gravity of composite breakwater has to be determined firstly before the ocean wave loading is applied on the seabed and the composite breakwater in the numerical model. In this section, the initial consolidation state of seabed is calculated using the integrated model PORO-WSSI II by applying the static water pressure on seabed and on the composite breakwater. The properties of seabed soil, rubble mound and caisson are listed in Table 5.1. Once the consolidation state of seabed under static water pressure, self-gravity and the gravity of composite breakwater reaches enough stable, the calculation of initial consolidation of seabed will be finished. The distribution of effective stresses and pore pressure in seabed and composite breakwater after the consolidation process of seabed is finished are illustrated in Figure 5.2. The horizontal and vertical displacement after consolidation in whole computational domain are shown in Figure 5.3.

As illustrated in Figure 5.3, the effective stresses σ'_x, σ'_z, σ'_y and τ_{xz} have been greatly affected by the composite breakwater in the seabed foundation which is in the range of about 350m to 450m. The value of effective stresses obviously increase due to the gravity of composite breakwater in the seabed foundation. In the region far away the composite breakwater, the effective stresses basically

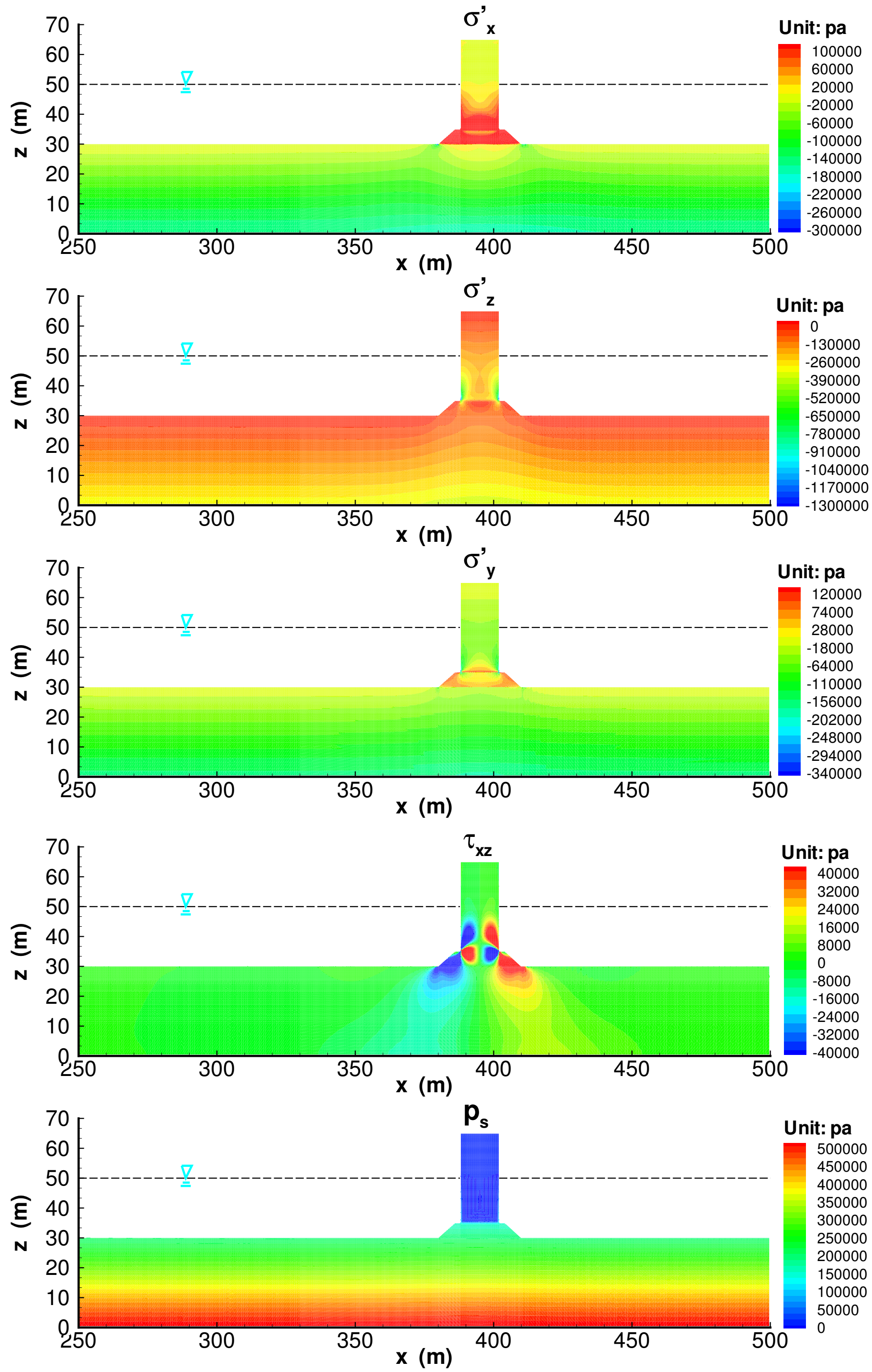

Figure 5.2: Distributions of the horizontal effective stresses σ'_x, σ'_y (into page), vertical effective stress σ'_z and pore pressure p_s in seabed and composite breakwater after consolidation under the loading of static water pressure, self-gravity and the gravity of composite breakwater. The negative value means compressive stress. The static water depth d=20m

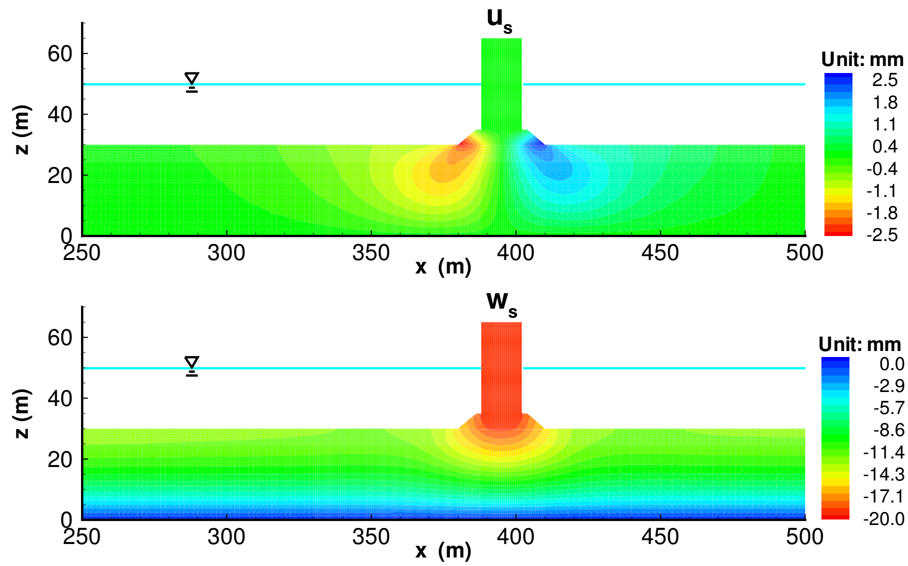

Figure 5.3: Distribution of horizontal (top figure) and vertical (bottom figure) displacement after consolidation in seabed and composite breakwater. The negative values of "u_s" and "w_s" mean moving to left and bottom respectively.

have not been affected. From the distribution of pore pressure in the seabed and composite breakwater after consolidation, the pore pressure in the rubble mound and seabed increase uniformly from the top of rubble mound to the bottom of seabed. The pore pressure in the caisson is 0 due to that it is impermeable medium.

5.2.3 Dynamic response of seabed

Once the initial consolidation state of seabed is determined under the static pressure, self-gravity and the gravity of composite breakwater, it will be taken as the initial stress state to calculate the dynamic response of seabed and composite breakwater under ocean wave loading. Taking the procedures shown in Figure 3.3, the wave model is used to generate ocean wave taking the seabed, rubble mound as porous medium, and taking the caisson as impermeable structure in sea water (see the vector field of flow velocity in Figure 5.4, it is noted that the velocity vectors of sea water in seabed, rubble mound and the region located at the left side of composite breakwater look like points due to that their velocity values are much smaller than that in the region located in the right side of composite breakwater); then the full pressure acting on seabed and composite breakwater is transmitted to the soil model, the soil model is used to determine the dynamic response of seabed and the composite breakwater under the

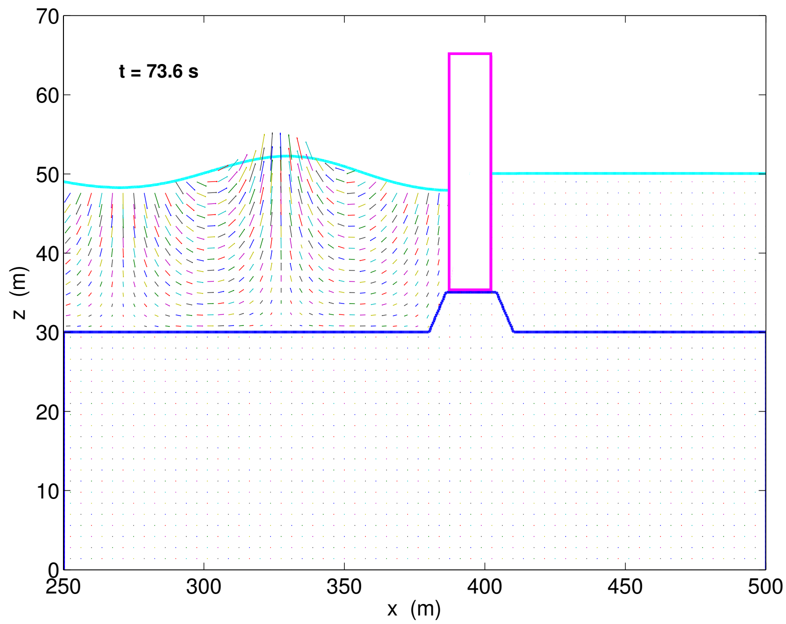

Figure 5.4: Velocity field of sea water in fluid domain and porous seabed and rubble mound at t=73.6s. Wave characteristics: T=10s, H=3m, d=20m.

ocean wave loading. Due to the fact that the full pressure acting on seabed and composite breakwater which includes the static water pressure and the wave induced dynamic pressure is adopted when determining the response of seabed and composite breakwater, the response of seabed and composite breakwater should be full response. The dynamic response of seabed and composite breakwater could be determined through subtracting the full response by the initial consolidation state. Here, the wave characteristics are chosen as: period T=10s, wave height H=3m, water depth d=20m. Figure 5.5 shows the distribution of dynamic effective stresses and pore pressure in seabed and composite breakwater at typical t=73.6s under the wave induced pressure loading.

From the distributions of effective stresses and pore pressure in seabed at t=73.6s in Figure 5.5, it is found that the values of dynamic effective stresses σ'_x, σ'_z, σ'_y and dynamic pore pressure p in the region near to seabed surface are negative when the wave trough propagates on it (250-300m and 360-390m); while they are positive in the region near to seabed surface when the wave crest propagates on it (300-360m). According to the momentary liquefaction mechanism, the decrease of dynamic effective stresses σ'_x, σ'_z, σ'_y and dynamic pore pressure p will make the total stresses

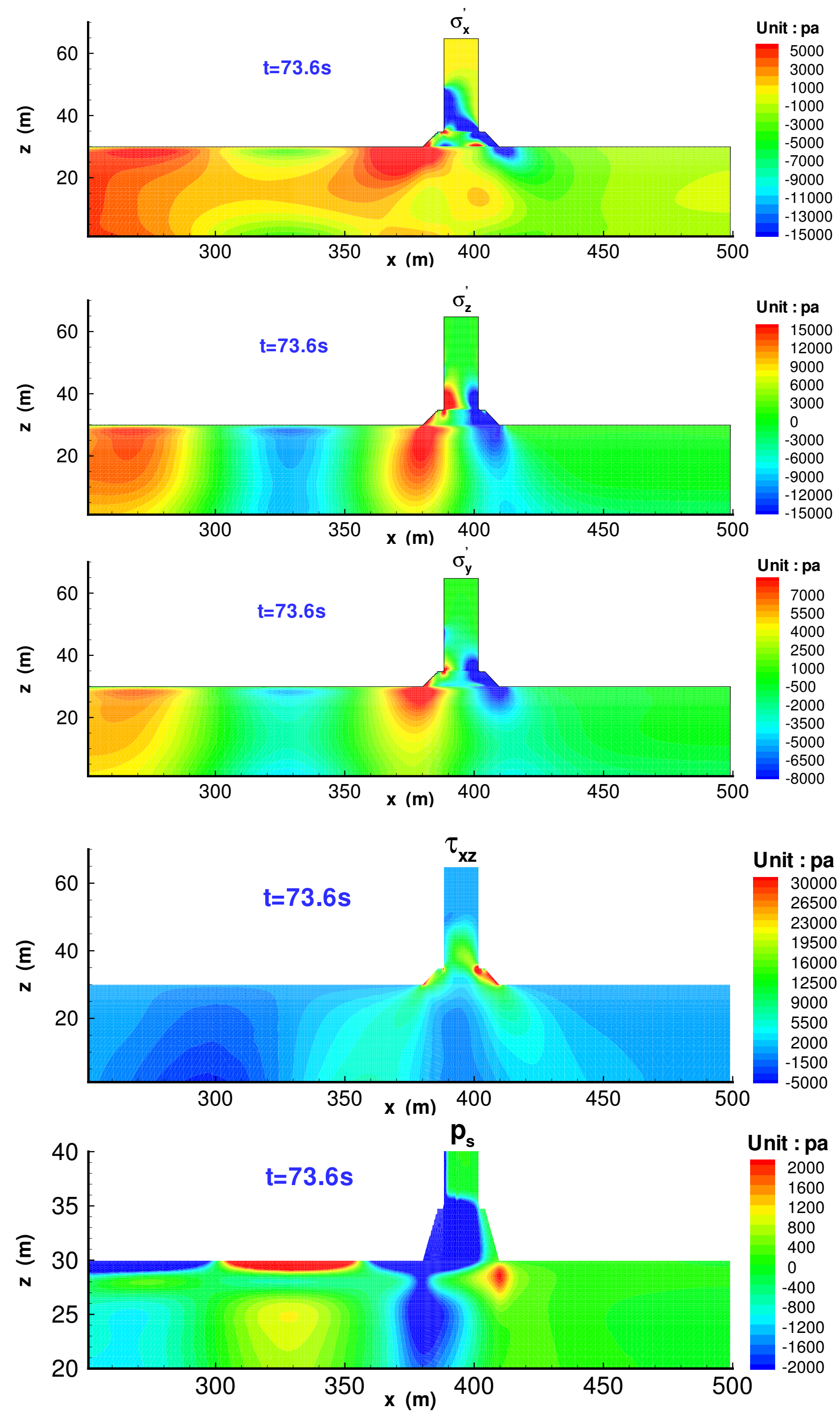

Figure 5.5: Dynamic response of the seabed and composite breakwater under the ocean wave loading at t=73.6s. Wave characteristics: T=10s, H=3m, d=20m. Note: p_s: pore pressure, σ'_x, σ'_z, σ'_y: effective normal stresses, τ_{xz}: shear stress.

(contact stresses between soil grains) decrease. When the total stresses become zero in the region, the seabed soil will liquefy, which would directly result in the failure of marine structures' foundations. From this point of view, the seabed under wave troughs has a greater potential to liquefy, while the liquefaction will not occur in the seabed under wave crests. At the right side of composite breakwater, the effect of the ocean wave is limited in a range which does not excess x=450m due to the blocking of breakwater. In the region far away the composite breakwater, the effect of ocean wave basically disappears. At time t=73.6s, as shown in Figure 5.4 and 5.5, the seabed near to the rubble mound are likely to liquefy due to that the wave trough is propagating on it, and the dynamic effective stresses and pore pressure are negative. This potential liquefaction would lead to the collapse of the composite breakwater. Therefore, it is very important for coastal engineers to predict the depth and area of this liquefaction zone; then some measurements could be adopted to prevent the seabed near to the rubble mound from liquefaction. More attention will be paid on the wave induced liquefaction in the lateral part.

5.2.4 Dynamic response of the composite breakwater

Before the ocean wave arrives the caisson, the composite breakwater mainly moves downward to subside on seabed due to its gravity. Once the ocean wave come to the caisson, the force acting the left side of composite breakwater and the bottom of caisson applied by the seabed water will variate periodically. It results in that the caisson moves periodically at horizontal and vertical direction based on the initial consolidation state when there is no ocean wave. Figure 5.6 shows the variation of horizontal and vertical displacements of the left corner of the caisson. As illustrated in Figure 5.6, there is no horizontal displacement; and the caisson subsides about 19mm before t=25s. After that, the ocean wave arrives the caisson; the caisson begins to vibrate horizontally and vertically with small amplitude. Due to the reflection of ocean wave at left side of the caisson, the wave height increases greatly after t=60s. It results in the vibration of caisson become more intensive.

Another important issue is to investigate the distribution and variation of the horizontal and vertical displacements and the pore pressure at the bottom of rubble mound under the ocean wave loading. Figures 5.7 and 5.8 illustrate the distribution and variation of the horizontal, vertical displacements and the pore pressure at the bottom of rubble mound at different time under ocean loading. From

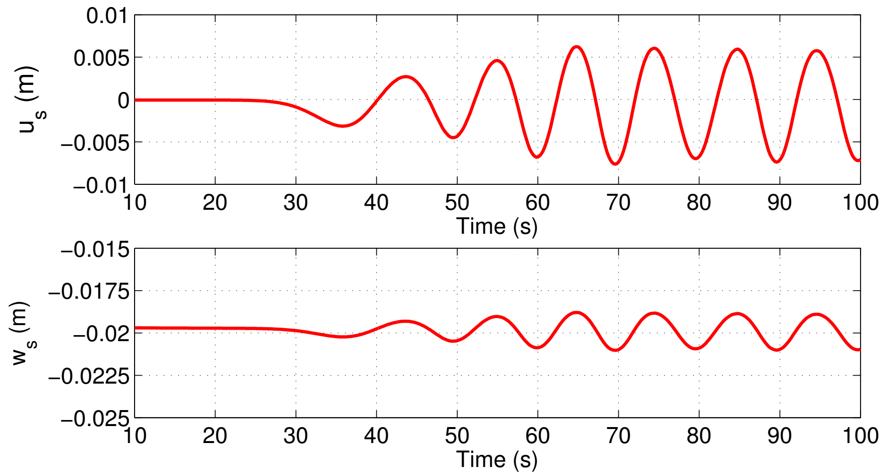

Figure 5.6: Variation of horizontal (top figure) and vertical (bottom figure) displacements of the left corner of the impermeable caisson under ocean wave. Negative value of "u_s" means moving toward left, negative value of "w_s" means moving toward down.

Figure 5.7, it is found that the horizontal and vertical displacements at the bottom of rubble mound both are symmetric in the 2^{nd} period; and there is no vibration due to the fact that the ocean wave generated has not arrived the composite breakwater. This horizontal and vertical displacements attribute to the self-gravity of rubble mound, gravity of caisson and the static sea water pressure acting on the composite breakwater. In the 4^{th} period, the horizontal and vertical displacements at the bottom of rubble mound begin to vibrate with a small magnitude because the ocean wave has arrived the breakwater. After that, due to the reflection of ocean wave at the left side of caisson, the interaction between ocean wave and composite breakwater become much more intensive. The vibration amplification of the horizontal and vertical displacements will increase greatly (see the 8^{th} period). From the distributions of the horizontal and vertical displacements at the bottom of rubble mound at different time, it is found that the rubble mound moves periodically toward right and toward left; meanwhile, the rubble mound swings periodically to right and to left under ocean wave loading.

As illustrated in Figure 5.8, in the 2^{nd} period (the ocean wave has not arrived the composite breakwater), the pore pressure on the bottom of rubble mound does not distribute uniformly; the pore pressure in rubble mound is a little greater than that on the positions outside of the rubble mound even if they are on the same elevation. In the 4^{th} period, the pore pressure on the bottom of rubble mound begins to variate due to the arrival of wave at the composite breakwater. After that, due to

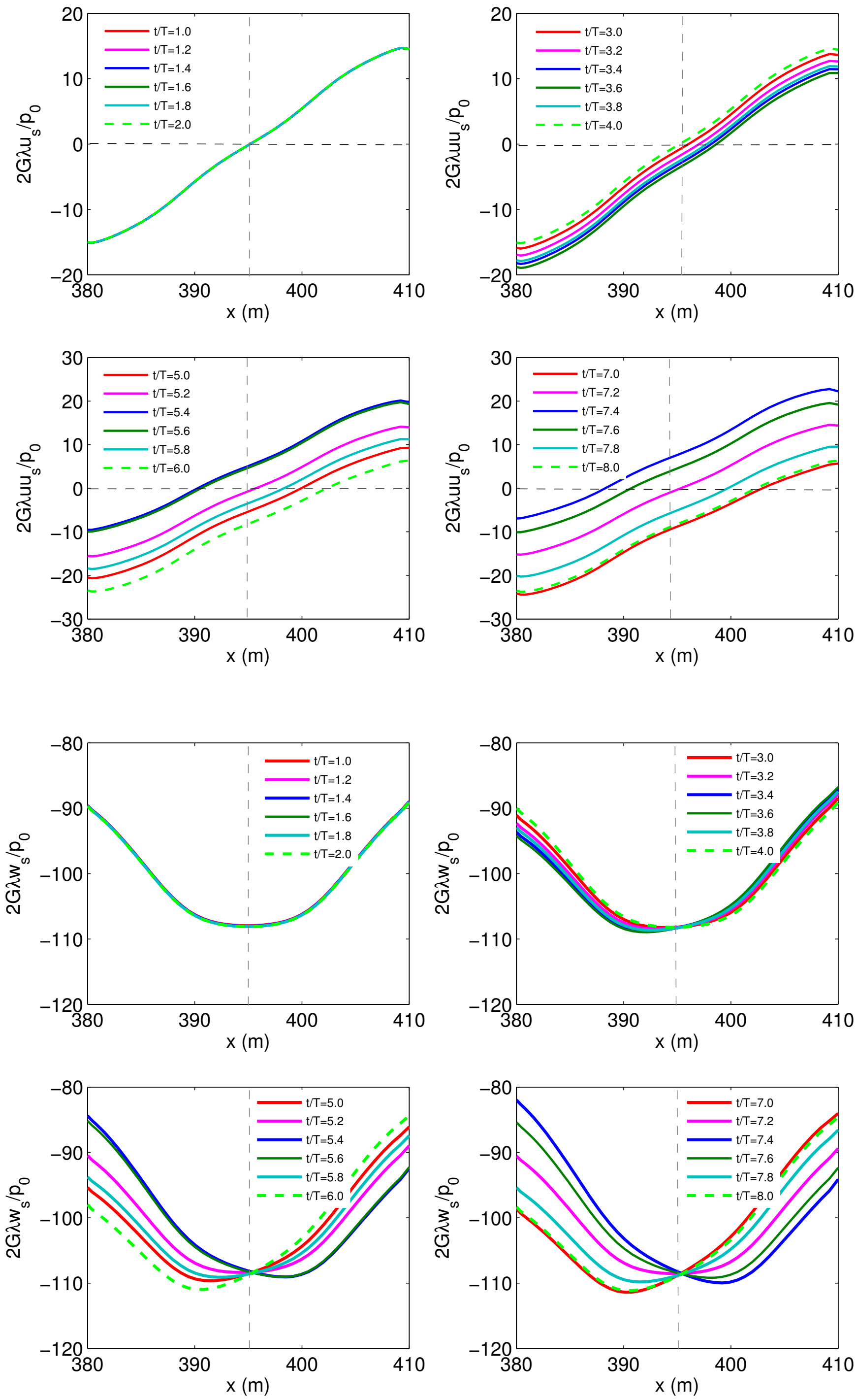

Figure 5.7: Distributions of the horizontal (top four figures) and vertical (bottom four figures) displacements at the bottom of rubble mound at different time under ocean wave loading. Noted: λ: wave number; $p_0 = \gamma_\omega H/(2\cosh(\lambda d))$.

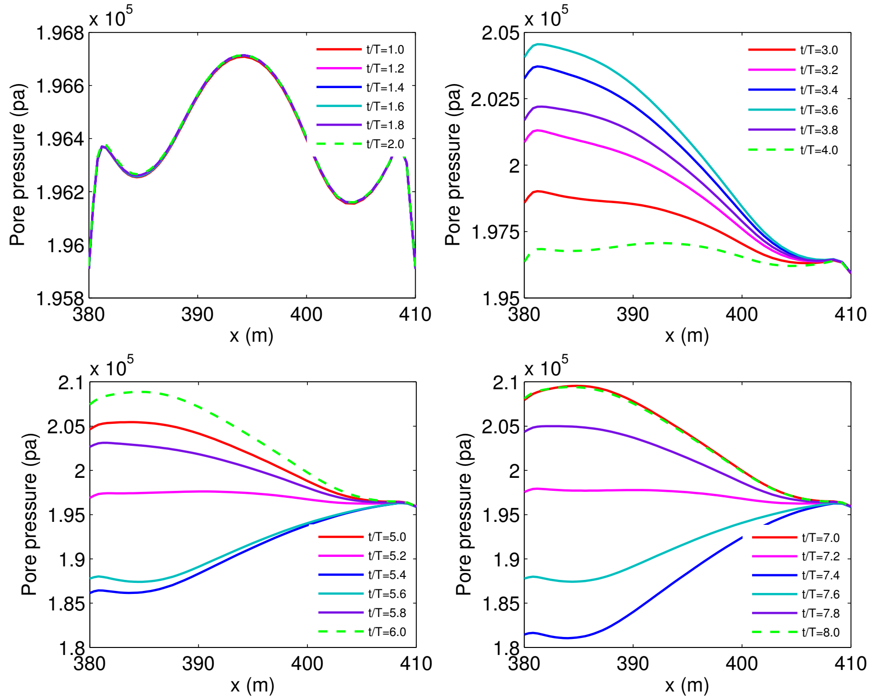

Figure 5.8: Distribution of the pore pressure at the bottom of rubble mound at different time under ocean wave loading.

the reflection of ocean wave at the left side of caisson, the wave height will almost become two times of the original wave height. It makes the magnitude of periodical vibration of pore pressure on the bottom of rubble mound increases. When the wave crest arrives at the composite breakwater, the pore pressure on the bottom of rubble mound increases; while the pore pressure decreases when the wave trough arrives the composite breakwater. Another important phenomenon is that the pore pressure in the region near to the right end of the bottom of rubble mound (x=407-410m) basically has not been affected by the ocean wave. It is indicated that the breakwater really could protect the offshore seabed and coastline from the erosion by ocean wave.

In the verification case related to Mizutani et al. (1998), it is demonstrated that Biot's equation is applicable for the turbulent flow if the Reynolds number (Re) is less than 200 for small-scale cases. Here, it is also interesting to demonstrate the applicability of Biot's equation for turbulent flow in large-scale cases. In this section, the composite breakwater consists of a rubble mound and a caisson. The mean particle size of this rubble mound is 400mm, and its permeability is 2.0×10^{-1}m/s.

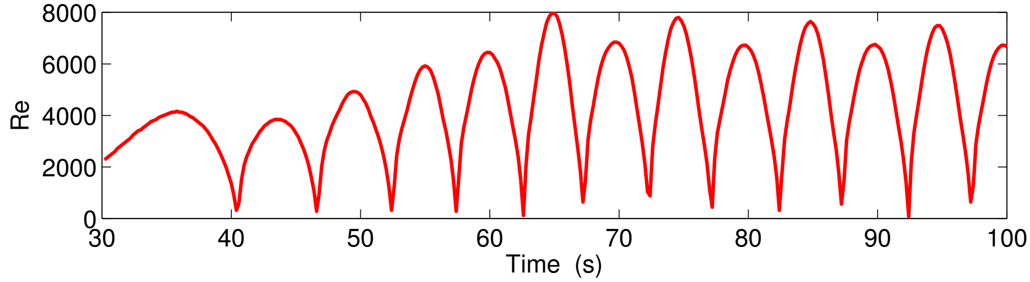

Figure 5.9: Variation of Reynolds number ($Re = \frac{\sqrt{u_{fx}^2+u_{fz}^2}d_{50}}{\nu}$) of the porous flow at x=395m, z=32.5m in the rubble mound

Undoubtedly, the wave induced flow in the rubble mound is turbulent due to that fact the the magnitude of velocity of pore water reaches up to 0.6m/s. Figure 5.9 shows the variation of Reynolds number of the porous flow at the center point (x=395m, z=32.5m) of the rubble mound. It is shown that the Reynolds number of the porous flow in the rubble mound reach up to 8000. Figure 5.10 shows the comparison of pore pressure at the center of rubble mound determined by Biots equation and VARANS equation, respectively. As illustrated in Figure 5.10, the pore pressure at the center of rubble mound is basically the same. It is again indicated that Biots equation can be used for turbulent porous flow when the magnitude of velocity is $O(10^{-1})$m/s or the Reynolds number is less than 10000 in large-scales cases.

It is well known that Biots equation includes consolidation equation, "$u - p$" approximation and fully dynamic equation. For the turbulent porous flow, the consolidation equation is not applicable because the effect of acceleration of pore water can not be ignored under this situation. The "$u - p$" approximation or fully dynamic equation must be used for turbulent porous flow in computation (Gu and Wang, 1991).

5.2.5 Liquefaction in seabed

It has been commonly recognized that the seabed would transiently liquefy under the ocean wave loading. This kind of liquefaction in seabed is attributed to the phase lag of the wave induced dynamic pressure in seabed when the ocean wave propagates on it. The wave-induced dynamic pressure make the effective stresses in seabed variate accordingly. As stated above, the effective stresses and pore pressure in seabed will decrease, based on its initial consolidation state when the wave trough

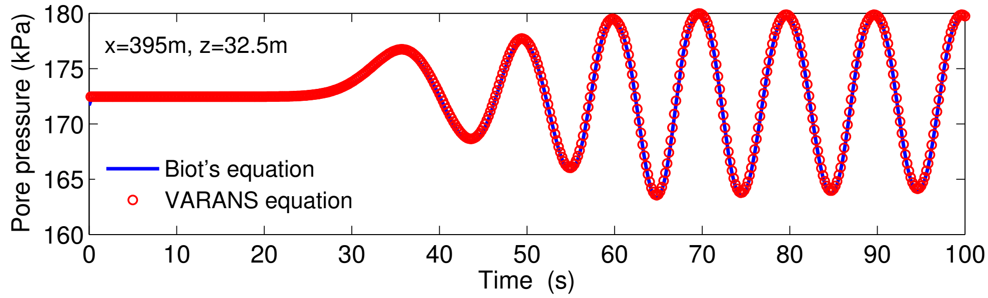

Figure 5.10: Comparison of the pore pressure at x=395m, z=32.5m in the rubble mound determined by the Biot's equation and the VARANS equation

propagates on seabed. When the effective stresses at some regions in seabed decrease to zero, the soil in the region liquefy immediately. As we know, the liquefied seabed can not support any loading. Therefore, the liquefied seabed is a fatal dangerous factor for the marine structures constructed on it. The liquefaction potential of seabed beneath and closed to a marine structure, such as breakwater, is an important issue for coastal engineers for designing and maintaining of the marine structures. The assessment and prediction of the liquefaction potential of seabed under ocean wave loading in the offshore environment is significantly necessary in engineering practice.

The seabed is a kind of porous medium, consisting of soil particles, pore water and air. The soil particles form the skeleton, and the pore water and air occupies the void between the soil particles. When a ocean wave propagating on the seabed, the seabed is applied by a wave induced dynamic pressure. The pore water is driven by the dynamic pressure to flow in seabed. Meanwhile, the seepage force in seabed acting on the soil particles applied by the flowing pore water is formed. The seepage force in seabed is dependent on the gradient of pore pressure in seabed, defined as:

$$j_x = \frac{\partial p_s}{\partial x} \quad \text{and} \quad j_z = \frac{\partial p_s}{\partial z}. \tag{5.3}$$

Figure 5.11 shows the distribution and vectors of seepage force in the region near to seabed surface at time t=73.6s and t=76.8s. From Figure 5.11, it is found that the vertical component of seepage force is much greater than the horizontal component; and the seepage force is upward under wave trough; while it is downward under wave crest. Generally, the liquefaction potential is directly related to the magnitude and direction of the seepage force. The seabed is likely to liquefy when the

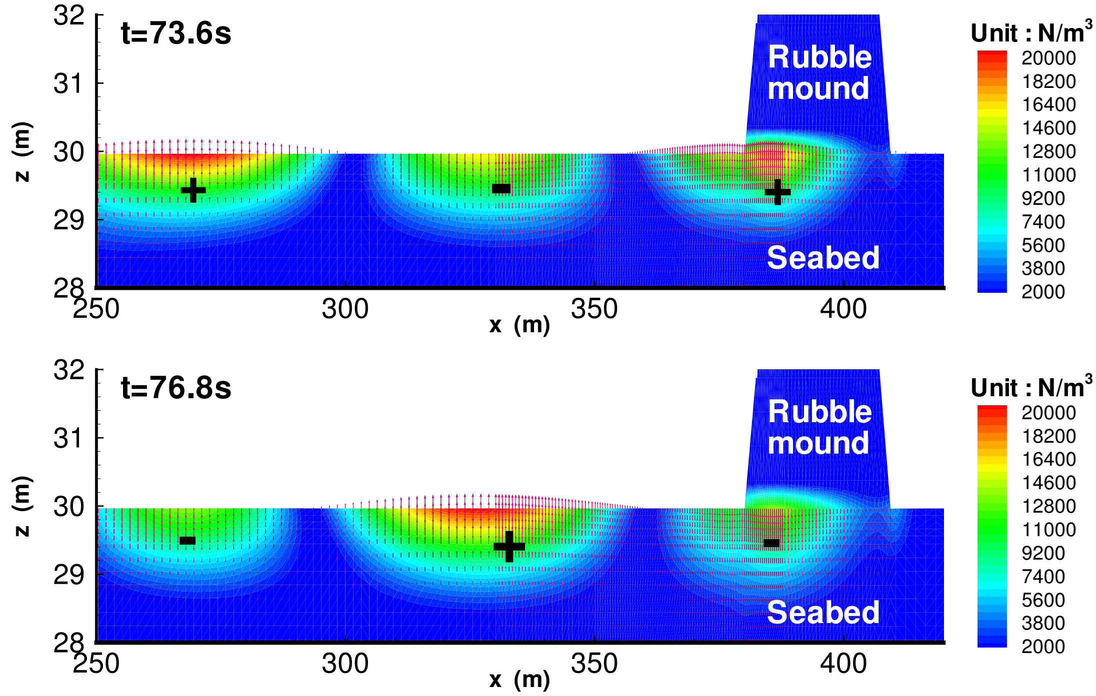

Figure 5.11: The seepage force in seabed under the ocean wave loading at t=73.6s and t=76.8s. "+": upward seepage force, "-": downward seepage force

seepage force is upward because it will decreases the contact effective stresses between soil particles. However, the seabed will absolutely not liquefy when the seepage force is downward because it will increase the contact effective stresses of soil particles.

In this section, in order to investigate the liquefaction properties in seabed under ocean wave loading, the liquefaction criterion proposed by Okusa (1985) are used. It is expressed as:

$$(\gamma_s - \gamma_w)(h - z) \leq \sigma'_{zd}, \tag{5.4}$$

where the γ_s is the saturation unit weight of seabed soil, γ_w is the unit weight of water, z is the depth, σ'_z is the wave induced vertical dynamic effective stress. Actually, the liquefaction criterion (equation (5.4)) means that the seabed will liquefy if the wave induced vertical dynamic effective stress σ'_{zd} (Noted: compressive stress is negative) is equal to or greater than original vertical effective stress $(\gamma_s - \gamma_w)z$. However, the equation (5.4) is only applicable for the cases in which there is no marine structures are constructed on the seabed, because the original vertical effective stress σ'_z in seabed could not be determined using formula $(\gamma_s - \gamma_w)z$ in the region beneath and close to the marine structures. The liquefaction criterion (equation (5.4)) has to be modified for the cases in which marine structures are constructed on seabed:

$$|(\sigma'_z)_{initial}| \leq \sigma'_{zd}, \tag{5.5}$$

where the $(\sigma'_z)_{initial}$ is the vertical effective stress in the initial consolidation state.

Figure 5.12 shows the liquefaction zones in seabed under the ocean wave loading at time t=73.6s and t=76.8s, in which the modified liquefaction criterion (equation (5.5)) are adopted.As illustrated in Figure 5.12, there are two liquefaction zones in the region near the seabed surface at time t=73.6s; they are located at the range of x=250m to x=290m, x=370m to x=380m, respectively. However, there are only one liquefaction zone in the region near the seabed surface at time t=76.8s, which is located at the range of x=310m to x=350m. Comparing the liquefaction zones in Figure 5.12 and the positions of wave trough in Figure 5.4, it is found that the seabed under wave trough indeed has liquefied; while the seabed under wave crest has no potential of liquefaction. In this study, we define the three liquefaction zones as Zone I, Zone II and Zone III, respectively as shown in Figure 5.12.

Due to the fact that the liquefaction Zone II and III are closed to the composite breakwater, especially the Zone III, which is located at the region very near to the lower right corner of the composite breakwater, the stability of the composite breakwater is greatly affected by the properties of the two liquefaction zones. For example, relatively large depth and area of the liquefaction Zone III would result in the failure of the foundation of composite breakwater, which would further lead to the collapse of the composite breakwater. In the following sections, we will focus our attention on the investigation of the variation of liquefaction properties (including depth, width and area) of the liquefaction Zone III and II.

Figure 5.13 and 5.14 illustrate the variation of liquefaction properties of the liquefaction Zone II and III under the ocean wave loading (T=10s, H=3m, d=20m). From Figure 5.13, it is found that the liquefaction depth and area of Zone II are very small when the first wave trough passes through; however, the liquefaction depth and area increase greatly when the second wave trough passing through. After the interference between the incident wave and reflective wave, the liquefaction depth, width and area of the Zone II further increase due to the fact that the wave height is about two times of the incident wave. From Figure 5.13, we know that the maximum liquefaction depth, width and area are

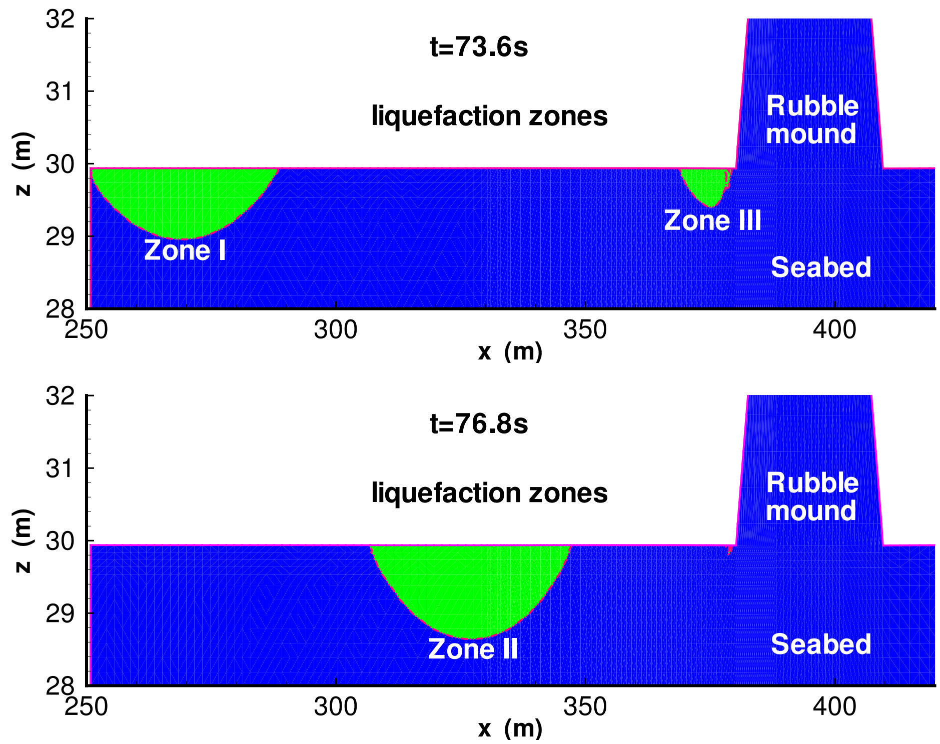

Figure 5.12: The three liquefaction zones in seabed under ocean wave at time t=73.6s and t=76.8s.

about 1.4m, 41.0m and 38.5m^2 which occur at t=79s. Similarly, from Figure 5.14, the same variation trend is observed in liquefaction Zone III which is located at the region closed to the lower left corner of the rubble mound. The liquefaction region is also very small when the first wave trough arrives the composite breakwater; however, the liquefaction depth and area increase greatly when the second wave trough arrives. After the interference between the incident wave and the reflective wave, the depth, width and area of the liquefaction Zone III further increase. The maximum liquefaction depth, width and area of Zone III are about 0.46m, 11.5m and 3.85m^2 which occur at t=74s. Comparing the properties of liquefaction Zone II and Zone III, it is found that the liquefaction depth, width and area of Zone II are much greater than that of Zone III. This phenomenon can be attributed to that the liquefaction Zone III is closed to the composite breakwater; the gravity of composite breakwater can effectively prevent from the enlargement of liquefaction Zone III. Another important phenomenon observed From Figure 5.13 and 5.14 is that the liquefaction in Zone II and Zone III occur alternately. In Figure 5.13 and 5.14, the results predicted by adopting the conventional Biot's equations are also plotted. It is observed that the conventional Biot's equations underestimate the maximum liquefaction

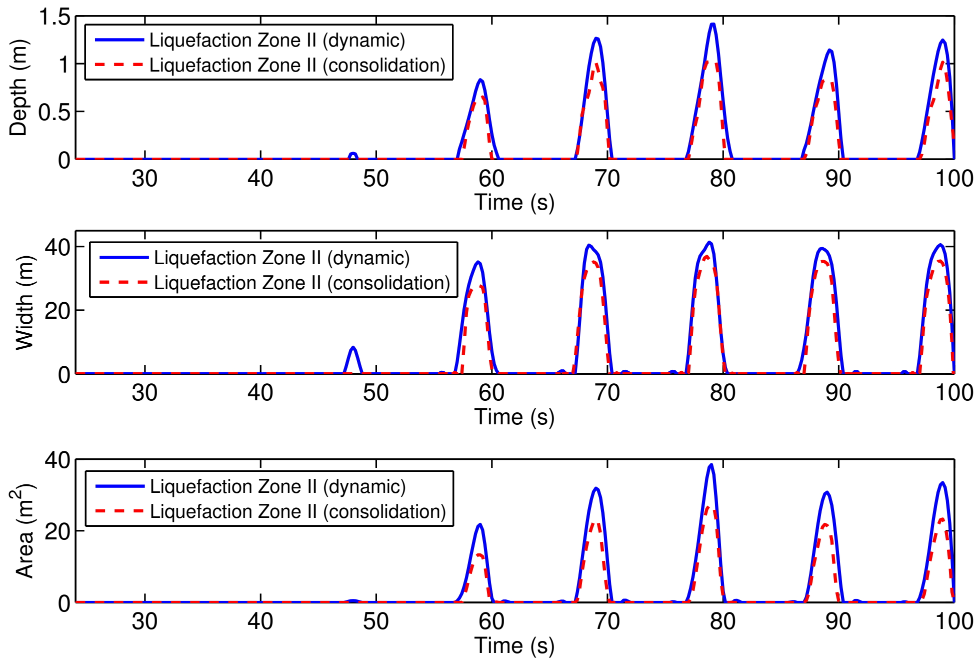

Figure 5.13: The liquefaction properties (depth, width and area) in liquefaction Zone II (the criterion proposed by Okusa (1985) is used)

depth in liquefaction zone II which is far away from the composite breakwater; while, the conventional Biot's equations overestimate the maximum liquefaction depth in liquefaction zone III which is close to the composite breakwater. This comparison sufficiently indicates that the inclusion of the acceleration of pore water and soil particles in the governing equation of porous seabed is necessary when investigating the wave-seabed-structure interactions.

Although the liquefaction Zone III is small relative to Zone II, liquefaction Zone III is very dangerous for the stability of the composite breakwater due to that it is very closed to the foundation of composite breakwater. Liquefied seabed soil is a kind of heavy fluid, it can not support any loading. The liquefaction Zone III is very likely to make the composite breakwater collapse. Therefore, in order to avoid the failure of marine structures due to the liquefied seabed foundation, some engineering measurements should be adopted to protect the seabed foundation from liquefaction if it is predicted that the liquefaction would occur under the ocean wave loading in the offshore environments. For example, replacement of the fine sand with gravel material.

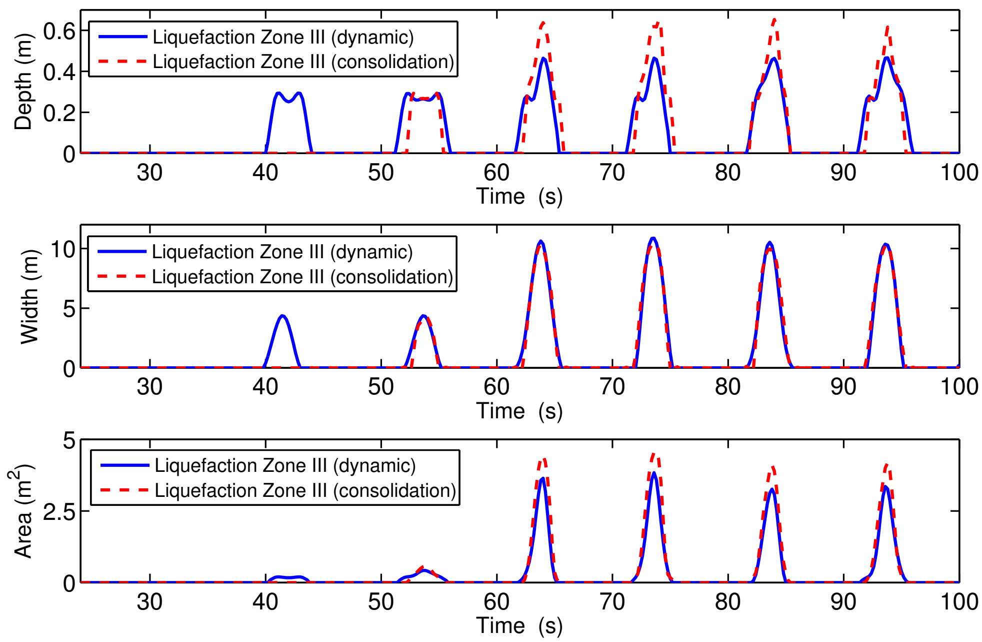

Figure 5.14: The liquefaction properties (depth, width and area) in liquefaction Zone III (the criterion proposed by Okusa (1985) is used)

5.2.6 Effect of the wave characteristics on the liquefaction properties

It is well known that the wave characteristics, including the wave height (H), wave period (T) and water depth (d) affect the liquefaction of seabed greatly when the ocean wave propagates on the seabed. Generally, the seabed is most likely liquefy under the long wave with a high wave height, and propagating in shallow water loading. Greater the wave height, wave period, and shallower the water depth, deeper the maximum liquefaction depth in seabed. In this part, how the wave characteristics affect the liquefaction properties in seabed is investigated parametrically. Due to the fact that the liquefaction Zone III is most dangerous for the stability of composite breakwater, only Zone III is involved in following part.

Figure 5.15 illustrates the effect of the wave characteristics on the liquefaction properties of Zone III. In Figure 5.15, the standard wave condition is T=10s, H=3m, d=20m. When investigating the effect of one of the wave characteristics on the liquefaction properties of Zone III, the other two wave characteristics are kept as same with the standard wave condition; only wave characteristic

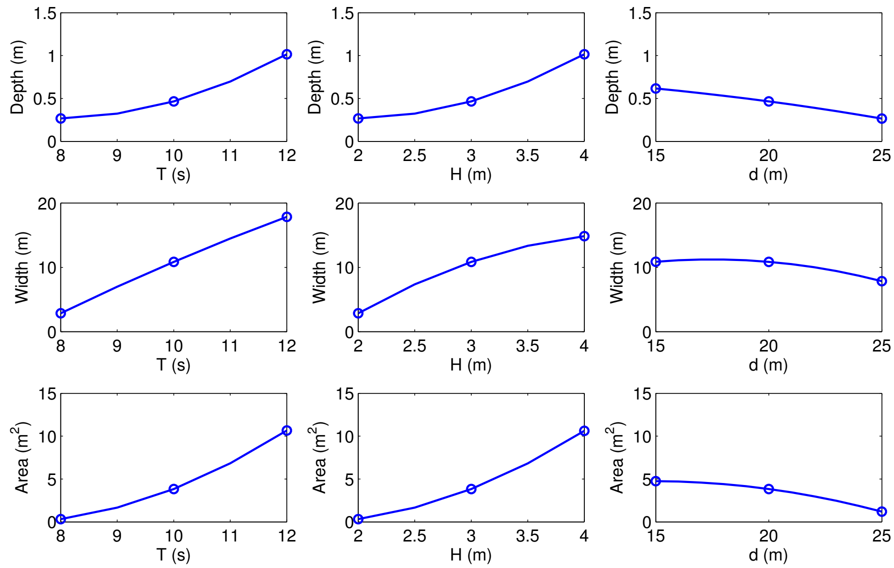

Figure 5.15: The effect of wave characteristics on the liquefaction properties (including maximum liquefaction depth, width and area) of liquefaction Zone III. The standard wave condition is: T=10s, H=3m, d=20m

investigated variates. From Figure 5.15, it is found that the wave characteristics have great effect on the liquefaction properties in seabed. The maximum liquefaction depth, width and area all increase as the wave period or wave height increases; while they all decrease as the water depth increases. This mainly attribute to the long wave or the wave with high height carries more energy, which lead to more intensive interaction between the wave and seabed. On the other side, the deep water can effectively reduce the wave induced dynamic pressure acting on seabed; then it can decrease the liquefaction potential of seabed under the wave loading.

Additionally, the saturation of seabed foundation is also a very important factor affecting the wave induced transient liquefaction. Under the same wave conditions, the dynamic response of a fully saturated seabed foundation is investigated. It is found that the transient liquefaction does not appear in the saturated seabed foundation (Figure 5.16). The reason is attributed to the mechanism of transient liquefaction in sand bed: phase lag of the wave induced pressure in seabed. For unsaturated seabed, the compressibility of pore water $1/\beta$ significantly increase compared to that in fully saturated seabed. The phase lag is positively related to the compressibility of pore water. Therefore, the phase lag along depth in unsaturated seabed is significantly greater than that in saturated seabed.

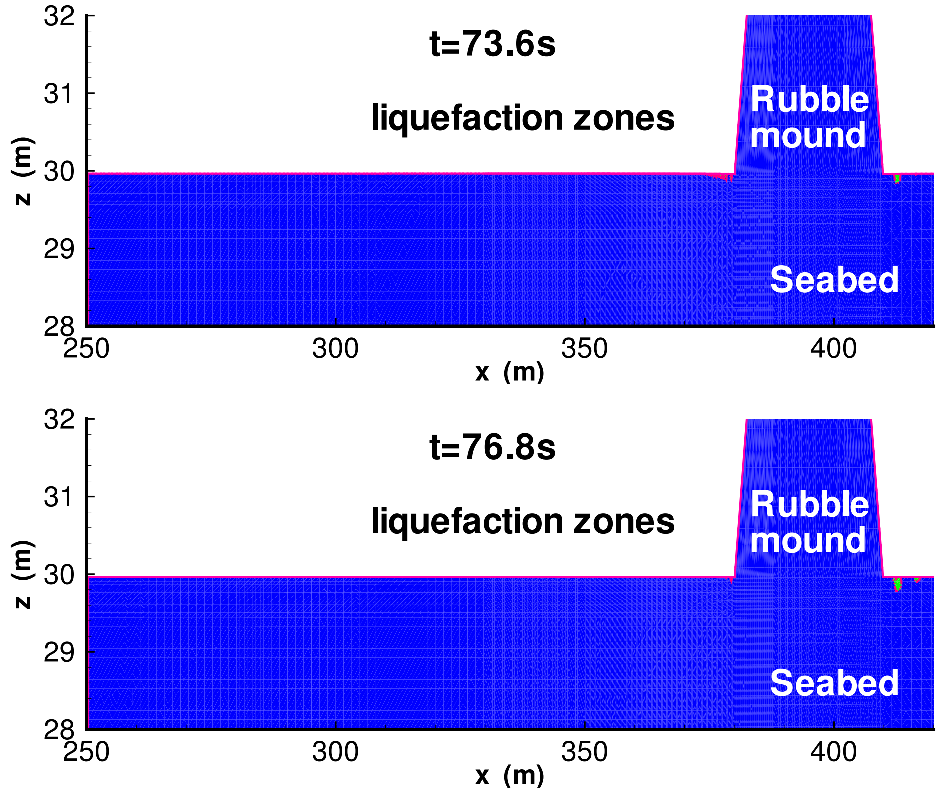

Figure 5.16: There is no liquefaction zones in fully saturated seabed foundation (S_r=100%) under the same ocean wave loading (T=10s, H=3m, d=20m) at time t=73.6s and t=76.8s.

Correspondingly, the wave induced upward seepage force in saturated seabed is much less than that in unsaturated seabed. Therefore, the unsaturated seabed is more likely to transient liquefy under wave loading.

5.2.7 Summary

In this section, the developed integrated model is applied to investigate the response of large-scale elastic seabed and composite breakwater under regular ocean wave loading, and the mechanism of WSSI. Following conclusions are drawn from the computational results:

(1) The wave induced dynamic effective stresses and pore pressure in seabed variate periodically under ocean wave loading based on the initial consolidation state. The seabed in the region where the dynamic effective stresses and pore pressure are negative under wave trough is likely to liquefy.

(2) The composite breakwater moves periodically toward right and left; meanwhile, it swings periodically to right and to left under the ocean wave loading.

(3) The pore pressure in rubble mound is a little higher than that in fluid domain even at the same elevation after consolidation. After the ocean wave arrives, the pore pressure also variates periodically. However, the pore pressure in the region near to the right edge of rubble mound is basically not affected by the ocean wave.

(4) There are intensive fluid exchange and seepage force in the region closed to seabed surface (Figure 5.11). The seepage force is upward under wave trough; and it is downward under wave crest. The upward seepage force makes the effective stresses decrease. When the effective stresses decrease to zero, the seabed in the region liquefy.

(5) There are three liquefaction zones near to the composite breakwater (shown in Figure 5.12) under ocean wave loading. The liquefaction in Zone I ,III and the Zone II occurs alternately. Among them, the liquefaction Zone III is smallest, but it is most dangerous for the stability of composite breakwater. It would lead to the collapse of the composite breakwater.

(6) The wave characteristics (T,H and d) greatly affect the liquefaction properties of Zone I, II and III. The maximum liquefaction depth, width and area increase as the wave period or wave height increases; while they all decrease as the wave depth increases. The transient liquefaction is unlikely to appear in fully saturated seabed foundation.

5.3 Elasto-plastic seabed foundation[4*]

In this section, the dynamic response of a composite breakwater and an elasto-plastic seabed foundation under wave loading is investigated by adopting the integrated model PORO-WSSI II. In the analysis, the composite breakwater is treated as elastic medium. The elsto-plastic model Paster-Zienkiewicz Model Mark-III is adopted for porous seabed. Total 16065 4-nodes iso-parametric elements are used to discretize the computational domain. The property parameters for the elasto-plastic seabed are the same as those used in Zienkiewicz et al. (1999) which is determined based on a series of tests for Nevada dense sand and Nevada fine sand. All the properties of seabed and composite breakwater are listed in Table 5.2. Beside the parametric study, the standard parameters for soil and wave are: k=1.0 $\times$ 10^{-5}m/s, S_r=98%, H=3.0m, T=8.0s. The Nevada fine sand only used in the parametric study.

5.3.1 Computional domain and Boundary conditions

The Computational domain is shown in Figure 5.17. The seabed foundation includes a flat part (-300m to -100m) and a sloped part (-100m to 550m). The thickness of the flat part is 20m. The gradient of the sloped part of the seabed foundation is 2:100. The composite breakwater is built on the sloped part (-200m to -236m). The dimension of the composite breakwater is illustrated in Figure 5.17. The water depth on the flat seabed foundation is 15m. In numerical calculation, following boundary conditions are applied:

(1) The bottom of seabed foundation is treated as rigid and impermeable.

$$u_s = w_s = 0 \quad \text{and} \quad \frac{\partial p_s}{\partial z} = 0 \quad \text{at } z\text{=0m.} \tag{5.6}$$

(2) The two lateral sides of computational domain are fixed in horizontal direction.

$$u_s = 0 \quad \text{at} \quad x\text{=-300m} \quad \text{and} \quad x\text{=850m.} \tag{5.7}$$

(3) The surface of seabed foundation and the composite breakwater are free to move. But the pressure including the hydrostatic pressure and wave induced dynamic pressure, is applied to the surface of seabed and the outer surface of composite breakwater. In this section, this pressure is determined by the wave model. The pressure is applied to the seabed surface and to the outer surface of the composite breakwater through the developed data exchange port.

[4*]Contents in this section are being prepared in a manuscript for journal paper.

Table 5.2: Properties and parameters used for seabed foundation, composite breakwater and wave in analysis and parametric study (Zienkiewicz et al., 1999)

Parameters for PZIII model (Nevada sand)			
Iterm	Nevada dense sand	Nevada loose sand	Unit
K_{evo}	2,000	770	[kPa]
G_{eso}	2,600	1155	[kPa]
p'_0	4	4	[kPa]
M_g	1.32	1.15	-
M_f	1.3	1.035	-
α_f	0.45	0.45	-
α_g	0.45	0.45	-
β_0	4.2	4.2	-
β_1	0.2	0.2	-
H_0	750	600	-
H_{U0}	40,000	40,000	[kPa]
γ_u	2.0	2.0	-
γ_{DM}	4.0	4.0	-
Soil characteristics			
Soil permeability		$1.0{\times}10^{-2}$, $1.0{\times}10^{-5}$ or $1.0{\times}10^{-7}$	[m/sec]
Poisson's ratio		0.3333	
Porosity		0.25	
Saturation		95, 98 or 100	%
Breakwater			
	Caisson	Rubble mound	
Soil permeability	1.0×10^{-10}	2.0×10^{-1}	[m/sec]
Poisson's ratio	0.25	0.3333	
Porosity	0.1	0.35	
Saturation	0	99	%
Young's modulus	1.0×10^{7}	1.0×10^{6}	[Mpa]
Wave characteristics			
Wave height		2.0, 3.0, 4.0	[m]
Wave period		6.0, 8.0, 10.0	[s]
Water depth		15	[m]

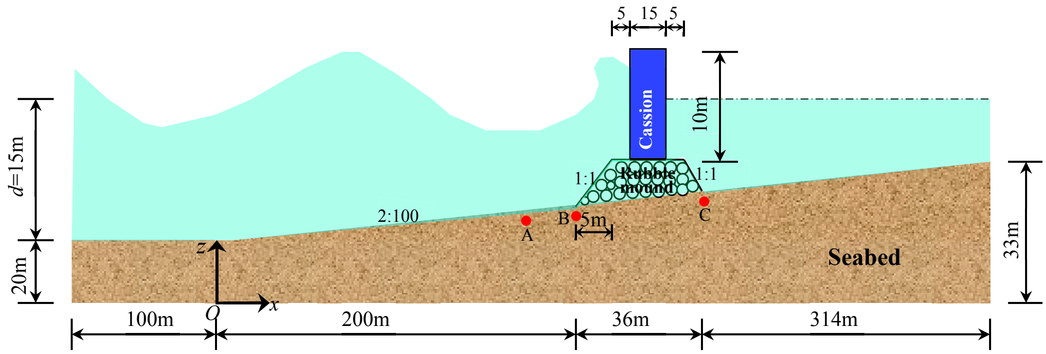

Figure 5.17: The schematic graph of the computational domain in this study, a composite breakwater is built on the sloped seabed foundation. A: x=170m, z=22.9m; B: x=200m, z=23.5m; C: x=236m, z=24.2m.

5.3.2 Wave field in front of composite breakwater

The wave model in PORO-WSSI II is used to govern the generation and propagation of wave on porous seabed, and also the interaction with seabed foundation and marine structures. In this section, the seabed foundation and rubble mound are treated as permeable medium. It means there is fluid exchange between the sea water and the pore water in seabed foundation or rubble mound at their interfaces. Due to the fact that the caisson is made of concrete, the caisson is considered to be an impermeable structure resting on the rubble mound.

Figure 5.18 is a typical graph that shows the interactions between the ocean wave, seabed and composite breakwater at time t=250s. In the wave model, the wave maker is placed over the flat part of seabed foundation. The ocean wave is generated by the wave maker based on the given wave height H=3m, period T=8s and water depth d=15m. After successfully being generated, the ocean wave propagates to the composite breakwater. Due to the sloped seabed foundation makes the water depth gradually decrease, the wave characteristics on the sloped seabed foundation is different with the given wave conditions at the wave maker. The wave height increases; meanwhile, the wave length decreases. Furthermore, the wave damping also exists due to the porous seabed. When the wave arrives at the composite breakwater, the wave partly reflects. The reflected wave interferes with the incident wave in front of the composite breakwater, making the wave height nearly double of the original wave height. Another small part of the wave energy drive the pore water to go through the rubble mound. It is easy to find that the wave energy is damped in the process of propagation

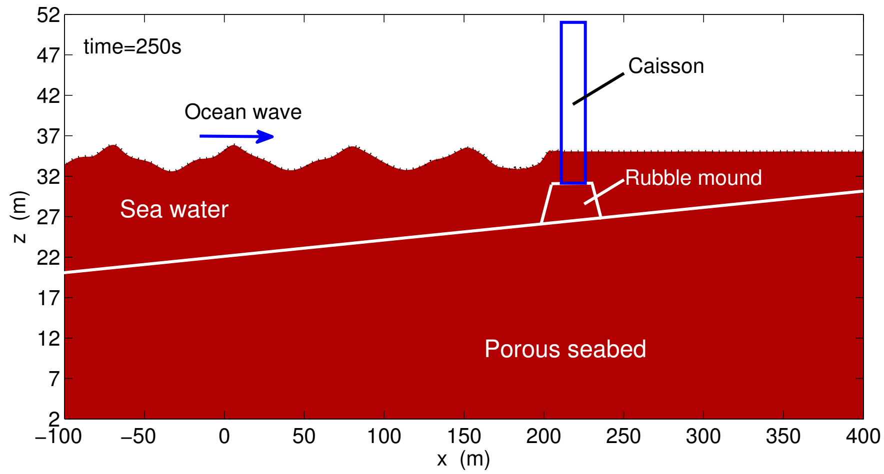

Figure 5.18: The wave profile in front of the composite breakwater at time t=250s (H=3m, T=8s, d=15m)

and interaction with porous seabed and marine structures. The interaction between the wave, porous seabed and rubble mound has been fully taken into consideration in the wave field. The flow field of sea water and the pore water in seabed and rubble mound is fully coupled field.

5.3.3 Dynamic response of composite breakwater and seabed foundation

In the real offshore environment, the seabed foundation generally has experienced the consolidation process under hydrostatic pressure and self-gravity in the geological history. There is no excess pore pressure in the seabed foundation. In this study, in order to simulate the interaction between the ocean wave, seabed and marine structures, as true as possible, the consolidation state of seabed foundation under hydrostatic pressure and the weight of composite breakwater is firstly determined, same as that in Part 5.2.2. This consolidation state is taken as the initial condition for the analysis of dynamic response of poro-elasto-plastic seabed foundation under ocean wave loading.

In coupling analysis, the pressure acting on seabed foundation and composite breakwater determined by wave model is applied to the soil model as the boundary conditions, to investigate the dynamic responses of the composite breakwater and elasto-plastic seabed foundation system.

Figure 5.19 illustrates the displacements of the caisson (x=200m, z=51m) during the process of wave, seabed foundation and composite breakwater interaction. The results based on both elastic and elasto-plastic seabed are shown. It can be easily observed that the displacements of caisson are

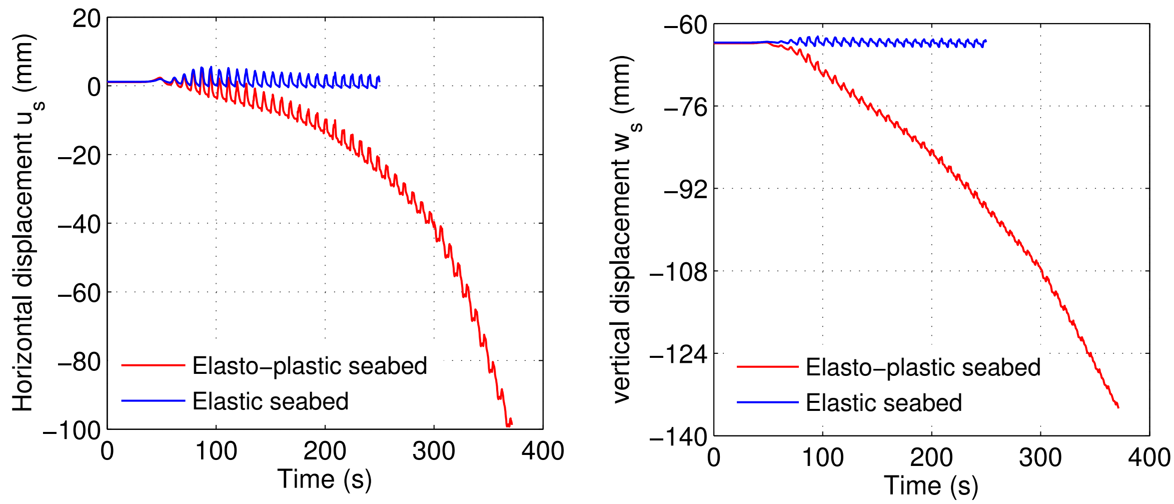

Figure 5.19: The horizontal (left figure) and vertical (right figure) displacements of caisson under the wave loading. It is shown that the breakwater built on elasto-plastic seabed foundation is tilting in the process of wave loading.

completely different for elastic, than those for elasto-plastic seabed foundation. For elastic seabed foundation, the caisson vibrates periodically under the wave loading, while in the case of elasto-plastic seabed foundation, the caisson continuously moves toward left and downward. It indicates that the elasto-plastic seabed foundation is subsiding under the wave loading due to the compaction of soil particls. Additionally, the tilting of caisson to the left side has no tendency of convergence. At the late stage of wave loading, the dumping of the caisson becomes faster and faster. The composite breakwater nearly tends to collapse.

Under the wave loading, the pore pressure in elasto-plastic seabed foundation increases continuously. This causes a reduction of the effective stresses between the soil particles. The reduction of effective stresses directly make the stiffness of seabed foundation significantly decrease, known as the softening. The bearing capacity of the seabed foundation is accordingly reduced. When the wave-induced excess pore pressure in seabed foundation is large enough, making the contact effective stresses becomes 0 (known as liquefaction), the seabed foundation completely loses its bearing capacity, behaving like a liquid. At this moment, the composite breakwater will collapse. Therefore, the prevention of the occurence of liquefaction in engineering design practice is necessary. For elastic seabed foundation, there is no build-up of pore pressure in the seabed foundation under wave loading.

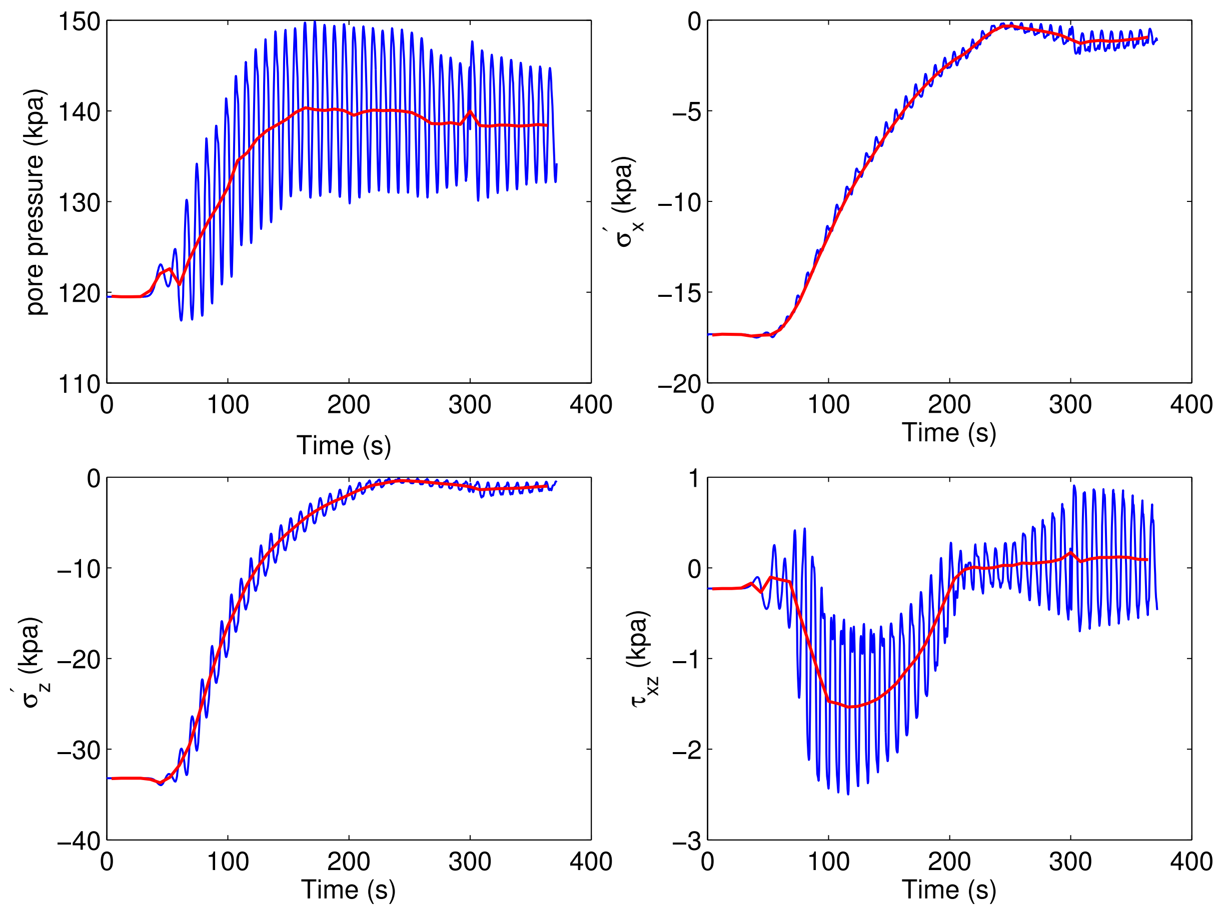

Figure 5.20: The build-up of pore pressure, reduction of effective stresses in seabed at A (x=170m, z=22.9m) which is at the left side of composite breakwater. Note: σ'_x, σ'_z: effective stresses, τ_{xz}: shear stress.

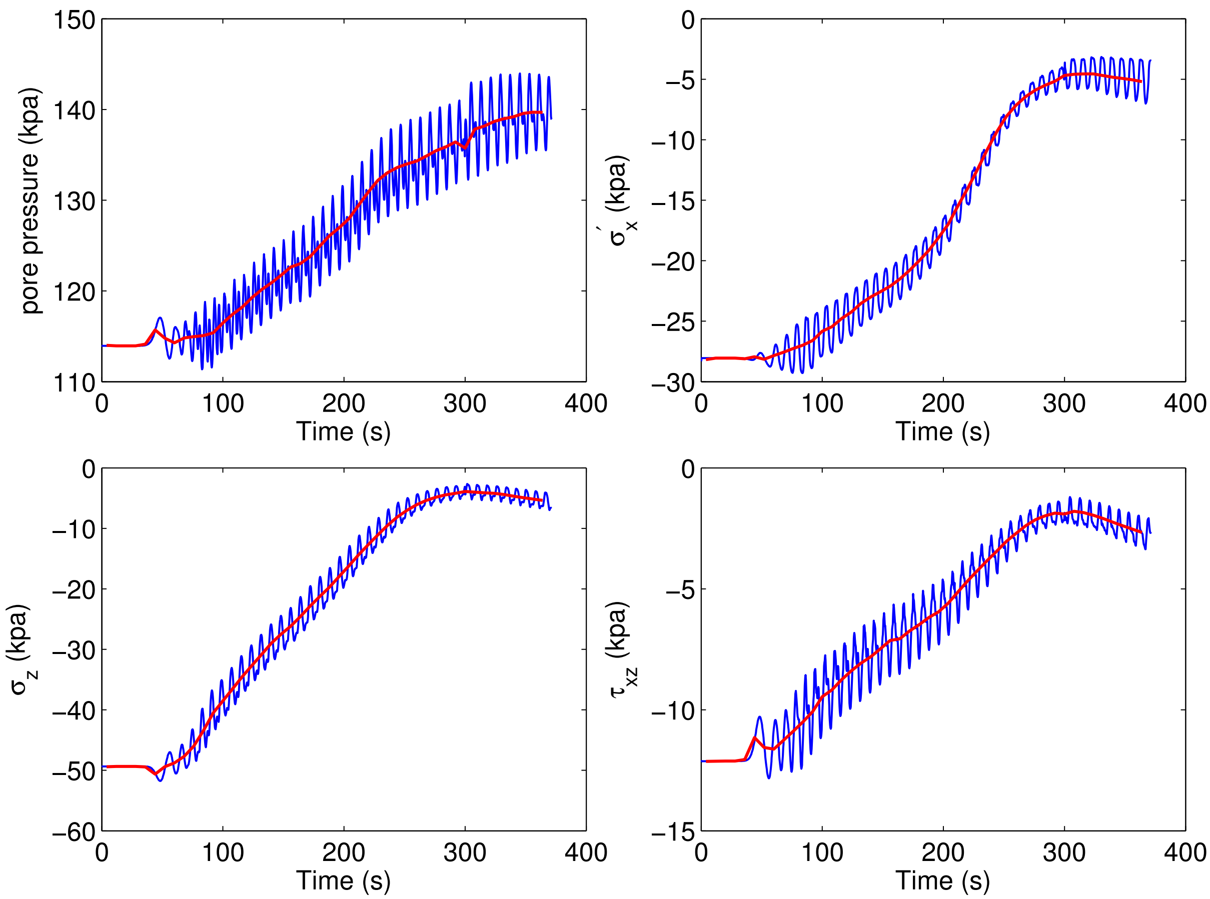

Figure 5.21: The build-up of pore pressure, reduction of effective stresses in seabed at B (x=200m, z=23.5m) which is under the left foot of composite breakwater. Note: σ'_x, σ'_z: effective stresses, τ_{xz}: shear stress.

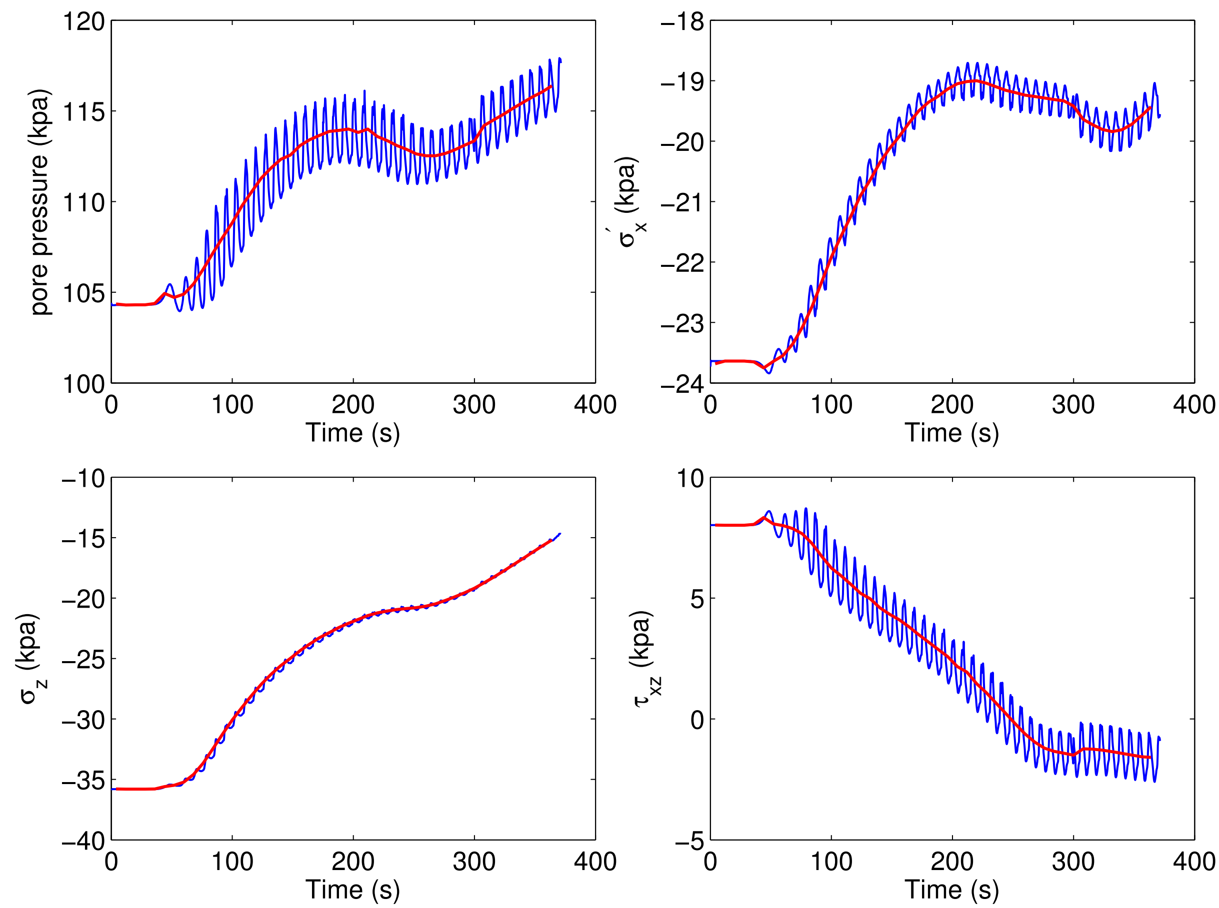

Figure 5.22: The build-up of pore pressure, reduction of effective stresses in seabed at C (x=236m, z=24.2m) which is under the right foot of composite breakwater. Note: σ'_x, σ'_z: effective stresses, τ_{xz}: shear stress.

Figure 5.20, 5.21 and 5.22 demonstrate the process of pore pressure built-up, effective stress reduction at three typical positions (x=170m, z=22.9m), (x=200m, z=23.5m) and (x=236m, z=24.2m). From the three figures, it is observed that the pore pressure in seabed foundation has two components: oscillatory pore pressure and residual pore pressure. The residual pore pressure makes the effective stresses between soil particles to reduce; the oscillatory pore pressure makes the effective stresses vary accordingly. In Figure 5.20, it is found that the wave-induced residual pore pressure doesn't increase continuously, but nearly is a constant after many wave loading cycle. It is also observed that the magnitude of effective stresses σ'_x and σ'_z gradually decrease accompanying the pore pressure build-up. At time t=250s, the σ'_x and σ'_z are nearly 0. It is indicated that position (x=170m, z=22.9m) is nearly liquefied at time t=250s under the wave loading. Another interesting phenomenon is that the shear stress τ_{xz} is also nearly 0 at the late stage of wave loading. This attributes to the fact that the contact effective stress between soil particles is very small in the zone nearly liquefied; naturally, the nearly liquefied soil can't bear a large shear stress.

In Figure 5.21, it is found that the magnitude of effective stresses σ'_x, σ'_z and τ_{xz} are also decreasing as the pore pressure builds up. However, the σ'_x, σ'_z and τ_{xz} don't approach 0. It is indicated that the seabed soil at position (x=200m, z=23.5m) doesn't liquefy under wave loading. This findings are different with that at position (x=170m, z=22.9m). The main reason is that the stress status at position (x=200m, z=23.5m) which is under the left foot of composite breakwater is greatly affected by the weight of composite breakwater. The weight of composite breakwater compresses the seabed foundation, making the effective stresses in the zone under the composite breakwater increase greatly in the consolidation status. Under the wave loading, the compression of composite breakwater also make the contact effective stresses in seabed foundation is much more difficult to become zero. If the effective stresses at this position become 0, the seabed foundation would liquefy; the marine structures would collapse.

In Figure 5.22, the pore pressure build-up at position (x=236m, z=24.2m), which is under the right foot of composite breakwater, is shown. Although the position (x=236m, z=24.2m) is located at the right side of caisson, there is basically no direct wave loading on the seabed surface; the pore pressure build up still occurs. This could be attributed to the dissipation of excess pore pressure in seabed foundation from high pressure zone to low pressure zone. Under the wave loading, the pore pressure

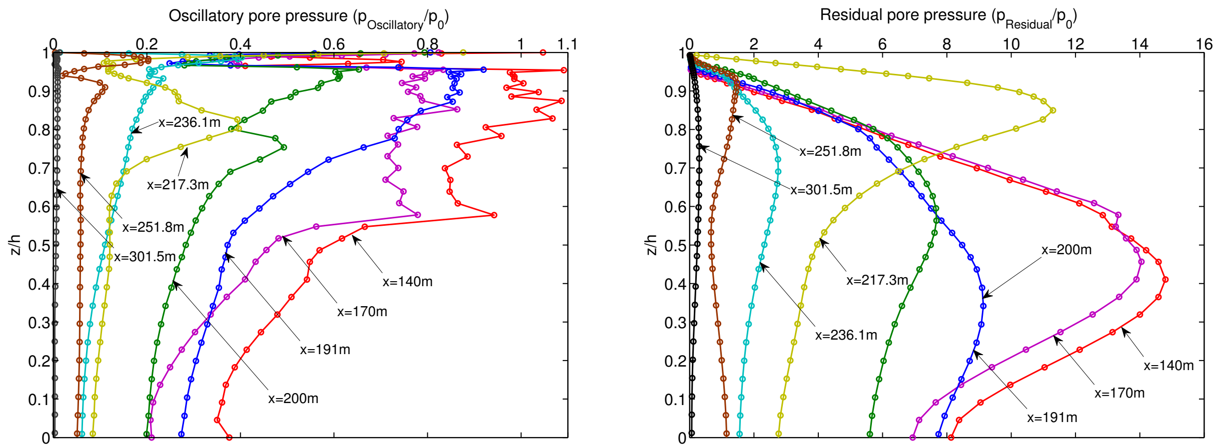

(a) Oscillatory pore pressure

(b) Residual pore pressure

Figure 5.23: Distribution of the wave-induced oscillatory and residual pore pressure in the elasto-plastic seabed foundation along seabed depth at positions *x*=140m, *x*=170m, *x*=200m, *x*=217.3m, *x*=236m at time *t*=371.5s.

in the left part of seabed is much higher than that in the right part of seabed. The pore water permeates through the seabed foundation from the zone located at left side of composite breakwater to the zone located at the right part of composite breakwater. It directly results in the generation of excess pore pressure in the zone located at the right side of composite breakwater. However, the influence range in the right part is also limited. The σ'_x, σ'_z also don't approach 0 at the late stage of wave loading. It is interesting to note that the shear stress τ_{xz} changes its direction (from positive to negative) at about *t*=240s. This is due to the excessive tilting of the composite breakwater.

As mentioned above, the pore pressure in seabed foundation consists of oscillatory pore pressure and residual pore pressure. It is meaningful to understand the distribution of the two kinds of pore pressure in the seabed foundation. Figure 5.23 shows the distribution of oscillatory and residual pore pressure along depth on several typical lines in seabed foundation at time t/T=46.4. From Figure 5.23, it is observed that the oscillatory pore pressure in the upper seabed is generally greater than that in the lower seabed on the same lines; and the oscillatory pore pressure in left part of seabed is generally greater than that in the right part of seabed. For the residual pore pressure, the distribution is significantly different. The residual pore pressure in lower seabed is generally much greater than that in upper seabed. However,the maximum residual pore pressure is not found at the bottom of seabed foundation. The distribution of residual pore pressure on line *x*=217.3m which is the middle line of composite breakwater, is significantly different with the distributions on other lines. The maximum residual pore pressure is found in the upper seabed. This kind of distribution of residual pore pressure is mainly related to the drainage condition. In the seabed foundation under the composite breakwater, the drainage of water is much more difficult relatively. Similar with that for oscillatory pore pressure, the residual pore pressure in the left part of seabed is also greater than that in the right part of seabed. This also is due to the fact that the left part of seabed is directly loaded by the wave loading, while, the right part of seabed generates the excess pore pressure depending on the pressure dissipation and seepage flow from the left part to the right part of seabed. From the distribution of oscillatory/residual pore pressure on the line x=301.5m, it is found that the effect of pore pressure build-up in the left part of seabed on the generation of excess pore pressure in the right part of seabed basically disappears in the zone far away from the composite breakwater.

5.3.4 Residual liquefaction potential

As analyzed in above section, the pore pressure in elasto-plastic seabed foundation builds up under the wave loading. This results in the reduction of the contact effective stresses between the soil particles. Correspondingly, the seabed foundation soil is softening in this process. When the contact effective stresses between soil particles become zero, the liquefaction occurs. Then, the liquefied seabed behavior like a liquid, and lose its bearing capacity. The marine structures built on the liquefied seabed foundation will collapse. The liquefaction of seabed foundation under wave loading is a serious problem that the coastal engineers have to face in structure design and maintaining. In this section, attention is paid to investigate the wave induced residual liquefaction potential in the elasto-plastic seabed foundation on which a composite breakwater is constructed.

The 1D liquefaction criterion based on the initial and wave induced vertical effective stress σ'_{z0} and σ'_{zd} proposed by Okusa (1985) is used to evaluate the residual liquefaction potential:

$$L_{potential} = \frac{\sigma'_{zd}}{|\sigma'_{z0}|}, \tag{5.8}$$

when the $L_{potential}$ is greater than or equal to 1.0 at a position, the soil is completely liquefied at that position.

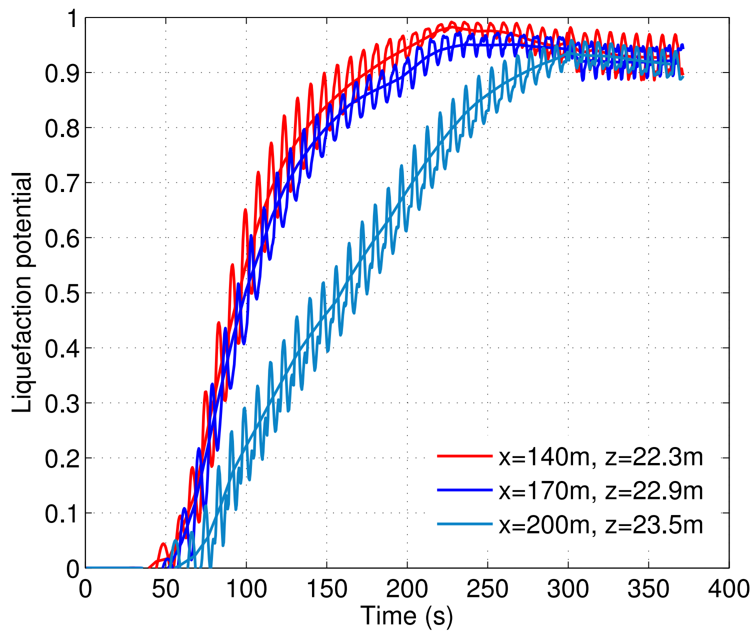

Figure 5.24: The historic curve of liquefaction potential at points (x=140m, z=22.5m), (x=170m, z=22.9m) and (x=200m, z=23.5m)

By adopting the definition of liquefaction potential in Equation (5.8), the liquefaction potential of elasto-plastic seabed foundation under wave loading is analyzed. Figure 5.24 demonstrates the historic curves of liquefaction potential at three typical positions (x=140m, z=22.3m), (x=170m, z=22.9m) and (x=200m, z=23.5m) in the process of wave loading. From Figure 5.24, it is found that the liquefaction potential in seabed foundation under wave loading increase gradually to its peak value; then it basically keeps at a constant or decreases a little. The existence of a peak liquefaction potential would attribute to the fact that the pore pressure build-up and pore pressure dissipation occur simultaneously in seabed foundation. Due to the fact that the three points chosen are all near to the seabed surface, the effect of pore pressure dissipation can't be ignored. When the rate of dissipation is greater than the rate of build up, the pore pressure will decrease. Then the contact effective stress between soil particles increases. In this case, the liquefaction potential certainly will also decrease. At the position (x=200m, z=23.5m), the initial effective stresses are relatively large due to the compression of the composite breakwater; the liquefaction potential is relatively small comparing with other two positions at the early stage of wave loading. Also due to the compression of the composite

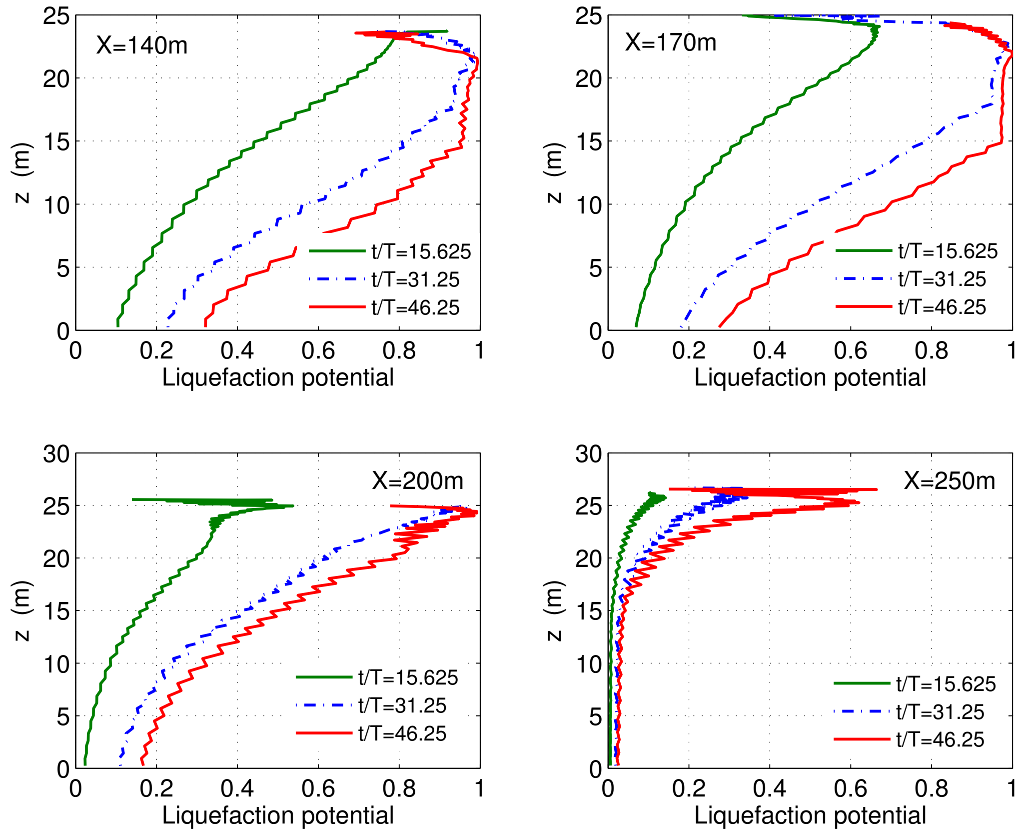

Figure 5.25: Wave-induced distribution of liquefaction potential on lines *x*=140m, *x*=170m, *x*=200m and *x*=250m

breakwater, the growth rate of liquefaction potential is also significantly less than that of other two positions. In the late stage of wave loading, the liquefaction potential is over 0.9 at position (*x*=200m, *z*=23.5m). It is nearly liquefied. This could be a reasonable explanation of the non-convergence of the composite breakwater's displacements. Actually, it is found that the breakwater is tilting faster and faster at the late stage of wave loading.

Figure 5.25 shows the distribution of liquefaction potential along the depth on several typical lines *x*=140m, *x*=170m, *x*=200m and *x*=250m. In Figure 5.25, it is observed that the liquefaction potential in seabed foundation increases with the time of wave loading. This is mainly related to the fact that the residual pore pressure becomes greater and greater in the process of wave loading. Due to that the lines *x*=140m, *x*=170m are far away from the composite, the effect of composite breakwater's compression on the effective stresses on the two lines is insignificant; the liquefaction potential on lines x=140m, x=170m is generally greater than that on line x=200m which is under the composite breakwater at the same time. Due to the fact that the right part of seabed foundation is not acted directly by the wave loading, the liquefaction potential in the right part of seabed foundation is relatively small comparing with that in the left part of seabed foundation. Here, it is interesting to note that the liquefaction potential in the zone near to seabed surface decreases sharply. This phenomenon also can be explained by the fact that the build-up and dissipation of pore pressure occur simultaneously in seabed foundation under wave loading. In the zone near to the seabed surface, the drainage distance is short; and the drainage is relatively unobstructed. The residual pore pressure is difficult to accumulate; and the pore pressure is easy to dissipate. Therefore, the reduction of contact effective stresses is small. The sharp decrease of the liquefaction potential is reasonable in the zones near to the seabed surface.

5.3.5 Parametric study

In the above analysis, the Nevada dense sand with standard parameters (k=1.0×10^{-5}m/s, S_r=98%, H=3.0m, T=8.0s, d=15m) are used for the seabed foundation. It is necessary to investigate how the parameters affect pore pressure build-up and the liquefaction potential in seabed foundation under wave loading. In this section, a parametric study is conducted to investigate the effect of soil properties and wave characteristics on the pore pressure build-up and the liquefaction potential. Here, the position (x=170m, z=22.9m) is taken as the representative point to demonstrate the effect of parameters.

Figure 5.26 demonstrates the effect of wave height and period on the liquefaction potential at (x=170m, z=22.9m) in the seabed foundation under wave loading. It is observed that the wave height and wave period indeed have a significant effect on the liquefaction potential in seabed foundation. The higher the wave height or the longer the wave period, the faster the pore pressure build-up, and the greater the growth rate of liquefaction potential in the seabed foundation. This phenomenon would mainly be attributed to the fact that the waves with higher height and/or longer period carries more energy, and make the wave loading acting on seabed is greater than others. The time for liquefaction potential variating from zero to the its peak value is relatively shorter. The existence of the peak

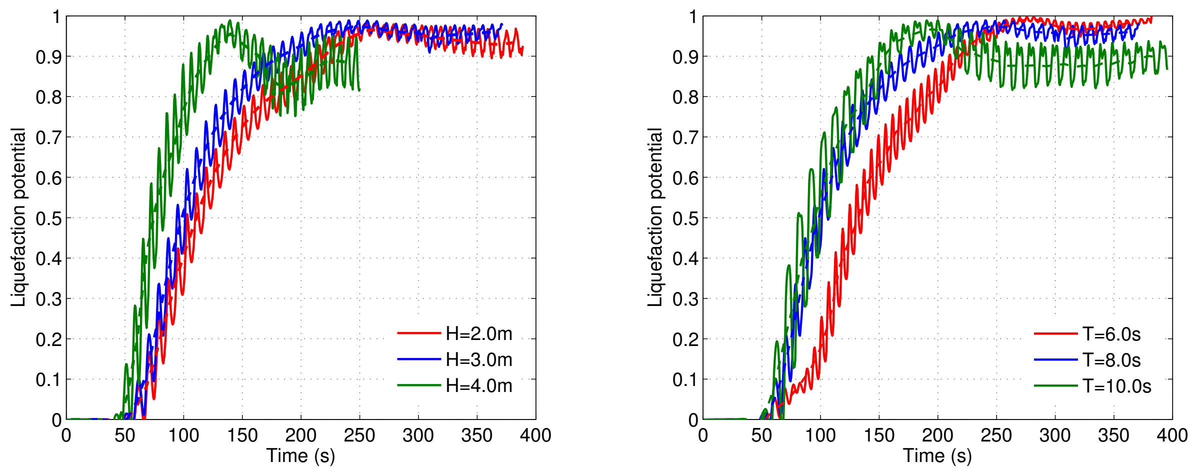

(a) wave height (b) wave period

Figure 5.26: The effect of wave height (a) and period (b) on the liquefaction potential at (x=170m, z=22.9m) in seabed foundation under wave loading

value of liquefaction potential has been explained in the former section. There is no such a peak value for the liquefaction potential in lower part of seabed foundation. After long term wave loading, the liquefaction potential of the seabed foundation with higher height and/or longer period is instead smaller than that under the wave loading with lower height and/or shorter period .

Figure 5.27 demonstrates the effect of permeability and saturation of seabed soil on the liquefaction potential at (x=170m, z=22.9m) in the seabed foundation under wave loading. From Figure 5.27, we can conclude that the permeability of soil is the most important parameter affecting the liquefaction of soil. It is found that it is difficult for the pore pressure to accumulate in the soil having large permeability. Therefore, the soil having large permeability, such as coarse sand, is unlikely to liquefy under wave loading due to that the residual pore pressure is easy to dissipate. It is also found that the saturation of soil also could significantly affect the liquefaction potential. Compared with saturated soil, the unsaturated soil is more likely to liquefy. The growth rate of liquefaction potential is negatively related to the saturation of soil.

5.3.6 Summary

In this section, adopting the integrated model PORO-WSSI II, the dynamic response of composite breakwater and its elasto-plastic seabed foundation under wave loading is investigated. The Pastor-

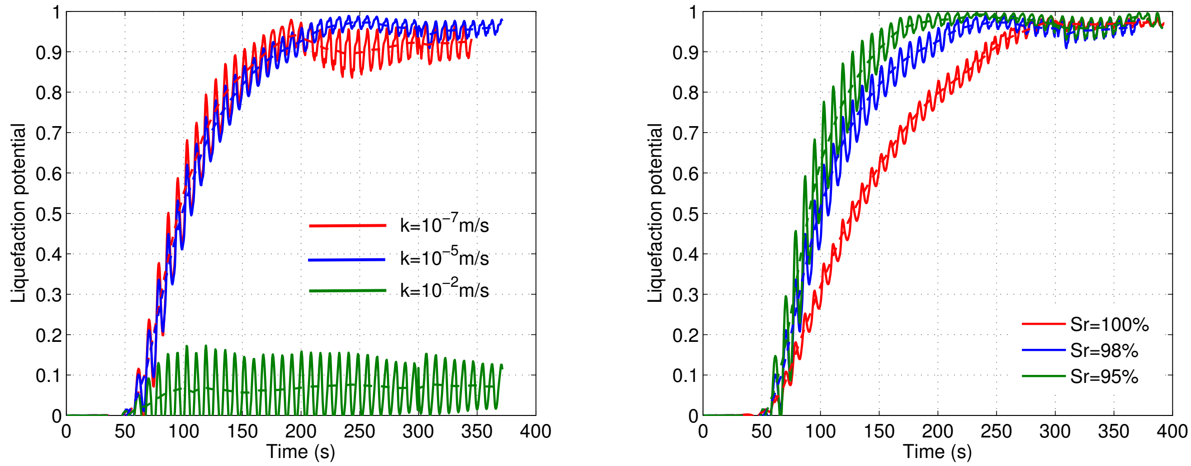

(a) soil permeability (b) soil saturation

Figure 5.27: The effect of permeability (a) and saturation (b) of seabed soil on the liquefaction potential at (x=170m, z=22.9m) in seabed foundation under wave loading

Zienkiewicz Model Mark-III model is used to model the elasto-plastic behavior of seabed foundation in analysis. Based on the results presented, the following conclusions are drawn:

(1) It is necessary and important to determine the initial consolidation status of seabed foundation under hydrostatic pressure and marine structures. This consolidation status of seabed foundation should be taken as the initial boundary condition for the analysis of dynamic response of composite breakwater and seabed foundation under wave loading. At the mean time, the initial prevention of the liquefaction potential is also determined.

(2) Under the wave loading, the pore pressure in elasto-plastic seabed foundation increases, making the contact effective stresses between soil particles decrease. It results in the softening of seabed foundation. The excessive settlement and tilting occur for the marine structures built on the seabed foundation. This is a harmful factor for the overall stability of marine structures in engineering.

(3) In the zone far away from the marine structures, the effective stresses status is basically not affected by the compression of marine structures. The pore pressure could sufficiently build up. At the late stage of wave loading, the effective stresses σ'_x, σ'_z and shear stress τ_{xz} could approach the zero stress status. The seabed foundation could liquefy within a certain depth.

However, in the zone near to marine structures, due to the compression of marine structures, the initial effective stresses are relatively large; and the contact effective stresses σ'_x, σ'_z and shear stress τ_{xz} is unlikely to become zero. Therefore, in the zone near to marine structures, the seabed foundation is more difficult to liquefy under loading.

(4) The pore pressure in seabed foundation, which includes two components: oscillatory and residual pressure. The oscillatory pore pressure in upper seabed is generally greater than that in lower seabed. Oppositely, the residual pore pressure in lower seabed is greater than the in upper seabed. Due to the fact that the right part of seabed is not directly acted by the wave loading, the oscillatory/residual pore pressure in the right part of seabed is much smaller than that in the left part of seabed. The generation of oscillatory and residual pore pressure in right part of seabed indicates that the pore water moves from the left part to the right part of seabed driven by the pressure gradient.

(5) There is a peak value for the liquefaction potential in the zone near to the seabed surface. This is due to the build up and dissipation of pore pressure that occurring simultaneously under wave loading. At the late stage of wave loading, the rate of dissipation is greater than the rate of build-up of pore pressure, the liquefaction potential decreases correspondingly. Due to that the drainage is relatively unobstructed, and the drainage distance is short in the zone near to seabed surface, the liquefaction potential decrease sharply in the zone near to the seabed surface.

(6) The parametric study indicates that the waves with higher height and longer period make the growth rate of liquefaction potential larger at the early stage of wave loading. However, the final liquefaction potential is less than that if loaded by the waves with lower height and shorter period. The permeability of soil is the most important parameter affecting the pore pressure build-up and liquefaction potential. The saturation of soil also has significant effect on the liquefaction potential.

Chapter 6

3D Wave-Seabed-Caisson breakwater Interaction: PORO-WSSI III

6.1 Introduction

In the past two decades, a number of investigations have been conducted on the problem of wave-seabed-breakwater interaction (see 2.4 in Chapter *Literature Review*). A series of analytical solutions have been proposed (Tsai, 1995; Hsu et al., 1993; Jeng, 1996a, 1997b, 1998b; Tsai et al., 2000; Oh et al., 2002). However, the breakwater is simplified as an impermeable line without weight, and the standing wave or short-crested wave are adopted to apply the wave induced pressure on seabed in these analytical solutions. The wave induced force acting on the breakwater is not be considered. Some numerical models, including decoupled and coupled models, have also been developed (Mase et al., 1994; Jeng et al., 2001, 2000; Ulker et al., 2010, 2012; Li and Jeng, 2008; Mizutani et al., 1998; Mostafa et al., 1999; Mizutani and Mostafa, 1998; Cheng et al., 2007). In most of these decoupled numerical models, the effect of a breakwater on the wave field around the breakwater can not be considered. For example, a standing wave was used to apply the pressure on seabed foundation in front of a composite breakwater in Mase et al. (1994); Jeng et al. (2001, 2000); Ulker et al. (2010). Additionally, most of the coupled numerical models are limited to two dimensional cases, such as Mizutani et al. (1998), Mostafa et al. (1999) and Cheng et al. (2007). The 2D numerical models are not applicable in the cases in which the interaction between the wave, seabed and breakwater head is involved. Under such a situation, a 3D numerical model is needed.

In this Chapter, adopting the developed integrated model PORO-WSSI III, the interaction between the 3D Wave, poro-elastic or poro-elasto-plastic seabed foundation and a caisson breakwater, and the wave induced transient liquefaction, residual liquefaction around the breakwater head are investigated. The dynamic response of caisson breakwater, and the wave induced momentary or residual liquefaction in the seabed foundation around the caission breakwater are given special attention in the analysis.

6.2 Elastic seabed foundation[5*]

6.2.1 Computational domain and boundary conditions

Figure 6.1 shows the top-view of the breakwater, seabed and ocean wave system involved in the chapter. A caisson breakwaters is constructed on the porous seabed foundation. The ocean wave propagates on the seabed, and passes through the two breakwaters in the interaction process.

Figure 6.2 (a) is the chosen computational domain for the breakwater, seabed and ocean wave system. The dimensions of seabed foundation are: L_x=250m (length), L_y=130m (width), h=15m (thickness). The breakwater is 90m long, 10m wide and 16m high. Its coordinate ranges on the seabed are: x=200-210m, y=40-130m, z=15-31m. The 27-nodes hexahedral iso-parametric elements are adopted to discretize the seabed foundation and the caisson breakwater. The 27-nodes iso-parametric elements have a third-order accuracy, the computational errors can be controlled more effectively. In addition, the size of elements could be significantly larger than that if the 8-nodes elements (first-order accuracy) are used.

In numerical computation, the following boundary conditions are applied according to the actual engineering environment the breakwater located.

First, the bottom of the seabed foundation is rigid and impermeable:

$$u_s = v_s = w_s = 0 \qquad \text{at} \qquad z = 0. \tag{6.1}$$

Second, the four lateral sides of seabed foundation are fixed in the x direction or in the y direction:

$$u_s = 0 \quad \text{at} \quad \text{x=80m} \quad \text{and} \quad \text{x=330m}, \tag{6.2}$$

$$v_s = 0 \quad \text{at} \quad \text{y=0m} \quad \text{and} \quad \text{y=130m}. \tag{6.3}$$

Third, on the surface of the seabed foundation (except the section below the caisson breakwater), the pore pressure is equal to the wave induced pressure plus the hydrostatic water pressure (pressure

[5*]Contents in this section are being prepared in a manuscript for journal paper.

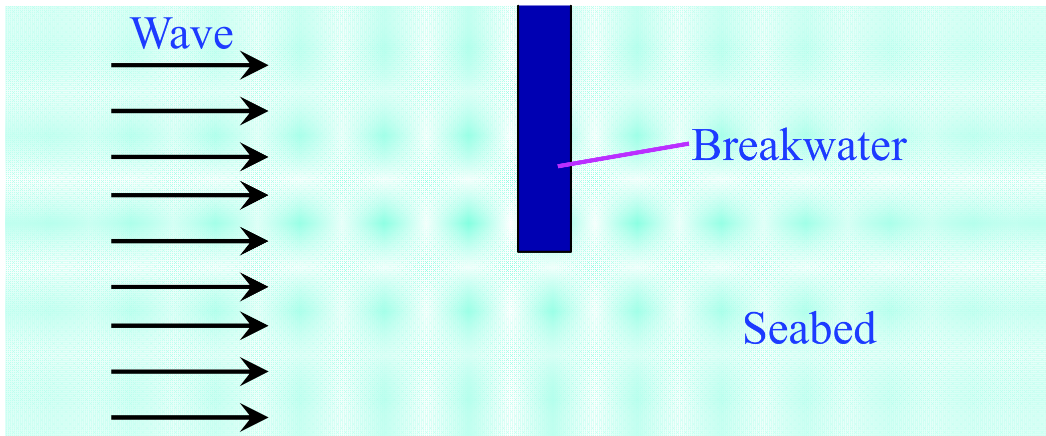

Figure 6.1: The top-view of the breakwater, seabed and ocean wave system in the computational domain.

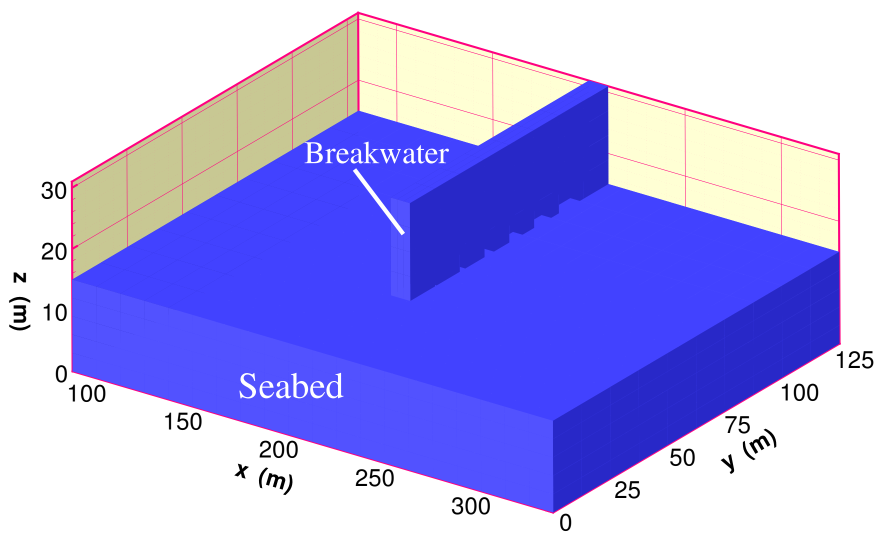

Figure 6.2: The chosen computational model: 3D seabed foundation and caisson breakwater system.

continuity); and the seabed surface is applied by the wave induced pressure and the hydrostatic water pressure.

Finally, on the surface of the breakwater (except the bottom surface), the pore pressure is zero due to the caisson is impermeable. However, the breakwater is applied by the wave induced pressure and the hydrostatic water pressure on its all lateral surfaces.

6.2.2 Consolidation of the seabed foundation[6*]

The seabed generally has experienced the consolidation process under the hydrostatic pressure and the self-gravity in the geological history. There is no any excess pore pressure in the seabed foundation. This consolidation status should be first determined, and taken as the initial condition for the thereafter wave induced dynamic analysis for the caisson breakwater and the seabed foundation. The properties of the seabed foundation and the caisson breakwater used in the model are listed in Table 6.1.

Table 6.1: The properties of the seabed foundation and the caisson breakwater used in the model

Medium	E (Pa)	ν	k (m/s)	S_r (%)	n	G_s
Seabed	2.0×10^7	0.3333	1.0×10^{-5}	98	0.25	2.65
Caisson breakwater	1.0×10^{10}	0.25	0.0	0.0	0.0	2.65

In engineering practice, after the construction of a caisson breakwater on seabed, the weight of the breakwater is initially transferred to the pore water in the seabed foundation, resulting in the generation of excess pore pressure and pressure gradient. As time passes, the pore water permeates, driven by the pressure gradient through the void of soil particles, promoting the pore pressure to dissipate gradually (Figure 6.3, t=4000s and Figure 6.4 (A)). From the distribution of the pore pressure on section y=85m, it is found that the pore pressure under the caisson breakwater is greater than other positions far away from the breakwater, and the maximum pore pressure is 280kpa. During the consolidation process, the weight of the breakwater is gradually transferred from the pore water to the soil particles (Figure 6.4 (B)); and the breakwater subsides correspondingly (Figure 6.4 (C)). Finally, the seabed foundation reaches a new equilibrium status in which the excess pore pressure and pressure gradients disappear (Figure 6.3, t=40000s). The maximum pore pressure in the seabed has

[6*] Contents in this section are included in Ye and Jeng (2012): Ye J H & Jeng D-S (2012). The Consolidation of 3D Porous Unsaturated Seabed under Rubble Mound Breakwater. Ocean Engineering, Resubmitted.

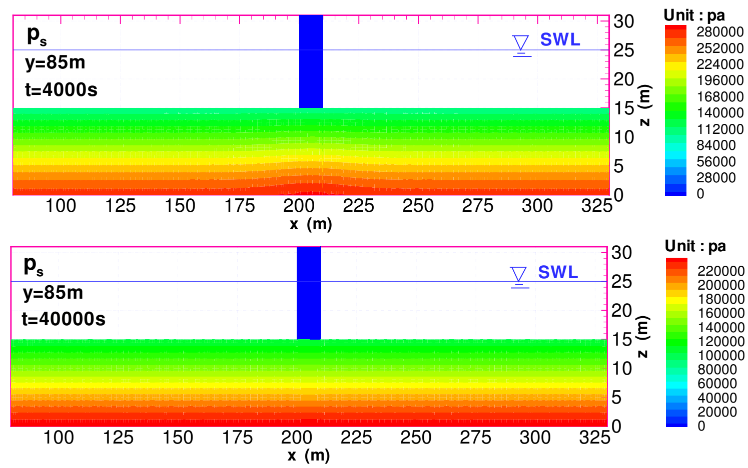

Figure 6.3: The distribution of pore pressure on section x=85m in seabed and caisson at time t=4000s and 40000s.

decreased from 280kPa to 220kPa. It is noted that the pore pressure in the rigid caisson breakwater is zero at any time due to it being impermeable. This newly reached consolidation status should be taken as the initial status for the evaluation of the dynamic response of seabed foundation and breakwater under ocean wave/earthquake loading.

Figure 6.5 show the distribution of effective stress σ'_x, σ'_y and σ'_z and shear stress on the two typical planes y=85m. As illustrated in Figure 6.5, the effect of the caisson breakwater on the stress field is significant. The effective stresses all increase significantly in the zone under or near to the caisson breakwater due to the gravity induced compression. The shear stress concentration appears under the bottom of caisson breakwater. However, the effect of marine structures on the stress field in the seabed foundation disappears in the zone far away from the marine structures; and the distribution of effective stresses are layered, which is nearly the same as when there is no marine structure on the seabed.

Figure 6.6 demonstrates the distribution of effective stresses and shear stresses in the seabed foundation on section x=205m and x=209m. Here, the symmetric plane x=205m is not chosen due to τ_{xy} and τ_{xz} equalling zero on the symmetric plane. The distribution of τ_{xy} and τ_{xz} on x=209m can be observed more clearly. From Figure 6.6, it can be seen that the concentration zone of shear stress only locates in the region under or near to the caisson breakwater. In the region far away from the caisson breakwater, there is no shear stress. It is indicated that the construction of marine structures on the

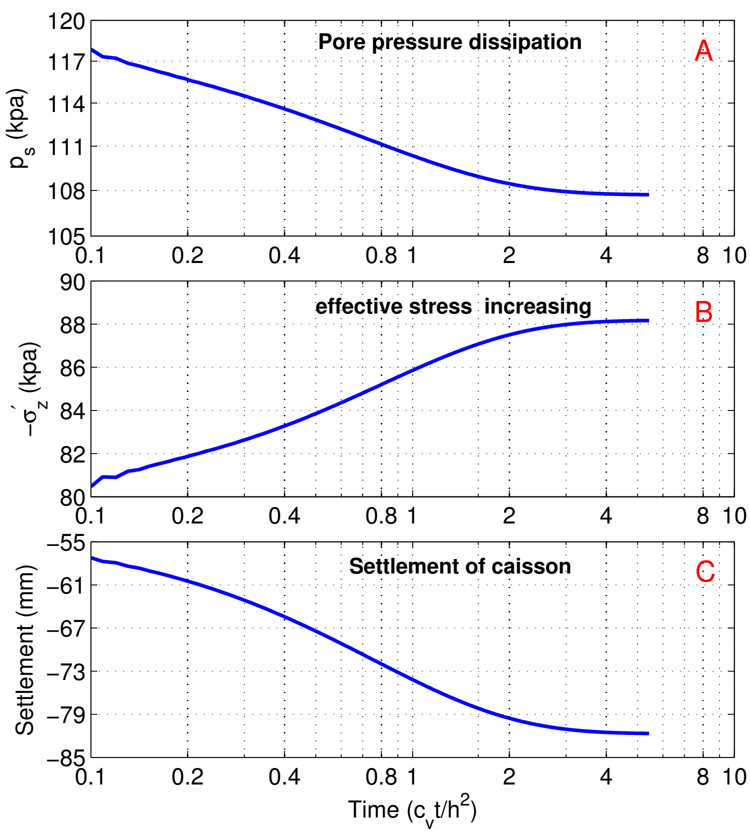

Figure 6.4: The historic curve in consolidation process for the dissipation of pore pressure (A), increasing of effective stress at position (x=205m, y=85m, z=6m) (B) and the settlement of caisson breakwater (C).

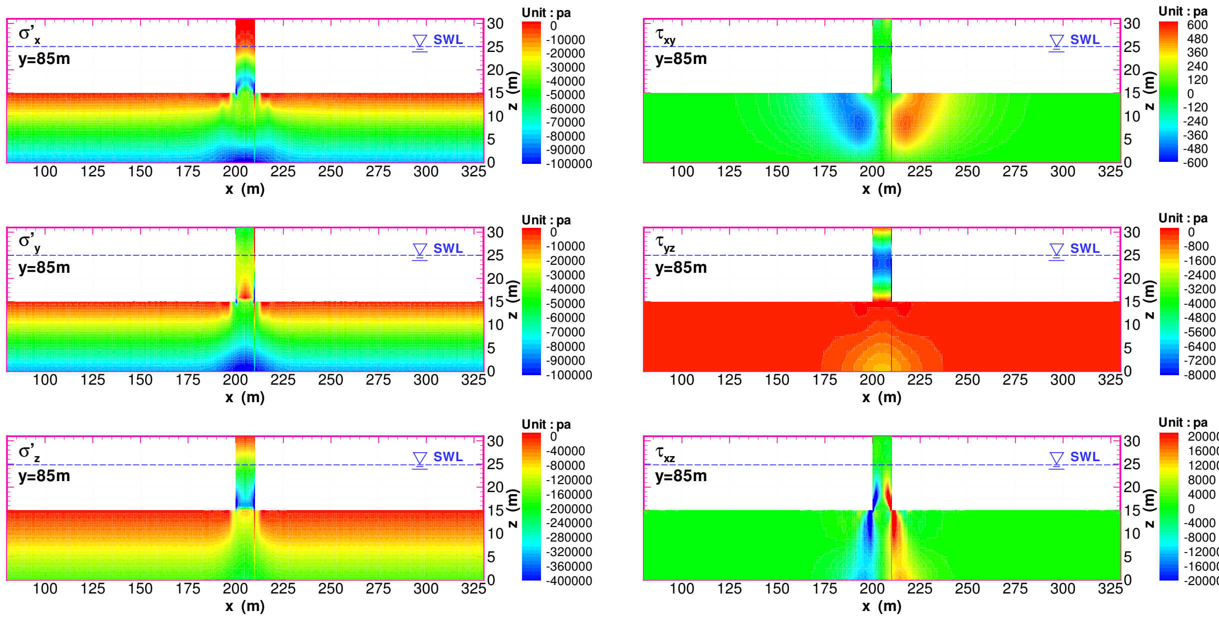

Figure 6.5: The distribution of effective stresses in the seabed foundation on section y=85m in the consolidation status. Note: σ'_x, σ'_y, σ'_z: effective normal stresses, τ_{xy}, τ_{yz}, τ_{xz}: shear stress.

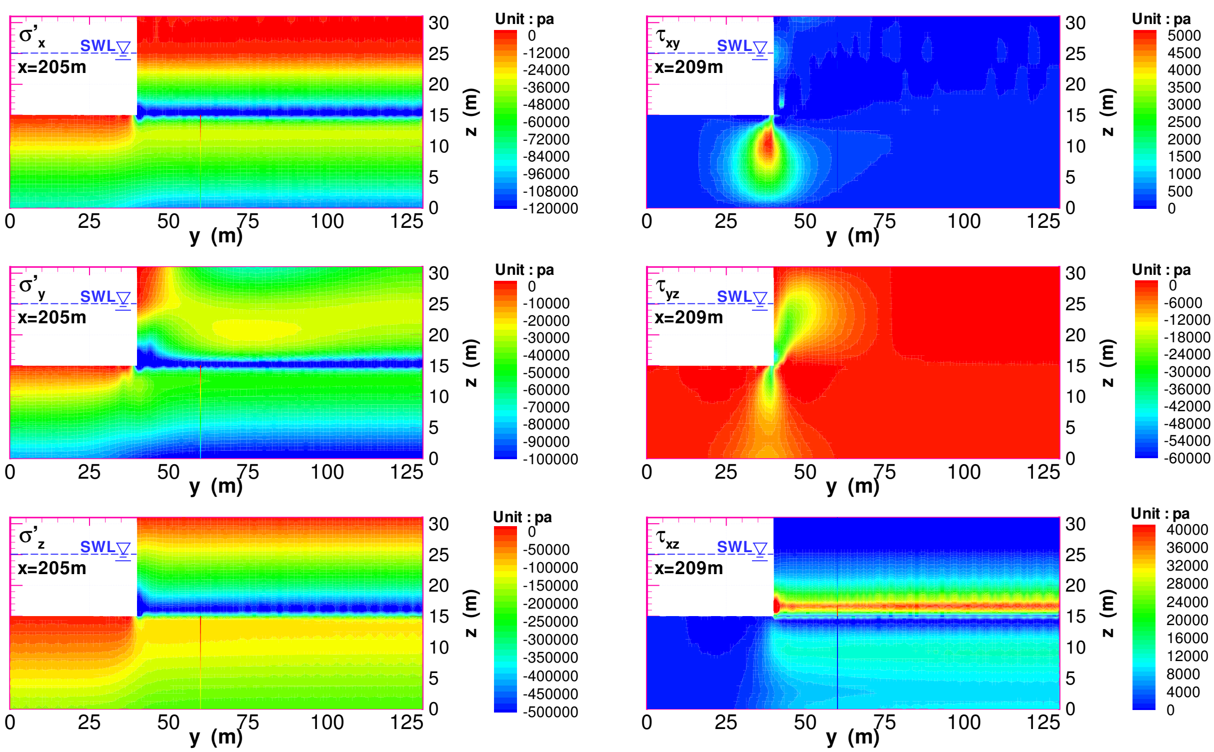

Figure 6.6: The distribution of stress in the seabed foundation on section x=205m in consolidation status. Note: σ'_x, σ'_y, σ'_z: effective normal stresses, τ_{xy}, τ_{yz}, τ_{xz}: shear stress.

seabed is the direct reason for the shear stress concentration in foundation. The magnitude of τ_{xy} is small (maximum 5kPa), However, the τ_{yz} is a little large, up to 25kPa. Differently, the τ_{xz} distributes in the whole zone under the caisson breakwater; and the magnitude can reach up to 70kpa. Therefore, τ_{yz} and τ_{xz} could be responsible for the shear failure of seabed foundation under marine structures. Coastal engineers should pay attention to the τ_{yz} and τ_{xz} developed in the seabed foundation due to the gravity loading of marine structures.

6.2.3 Dynamic response of caisson breakwater

Under the environmental load (ocean wave) applied, the breakwater built on the seabed would lose its stability due to the excess dynamic shear stress and the liquefaction of the seabed foundation. The dynamic response of the breakwater and its seabed foundation is the main concern for coastal engineers. Taking the above determined consolidation status as the initial condition, the dynamic response of caisson breakwater and its seabed foundation under the 3D wave loading is studied.

The 3D ocean wave field propagating on seabed around the caisson breakwater is first determined. The wave characteristics for the 3D wave maker is: wave height H=1.5m, water depth d=10m, and wave period T=8.0s. Figure 6.12 shows the wave profile around the caisson breakwater at four typical times (all in one wave period). In the computational domain for the 3D ocean wave, three absorption zones are set to absorb the incident wave, and to eliminate the unexpected reflected wave due to the limited computational domain. The three absorption zones are at: zone one (x=-190m to -100m ,y=0m to 130m), zone two (x=400m to 500m, y=0m to 130m), zone three: (x=210m to 400m, y=130m to 230m). The wave maker is located at position x=0m. From Figure 6.12, it can be seen that there are three wave zones: the standing wave in front of the caisson breakwater, the diffracted wave behind the caisson breakwater and the progressive wave near the head of the breakwater. The standing wave is formed due to the interference between the incident wave and reflected wave in front of the breakwater; the wave height of this standing wave is about 3.0m, two times the original wave height. The diffracted wave behind the caisson breakwater is formed due to the block effect of the breakwater to incident wave coming from the wave maker.

During the process of wave-breakwater-seabed interaction, the wave impact force acting on the lateral sides of the caisson breakwater is the main driving force that causes the breakwater to vibrate

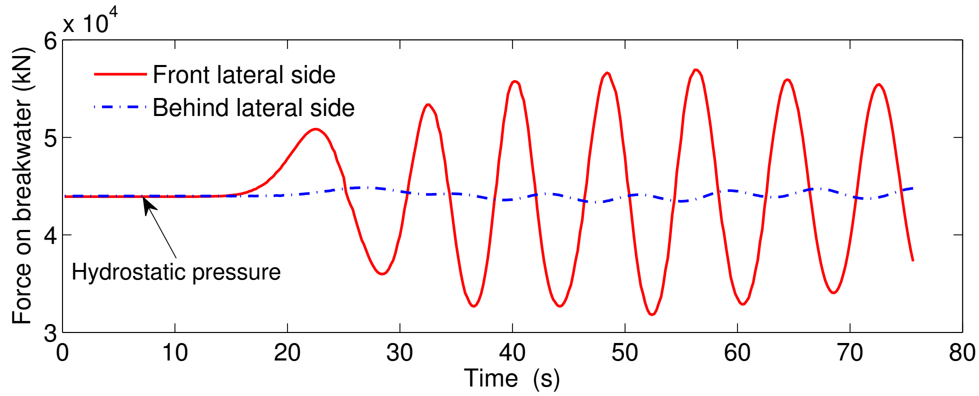

Figure 6.7: The total wave impact force acting on the front and rear lateral sides of caisson breakwater (hydrostatic plus wave induced pressure).

periodically. Figure 6.7 illustrates the wave impact force acting on the front and rear lateral sides of the caisson breakwater. It can be seen that the wave impact force on front lateral side of breakwater due to the standing wave loading is significantly much larger than that on the rear lateral side of breakwater. It is indicated that the diffracted wave induced dynamic pressure on the caisson breakwater is very small. Therefore, the standing wave in front of the caisson breakwater should be the dominant factor for the shear failure and liquefaction of the seabed foundation.

Under the 3D wave loading on the lateral sides, the caisson breakwater vibrates periodically. This vibration can be clearly seen in Figure 6.8. Before the wave arrives at the breakwater, the breakwater keep its static status. After the wave arrives, the breakwater begins to move forward and backward in a horizontal direction, and swing in the vertical direction periodically. As a whole, the breakwater moves and swings to the right hand side when the wave crest arrives; and it moves and swing to the left hand side when the wave trough arrives. Figure 6.9 demonstrates the displacements of the top corner of the caisson breakwater under the 3D ocean wave loading. It further shows the motion characteristics of the breakwater under wave loading.

6.2.4 Dynamic response of seabed foundation

The wave-induced dynamic response of the seabed foundation in the region around the caisson breakwater is particularly important for the stability of the caisson breakwater due to the fact that the liquefaction, shear failure could occur. In this section, the wave-induced dynamic response, transient liquefaction, and dynamic shear failure are investigated in detail.

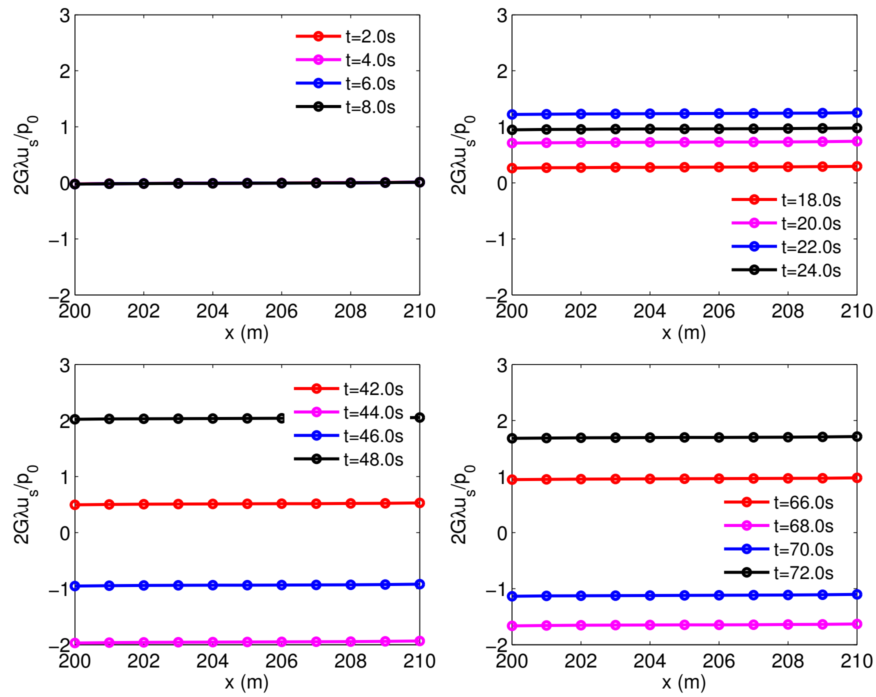

(a) Horizontal displacement

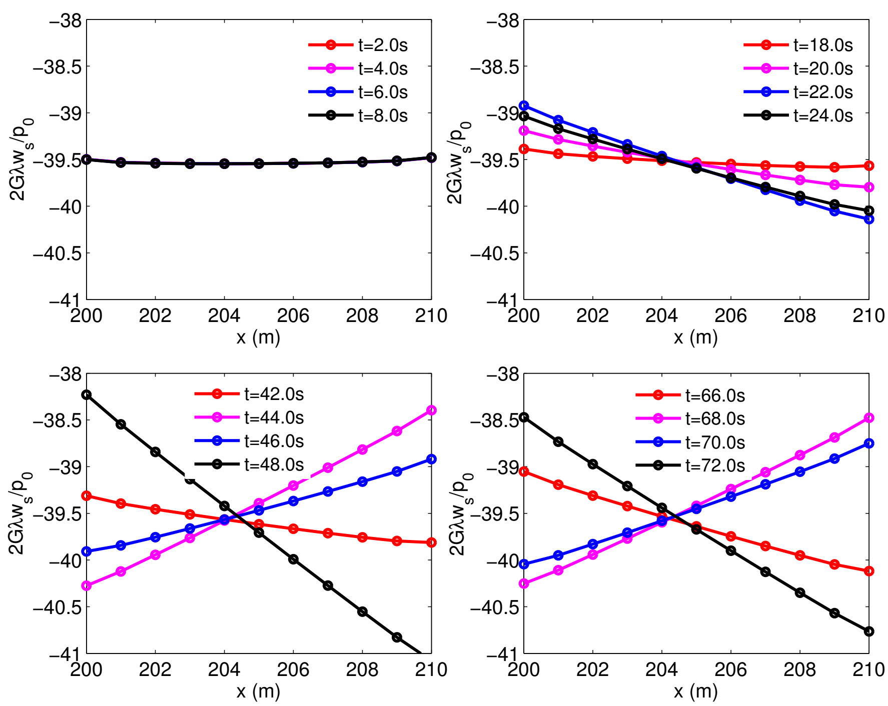

(b) Vertical displacement

Figure 6.8: The motion of the bottom of the caisson breakwater under a nonlinear wave loading.

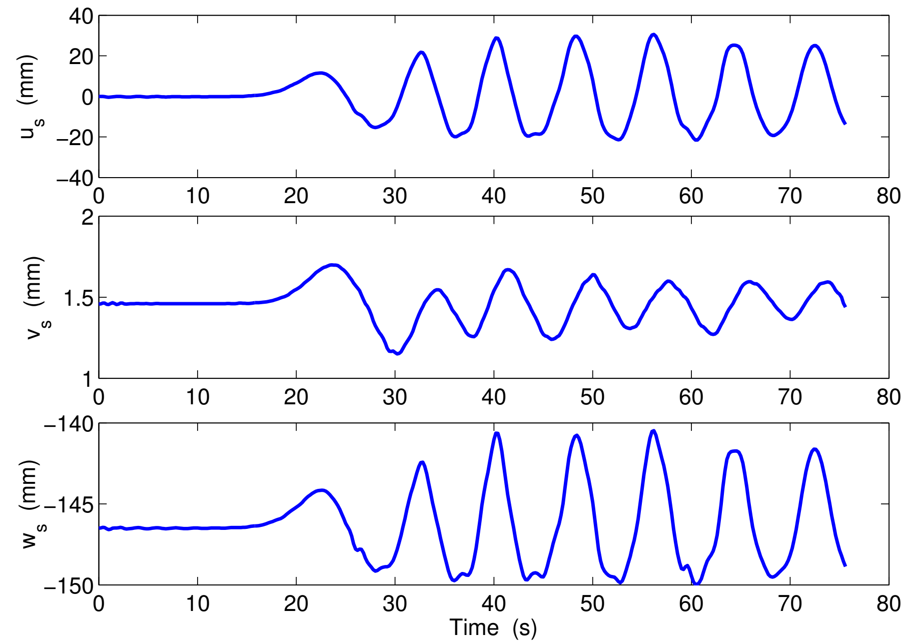

Figure 6.9: The displacements of the top corner of the caisson breakwater under a nonlinear wave loading.

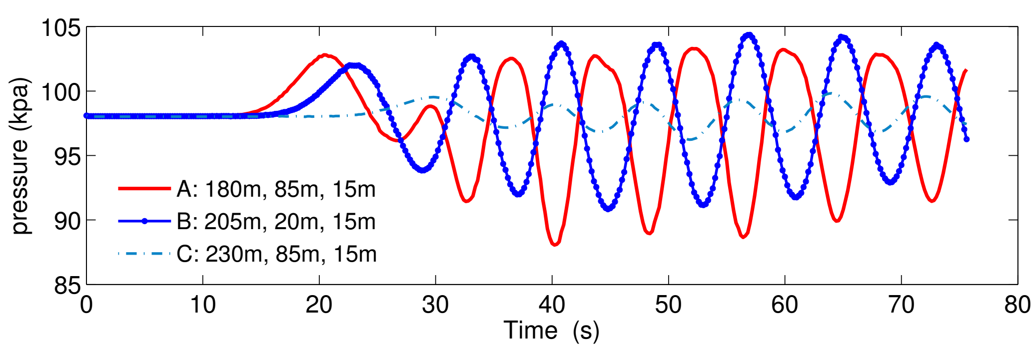

Figure 6.10: The nonlinear wave induced water pressure acting on the seabed surface at different location.

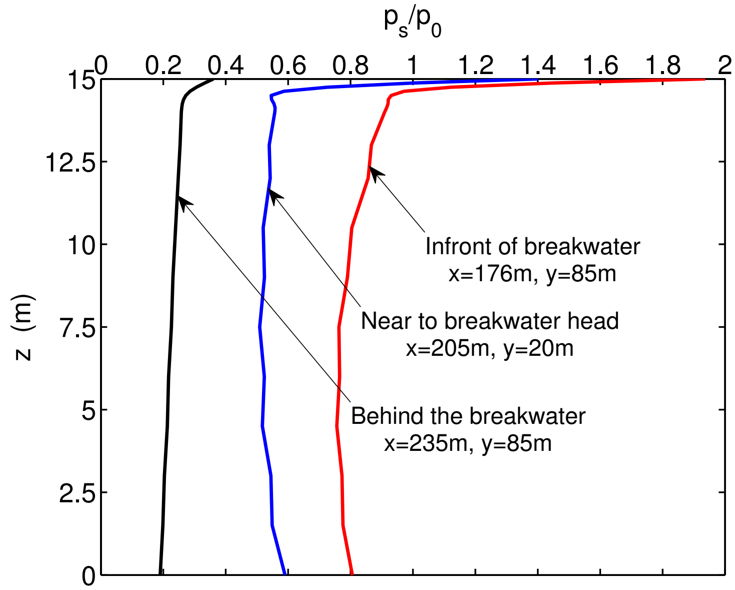

Figure 6.11: The distribution of the nonlinear wave induced maximum dynamic pressure in seabed foundation at three typical locations. p_0 is the pressure induced by linear wave $p_0 = \gamma_w H/2 \cosh(\lambda d)$, where λ is the wave number.

As mentioned in the previous section, there are three kinds of wave around the caisson breakwater: the standing wave in front of breakwater, the diffracted wave behind the breakwater and the progressive wave near to the breakwater head. Certainly, the wave induced water pressure acting on the seabed is significantly different. Figure 6.10 illustrates the wave induced water pressure acting on the seabed surface at three typical positions: in front of breakwater (x=180m, y=85m, z=15m), behind the breakwater (x=230m, y=85m, z=15m) and near to the breakwater head (x=205m, y=20m, z=15m). It can be seen from Figure 6.10 that the standing wave induced pressure on seabed in front of breakwater is greatest; and the nonlinearity is clear. The diffracted wave induced pressure on the seabed behind the breakwater is smallest. It is indicated that the breakwater indeed can effectively protect the seabed behind the breakwater.

The wave induced pressure acting on the seabed in different zones around the breakwater is also significantly different. The wave induced seabed response is correspondingly different in the seabed foundation. Figure 6.11 demonstrates the vertical distribution of wave induced maximum pore pressure in seabed foundation at three typical locations. It can also be seen from Figure 6.11 that the standing wave induced pore pressure in the seabed in front of the breakwater is strongest, while the

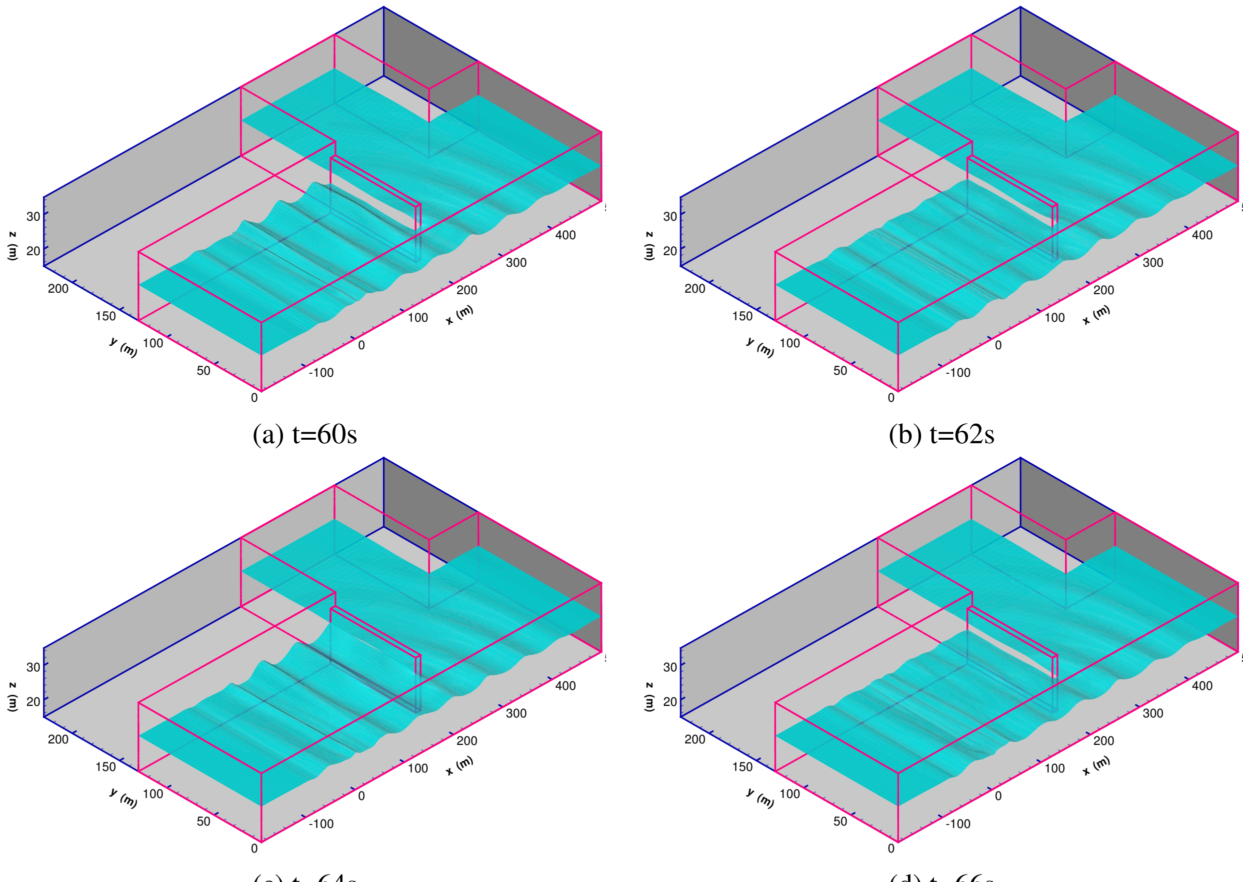

(a) t=60s (b) t=62s

(c) t=64s (d) t=66s

Figure 6.12: The wave profile around the caisson breakwater at different times.

diffracted wave induced pore pressure in the seabed behind the breakwater is smallest. The progressive wave induced pore pressure in the seabed near to the breakwater head is between that the standing wave induced and the diffracted wave induced. It indicates that the wave induced liquefaction is most likely to occur in the region in front of the caisson breakwater.

Under the 3D ocean wave loading, the seabed foundation will respond to the wave loading correspondingly. The pore pressure, effective stresses, and shear stresses in the seabed foundation vary periodically. Here, a typical time t=60s is chosen to illustrate the dynamic response of seabed foundation to the 3D wave loading. At time t=60s, the wave trough arrives at the breakwater (Figure 6.12 (a))

Figure 6.13 demonstrates the wave induced dynamic response in the seabed foundation at time t=60s, including the pore pressure, effective stresses and shear stress. From Figure 6.13, it can be further clearly observed that the seabed response under the standing wave loading in the region in front

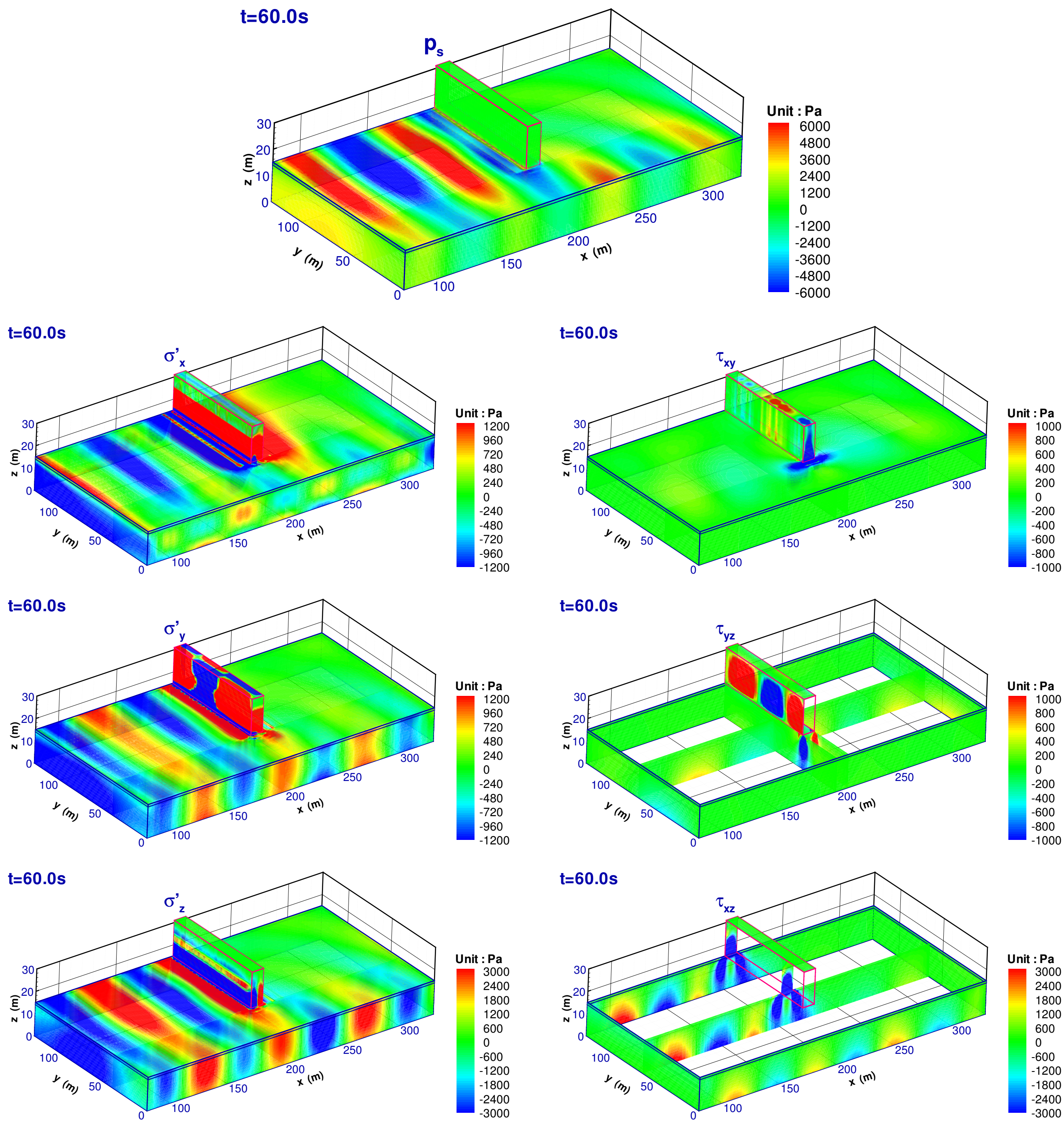

Figure 6.13: The wave induced dynamic response in the seabed foundation at time t=60s. Note: p_s: pore pressure, σ'_x; σ'_y, σ'_z: effective normal stresses; τ_{xy}, τ_{yz}, τ_{xz}: shear stresses.

of the caisson breakwater is strongest; while, the seabed response under the diffracted wave loading in the region behind the caisson breakwater is weakest. It is also further indicated that the breakwater can effectively block the wave, and protect the seabed foundation behind the breakwater. Another phenomenon observed is that the wave induced pore pressure in seabed is positive, the dynamic effective stress σ'_z and σ'_y is compressive, and the the dynamic effective stress σ'_x is tensile under the wave crest. While the wave induced pore pressure in the seabed is negative, the dynamic effective stress σ'_z and σ'_y is tensile, and the the dynamic effective stress σ'_x is compressive under the wave trough. According to the liquefaction criterion proposed by Okusa (1985), if the tensile dynamic effective stress σ'_z is great enough to overcome the overburdened soil weight, the seabed foundation could liquefy transiently. As analyzed in Chapter 5, the seabed foundation would not liquefy under the wave crest due to the compression by the wave crest. At time t=60s, the wave trough arrives at the breakwater, the wave induced pore pressure is negative, and the dynamic effective stress σ'_z is tensile in the zone close to the bottom of the breakwater. It is highly possible for the seabed foundation in the zone close to the bottom of the breakwater to transiently liquefy. When the wave crest arrives at the breakwater, the seabed foundation in the zone close to the bottom of the breakwater is not likely to liquefy. However, the strong pushing wave impact force would overthrow the breakwater. Therefore, the liquefaction of seabed foundation and tilt of the breakwater should both be taken into consideration in engineering design. The liquefaction characteristics of the seabed foundation under the 3D wave loading will be investigated in detail in the following section.

The wave induced shear stress τ_{xy} and τ_{yz} are only concentrated in the region under the caisson breakwater head. The magnitude of the concentrated τ_{xy} and τ_{yz} under the breakwater head can reach up to 2kPa. In the region away from the breakwater, the wave induced τ_{xy} and τ_{yz} are relatively small, only up to about 500Pa. The wave induced τ_{xy} and τ_{yz} in seabed foundation is the secondary factor for the stability of the breakwater. The wave induced shear stress τ_{xz} is the dominant factor for the shear failure in seabed foundation under the caisson breakwater. The wave induced shear stress τ_{xz} in the region far away the breakwater is located at the lower part of seabed foundation. Its magnitude can reach up to 3kPa. However, the shear failure would not occur in the lower part of seabed foundation. It is observed that the wave induced τ_{xz} is highly concentrated in the zone under the caisson breakwater. The maximum magnitude can reach up to 10kPa. Under the periodical wave loading, the direction of dynamic τ_{xz} correspondingly is changed from right to left periodically. This wave induced cycle dynamic shear stress is a very dangerous factor for the stability of breakwater.

6.2.5 Momentary liquefaction prediction in seabed foundation

The wave induced liquefaction in the seabed foundation is one of the primary reasons for the instability of breakwater in the offshore environments. The liquefaction characteristics of the seabed foundation under wave loading should be paid special attention by coastal engineers in structures design. In this section, the liquefaction of the seabed around the caisson breakwater is investigated in detail. There are generally two kinds of liquefaction mechanism: transient liquefaction and residual liquefaction. The transient liquefaction frequently occurs in elastic seabed foundations; and the residual liquefaction always appears in elasto-plastic seabed foundations. Here, only the transient liquefaction is involved due to the seabed foundation being treated as an elastic porous medium in this section.

The essence of transient liquefaction in seabed foundation under wave loading is that the wave induced upward seepage force could overcome the overburdened soil weight, and make the contact effective stresses between the soil particles become zero. As analyzed in Chapter 5, the upward seepage force only exists in the zone under wave trough; and the seepage force in the zone under wave crest is downward. The seabed under the wave trough could liquefy transiently; however, the seabed under the wave crest is impossible to liquefy. Therefore, the liquefaction in the seabed foundation is mainly dependent on the magnitude of the seepage force and its direction. The three components of the seepage force in the seabed foundation are expressed as:

$$j_x = \frac{p_s}{\partial x} \qquad j_y = \frac{p_s}{\partial y} \qquad j_z = \frac{p_s}{\partial z}. \tag{6.4}$$

Figure 6.14 illustrates the distribution of the wave induced seepage force j_x, j_y and j_z at two typical time t=60s. From Figure 6.14, it is found that the wave induced seepage force j_x, j_z in the region in front of the caisson breakwater is much greater than that behind the caisson breakwater. This phenomenon indicates that the protection of the breakwater for the seabed behind it is effective. Comparing with the vertical seepage force j_z, the horizontal seepage force j_x and j_y is very small. The

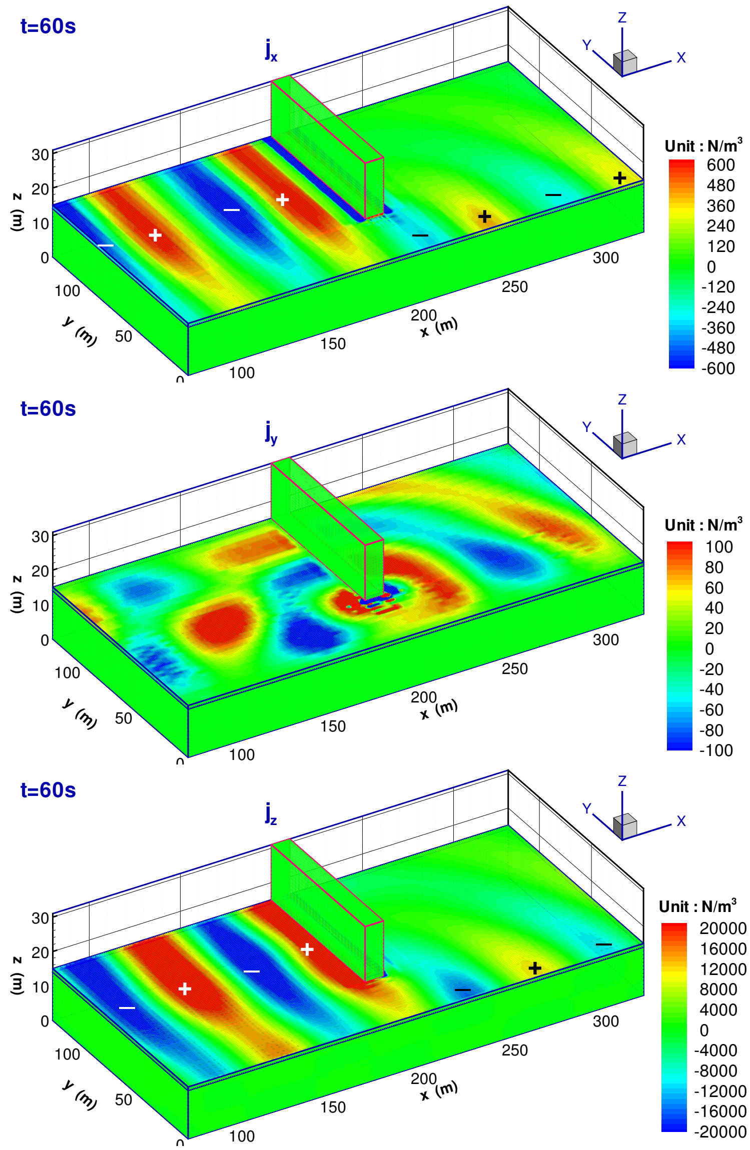

Figure 6.14: The distribution of the wave induced seepage force j_x, j_y and j_z at two typical time t=60s. The positive seepage force is upward; and the negative seepage is downward.

maximum magnitude of j_x and j_y are only 2kN/m^3 and 0.2kN/m^3. And it seems that the distribution of j_y in seabed foundation has no clear relation with the wave profile propagating on the seabed foundation. The wave induced vertical seepage force j_z is huge and the dominant factor for the seabed liquefaction; its magnitude could reach up to 30kN/m^3. At time t=60s, the wave trough arrives at the caisson breakwater; the j_z in the zone near to the caisson breakwater is upward. Transient liquefaction in this zone is most likely to occur.

Figure 6.15 shows the transient liquefaction zone in the seabed foundation under wave loading in a typical wave period from t=60s to t=66s. Here, the liquefaction criterion proposed by Okusa (1985) is used. Comparing the distribution of liquefaction zones in seabed foundation shown in Figure 6.15 with the wave profile shown in Figure 6.12 and the distribution of vertical seepage force J_z shown in Figure 6.14, it is found that the transient liquefaction can only appear in the zone where the j_z is upward and under the wave trough; the seabed foundation cann't liquefy transiently in the zone under the wave crest in which the vertical seepage force j_z is downward. At time t=60s, the wave trough arrives the caisson breakwater. The seabed foundation in the region near to the front lateral side and the head of caisson breakwater liquefy. This liquefaction may result in the collapse or tilt of the caisson breakwater. At time t=64s, the wave crest arrives the caisson breakwater. The vertical seepage force j_z is downward, which makes the soil particles in the zone near to the front lateral side and the head of caisson breakwater contact more closely. The soil can not liquefy at this time. A important phenomenon observed from Figure 6.15 is that the seabed foundation behind the caisson breakwater doesn't liquefy during the diffracted wave loading. This phenomenon indicates again that the breakwater has effectively protected the seabed and coastline behind it. The area of liquefaction zone induced by the standing wave in the region in front of caisson breakwater is much greater than that induced by the progressive wave. The liquefaction zones induced by the standing wave and progressive wave attach together sometimes, separate at other times.

The liquefaction depth in the seabed foundation under wave loading is an important parameter for coastal engineers involved in the design of marine structures. Figure 6.16 demonstrates the historic variation of the liquefaction depth in the seabed foundation at three typical positions: in front of breakwater, behind breakwater and near to the breakwater head. It is found that the maximum depth of liquefaction zone in front of breakwater under standing wave loading is about 0.528m, which is

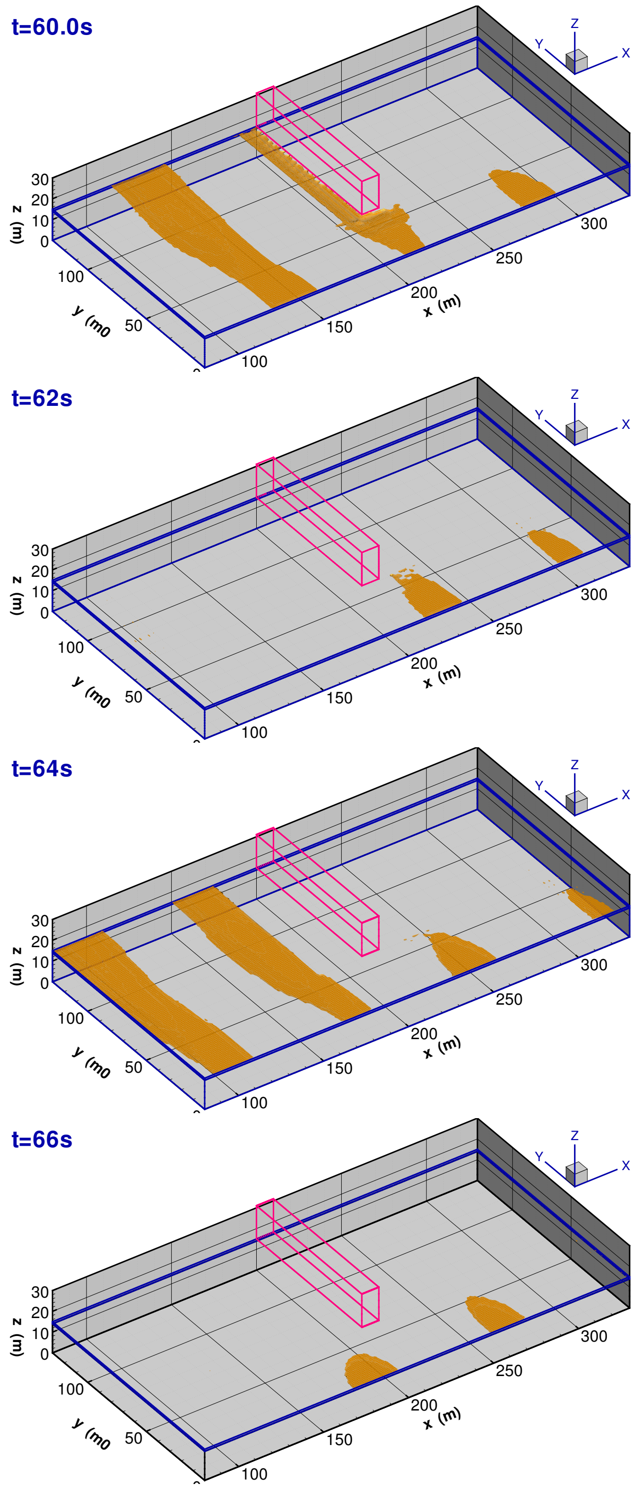

Figure 6.15: The predicted transient liquefaction zone near the seabed surface under the 3D wave loading in a typical wave period from t=60s to t=68s.The liquefaction criterion proposed by Okusa (1985) is used.

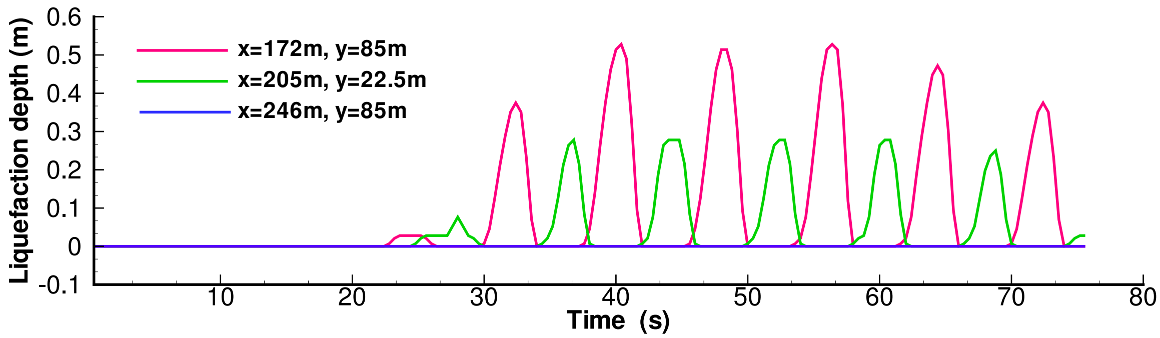

Figure 6.16: The historical curve of the liquefaction depth at three typical positions.

Table 6.2: The effect of the wave and soil characteristics on the wave induced maximum liquefaction depth in seabed foundation in front of the caisson breakwater.

Wave characteristics						Soil characteristics					
H (m)	d_{lique} (mm)	T (s)	d_{lique} (mm)	d (m)	d_{lique} (mm)	E (Mpa)	d_{lique} (mm)	k (m/s)	d_{lique} (mm)	S_r (%)	d_{lique} (mm)
0.5	0.028	6	0.278	8	1.225	10	0.528	10^{-7}	0.528	95	0.778
1.5	0.528	8	0.528	10	0.528	20	0.528	10^{-5}	0.528	98	0.528
2.5	0.972	10	0.778	12	0.375	100	0.778	10^{-3}	0.028	100	0.028

greater than that induced by the progressive wave (0.278m). The liquefaction depth in the region behind the caisson breakwater is always 0. It indicates that on liquefaction does not occur in this region.

6.2.6 Parametric study

6.2.6.1 Effect of wave and soil characteristics

In engineering practice, the porous seabed chosen as the foundation of marine structures is different from case to case. The property of seabed foundation are various. How the wave characteristics and seabed properties affect the wave-seabed-breakwater interaction is a problem for coastal engineers. Here, the wave induced maximum liquefaction depth in the region in front of the caisson breakwater is taken as the representative quantity to investigate the effect of wave and soil characteristics on the wave-seabed-breakwater interaction.

Table 6.2 lists the wave induced maximum liquefaction depth in the seabed foundation in front of the caisson breakwater under different soil and wave characteristics. The standard parameters used here are the same with that listed in table 6.1. When investigating the effect of one of those parameters, the other parameters are kept the same with the standard parameters. From Table 6.2, it is found that the maximum wave induced liquefaction depth in seabed foundation in front of the caisson breakwater is mainly dependent on the wave height, wave period, water depth, permeability and saturation of the seabed. The Young's modulus of the seabed could only insignificantly affect the maximum liquefaction depth. The maximum liquefaction depth is proportional to the wave height and wave period and Young's modulus of seabed; and inversely proportional to the water depth, permeability and saturation of the seabed.

6.2.6.2 Effect of breakwater's direction

In the offshore environment, the caisson breakwater is not always perpendicular to the incident wave. There are a lot of cases in which the breakwater is oblique with the incident wave. Obviously, the angle between the caisson breakwater and incident wave (defined as θ) is an important factor for the wave-seabed-structures interaction. In this part, the effect of the angle between the caisson breakwater and incident wave θ on the wave induced dynamics of breakwater and seabed is investigated. Except for the configuration in which the θ=90°, another two configurations θ=60° and θ=120° are taken as the typical cases (see Figure 6.17) to investigate the effect of θ on the wave-seabed-structures interaction.

The position of caisson breakwater relative to the propagation direction of ocean wave has significant effect on the wave field around the caisson breakwater. If the caisson breakwater is perpendicular to the incident wave (θ=90°), the wave in front of the breakwater is a standing wave or a short-crested wave. However, if the caisson breakwater is oblique with the incident wave, it is a crested wave in front of the breakwater. Regardless of the standing wave or the short-crested wave in front of the breakwater, there is still some wave energy passing through the breakwater in the form of a progressive wave going through the gap between breakwaters; then, the diffracted wave is formed behind the breakwater. In the configurations θ=60° and θ=120°, the crested wave is formed due to the interference between the incident wave and reflected wave in front of breakwater.

Different wave fields around the caisson breakwater certainly will result in different responses of the breakwater and its seabed foundation to the wave field. First of all, the wave induced force acting on the caisson breakwater would be significantly different. Figure 6.18 demonstrates the wave

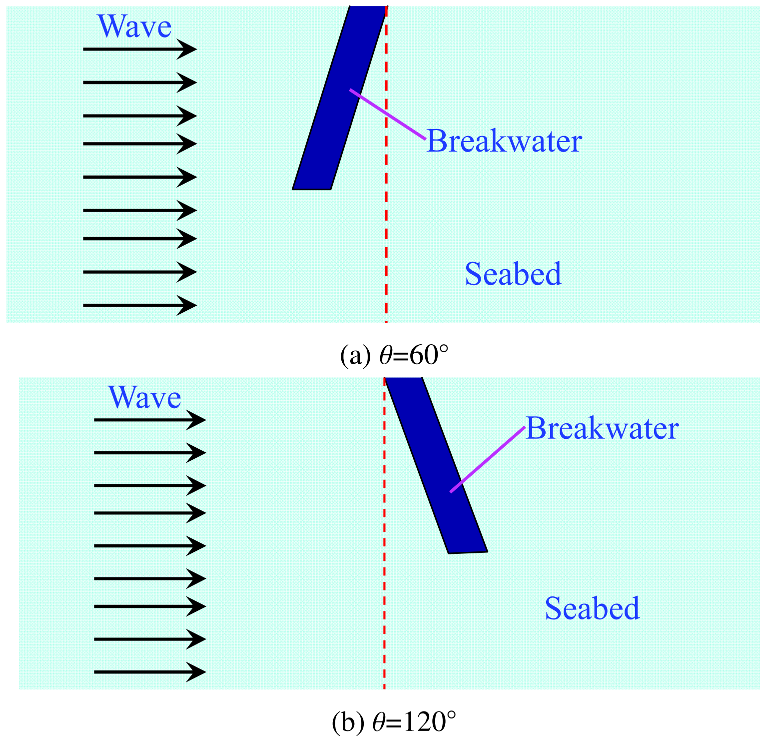

Figure 6.17: The top-view of the breakwater, seabed and ocean wave system for θ=60° and θ=120°.

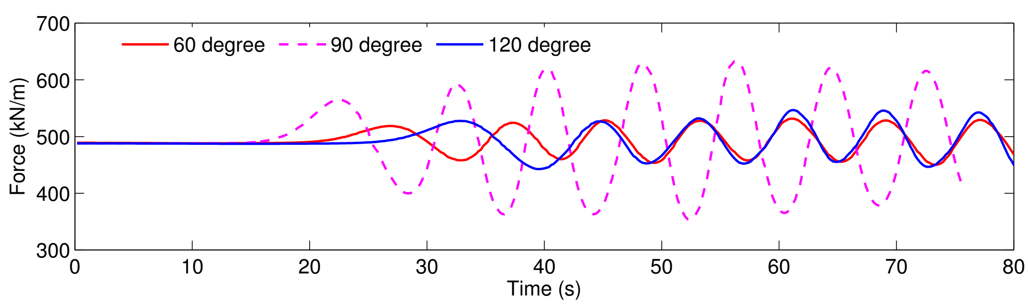

Figure 6.18: The wave induced force acting on the front lateral side of caisson breakwater in 1m length.

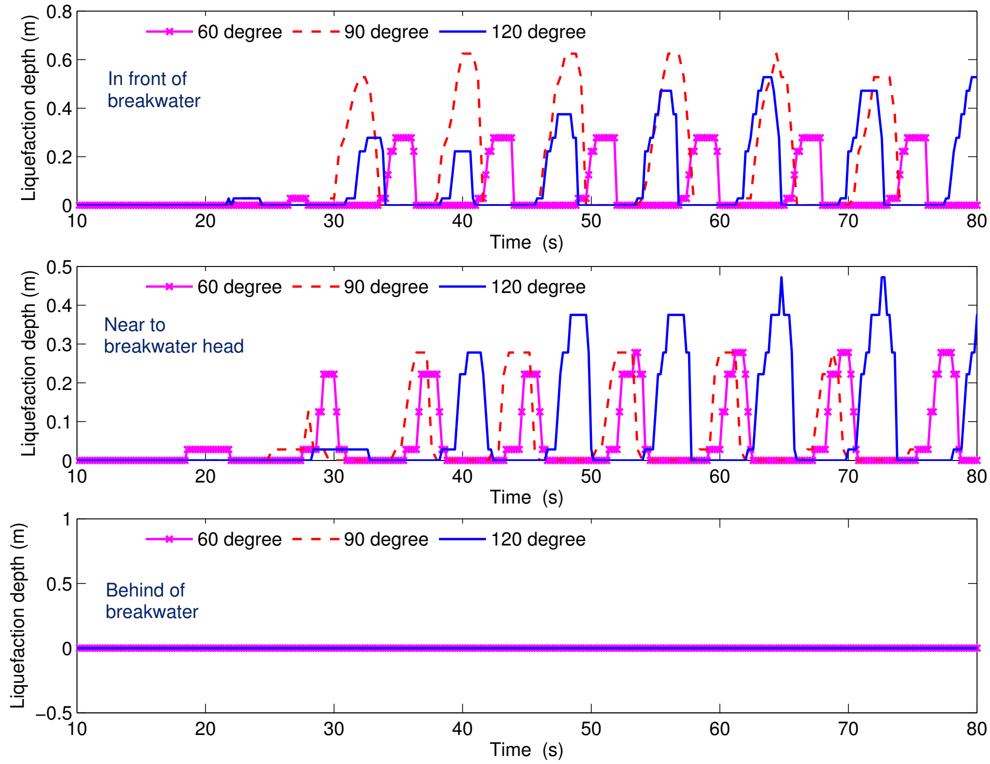

Figure 6.19: The wave induced liquefaction depth at typical positions in seabed foundation.

induced force acting on the front lateral side of the caisson breakwater in 1m length. From Figure 6.18 , it is found that the wave induced force acting on the breakwater is greatest if the wave is normally incident to the breakwater. For configuration θ=60° and θ=120°, the wave induced force acting on the breakwater is only about half of that when θ=90°. It seems that the normal incident wave is most dangerous for the stability of caisson breakwater due to the greatest applying force on breakwater.

Wave induced liquefaction in the seabed foundations around the caisson breakwater under different wave loading is the problem most being concerned in this parametric study. Figure 6.19 demonstrates the wave induced liquefaction depth in seabed foundation at three typical positions: in front of the breakwater, near to the breakwater head and behind breakwater. In Figure 6.19, the wave induced liquefaction depth in front of the breakwater in the three configurations has the following relation: $d_{Lique-90} > d_{Lique-120} > d_{Lique-60}$. For the seabed near to the breakwater head, the liquefaction depth has another relation: $d_{Lique-120} > d_{Lique-90} \geq d_{Lique-60}$. For the seabed behind the breakwater, the liquefaction does not occur in any configuration. In general, it seems that the stability of breakwaters oblique with incident wave is better than the breakwaters perpendicular with incident wave.

6.2.7 Summary

In this section, the interaction between the 3D wave, poro-elastic seabed foundation and a caisson breakwater is investigated adopting the developed 3D integrated model PORO-WSSI III. Based on the analysis of the numerical results, some conclusions are summaried as:

(1) In the initial consolidation status, the caisson breakwater has significant effect on the stress field in seabed foundation near to the caisson breakwater. The initial effective stresses increase greatly, and the shear stress τ_{xz} concentrates in the seabed foundation under caisson breakwater.

(2) In the interaction process between the wave, seabed and caisson breakwater, there are three types of wave around the breakwater head: standing wave in front of breakwater, progressive wave near to the breakwater head, and diffracted wave behind the breakwater. The 3D wave applies huge force on the front lateral side of caisson breakwater periodically, which is significantly greater than that on the behind lateral side of breakwater. Under the 3D wave loading, the caisson breakwater sways accordingly.

(3) The seabed response to the 3D wave at different positions around the breakwater head is also significantly different. The seabed response in front of caisson breakwater is most strong; while, it is weakest behind the breakwater.

(4) Under wave loading, the momentary liquefaction could occur in seabed foundation in front of and near to the caisson breakwater. However, it is impossible for the seabed foundation behind the caisson breakwater to liquefy due to the effective protection provided by the caisson breakwater.

(5) The parametric study indicates that the maximum liquefaction depth in front of the caisson breakwater is mainly dependent on the wave height, wave period, water depth, permeability and saturation of seabed. The Young's modulus of the seabed could only insignificantly affect the maximum liquefaction depth. The direction of breakwater also significantly affects the interaction process between the wave, seabed and breakwater. When the angle θ=90°, the maximum liquefaction depth in front of breakwater is greatest, because the standing wave is formed due to the fact that the normal incident wave is nearly completely reflected by the breakwater.

6.3 Elasto-plastic seabed foundation[7*]

In previous section, the wave induced response in the poro-elastic seabed foundation around a caisson breakwater has been investigated. In this section, using the same configuration set-up (see 6.2), the wave induced response in a poro-elasto-plastic seabed foundation around the same caisson breakwater is investigated. The wave induced pore pressure build up, and the residual liquefaction potential in the seabed foundation are the focus of this analysis.

As that in the analysis of wave induced response in the poro-elastic seabed foundation, the wave characteristics for the wave maker here are also: H=1.5m, d=10.0m, and T=8.0s. The three-dimension wave field around the caisson breakwater is determined by the 3D wave model. The Pastor-Zienkiewicz Model Mark-III model is adopted to describe the behavior of elasto-plastic seabed foundation under wave loading. Nevada dense sand is taken as the seabed soil. The property parameters used for the seabed soil are listed in Table 5.2. The same boundary conditions are applied in this analysis as that in the analysis of wave induced response in the poro-elastic seabed foundation.

The final consolidation status of seabed foundation under the caisson breakwater and hydrostatic pressure is also first determined. The consolidation process and the effect of caisson breakwater on the effective stresses status of the seabed foundation in the final consolidation status have been analyzed in part 6.2.2 in this Chapter. For the sake of simplicity, the consolidation is not discussed again here.

6.3.1 Dynamic response of caisson breakwater

Taking the final consolidation status of seabed foundation as the initial conditions, the wave induced response in a poro-elasto-plastic seabed foundation is investigated, on which a caisson breakwater is constructed.

Figure 6.20 illustrates the wave induced displacements of the caisson breakwater constructed on the poro-elasto-plastic seabed foundation. From Figure 6.20, it can be found that the caisson breakwater sways in the x direction, the vibration magnitude is about 70mm, which is nearly twice the magnitude if the caisson breakwater is constructed on a poro-elastic seabed (see Figure 6.9). It is indicated that the wave induced dynamic response of the caisson breakwater on a poro-elasto-plastic seabed foundation is much stronger than that on a poro-elastic seabed foundation. Another

[7*]Contents in this section are being prepared in a manuscript for jounal paper.

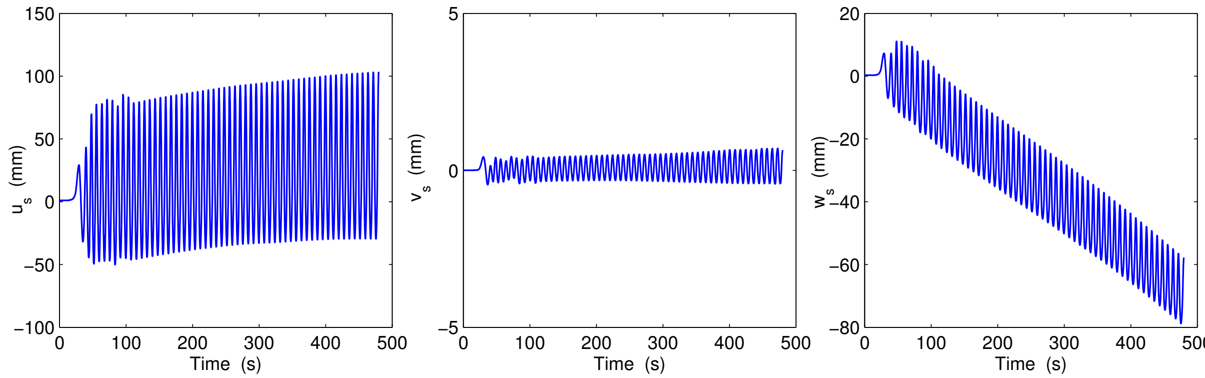

Figure 6.20: Displacements of caisson breakwater on the elasto-plastic seabed foundation under wave loading

phenomenon observed in Figure 6.20 is that the caisson breakwater on a poro-elasto-plastic seabed foundation gradually subsides in the process of wave loading. While, the caisson breakwater only vibrates upward and downward under the wave loading if it is constructed on a poro-elastic seabed. Therefore, the response mechanism to the wave loading of breakwater built on an elastic and elasto-plastic seabed foundation is completely different. The breakwater continuously subsides after the consolidation settlement if built on an elasto-plastic seabed floor. This is a harmful factor for the stability of the caisson breakwater.

6.3.2 Dynamic response of seabed foundation

In section 5.3 of Chapter 5, it has been recognized that the pore pressure in a elasto-plastic seabed foundation build up under the wave loading. The distribution and characteristics of the wave induced pore pressure build up in a elasto-plastic seabed foundation has been investigated in detail in section 5.3. However, the analysis is limited to the two dimensional case. How the breakwater affects the pore pressure build up in the region around the breakwater head is not fully understood. In this part, taking the developed 3D model, the effect of the breakwater on the pore pressure build up in the region around the breakwater head is studied, Three typical positions are chosen for the analysis: x=164m, y=85m, z=13m (in front of breakwater), x=205m, y=15m, z=13m (near to the breakwater head), and x=246m, y=85m, z=13m (behind the breakwater).

Figure 6.21, 6.22 and 6.23 illustrate the historic curve of pore pressure build up at the chosen three typical positions around the caisson breakwater. In Figure 6.21, it can be seen that the pore

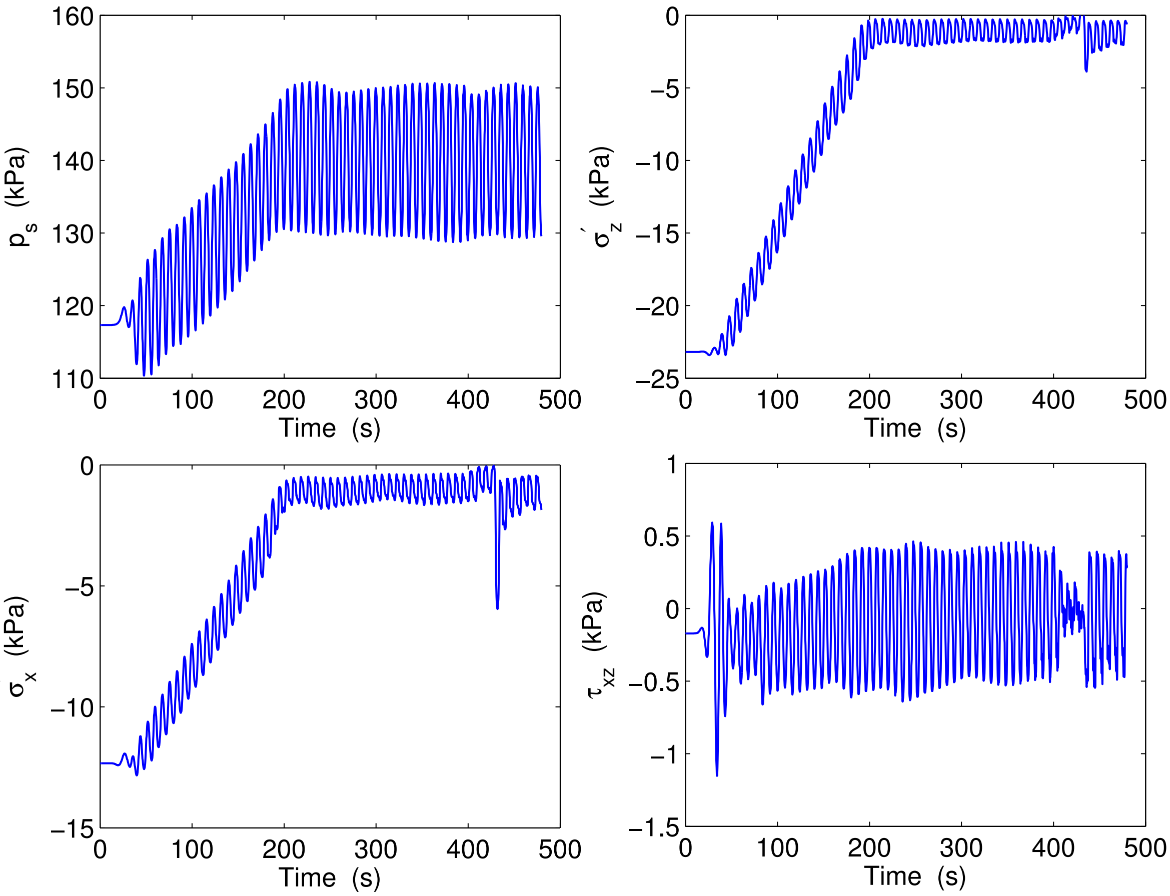

Figure 6.21: Pore pressure build up, and reduction of effective stresses at typical position (x=164m, y=85m, z=13m) in front of the breakwater. Note: p_s: pore pressure, σ'_x,σ'_z: effective stresses, τ_{xz}: shear stress.

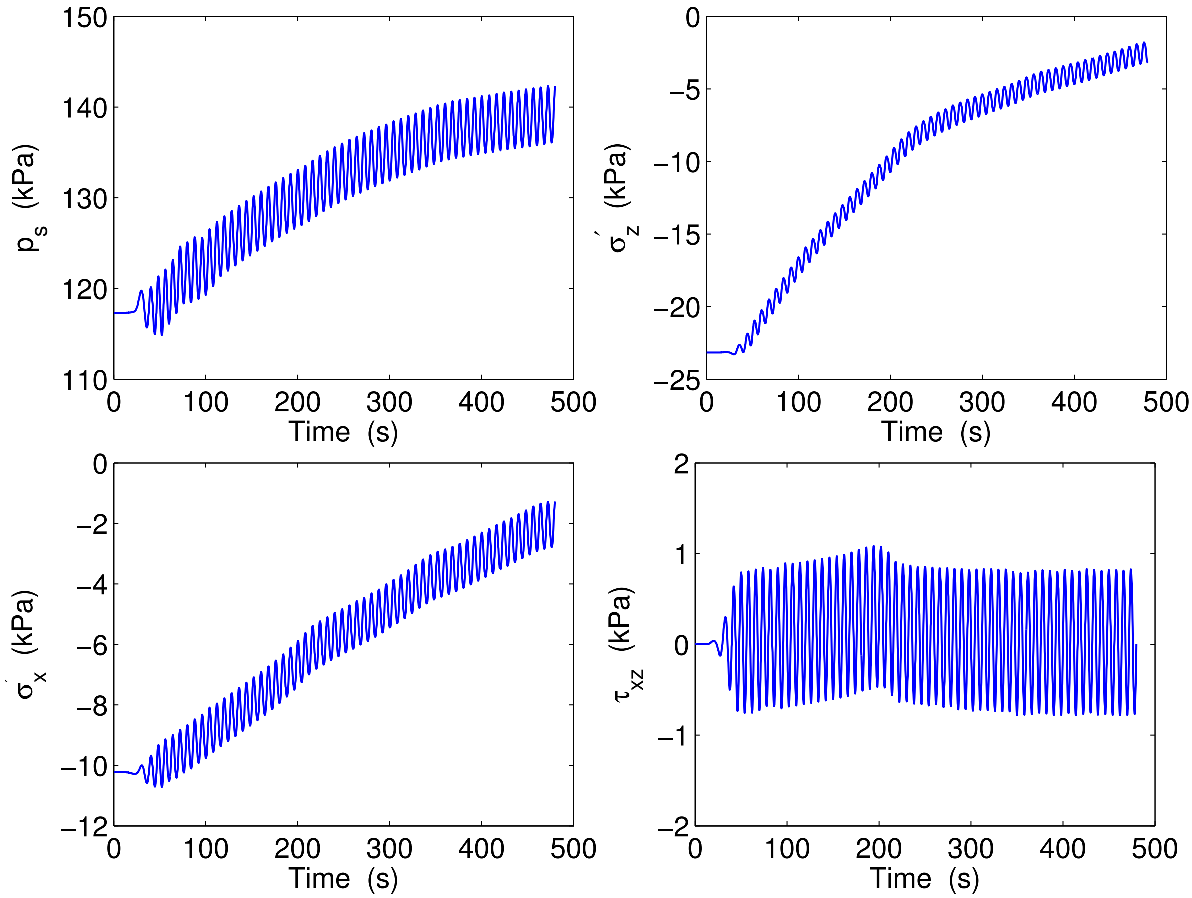

Figure 6.22: Pore pressure build up, and reduction of effective stresses at typical position (x=205m, y=15m, z=13m) near to the head of the breakwater. Note: p_s: pore pressure, σ'_x,σ'_z: effective stresses, τ_{xz}: shear stress.

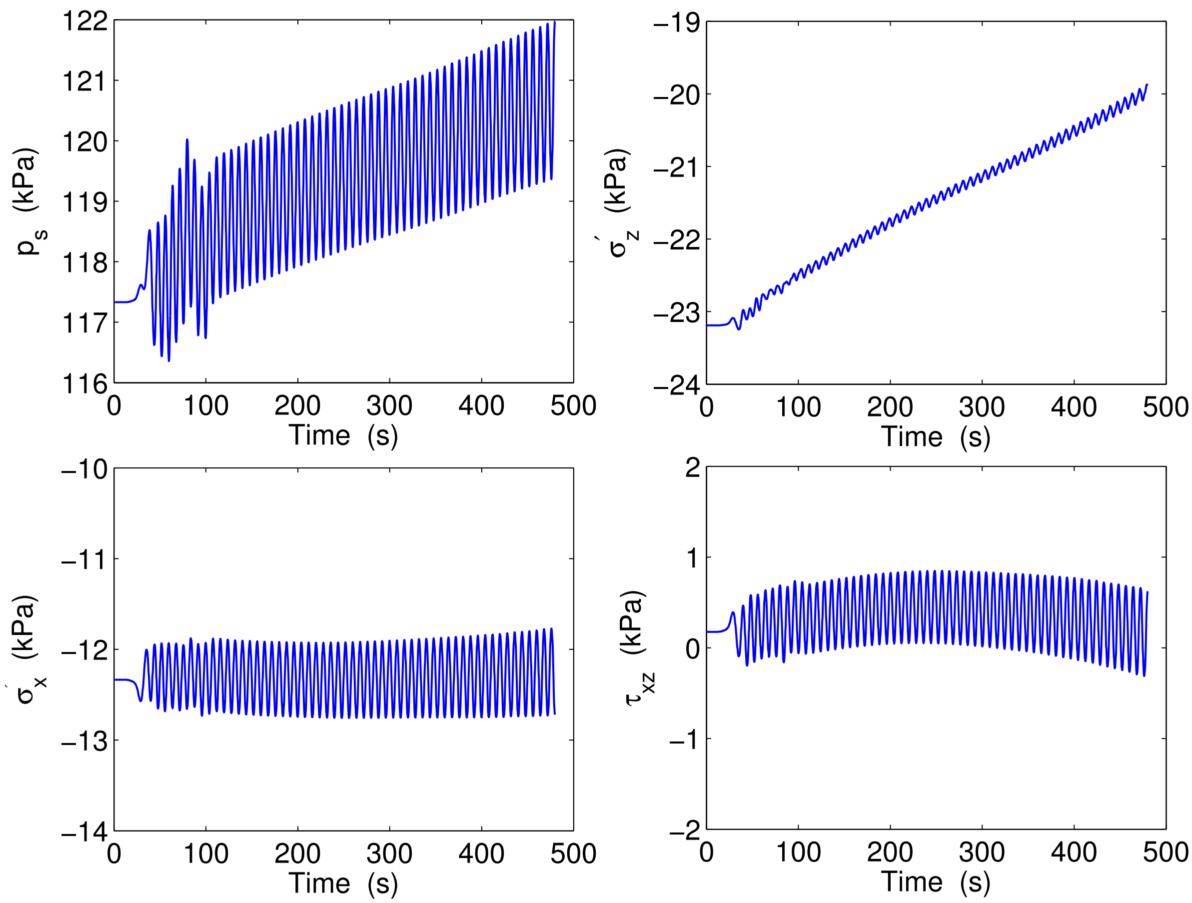

Figure 6.23: Pore pressure build up, and reduction of effective stresses at typical position (x=246m, y=85m, z=13m) behind the breakwater. Note: p_s: pore pressure, σ'_x,σ'_z: effective stresses, τ_{xz}: shear stress.

pressure at (x=164m, y=85m, z=13m) does not continuously build up after t=200s. Meanwhile, the effective stress σ'_x and σ'_z approaches zero from the initial compressive state. The seabed soil at position (x=164m, y=85m, z=13m) in front of the breakwater is nearly approaching the liquefaction status after t=200s. In Figure 6.22 and 6.23, it is found that the pore pressure continuously builds up in the whole process of wave loading at position x=205m, y=15m, z=13m (near to breakwater head), and x=246m, y=85m, z=13m (behind the breakwater). The effective stresses between the soil particles at the two positions continuously decrease. However, the gap to the zero stress (liquefaction status) exists. For example, the difference between the zero vertical effective stress is about 2.5kPa and 20kPa respectively at the two typical positions. However, it is still shown that the seabed soil at x=205m, y=15m, z=13m (near to the breakwater head) is much closer to the liquefaction status than the soil at x=246m, y=85m, z=13m (behind the breakwater). From the above analysis, it is indicated that the liquefaction potential is highest in the seabed foundation in front of the breakwater; and it is smallest in the seabed foundation behind the breakwater.

As analyzed in section 6.2 about the 3D wave field around the caisson breakwater, there are three kinds of wave: standing wave in front of the caisson breakwater, the diffracted wave behind the caisson breakwater and the progressive wave near the head of the breakwater. The wave height of this standing wave in front of the breakwater is about 3.0m, two times the original wave height at the wave maker. The height of the diffracted wave behind the breakwater is relatively much smaller due to the blocking effect of the breakwater to the wave. Correspondingly, the wave induced dynamic pressure acting on the seabed foundation is greatest in front of the breakwater, and weakest behind the breakwater. That is the reason why the pore pressure build up and residual liquefaction potential around the breakwater head is significantly different.

6.3.3 Residual liquefaction prediction in seabed foundation

From the above analysis about the wave induced pore pressure build up in elasto-plastic seabed, we know that the seabed soil could liquefy if the pore pressure is sufficient to overcome the overburdened weight of soil and/or breakwater. In this part, the residual liquefaction potential in the seabed foundation around the caisson breakwater under the 3D wave loading is investigated. Similarly, the residual liquefaction potential is evaluated adopting the definition equation (5.8) defined in Chatper 5.

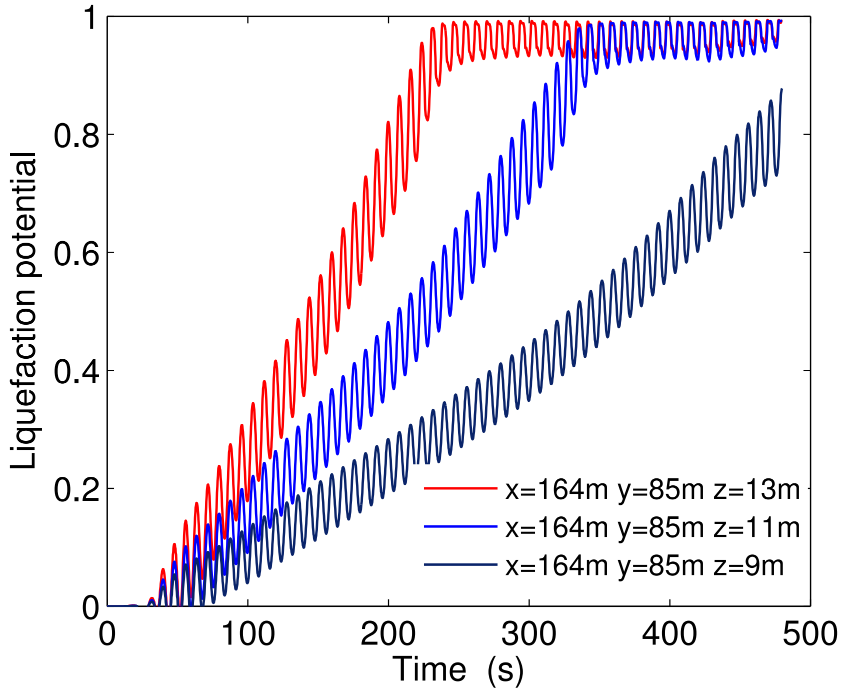

Figure 6.24: Liquefaction potential at typical position (x=164m, y=85m, z=13m) in front of the breakwater

Figure 6.24, 6.25 and 6.26 show the historic curve of wave induced residual liquefaction potential at three typical positions around the breakwater. From Figure 6.24, it can be seen that the wave induced residual liquefaction potential in the elasto-plastic seabed foundation gradually increases until reaching a value near to 1.0. However, the residual liquefaction potential in the elasto-plastic seabed foundation never equals to 1.0. This is because the adopted elasto-plastic model PZIII can not describe the behavior of liquefied soil (zero inter-granular effective stresses). Another phenomenon observed from Figure 6.24 is that the time for the residual liquefaction potential reaching the highest value along the depth of seabed foundation is significantly different. The time needed for the residual liquefaction potential reaching the highest value is positively related to buried depth of soil. For example, the time is about 230s for the liquefaction potential reaching the highest value when the depth is 2m (z=13m); while it is about 330s when the depth is 4m (z=11m). Until time t=480s, the liquefaction potential does not reach the highest value at position z=9m.

Figure 6.25 and 6.26 indicate that the residual liquefaction potential in the seabed foundation near to and behind the caisson breakwater is significantly less than that in front of the breakwater

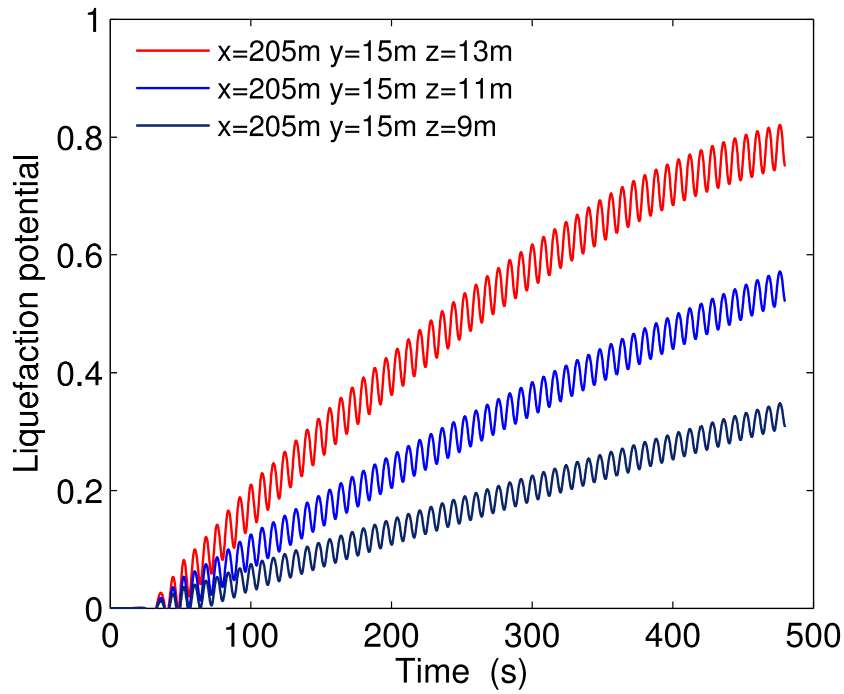

Figure 6.25: Liquefaction potential at typical position (x=205m, y=15m, z=13m) near to the head of the breakwater

at the same time. At time t=480s, the residual liquefaction potential at position x=205m, y=15m, z=13m (near to the head of breakwater)is only about 0.8; and it is only less than 0.1 at position x=246m, y=85m, z=13m (behind the breakwater), which is far away from the liquefaction. These two figures show that the residual liquefaction potential in the seabed foundation near to and behind the caisson breakwater is much less than that in the seabed foundation in front of the caisson breakwater. This attributes to 3D wave field around the caisson breakwater. The wave induced pressure in front of the breakwater is strongest; while it is weakest behind the breakwater. It is indicated that the cassion breakwater constructed on the seabed could effectively protect the seabed floor behind the breakwater. This conclusion is further shown by Figure 6.27. The distribution of wave induced residual liquefaction potential in the seabed foundation at the three positions around the breakwater is illustrated.

Figure 6.28 shows the the distribution of wave induced residual liquefaction potential in seabed foundation on plane z=12.5m at time t/T=20 and 60. As illustrated in Figure 6.28, the residual liquefaction potential in seabed foundation at time t/T=60 is significantly greater than that at time

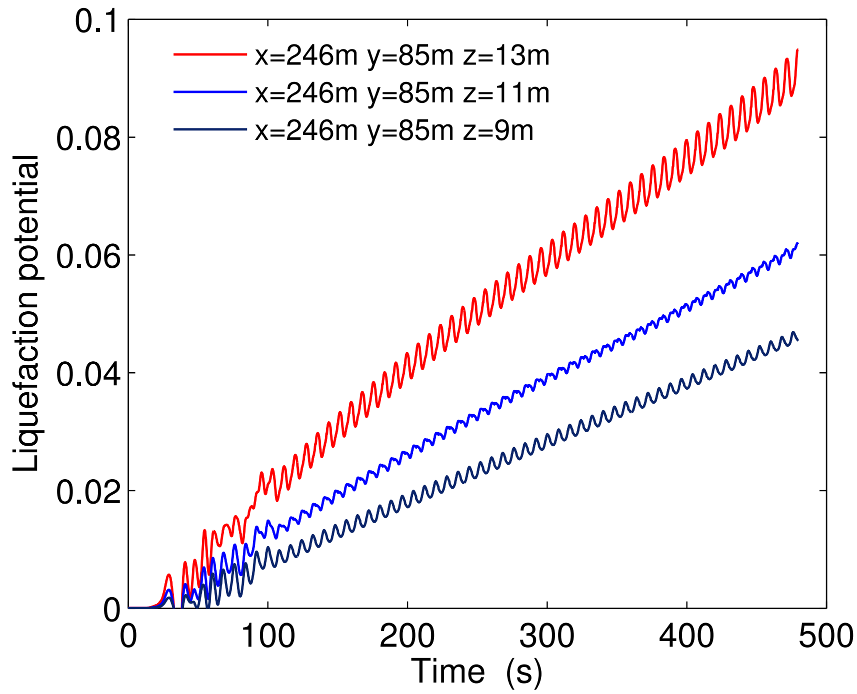

Figure 6.26: Liquefaction potential at typical position (x=246m, y=85m, z=13m) behind the breakwater

t/T=20. It is indicated that the pore pressure in the seabed foundation significantly builds up from time t/T=20 to 60 under the 3D wave loading. From Figure 6.28, it can be seen that the residual liquefaction potential behind the caisson breakwater is much less than that in front of the caisson breakwater at the same time. This phenomenon has been recognized in the above analysis. The protection effect of the caisson breakwater on the stability of the seabed behind it is also shown. The residual liquefaction potential in the seabed foundation under the caisson breakwater is nearly zero both at time t/T=20 and 60. This attributes to the fact that the gravity of breakwater compresses the soil beneath it, and makes it impossible for the inter-granular effective stresses to reach zero.

Another interesting phenomenon observed from Figure 6.28 is that the zones with high and small liquefaction potential appear alternatively in front of the breakwater. This can be attributed to the reason that the wave field in front of the breakwater is standing wave due to the interference between the incident wave and reflected wave. Under the nodes of standing wave, the liquefaction potential is high; while the liquefaction potential is small under the anti-nodes of the standing wave.

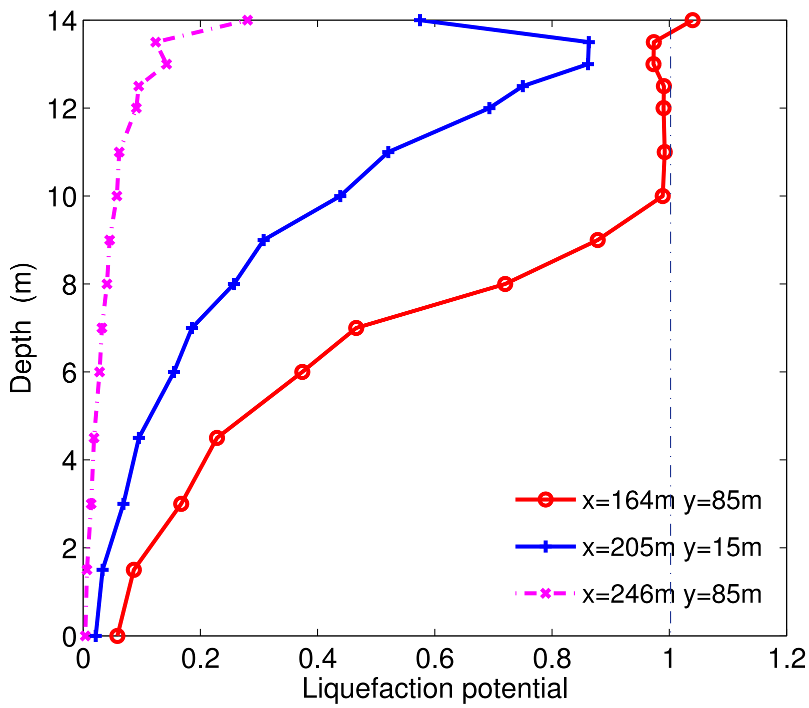

Figure 6.27: Distribution of liquefaction potential along the depth of seabed foundation around the caisson breakwater at time t/T=60

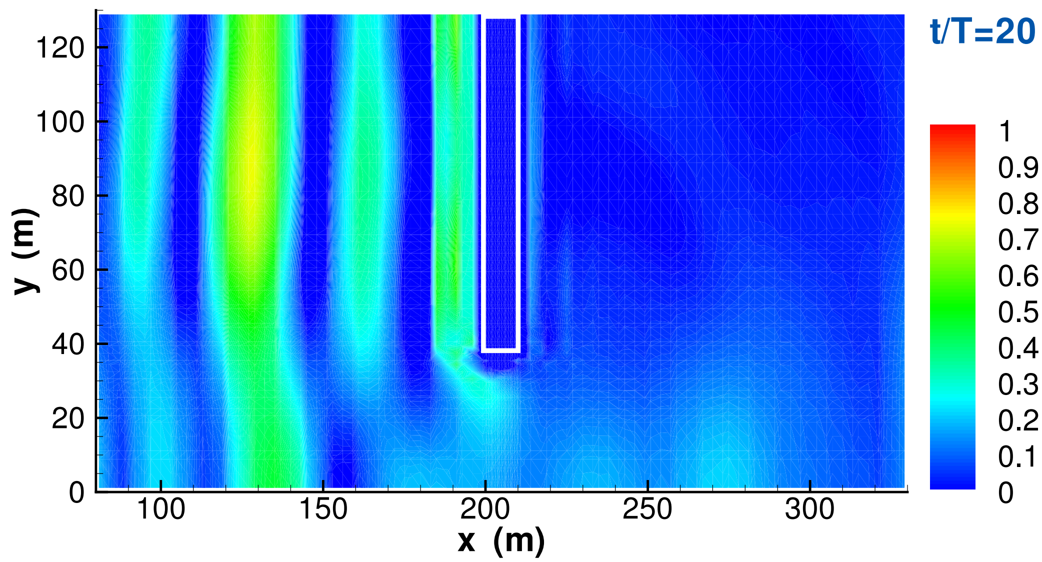

(a) t/T=20

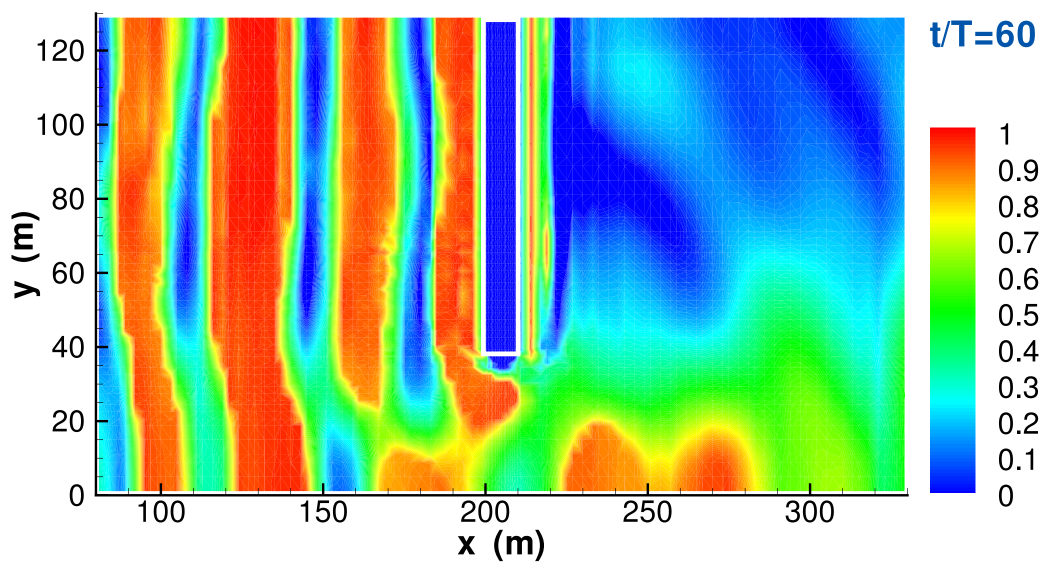

(b) t/T=60

Figure 6.28: Distribution of liquefaction potential in the seabed foundation on z=12.5m when t/T=20 (a) and t/T=60 (b)

6.3.4 Effect of the direction of breakwater

The effect of wave characteristics (wave height H and wave period T) , and the soil properties (permeability k and saturation S_r) have been investigated in Section 5.3 in Chapter 5. The effect of the direction of the breakwater on the wave induced residual liquefaction potential can not be studied in the 2D model. Here, adopting the developed 3D model, the effect of the direction of the breakwater on the wave induced residual liquefaction potential under 3D wave loading is investigated.

The same configurations shown in Figure 6.17 are adopted here. The angle between the incident wave and the caisson breakwater is θ=60° and θ=120° respectively. The 3D waves are generated at the wave maker adopting the same wave characteristics with the case when the θ=90°: H=1.5m, d=10m, and T=10s. As analyzed in part 6.2.6.2, the wave field in front of the caisson breakwater is the short-crested wave, rather than the standing wave if the incident waves obliquely propagating to the caisson breakwater. The wave induced force per metre length acting on the front lateral side of the breakwater is also much smaller than that if the breakwater is perpendicular with the incident wave. The different wave fields around the caisson breakwater head directly lead to the different distribution of the residual liquefaction zone in the seabed foundation around the caisson breakwater head.

Figures 6.29 and 6.30 show the 3D wave induced distribution of the residual liquefaction potential on the plane z=12.5m in the seabed foundation around the caisson breakwater when the θ=60° and θ=120° respectively. In Figures 6.29 and 6.30, some the same phenomenon with that when θ=90° can be observed. The residual liquefaction potential in the seabed foundation increases with the time of wave loading. The residual liquefaction potential in the seabed foundation when t/T=60 is significantly greater than that when t/T=20. The residual liquefaction potential behind the caisson breakwater is much less than that in front of the caisson breakwater at the same time. Also due to the compression of the caisson breakwater, the residual liquefaction potential in the seabed foundation under the caisson breakwater is apparently small, nearly zero.

Comparing the distributions of the residual liquefaction potential shown in Figures 6.28, 6.29 and 6.30, it is found that the direction of the caisson breakwater indeed has significant effect on distribution of the 3D wave induced residual liquefaction in the seabed foundation around the caisson breakwater head. The zones with high and low residual liquefaction potential distribute alternately

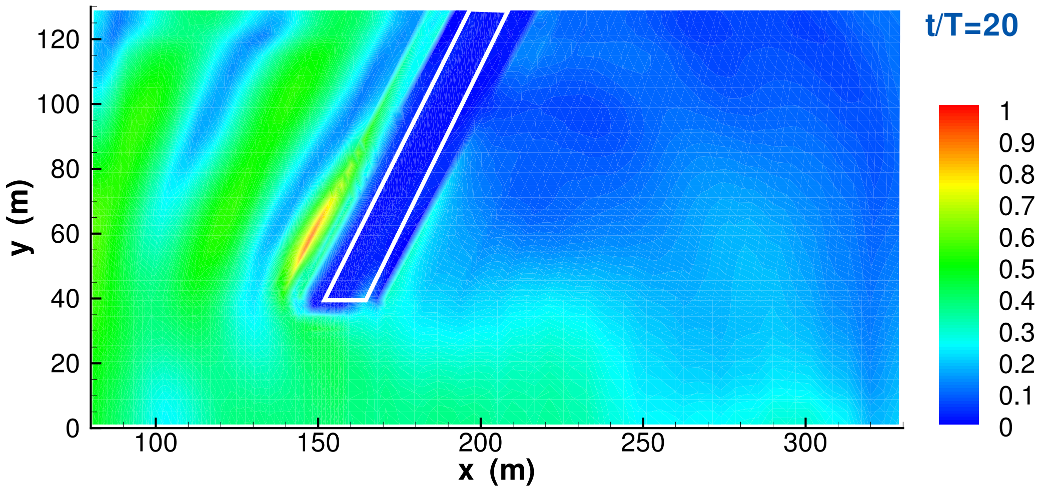

(a) t/T=20

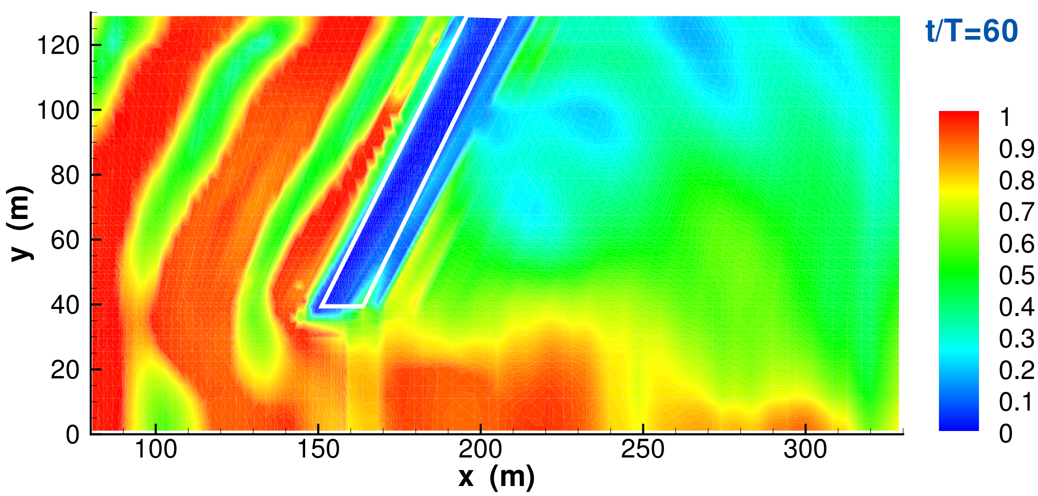

(b) t/T=60

Figure 6.29: Distribution of liquefaction potential in the seabed foundation on z=12.5m when t/T=20 (a) and t/T=60 (b) for the cases θ=60°

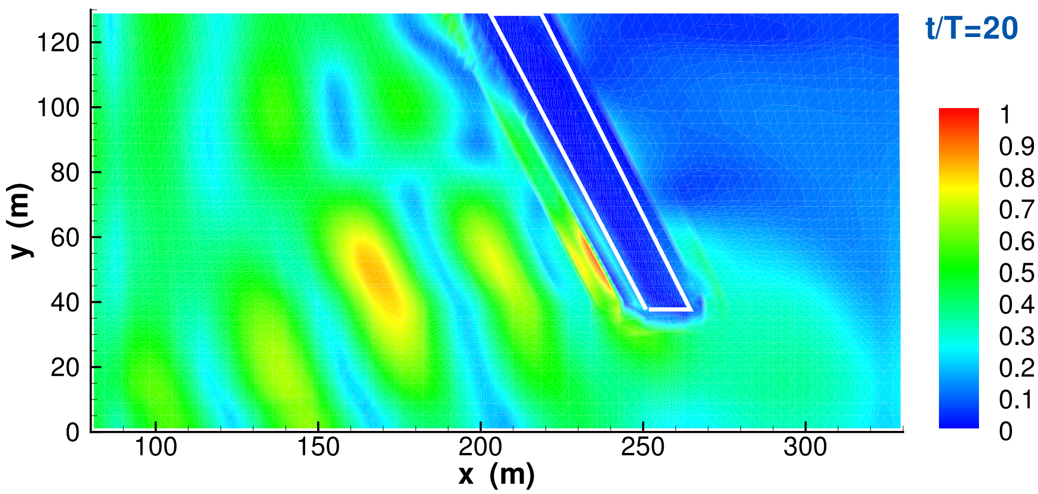

(a) t/T=20

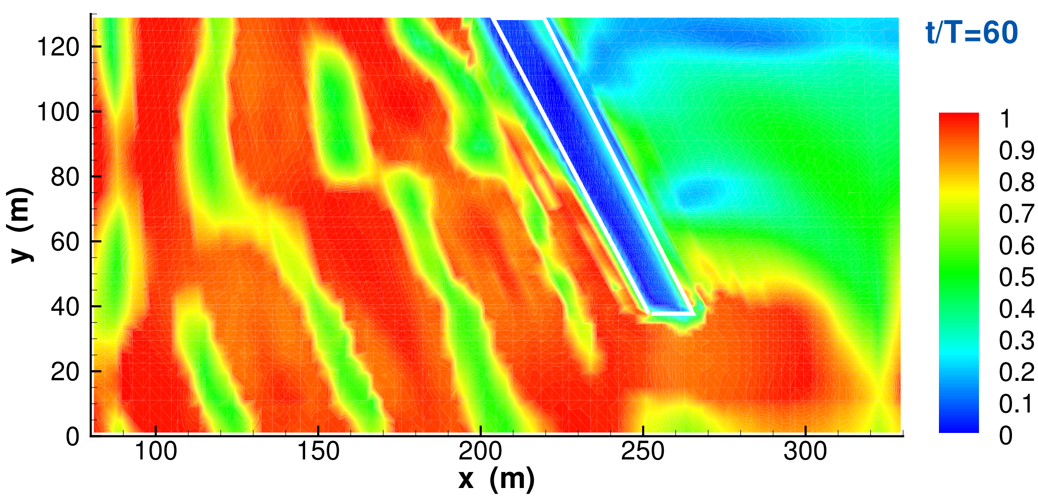

(b) t/T=60

Figure 6.30: Distribution of liquefaction potential in the seabed foundation on z=12.5m when t/T=20 (a) and t/T=60 (b) for the cases θ=120°

in the seabed foundation in front of the caisson breakwater; and they are basically parallel with the direction of the breakwater. In the zones with low residual liquefaction potential, the residual liquefaction potential can reach up to 0.5-0.6 when θ=60° and θ=120° . However, the residual liquefaction potential in these counterpart zones is nearly zero in the case θ=90°. Overall, the 3D wave induced residual liquefaction in the seabed foundation in front of the caisson breakwater is most intensive when θ=120°.

6.3.5 Summary

In this section, the interaction between the 3D wave, poro-elasto-plastic seabed foundation and a caisson breakwater is investigated adopting the developed 3D integrated model PORO-WSSI III. Based on the analysis of the numerical results, some conclusions are summaried as:

(1) Due to the compaction of the seabed soil under the wave induced cyclic loading, the caisson breakwater continuously subsides in the interaction process between the 3D wave, poro-elasto-plastic seabed foundation and the caisson breakwater.

(2) Under the 3D wave loading, the pore pressure in the seabed foundation builds up. The rate of the pore pressure build up in the seabed foundation in front of the caisson breakwater is much greater than that in the the seabed foundation behind the cassion breakwater; and the rate of the pore pressure build up in the seabed foundation is negatively related to the buried depth of seabed soil. The pore pressure in the seabed foundation can not build up continuously. When the excess pore pressure is large enough to overcome the overburdened soil weight, the inter-granular effective stresses decrease to or nearly to zero; the seabed soil become liquefied. The liquefaction analysis indicates that the 3D wave induced residual liquefaction potential is much greater in the seabed foundation in front of the caisson breakwater than that in the seabed foundation behind the caisson breakwater, and increases with the time of wave loading. The zones with high and low residual liquefaction potential in the seabed foundation in front of the caisson breakwater distribute alternately, and basically are parallel with the direction of the caisson breakwater.

(3) The parametric study indicates that the direction of the breakwater has significant effect on the distribution of the 3D wave induced residual liquefaction in the seabed foundation around the breakwater head. This is attributed to the different wave field being formed around the breakwater head.

Chapter 7

Conclusions and Future Works

7.1 Conclusion

The objective of this thesis is to develop integrated numerical models to investigate the mechanism of wave-seabed-marine structures interaction. A 2D integrated numerical model (PORO-WSSSI II) and its 3D version (PORO-WSSI III) have been developed in this thesis. In the two integrated numerical models, two sub-models are involved: wave model and soil model. In the wave model, the Volume-Averaged Reynolds Averaged Navier-Stokes (VARANS) equation is adopted as the governing equation for the wave motion and porous flow in porous medium; and it is solved using the finite difference method. The VOF method is used to trace the free surface of wave. In the soil model, the Biot's dynamic equation known as "$u - p$" is adopted to govern the behavior of seabed soil; and it is solved using finite element method. A coupling algorithm is developed to integrate the two sub-models together, in which the non-match mesh scheme and non-match time scheme are used. The integrated numerical models have been validated by a series of laboratory wave flume tests available in previous literatures. The well agreement between the numerical results determined by developed model and the experimental data shows that the developed integrated numerical model is reliable.

By adopting the analytical solution of third-order wave and current interaction, the seabed response under wave-current loading is investigated. The results indicate that the ocean current has significant effect on the seabed response. The following current makes the seabed responses to the loading more strongly; while, the opposing current weakens the seabed response. The maximum depth of momentary liquefaction is positively related to the velocity of ocean current (the velocity of opposing current is negative).

By using the developed 2D integrated model PORO-WSSI II, the interaction between wave, poro-elastic seabed and breakwater is studied. The sway of breakwater under wave loading can be captured. The numerical analysis shows that the wave induced oscillatory pore pressure, and effective stresses vibrate periodically in poro-elastic seabed. The upward and downward wave induced seepage force in the zone near to the surface of seabed appears alternatively, lead to that the seabed under wave trough liquefies periodically. The parametric study indicates that the wave induced momentary liquefaction in poro-elastic seabed is affected by the wave characteristics.

The interaction between wave, poro-elasto-plastic seabed and breakwater is further examined. Due to the compaction of soil particles under cyclic loading, the breakwater built on elasto-plastic seabed also sways under the wave loading; at the meantime, the breakwater subsides downward. This phenomenon is a obvious difference between the poro-elastic seabed and poro-elasto-plastic seabed. The pore pressure in elasto-plastic seabed obviously builds up under the wave loading. When the residual pore pressure at a position in seabed is enough to overcome the overburden soil weight, then the soil at this position is liquefied. The liquefied soil behavior like a kind of liquid without any shear resistance. The occurrence of liquefaction in seabed foundation is a very dangerous factor for the stability of marine structures. In the 2D model, the regular ocean wave can not pass through the breakwater. This results in no obvious wave loading on the seabed behind the breakwater. Therefore, the liquefaction potential in the seabed in front of breakwater is much significantly greater than that in the seabed behind the breakwater. This is a limitation of the developed integrated 2D model; and can be solved by using the 3D model. The liquefaction potential in the seabed in front of breakwater increases continuously to a value which is nearly 1.0 under long term wave loading. At the same time, the liquefaction potential in upper seabed is greater than that in lower seabed. After the long term wave loading, the wave induced residual pore pressure can not further increase in the zone near to the seabed surface due to the fact that the plastic deformation in seabed soil nearly reaches its maximum value. Furthermore, the dissipation rate of pore pressure begin to be greater than the rate of pore pressure build up. The liquefaction potential decreases in the zone near to the seabed surface in the late stage of wave loading. The parametric study shows that the liquefaction potential, related to the pore pressure build up is positively related to wave height, wave period; and negatively related to permeability and saturation of seabed soil.

The developed integrated model PORO-WSSI III is adopted to investigate the interaction between 3D wave, poro-elastic seabed and breakwater. There are three kinds of wave field around the breakwater head: standing wave or short-crested wave in front of breakwater, progressive wave near to the breakwater head, and diffracted wave behind breakwater. The wave induced pressure acting on seabed is greatest in front of breakwater, and makes the seabed in front of breakwater response to the standing wave or the short-crested wave most strongly. The maximum depth of wave induced momentary liquefaction in the seabed in front of breakwater is also deepest. The seabed response in the seabed behind breakwater is weakest. There is no momentary liquefaction occurred in the wave loading process. It is indicated that the breakwater indeed could effectively protect the seabed behind it. The direction of breakwater also has effect on the interaction. It is shown that the oblique breakwater with the incident wave is favourable in design.

Under the same frame, the interaction between 3D wave, poro-elasto-plastic seabed and breakwater is also studied. There are also three kinds of wave field around breakwater head. The numerical analysis shows that the wave induced pore pressure build up and the characteristics of residual liquefaction potential in the seabed in front of breakwater are basically the same with that in 2D elasto-plastic seabed. However, the differences are huge in the seabed behind breakwater. In 2D model, there is basically no pore pressure build up due to the fact that there is no wave loading on the seabed behind breakwater. While, in 3D model, there is diffracted wave induced pressure acting on the seabed behind breakwater. There is pore pressure build up in the seabed behind breakwater. However, the rate of pore pressure build up in this area is significantly less than that in the seabed in front of breakwater. Correspondingly, the residual liquefaction potential in the seabed behind breakwater is also significantly less than that in the seabed in front of breakwater. The parametric study indicates that the direction of the breakwater has significant effect on the distribution of the 3D wave induced residual liquefaction potential in the seabed foundation around the breakwater head due to the different wave field around the breakwater head.

7.2 Future works

In the governing equation for seabed soil, the Darcy's law is used to describe the porous flow in seabed soil. Actually, the Darcy's law is only applicable for the laminar flow. It requires that the flowing velocity of pore water is apparently small, and the Reynolds number is generally less than 1 (Gu and Wang, 1991). In some cases, the laminar flow and the turbulent flow would both exist. Under such situation, more complicated formulation, for example, Forchheimer equation, should be used to describe the porous flow in the future. Then, the porous flow in coarse sand, gravel could be modeled more accurately. Another aspect is that the relative displacement of pore water to the soil particles need to be considered for the porous flow with large Reynolds number.

Here, it is interesting to mention that the wave induced pore pressure in rubble mound (the Reynolds number R_e reaches up to 200-8000) predicted by using "$u - p$" approximation is basically the same with that determined by the VARANS equation in this thesis (see Section 3.4.4 and Section 5.2). It is indicated that the previous knowledge on the applicability of Biot's equations for the turbulent porous flow is debatable. In future, we can further identify the application range of Reynold number (R_e) of porous flow that could be described by the Biot's equation.

The elasto-plastic model PZIII used in this thesis is an excellent model to describe the soil behavior under monotonic and cyclic loading. It has been validated by a series of laboratory tests. However, it can not describe the post-liquefaction behaviour of soil, including the liquefaction and densification. The PZIII model alway makes the inter-granular effective stresses approach 0 (nearly liquefied). But the fully liquefied status is never reached. In future, a new constitutive model for seabed soil can be developed, and integrated into PORO-WSSI II/III to investigate the process of liquefaction and densification of seabed soil under long term wave loading.

In the practice of engineering, the breakwater and the seabed foundation are two separate parts. The contact interaction between the breakwater and seabed foundation at their interface is very complicated. Under wave loading, the breakwater would have permanent relative slipping displacement. In the future, a kind of slip element considering the contact effect between the breakwater and seabed could be developed to estimate the permanent slipping displacement of breakwater under wave loading.

The demand for the memory in the 3D computation is huge, for example, the 3D program need nearly 30G memory when the number of 3D FEM element is only 6330. In future, some optimizations must be performed in 3D program codes to reduce the memory demand. Otherwise, the application of the 3D integrated model PORO-WSSI III to some large-scale cases basically becomes impossible.

Bibliography

Bennett, R. H. (1978). Pore-water pressure measurements: Mississippi delta submarine sediments. *Marine Geotechnology*, 2:177–189.

Bennett, R. H. and Faris, J. R. (1979). Ambient and dynamic pore pressures in fine-grained submarine sediments. *Applied Ocean Reserach*, 1(3):115–123.

Bierawski, L. G. and Maeno, S. (2004). Vof-fem numerical model of submerged breakwater on permeable bottom. *Journal of Applied Mechanics JSCE*, 7:945–952.

Biot, M. A. (1941). General theory of three dimensional consolidation. *Journal of Applied Physics*, 12(2):155–164.

Biot, M. A. (1955). Theory of deformation of a porous viscoelastic anisotropic solid. *Journal of Applied Physics*, 27(5):459–467.

Biot, M. A. (1956a). Theory of elasticity and consolidation for a porous anisotropic solid. *Journal of Applied Physics*, 26(2):182–185.

Biot, M. A. (1956b). The theory of propagation of elastic waves in a fluid-saturated porous solid. high-frequency range. *J. Acoustical Society of America*, 28(2):179–191.

Biot, M. A. (1956c). The theory of propagation of elastic waves in a fluid-saturated porous solid. low-frequency range. *J. Acoustical Society of America*, 28(2):168–178.

Biot, M. A. (1962). Mechanics of deformation and acoustic propagation in porous media. *Journal of Applied Physics*, 33(4):1482–1498.

Bjerrum, J. (1973). Geotechnical problem involved in foundations of structures in the North Sea. *Géotechnique*, 23(3):319–358.

Campo, J. M. and Vicente, N. (2011). Failures of harbour walls at malaga and barcelona. *Bulletin of Engineering Geology and the Environment*, 70(1):1–6.

Cha, D., Zhang, H., and Blumenstein, M. (2011). Prediction of maximum wave-induced liquefaction in porous seabed using multi-artificial neural network model. *Ocean Engineering*, 38(7):878–887.

Cha, D. H., Jeng, D. S., Rahman, M. S., Sekiguchi, H., Zen, K., and Yamazaki, H. (2002). Effects of dynamic soil behaviour on the wave-induced seabed response. *International Journal of Ocean Engineering and Technology*, 16(5):21–33.

Chan, A. H. C. (1988). *A unified finite element solution to static and dynamic problems of geomechanics*. PhD thesis, University of Wales, Swansea Wales.

Chen, C. Y. and Hsu, J. R. C. (2005). Interaction between internal waves and a permeable seabed. *Ocean Engineering*, 32(5-6):587–621.

Cheng, L., Sumer, B. M., and Fredsoe, J. (2001). Solution of pore pressure build up due to progressive waves. *International Journal for Numerical and Analytical Method in Geomechanics*, 25(9):885–907.

Cheng, Y.-Z., Wang, Y.-X., and Jiang, C.-B. (2007). Coupling model of nonlinear wave and sandy seabed dynamic interaction. *China Ocean Engineering*, 21(1):77–89.

Cheng, Y. Z., Wang, Y. X., and Jiang, C. B. (2008). Numerical analysis of pore water pressure response in sandy seabed under nonlinear wave in shallow water. *Ocena Engineering*, 26(2):63–68.

Choudhury, B., Dasari, G. R., and Nogami, T. (2006). Laboratory study of liquefaction due to wave-seabed interaction. *Journal of Geotechnical and Geoenvironmental Engineering ASCE*, 132(7):842–851.

Chung, S. G., Kim, S. K., Kang, Y. J., Im, J. C., and Prasad, K. N. (2006). Failure of a breakwater founded on a thick normally consolidated clay layer. *Géotechnique*, 56(3):393–409.

Di, Y. and Sato, T. (2003). Liquefaction analysis of saturated soils taking into account variation in porosity and permeability with large deformation. *Computers and Geotechnics*, 30(7):623–635.

Dunn, S. L., Vun, P. L., Chan, A. H. C., and Damgaard, J. S. (2006). Numerical modeling of wave-induced liquefaction around pipelines. *Journal of Waterway, Port, Coastal and Ocean Engineering*, 132(4):276–288.

Esrig, M. I. and Kirby, R. C. (1977). Implication of gas content for predicting the stability of submarine slopes. *Marine Geotechnology*, 17:58–67.

Franco, L. (1994). Vertical breakwaters: the italian experience. *Coastal Engineering*, 22(1-2):31 – 55.

Gatmiri, B. (1990). A simplified finite element analysis of wave-induced effective stress and pore pressures in permeable sea beds. *Géotechnique*, 40(1):15–30.

Gatmiri, B. (1992). Response of cross-anisotropic seabed to ocean waves. *Journal of Geotechnical Engineering ASCE*, 118(9):1295–1314.

Groot, M. B. D., Bolton, M. D., Foray, P., Meijers, P., Palmer, A. C., Sandven, R., Sawicki, A., and Teh, T. C. (2006a). Physics of liquefaction phenomena around marine structures. *Journal of Waterway, Port, Coastal and Ocean Engineering ASCE*, 132(4):227–243.

Groot, M. B. D., Kudella, M., Meijers, P., and Oumeraci, H. (2006b). Liquefaction phenomena underneath marine gravity structures subjected to wave loads. *Journal of Waterway, Port, Coastal and Ocean Engineering ASCE*, 132(4):325–335.

Gu, Z. and Wang, H. (1991). Gravity waves over porous bottoms. *Coastal Engineering*, 15(5-6):497–524.

Guillen, P. M. (2008). Large breakwaters in deep water in northern spain. *Proceeding of the institution of Civil Engineers, Maritime Engineering*, 161(MA4):175–186.

Harlow, H. E. (1980). Large rubble-mound breakwater failures. *Journal of Waterway, Port, Coastal and Ocean Engineering ASCE*, 106(2):275–278.

Hsieh, P. C. (2006). A viscoelastic model for the dynamic response of soils to periodical surface water disturbance. *International Journal for Numerical and Analytical Methods in Geomechanics*, 30(12):1201–1212.

Hsu, H. C., Chen, Y. Y., Hsu, J. R. C., and Tseng, W. J. (2009). Nonlinear water waves on uniform current in lagrangian coordinates. *Journal of Nonlinear Mathematical Physics*, 16(1):47–61.

Hsu, J. R. and Jeng, D. S. (1994). Wave-induced soil response in an unsaturated anisotropic seabed of finite thickness. *International Journal for Numerical and Analytical Methods in Geomechanics*, 18(11):785–807.

Hsu, J. R. C., Jeng, D. S., and Lee, C. P. (1995). Oscillatory soil response and liquefaction in an unsaturated layered seabed. *International Journal for Numerical and Analytical Methods in Geomechanics*, 19(12):825–849.

Hsu, J. R. C., Jeng, D. S., and Tsai, C. P. (1993). Short-crested wave-induced soil response in a porous seabed of infinite thickness. *International Journal for Numerical and Analytical Methods in Geomechanics*, 17(8):553–576.

Hsu, T. J., Sakakiyama, T., and Liu, P. L. F. (2002). A numerical model for wave motions and turbulence flows in front of a composite breakwater. *Coastal Engineering*, 46:25–50.

Hua, L. N. and Yu, X. P. (2009a). Element-free galerkin method for response of stratified seabed under wave action. *Journal of Hydrodynamics, Ser. B*, 21(4):550 – 556.

Hua, L. N. and Yu, X. P. (2009b). An enhanced element-free galerkin method for dynamic response of poroelastic seabed. *Journal of Hydrodynamics, Ser. B*, 21(3):429 – 435.

Hur, D. S., Kim, C. H., Kim, D. S., and Yoon, J. S. (2008). Simulation of the nonlinear dynamic interactions between waves, a submerged breakwater and the seabed. *Ocean Engineering*, 35:511–522.

Hur, D. S., Kim, C. H., and Yoon, J. S. (2010). Numerical study on the interaction among a nonlinear wave, composite breakwater and sandy seabed. *Coastal Engineering*, 57(10):917–930.

Hur, D.-S. and Mizutani, N. (2003). Numerical estimation of the wave forces acting on a three - dimensional body on a submerged breakwater. *Coastal Engineering*, 47(3):329–345.

Jeng, D. S. (1996a). Wave-induced liquefaction potential at the tip of a breakwater. *Applied Ocean Research*, 18(5):229–241.

Jeng, D. S. (1996b). Wave-induced liquefaction potential in a cross-anisotropic seabed. *Journal of the Chinese Institute of Engineering*, 19(1):59–70.

Jeng, D. S. (1997a). Soil response in cross-anisotropic seabed due to standing waves. *Journal of Geotechnical and Geoenvironmental Engineering ASCE*, 123(1):9–19.

Jeng, D. S. (1997b). Wave-induced seabed instability in front of a breakwater. *Ocean Engineering*, 24(10):887–917.

Jeng, D. S. (1997c). *Wave-induced seabed response in front of a breakwater*. PhD thesis, University of Western Australia.

Jeng, D. S. (1998a). Effect of cross-anisotropic soil behaviour on the wave-induced seabed response. *Géotechnique*, 48(4):555–561.

Jeng, D. S. (1998b). Wave-induced seabed response in a cross-anisotropic seabed in front of a breakwater: An analytical solution. *Ocean Engineering*, 25(1):49–67.

Jeng, D. S. (2000). On calculating the length of a short-crested wave over a porous seabed. *Applied Ocean Research*, 22(2):63–73.

Jeng, D.-S. (2001). A new wave dispersion equation: Effects of soil characteristics. *Journal of Offshore Mechanics and Arctic Engineering, ASME*, 125(4):177–181.

Jeng, D.-S. (2003). Wave-induced sea floor dynamics. *Applied Mechanics Reviews*, 56(4):407–429.

Jeng, D.-S. (2007). Random wave induced pore-pressure build-up in marine sediments. In *Proceedings of the International Offshore and Polar Engineering Conference*, pages 2405–2410.

Jeng, D.-S., Cha, D. F., and Blumenstein, M. (2004). Neural network model for the prediction of wave-induced liquefaction potential. *Ocean Engineering*, 31(17-18):2073–2086.

Jeng, D. S. and Cha, D. H. (2003). Effects of dynamic soil behavior and wave non-linearity on the wave-induced pore pressure and effective stresses in porous seabed. *Ocean Engineering*, 30(16):2065–2089.

Jeng, D. S., Cha, D. H., Lin, Y. S., and Hu, P. S. (2000). Analysis on pore pressure in an anisotropic seabed in the vicinity of a caisson. *Applied Ocean Research*, 22:317–329.

Jeng, D. S., Cha, D. H., Lin, Y. S., and Hu, P. S. (2001). Wave-induced pore pressure around a composite breakwater. *Oceaning Engineering*, 28(10):1413–1435.

Jeng, D. S. and Hsu, J. R. C. (1996). Wave-induced soil response in a nearly saturated seabed of finite thickness. *Géotechnique*, 46(3):427–440.

Jeng, D. S. and Lin, Y. S. (1996). Finite element modelling for water waves-seabed interaction. *Soil Dynamics and Earthquake Engineering*, 15(5):283–300.

Jeng, D. S. and Lin, Y. S. (1997). Non-linear wave induced response of porous seabeds: A finite element analysis. *International Journal for Numerical and Analytical Methods in Geomechanics*, 21(1):15–42.

Jeng, D. S. and Ou, J. (2010). 3d models for wave-induced pore pressures near breakwater heads. *Acta Mechanica*, 215(1-4):85–104.

Jeng, D. S. and Rahman, M. S. (2000). Effective stresses in a porous seabed of finite thickness: Inertia effects. *Canadian Geotechnical Journal*, 37(4):1388–1397.

Jeng, D. S. and Seymour, B. R. (1997). Wave-induced pore pressure and effective stresses in a porous seabed with variable permeability. *Journal of Offshore Mechanics and Arctic Engineering Transaction ASME*, 119(4):226–233.

Jeng, D.-S. and Seymour, B. R. (2007). Simplified analytical approximation for pore-water pressure buildup in marine sediments. *Journal of Waterway, Port, Coastal and Ocean Engineering ASCE*, 133(4):309–312.

Jeng, D.-S., Seymour, B. R., and Li, J. (2007). A new approximation for pore pressure accumulation in marine sediment due to water waves. *International Journal for Numerical and Analytical Methods in Geomechanics*, 31(1):53–69.

Karim, M. R., Nogami, T., and Wang, J. G. (2002). Analysis of transient response of saturated porous elastic soil under cyclic loading using element-free galerkin method. *International Journal of Solids and Structures*, 39(6):6011–6033.

Karunarathna, S. A. S. A. and Lin, P. (2006). Numerical simulation of wave damping over porous seabeds. *Coastal Engineering*, 53(10):845–855.

Katona, M. G. and Zienkiewicz, O. C. (1985). A unified set of single step algorithms. part 3: The beta-m method, a generalisation of the newmark scheme. *Internationial Journal of Numerical Methods in Engineering*, 21:1345–1359.

Kim, N. H., Young, Y. L., Yang, S. B., and Park, K. I. (2006). Wave damping analysis in a porous seabed. *KSCE Journal of Civil Engineering*, 10(5):305–310.

Kitano, T. and Mase, H. (2001). Wave-induced porewater pressure in a seabed with inhomogeneous permeability. *Ocean Engineering*, 28(3):279–296.

Kitano, T., Mase, H., and Nakano, S. (1999). Effects of inhomogeneity of permeability on wave-induced porewater pressure in seabed. In *Proceeding of Candian Coastal Conference*, volume 2, pages 611–623.

Kumagai, T. and Foda, M. A. (2002). Analytical model for response of seabed beneath composite breakwater to wave. *Journal of Waterway, Port, Coastal and Ocean Engineering ASCE*, 128(2):62–71.

Lee, J. F. and Lan, Y. J. (2002). On waves propagating over poro-elastic infinite seabed. *Ocean Engineering*, 29(8):931–946.

Lee, T. C., Tsai, C. P., and Jeng, D. S. (2002a). Ocean wave propagating over a porous seabed of finite thickness. *Ocean Engineering*, 29:1577–1601.

Lee, T. L., Tsai, C. P., and Jeng, D.-S. (2002b). Ocean waves propagating over a coulomb-damped poroelastic seabed of finite thickness: An analytical solution. *Computers and Geotechnics*, 29(2):119–149.

Li, J. and Jeng, D. S. (2008). Response of a porous seabed around breakwater heads. *Ocean Engineering*, 35(8-9):864–886.

Lin, M. and Jeng, D.-S. (2003). Comparison of existing poroelastic models for wave damping in a porous seabed. *Ocean Engineering*, 30(11):1335–1352.

Lin, M. and Jeng, D. S. (2004). A 3-d model for ocean waves over a columb-damping poroelastic seabed. *Ocean Engineering*, 31(5-6):561–585.

Lin, P. and Liu, P. L. F. (1998). A numerical study of breaking waves in the surf zone. *Journal of Fluid Mechanics*, 359:239–264.

Lin, Y. S. and Jeng, D. S. (1996). Response of poro-elastic seabed to a 3-d wave system: A finite element analysis. *Coastal Engineering in Japan*, 39(2):165–183.

Lin, Y. S. and Jeng, D. S. (1997). The effect of variable permeability on the wave-induced seabed response. *Ocean Engineering*, 24(7):623–643.

Lin, Y. S. and Jeng, D. S. (2000). Short-crested wave-induced liquefaction in porous seabed. *Journal of Geotechnical and Geoenvironmental Engineering ASCE*, 126(5):448–494.

Lin, Z. P. and Liu, P. L.-F. (1999). Internal wave-maker for navier-stokes equations models. *Journal of Waterway, Port, Coastal, and Ocean Engineering*, 99(4):207–215.

Liu, P. (1973). Damping of water waves over porous bed. *Journal of the Hydraulics Division ASCE*, 99(12):2263–2271.

Liu, P. (1977). On gravity waves propagated over a layered permeable bed. *Coastal Engineering*, 1:135–148.

Liu, P. L. F., Lin, P. Z., Chang, K. A., and Sakakiyama, T. (1999). Numerical modeling of wave interaction with porous structures. *Journal of Waterway, Port, Coastal and Ocean Engineering, ASCE*, 125:322–330.

Liu, P. L. F., Park, Y. S., and Lara, J. L. (2007). Long wave induced flows in an unsaturated permeable seabed. *Journal of Fluid Mechanics*, 586:323–345.

Liu, X. and Garcia, M. H. (2007). Numerical investigation of seabed response under waves with free-surface water flow. *International Journal of Offshore and Polar Engineering*, 17(2):97–104.

Liu, X. F. and Garcia, M. H. (2006). Numerical simulation of sea bed response under waves with coupled solver of biot consolidation equations and free surface water flow. In *Proceedings of the Seventh 2006 ISOPE Pacific/Asia Offshore Mechanics Symposium, ISOPE PACOMS 2006*, pages 127–134.

Liu, Z., Jeng, D.-S., Chan, A. H. C., and Luan, M. (2009). Wave-induced progressive liquefaction in a poro-elastoplastic seabed: A two-layered model. *International Journal for Numerical and Analytical Methods in Geomechanics*, 33(5):591–610.

Lu, H. B. (2005). The research on pore water pressure response to waves in sandy seabed. Master's thesis, Changsha University of Science & Technology, Changsha, Hunan China.

Lu, X. (1999). *The analysis on liquefaction of saturated sand under vertical vibration loading*. PhD thesis, Institute of Mechanics, Chinese Academy of Sciences, Beijing.

Lu, X. and Cui, P. (2004). The liquefaction and displacement of highly saturated sand under water pressure oscillation. *Ocean Engineering*, 31(7):795–811.

Luan, M. T. and Wang, D. (2001). Numerical analyses of dynamic response of porous seabed under wave loading. *Chinese Ocean Engineering*, 19(4):40–45.

Lundgren, H., Lindhardt, J. H. C., and Romold, C. J. (1989). Stability of breakwaters on porous foundation. In *Proceeding of 12th International Conference on Soil Mechanics and Foundation Engineering*, volume 1, pages 451–454.

Madga, W. (1990). On one-dimensional model of pore pressure generation in highly saturated sandbed due to cyclic loading acting on a sand surface, I: Theory description and numerical approach. Technical report, Internal Report NO.5 SFB-205, TPA13, Kusteningenieurwesen, University Hannover.

Madsen, O. S. (1978). Wave-induced pore pressure and effective stresses in a porous bed. *Géotechnique*, 28(4):377–393.

Mase, H., Sakai, T., and Sakamoto, M. (1994). Wave-induced porewater pressure and effective stresses around breakwater. *Ocean Engineering*, 21(4):361–379.

Miyamoto, J., Sassa, S., and Sekiguchi, H. (2004). Progressive solidification of a liquefied sand layer during continued wave loading. *Géotechnique*, 54(10):617–629.

Mizutani, N. and Mostafa, A. M. (1998). Dynamic interaction of nonlinear waves and a seawall over sand seabed. *International Journal of Offshore and Polar Engineering*, 8(1):30–38.

Mizutani, N., Mostafa, A. M., and Iwata, K. (1999). Numerical modeling of nonlinear interaction between wave and composite breakwater over sand bed. *Journal of Hydraulic, Coastal and Environmental Engineering JSCE*, 614(II-14):121–133.

Mizutani, N., Mostarfa, A., and Iwata, K. (1998). Nonliear regular wave, submerged breakwater and seabed dynamic interaction. *Coastal Engineering*, 33:177–202.

Mory, M., Michallet, H., Bonjean, D., Piedra-Cueva, I., Barnoud, J. M., Foray, P., Abadie, S., and Breul, P. (2007). A field study of momentary liquefaction caused by waves around a coastal structure. *Journal of Waterway, Port, Coastal and Ocean Engineering ASCE*, 133(1):28–38.

Moshagen, H. and Torum, A. (1975). Wave induced pressures in permeable seabeds. *Journal of the Waterways Harbors and Coastal Engineering ASCE*, 101(1):49–57.

Mostafa, A., Mizutani, N., and Iwata, K. (1999). Nonlinear wave, composite breakwater, and seabed dynamic interaction. *Journal of Waterway, Port, Coastal, and Ocean Engineering ASCE*, 25(2):88–97.

Nago, H., Maeno, S., Matsumoto, T., and Hachiman, Y. (1993). Liquefaction and densification of loosely deposited sand bed under water pressure variation. In *Proceeding of the 3rd international offshore and Polar Engineering Conference*, pages 578–584, Singapore.

Nakamura, H., Onishi, R., and Minamide, H. (1973). On the seepage in the seabed due to waves. In *Proceeding of 9th Annual Offshore Technology conference*, pages 141–145.

Newmark, N. M. (1959). A method of computation for structural dynamics. *Journal of Engineering Mechanics Division, ASCE*, 85:67–94.

Oh, Y. H., Jeng, D. S., Teo, H. T., and Cha, D. H. (2002). Effects of wave non-linearity on the wave-induced seabed response. In *12th international offshore and Polar Engineering Conference*, pages 738–744.

Oka, F., Yashima, A., Shibata, T., Kato, M., and Uzuoka, R. (1994). Fem-fdm coupled liquefaction analysis of a porous soil using an elasto-plastic model. *Applied Scientific Research*, 52(3):209–245.

Okusa, S. (1985). Wave-induced stress in unsaturated submarine sediments. *Géotechnique*, 35(4):517–532.

Ou, J. H. (2009). *Three-dimension numerical modeling of interaction between soil and pore fluid*. PhD thesis, University of Birmingham, Birmingham UK.

Oumeraci, H. (1994). Review and analysis of vertical breakwater failures ł lessons learned special issue on vertical breakwaters. *Coastal Engineering*, 22:3–29.

Oumeraci, H., Kortenhaus, A., Allsop, W., Groot, M., Crouch, R., and Voortman, H. (2001). *Probabilistic design tools for vertical breakwaters*. A A Balkema, Tokyo, Japan.

Pastor, M., Zienkiewicz, O. C., and Chan, A. H. C. (1990). Generalized plasticity and the modelling of soil behaviour. *International Journal for Numerical and Analytical Methods in Geomechanics*, 14:151–190.

Pietruszczak, S. and Pande, G. N. (1996). Constitutive relations for partially saturated soils containing gas inclusions. *Journal of Geotechnical Engineering, ASCE*, 122(1):50–59.

Putnam, J. A. (1949). Loss of wave energy due to percolation in a permeable sea bottom. *Transactions-American Geophysical Union*, 30(3):349–356.

Puzrin, A. M., Alonso, E. E., Pinyol, N., Puzrin, A. M., Alonso, E. E., and Pinyol, N. M. (2010). Caisson failure induced by liquefaction: Barcelona harbour, spain. In *Geomechanics of Failures*, pages 85–148. Springer Netherlands.

Rahman, M. S. and Jaber, W. Y. (1986). Simplified drained analysis for wave-induced liquefaction in ocean floor sands. *Soils and Foundations*, 26(3):57–68.

Raman, N. W. and Sabin, G. (1991). Wave-induced failure of poro-plastic seabed slopes: A boundary element study. *Proceeding of Institute of Civil Engineering*, Part 2(91):771–794.

Sassa, S. and Sekiguchi, H. (1999). Wave-induced liquefaction of beds of sand in a centrifuge. *Géotechnique*, 49(5):621–638.

Sassa, S. and Sekiguchi, H. (2001). Analysis of wave-induced liquefaction of sand beds. *Géotechnique*, 51(2):115–126.

Sassa, S., Sekiguchi, H., and Miyamoto, J. (2001). Analysis of progressive liquefaction as a moving-boundary problem. *Géotechnique*, 51(10):847–857.

Sassa, S., Takayama, T., Mizutani, M., and Tsujio, D. (2006). Field observations of the build-up and dissipation of residual porewater pressures in seabed sands under the passage of stormwaves. *Journal of Coastal Research*, 39:410–414.

Sawicki, A. and Staroszczyk, R. (2008). Wave-induced stresses and pore pressures near a mudline. *Oceanologia*, 50(4):539–555.

Seed, H. B., Martin, P. O., and Lysmer, J. (1976). Pore-water pressure changes during soil liquefaction. *Journal of Geotechnical Engineering ASCE*, 102(4):323–346.

Seed, H. B. and Rahman, M. S. (1978). Wave-induced pore pressure in relation to ocean floor stability of cohesionless soils. *Marine Geotechnology*, 3(2):123–150.

Sekiguchi, H., Kita, K., and Okamoto, O. (1995). Response of poro-elastoplastic beds to standing waves. *Soils and Foundation*, 35(3):31–42.

Seymour, B. R., Jeng, D. S., and Hsu, J. R. C. (1996). Transient soil response in a porous seabed with variable permeability. *Ocean Engineering*, 23(1):27–46.

Silvester, R. and Hsu, J. R. C. (1989). Sines revisited. *Journal of Waterway, Port, Coastal, Ocean Engineering, ASCE*, 115(3):327–344.

Sleath, J. (1970). Wave-induced pressures in beds of sand. *Journal of the Waterways Harbors and Coastal Engineering ASCE*, 96(2):367–378.

Sorenson, T. (1992). Breakwater failure brings lessons (ltr). *Civil Engineering-ASCE*, 62(9):37–38.

Sumer, B. M., Fredsoe, J., Christensen, S., and Lind, M. T. (1999). Sinking/floatation of pipelines and other objects in liquefied soil under waves. *Coastal Engineering*, 38(2):53–90.

Sumer, B. M., Kirca, V. S. O., and Fredsoe, J. (2011). Experimental validation of a mathematical model for seabed liquefaction in waves. In *Proceedings of the International Offshore and Polar Engineering Conference*, pages 1010–1018.

Sumer, B. M., Truelsen, C., and Fredsoe, J. (2006a). Liquefaction around pipelines under waves. *Journal of Waterway, Port, Coastal and Ocean Engineering ASCE*, 132(4):266–275.

Sumer, M. B., Dixen, F. H., and Fredsoe, J. (2010). Cover stones on liquefiable soil bed under waves. *Coastal Engineering*, 57(9):864–873.

Sumer, M. B., Hatipoglu, F., Fredsoe, J., and Kaan, S. S. (2006b). The sequence of sediment behaviour during wave-induced liquefaction. *Sedimentology*, 53(3):611–629.

Takahashi, S., Shimosako, K. I., Kimura, K., and Suzuki, K. (2000). Typical failures of composite breakwaters in japan. In *Coastal Engineering 2000 - Proceedings of the 27th International Conference on Coastal Engineering, ICCE 2000*, volume 276, pages 1899–1910.

Teh, T. C., Palmer, A. C., and Damgaard, J. S. (2003). Experimental study of marine pipelines on unstable and liquefied seabed. *Coastal Engineering*, 50(1-2):1–17.

Terzaghi, K. (1925). *Erdbaumechanik auf Bodenphysikalischer Grundlage*. F. Duticke, Vienna.

Truchas (2009). *TRUCHAS Physics and Algorithms*. Los Alamos National Laboratory, version-2.5.3 edition.

Tsai, C. P. (1995). Wave-induced liquefaction potential in a porous seabed in front of a breakwater. *Ocean Engineering*, 22(1):1–18.

Tsai, C. P., Chen, H.-B., and Jeng, D.-S. (2009). Wave attenuation over a rigid porous medium on a sandy seabed. *Journal of Engineering Mechanics ASCE*, 135(11):1295–1304.

Tsai, C. P. and Lee, T. L. (1995). Standing wave induced pore pressure in a porous seabed. *Ocean Engineering*, 22(6):505–517.

Tsai, C. P., Lee, T. L., and Hsu, J. (2000). Effects of wave nonlinearity on the standing wave-induced seabed response. *International Journal of Numerical and Analytical Method in Geomechanics*, 24(11):869–892.

Tzang, S.-Y., Chen, Y. L., and Ou, S.-H. (2011). Experimental investigations on developments of velocity field near above a sandy bed during regular wave-induced fluidized responses. *Ocean Engineering*, 38(7):868–877.

Tzang, S.-Y. and Ou, S. H. (2006). Laboratory flume studies on monochromatic wave-fine sandy bed interactions. part 1. soil fluidization. *Coastal Engineering*, 53(11):965–982.

Tzang, S.-Y., Ou, S.-H., and Hsu, T. W. (2009). Laboratory flume studies on monochromatic wave-fine sandy bed interactions part 2. sediment suspensions. *Coastal Engineering*, 56(3):230–243.

Ulker, M. B. C. and Rahman, M. S. (2009). Response of saturated and nearly saturated porous media: Different formulations and their applicability. *International Journal for Numerical and Analytical Methods in Geomechanics*, 33(5):633–664.

Ulker, M. B. C., Rahman, M. S., and Guddati, M. N. (2010). Wave-induced dynamic response and instability of seabed around caisson breakwater. *Ocean Engineering*, 37(17-18):1522–1545.

Ulker, M. B. C., Rahman, M. S., and Guddati, M. N. (2012). Breaking wave-induced response and instability of seabed around caisson breakwater. *International Journal for Numerical and Analytical Methods in Geomechanics*, 36(3):362–390.

Ulker, M. B. C., S, R. M., and Jeng, D. S. (2009). Wave-induced response of seabed: Various formulation and their applicability. *Applied Ocean Research*, 31:12–24.

Verruijt, A. (1969). Elastic storage of aquifers. *Flow Through Porous Media*, pages 331–376.

Wang, J. G., Karim, M., and Lin, P. (2007). Analysis of seabed instability using element free galerkin method. *Ocean Engineering*, 34(2):247 – 260.

Wang, J. G., Nogami, T., Dasari, G. R., and Lin, P. Z. (2004a). A weak coupling algorithm for seabed-wave interaction analysis. *Computer Methods in Applied Mechanics and Engineering*, 193(36-38):3935–3956.

Wang, J. G., Zhang, B., and Nogami, T. (2004b). Wave-induced seabed response analysis by radial point interpolation meshless method. *Ocean Engineering*, 31(1):21–42.

Williams, S. J. and Jeng, D.-S. (2007). The effects of a porous-elastic seabed on interfacial wave propagation. *Ocean Engineering*, 34(13):1818–1831.

Xiao, H., Young, Y. L., and Prevost, J. H. (2010a). Hydro- and morpho-dynamic modeling of breaking solitary waves over a fine sand beach. part ii: Numerical simulation. *Marine Geology*, 269(3-4):119–131.

Xiao, H., Young, Y. L., and Prevost, J. H. (2010b). Parametric study of breaking solitary wave induced liquefaction of coastal sandy slopes. *Ocean Engineering*, 37(17-18):1546–1553.

Xu, H. and Dong, P. (2011). A probabilistic analysis of random wave-induced liquefaction. *Ocean Engineering*, 38(7):860–867.

Yamamoto, T. (1977). Wave induced instability seabeds. In ASCE, editor, *Proceeding of A.S.C.E. Special Conference, Coastal Sediments 77, Charleston, SC*, pages 898–913.

Yamamoto, T. (1981). Wave-induced pore pressures and effective stresses in inhomogeneous seabed foundations. *Ocean Engineering*, 8:1–16.

Yamamoto, T., Koning, H., Sellmeijer, H., and Hijum, E. V. (1978). On the response of a poro-elastic bed to water waves. *Journal of Fluid Mechanics*, 87(1):193–206.

Yang, S.-L., Shen, W.-Q., and Yang, Z.-S. (1995). The mechanism analysis of seafloor silt liquefaction under wave loading. *Chinese Journal of Geotechnic Engineering*, 17(4):28–37.

Young, Y. L., White, J. A., Xiao, H., and Borja, R. I. (2009). Liquefaction potential of coastal slopes induced by solitary waves. *Acta Geotechnica*, 4(1):17–34.

Yuhi, M. and Ishida, H. (2002). Simplified solution for wave-induced response of anisotropic seabed. *Journal of Waterway, Port, Coastal, and Ocean Engineering*, 128(1):46–50.

Zen, K., Jeng, D.-S., Hsu, J. R. C., and Ohyama, T. (1998). Wave-induced seabed instability: Difference between liquefaction and shear failure. *Soils and Foundations*, 38(2):37–47.

Zen, K., Umehara, Y., and Finn, W. D. L. (1985). A case study of the wave-induced liquefaction of sand layers under damaged breakwater. In *Proceeding 3rd Canadian Conference on Marine Geotechnical Engineering*, pages 505–520, Canada.

Zen, K. and Yamazaki, H. (1990a). Mechanism of wave-induced liquefaction and densification in seabed. *Soil and Foundations*, 30(4):90–104.

Zen, K. and Yamazaki, H. (1990b). Oscillatory pore pressure and liquefaction in seabed induced by ocean waves. *Soils and Foundations*, 30(4):147–161.

Zen, K. and Yamazaki, H. (1991). Field observation and analysis of wave induced liquefaction in seabed. *Soils and Foundations*, 31(4):161–179.

Zhang, F. G. and Ge, Z. J. (1996). A study on some causes of rubble mound breakwater failure. *China Ocean Engineering*, 10(4):473–481.

Zhang, G. D. and Gu, X. Y. (1993). The response of finite thickness sand-bed to wave loading. *Acta Mechanica Sinica*, 25(1):56–68.

Zhang, Y.-L. and Li, J. (2010). Analytical solution for wave-induced response of isotropic poro-elastic seabed. *Science China-Technological Sciences*, 53(10):2619–2629.

Zhou, X.-L., Xu, B., Wang, J.-H., and Li, Y.-L. (2011). An analytical solution for wave-induced seabed response in a multi-layered poro-elastic seabed. *Ocean Engineering*, 38(1):119 – 129.

Zhou, Y. H., Lu, H. B., and Chen, Z. J. (2005). Numerical simulation of pore water pressure response of elastic seabed under wave loading. *Journal of Waterway and Harbour*, 26(2):67–70.

Zienkiewicz, O. C., Chan, A. H. C., Pastor, M., Schrefler, B. A., and Shiomi, T. (1999). *Computational Geomechanics with Special Reference to Earthquake Engineering*. John Wiley and Sons, England.

Zienkiewicz, O. C., Chang, C. T., and Bettess, P. (1980). Drained, undrained, consolidating and dynamic behaviour assumptions in soils. *Géotechnique*, 30(4):385–395.

Zienkiewicz, O. C. and Mroz, Z. (1984). Generalized plasticity formulation and applications to geomechanics. In *Mechanics of Engineering Materials*. Chichester: John, Cambridge UK.

Zienkiewicz, O. C. and Scott, F. C. (1972). On the principle of repeatability and its application in analysis of turbine and pump impellers. *International Journal for Numerical Methods in Engineering*, 9:445–452.